EVALUATION OF THE IMPACT OF PHYSICAL MIXING ON OPTIMAL LOW SALINITY WATERFLOOD DESIGN CONSIDERING UNCERTAINTY

OLALEKAN AZEEZ LADIPO

A thesis presented for the degree of

Doctor of Philosophy (PhD)

IMPERIAL COLLEGE LONDON

Department of Earth Science and Engineering

October 2021

Supervised by:

Professor Peter R. King
Professor Martin J. Blunt

Declaration

I hereby declare that this thesis titled '**EVALUATION OF THE IMPACT OF PHYSICAL MIXING ON OPTIMAL LOW SALINITY WATERFLOOD DESIGN CONSIDERING UNCERTAINTY**' is entirely my own work and all else is appropriately referenced. This work has not been previously submitted in its entirety or in part to any other academic institute for a degree or qualification.

Olalekan Azeez Ladipo

© 2021 'Lekan Ladipo

The copyright of this thesis rests with the author and is made available under a Creative Commons Attribution Non-Commercial No Derivatives licence. Researchers are free to copy, distribute or transmit the thesis on the condition that they attribute it, that they do not use it for commercial purposes and that they do not alter, transform or build upon it. For any reuse or redistribution, researchers must make clear to others the licence terms of this work.

Abstract

This thesis investigates the impact of physical mixing in controlled/low salinity waterflooding (LSWF) on optimal slug injection taking into account uncertainties in the reservoir description. The main motivation is that uncertainty can be detrimental to optimal field-scale implementation with poor scale-up performance even if cm-scale laboratory experiments suggest favourable recoveries. Mixing of the injected low salinity (LS) brine with high salinity (HS) formation brine potentially compromises the low salinity effect especially if injected as slugs. Other physical effects including reservoir heterogeneity and crossflow exacerbate such interaction between the distinct brines. It is challenging to capture this physical mixing accurately in reservoir simulations of LSWF because of numerical dispersion.

In this thesis, a new methodology, based on 'effective or pseudo' salinity-thresholds, is proposed to allow accurate and representative field-scale simulation of the effect of physical mixing accounting for numerical errors. The effect of inter-well mixing is quantitatively evaluated on LS slug performance, its displacement stability, and the optimal amounts to inject considering associated flow and geological uncertainties. The influence of LS injection start-time and flood or well pattern is examined. Injection optimization and performance uncertainty are assessed through validated experimental designs and response surfaces, in addition to a practical and effective approach to select representative geological realizations to minimize computational resources. Crossflow effects on LS displacement are explored for different mobility ratios with the more realistic non-piston-like shock-front using dimensionless numbers.

The procedure to constrain numerical dispersion shows improved effectiveness both in 1D and higher dimensions. Incremental recovery and the optimal slug injection are observed to be relatively insensitive to LS injection start-time for the line-drive, but not the quarter five-spot pattern, until tertiary-mode displacement becomes established. A favourable influence of the spatial distribution of heterogeneity is seen for both flood patterns, due to transverse dispersion. The optimal slug sizes from existing studies are, at best, only suitable as thresholds for stable LS displacement of the injected slug. For a cumulative water injection of 2 PV, LS slug design would require at least 0.8 PV optimal size and 0.24 PV minimum stability-threshold size across flood patterns. This can vary with the cumulative water injected and flood pattern but remains generally favoured by an early injection. The optimal slug size is found to be largely insensitive to heterogeneity for the Q5S flood pattern. It is found that the slug size dependence of performance and LS displacement stability – under the effects of physical mixing in multidimensional models – is a function of well arrangement. An unfavourable mobility-ratio

case is identified for viscous-dominated crossflow effects on LS recovery efficiency. Ways to improve the flood design for favourable displacements given this mobility-ratio case are presented.

Publications

Parts of this thesis have been published in the following:

Ladipo, L., Blunt, M.J., King, P.R., 2020. A salinity cut-off method to control numerical dispersion in low-salinity waterflooding simulation. J. Pet. Sci. Eng. 184, 106586.

Ladipo, L., Blunt, M.J., King, P.R., 2020. Optimizing Low Salinity Waterflooding with Controlled Numerical Influence of Physical Mixing Considering Uncertainty. In: ECMOR XVII - 17th European Conference on the Mathematics of Oil Recovery. pp. 1–23.

Ladipo, L., Blunt, M.J., King, P.R., 2022. Crossflow effects on low salinity displacement in stratified heterogeneity. J. Pet. Sci. Eng. 208 (C), 109565.

Acknowledgements

Prof. Peter King, Prof. Martin Blunt, Prof. Ann Muggeridge, Dr. Sam Krevor, and all the support staff at Imperial College London.

This work was carried out under the Presidential Special Scholarship for Innovation and Development (PRESSID) of the National Universities Commission (NUC). I gratefully acknowledge the funding provided by the Petroleum Technology Development Fund (PTDF). Imperial College London and the Department of Earth Science and Engineering (ESE) are sincerely thanked for their financial supports towards completing this research. Schlumberger and the Computer Modelling Group (CMG) are acknowledged for providing the reservoir simulation software used in this study.

A special appreciation to my family and friends for their immeasurable supports and encouragement during this endeavour.

Contents

Abstract **3**
Publications **5**
Contents **7**
List of Figures **10**
List of Tables **15**
1 Introduction **16**
2 Enhanced Oil Recovery: Low Salinity Waterflooding **20**
2.1 Description of the Local Displacement Process 20
2.2 Mechanisms Governing the Low Salinity Effect 21
2.3 Wettability Alteration 23
2.4 Low Salinity Effect (LSE) and Wettability Alteration: Experimental and Field Tests 26
2.5 Approaches to Modelling Low Salinity Waterflooding (LSWF) 27
2.5.1 Standard Tracer-component Model 27
2.5.2 Ion Exchange (Mechanistic) Model 29
2.5.3 Hybrid (Mechanistic) Model 30
2.6 Numerical Dispersion in Conventional LSWF Simulations 31
2.7 Impact of Reservoir Interactions and Mechanisms on Field-scale LSE Potential 35
2.7.1 Mixing 35
2.7.2 Reservoir Heterogeneity 42
2.7.3 Crossflow 47
3 Optimization of Injection Design under Uncertainty **51**
3.1 Sources of Uncertainty 51
3.2 Optimal Injection Design or Strategy 54
3.3 Recovery Uncertainty Assessment and Injection Design Optimization 55
3.3.1 Uncertainty Quantification (UQ) 55
3.3.2 Optimization 60
3.4 Concluding Remarks and Research Contributions 63
4 Controlling Numerical Dispersion Effects in Low Salinity Waterflooding Models **65**
4.1 Introduction 65
4.2 Numerical Dispersion in LSWF Simulations 67
4.2.1 Model Description 67
4.2.2 Analytical and Numerical Solutions 68
4.2.3 Discussion of Results 69

4.3 Correctional Procedure: Representing Advective (Non-Dispersive) Flow Effects in Simulations 73
4.3.1 1D Validation of the Correctional Approach 78
4.3.2 Extension to multidimensional systems 82
4.3.2.1 2D-System 83
4.3.2.2 3D-System 84
4.4 Modelling and Characterization of Effective Longitudinal Dispersion 85
4.4.1 1D Demonstration 86
4.5 Effective Dispersion in Models: Incorporating the Transverse Component 87
4.5.1 Description of Models 88
4.5.2 Discussion of Results 88
4.6 Modelling Physical Dispersion for Multidirectional Flows 93
4.7 Summary 94
5 Impact of Physical Mixing and Heterogeneity Interaction on the Optimal Low Salinity Slug Injection Considering Uncertainty 96
5.1 Introduction 96
5.2 Method 99
5.2.1 Description of the Models Used 99
5.2.2 Flow Variables and LS Slug Performance Indicators 104
5.2.3 Slug Performance Uncertainty Assessment and Injection Design Optimization 108
5.3 Results 110
5.3.1 Inter-well Homogeneity 110
5.3.1.1 Nominal Slug Performance 110
5.3.1.2 Slug Performance Considering Uncertainty 112
5.3.2 Sensitivity of Slug Performance and its Optimal Injection Design to Inter-well Heterogeneity 119
5.3.2.1 Set A Models Modified from SPE 10 Model 1 119
5.3.2.2 Set B Models from Geostatistical Property Modelling 124
5.4 Summary 128
6 Influence of Flood Pattern and Geological Uncertainty on the Impact of Mixing on Optimal Low Salinity Slug Injection 130
6.1 Introduction 130
6.2 Method 130
6.2.1 Description of the Models Used 130
6.3 Results 137
6.3.1 2D Models 137
6.3.1.1 Nominal Slug Performance Under Inter-well Homogeneity 137

6.3.1.2 Slug Performance Under Inter-well Homogeneity Considering Uncertainty 139
6.3.1.3 Sensitivity of Optimal Slug Injection to Inter-well Heterogeneity 143
6.3.1.4 Optimal Slug Injection Design Considering Geological Uncertainty 148
6.3.1.5 Optimal Slug Injection Design for More Representative Inter-well Heterogeneities. 151
6.3.2 3D Models 161
6.3.2.1 Optimal Slug Injection Sensitivity to Heterogeneity 162
6.3.2.2 Optimal Slug Injection for More Heterogeneous Reservoir Connectivity 166
6.4 Summary 172
7 Crossflow Effects on Low Salinity Displacement in Stratified Heterogeneity 175
7.1 Introduction 175
7.2 Model and Method: Scaling Analysis with Dimensionless Numbers 177
7.3 Results 183
7.3.1 Effect of Property Contrasts on Viscous-dominated Crossflow (VC) 183
7.3.2 Prediction of Viscous Crossflow (VC) Regimes in LSWF 185
7.3.3 Viscous Crossflow During Non-piston-like Displacements in LSWF 189
7.3.4 Viscous Crossflow Recovery Efficiency as Function of Shock-front Mobility Ratios 190
7.3.5 Designing Favourable Crossflow Effects with $\boldsymbol{MF, HS < 1 < MF, LS}$ 196
7.4 Summary 199
8 Summary and Recommendations 202
8.1 Summary 202
8.2 Research Directions for Future Work 206
References 208
Appendices 228
Appendix A – Evaluation of Longitudinal Dispersivity 228
Appendix B – Evaluation of Transverse Dispersivity in a Model 230
Appendix C – Relative permeabilities resulting from the Corey exponents and end-point relative permeabilities set for the different mobility-ratio cases 232
Appendix D – Viscous Crossflow Recovery Efficiency as Function of Shock-front Mobility Ratios in the Presence of Physical Dispersion 233
Appendix E – Influence of Gravity-Induced Crossflow on Recovery Efficiency Under Physical Mixing 236

List of Figures

Fig. 2.1: Relative permeabilities for different stages of more water-wetness of pore surfaces 24
Fig. 2.2: Typical one-dimensional Buckley Leverett water saturation and fractional flow profiles for secondary-mode LSWF 24
Fig. 2.3: Produced water during field-scale LSWF 25
Fig. 2.4: Schematic illustration of Taylor dispersion in two-layer porous media 38
Fig. 2.5: Simulation results demonstrating the use of numerical dispersion to approximate physical dispersion effects 41
Fig. 2.6: Displacement channelling through high permeability areas in fluvial sands 42
Fig. 2.7: Scales of subsurface geological heterogeneity 43
Fig. 2.8: Experimental and model variogram key parameters 45
Fig. 2.9: Typical transition variograms for constructing a variogram model 46
Fig. 3.1: Dispersivity as a function of length travelled 52
Fig. 3.2: Reported salinity-thresholds for the LSE 53
Fig. 3.3: Experimental design points 57
Fig. 3.4: Two-dimensional projections of columns for sampled input variable-pairs 58
Fig. 4.1. Analytical water saturation and fractional flow profiles for a 1D-homogeneous secondary-mode low-salinity waterflood 65
Fig. 4.2. Flow properties of systems used in this work 67
Fig. 4.3. Simulated profiles with different numbers of grid-blocks (GB) in comparison to the reference (analytical) solution 70
Fig. 4.4. Watercut as a function of pore volumes injected showing the characteristic signatures of numerical dispersion in LSWF simulations 71
Fig. 4.5. Error evaluation of the predicted watercut as a function of pore volumes injected 72
Fig. 4.6. A comparison of predicted normalized effluent profiles from the method of Muggeridge and Hongtong (2014), the method of Al-Ibadi et al. (2018a), and simulation results at different levels of dispersion 74
Fig. 4.7. Watercut as a function of pore volumes injected showing the simulated performance 75
Fig. 4.8. Typical evaluations of the LS water front velocity at different combinations of dispersion levels and salinity-thresholds using simulator output fractional flow 76
Fig. 4.9. (Step 1) Evaluation of effective salinity-thresholds for zero-dispersion (advective) effect 79
Fig. 4.10. (Step 2) Simulation results with and without the effective threshold salinities 81
Fig. 4.11. Simulation results with and without the effective threshold salinity procedure at different numbers of grid-blocks 82
Fig. 4.12. 2D permeability map and simulated performance 83
Fig. 4.13. 3D permeability map and simulated performance 84
Fig. 4.14. Production profiles of a simulation grid at different salinity-threshold ranges 86
Fig. 4.15. (a) Dispersion-characteristics (Peclet number) as a function of effective salinity-threshold range 87
Fig. 4.16. Influence of numerical dispersion on input physical longitudinal dispersion 89
Fig. 4.17. Influence of numerical dispersion on input physical transverse dispersion 90
Fig. 4.18. Steady-state salt concentration and oil saturation profiles in the transverse direction with zero input transverse dispersivity 91
Fig. 4.19. Steady-state salt concentration and oil saturation profiles in the transverse direction with different input transverse dispersivities 92

Fig. 4.20. Estimation of the critical input dispersivity for the 2D model at its non-zero effective longitudinal dispersion.....94
Fig. 5.1: LS displacement stability and performance of an injected slug under flow (mixing) uncertainty at different injection stages 97
Fig. 5.2: Relative permeabilities.....98
Fig. 5.3: Base models considered.....100
Fig. 5.4: Statistical moments of the permeability distributions in the realizations as a function of the defined degrees of heterogeneity 102
Fig. 5.5: Heterogeneous realizations considered.....103
Fig. 5.6: Typical profiles of total and marginal efficiencies for LS slug injection under physical dispersion.....107
Fig. 5.7: Watercut (WC) as a function of cumulative pore volumes injected (PVI) in a LSWF of 0.35 PV slug size injected after pre-injecting different volumes (PV) of HS formation water.....110
Fig. 5.8: Water saturation and salinity distribution just before breakthrough of a 0.35 PV LS-slug size injected after pre-injecting different volumes (PV) of HS formation water showing the effective displacement mode. 111
Fig. 5.9: Incremental recovery as a function of initialization times of LS water injection at different injected slug sizes (PV) in the homogeneous model 111
Fig. 5.10: Estimation of the stability-threshold injection from different optimization techniques....112
Fig. 5.11: Tornado plots showing the sensitivity of the base performance of the stability-threshold injection to the flow variables 113
Fig. 5.12: Sampling quality of 5,000 realizations of input variables 114
Fig. 5.13: Statistical moments of predicted stability-threshold slug performance distributions at different injection times using proxy-models in comparison with real reservoir simulation results. 116
Fig. 5.14: Blind tests with some injection strategies or scenarios.....116
Fig. 5.15: Statistical moments of performance distributions at different injected slug sizes 117
Fig. 5.16: Statistical moments of performance distributions at different LS injection times after pre-injecting different volumes (PV) of high-salinity formation water 118
Fig. 5.17: Statistical moments of performance distributions at different LS injection times relative to the breakthrough of any pre-injected high-salinity formation water 118
Fig. 5.18: Base performance as a function of injected slug size at different degrees of heterogeneity 119
Fig. 5.19: Threshold slug size and maximum total efficiency from nominal optimization techniques as a function of heterogeneity 120
Fig. 5.20: Sensitivity of slug performance and recovery to flow variables as a function of heterogeneities.....121
Fig. 5.21: Salinity and oil saturation distributions illustrating the favourable influence of transverse dispersion in areal heterogeneity on recovery. 122
Fig. 5.22: Mean performance under flow uncertainties as a function of injected slug size at different degrees of heterogeneity.....123
Fig. 5.23: Performance risks under flow uncertainties as a function of injected slug sizes at different degrees of heterogeneity.....123
Fig. 5.24: Base performance as a function of injected slug size at different degrees of heterogeneity 124
Fig. 5.25: Threshold slug size and maximum total efficiency from nominal optimization techniques as a function of heterogeneities 125
Fig. 5.26: Sensitivity of slug performance and recovery to flow variables as a function of heterogeneities.....126

Fig. 5.27: Salinity and oil saturation distributions with areal heterogeneity....126
Fig. 5.28: Mean performance under flow uncertainties as a function of injected slug size at different degrees of heterogeneity....127
Fig. 5.29: Performance risks under flow uncertainties as a function of injected slug sizes at different degrees of heterogeneity....128
Fig. 6.1: 2D base models considered....131
Fig. 6.2: 3D base model considered under a quarter five-spot flood pattern....132
Fig. 6.3: 2D heterogeneous realizations considered for each well pattern....133
Fig. 6.4: 3D heterogeneous realizations considered under quarter five-spot (Q5S) well pattern....134
Fig. 6.5: Watercut (WC) as a function of cumulative pore volumes injected (PVI) in a LSWF of 0.35 PV slug size injected after pre-injecting different volumes (PV) of HS formation water with different flood patterns....137
Fig. 6.6: Water saturation and salinity distributions just before breakthrough of a 0.35 PV LS-slug size injected after pre-injecting different volumes (PV) of HS formation water showing the effective displacement mode in a Q5S flood pattern....138
Fig. 6.7: Incremental recovery as a function of initialization times of LS water injection at different injected slug sizes (PV) for the homogeneous case under different flood patterns....139
Fig. 6.8: Statistical moments of performance distributions at different injected slug sizes....140
Fig. 6.9: Statistical moments of performance distributions at different LS injection times after pre-injecting different volumes (PV) of high-salinity formation water....141
Fig. 6.10: Statistical moments of performance distributions at different LS injection times relative to the breakthrough of any pre-injected high-salinity formation water....142
Fig. 6.11: Base performance as a function of injected slug size at different degrees of heterogeneity....143
Fig. 6.12: Sensitivity of slug performance and recovery to flow variables as a function of heterogeneities....144
Fig. 6.13: Salinity and oil saturation distributions illustrating the favourable influence of transverse dispersion in areal heterogeneity on recovery in a Q5S flood pattern....145
Fig. 6.14: Mean performance under flow uncertainties as a function of injected slug size at different degrees of heterogeneity....146
Fig. 6.15: Performance risks under flow uncertainties as a function of injected slug size at different degrees of heterogeneity....147
Fig. 6.16: Random geostatistical realizations of spatial permeability distribution for inter-well heterogeneity at a normalized correlation length or range of 0.033 in both coordinate directions 149
Fig. 6.17: Mean performance under only flow uncertainties and in combination with geological uncertainty as a function of injected slug size for the base heterogeneous case in comparison to the homogeneous equivalence for both well patterns....150
Fig. 6.18: Performance risks under only flow uncertainties and in combination with geological uncertainty as a function of injected slug size for the base heterogeneous case in comparison to the homogeneous equivalence for both well patterns....151
Fig. 6.19: Statistical moments of the computed ultimate recovery factor from both case-simulations as a function of normalized correlation length for inter-well heterogeneity with an exponential variogram model....152
Fig. 6.20: Statistical moments of the computed ultimate recovery factor from both case-simulations as a function of normalized correlation length for inter-well heterogeneity with a Gaussian variogram model....152
Fig. 6.21: Random geostatistical realizations of spatial permeability distribution for inter-well heterogeneity at different normalized correlation lengths and variogram models....154

Fig. 6.22: Mean performance as a function of injected slug size for inter-well heterogeneity with an exponential variogram model at different correlation lengths 155
Fig. 6.23: Performance risks as a function of injected slug size for inter-well heterogeneity with an exponential variogram model at different correlation lengths 156
Fig. 6.24: Flood fronts and recovery from the optimal slug injection for inter-well heterogeneity with an exponential variogram model at different correlation lengths 157
Fig. 6.25. Mean performance as a function of injected slug size for inter-well heterogeneity with a Gaussian variogram model at different correlation lengths 158
Fig. 6.26. Performance risks as a function of injected slug size for inter-well heterogeneity with a Gaussian variogram model at different correlation lengths 159
Fig. 6.27: Flood fronts and recovery from the optimal slug injection for inter-well heterogeneity with a Gaussian variogram model at different correlation lengths 161
Fig. 6.28: Mean performance under flow uncertainties as a function of injected slug size at different degrees of heterogeneity 162
Fig. 6.29: Performance risks under flow uncertainties as a function of injected slug size at different degrees of heterogeneity 163
Fig. 6.30: Random geostatistical realizations of spatial permeability distribution for inter-well heterogeneity at a normalized correlation length or range of 0.033 in all coordinate directions 164
Fig. 6.31: Mean performance under only flow uncertainties and in combination with geological uncertainty as a function of injected slug size for the base heterogeneous models 165
Fig. 6.32: Performance risks under only flow uncertainties and in combination with geological uncertainty as a function of injected slug size for the base heterogeneous models 166
Fig. 6.33: Random geostatistical realizations of spatial permeability distribution for inter-well heterogeneity at different normalized correlation lengths and variogram models 168
Fig. 6.34: Mean performance as a function of injected slug size for inter-well heterogeneity with an exponential variogram model at different correlation lengths 169
Fig. 6.35: Performance risks as a function of injected slug size for inter-well heterogeneity with an exponential variogram model at different correlation lengths 170
Fig. 6.36: Mean performance as a function of injected slug size for inter-well heterogeneity with a Gaussian variogram model at different correlation lengths 171
Fig. 6.37: Performance risks as a function of injected slug size for inter-well heterogeneity with a Gaussian variogram model at different correlation lengths 172
Fig. 7.1: Schematics of the displacing-phase distribution and regions contacted along a two-layered porous medium neglecting capillarity and gravity 175
Fig. 7.2: Schematic diagram of the two-layer model used 177
Fig. 7.3: Recovery efficiency as a function of property-contrast ratios 184
Fig. 7.4: Displacing-phase (water) saturation profile showing its relative velocity or mobility in the layers just before breakthrough at different property-contrast ratios 185
Fig. 7.5: Schematic of pressure profiles obtained in the fast and slow layers for a typical waterflood without crossflow 187
Fig. 7.6: Schematic of pressure profiles obtained in the fast and slow layers for a LSWF without crossflow 188
Fig. 7.7: Displacing-phase viscous crossflow behaviours relative to a no crossflow displacement as a function of the characterized shock-front mobility-ratio cases 189
Fig. 7.8: Change in recovery efficiency due to crossflow as a function of crossflow amount for various shock-front mobility-ratio cases in a convective secondary LSWF 191

Fig. 7.9: Change in recovery efficiency due to crossflow as a function of crossflow amount for various shock-front mobility-ratio cases in a secondary LSWF with significant dispersion (Pe of 2.0% of the model-length) 192
Fig. 7.10: Water saturation and salinity profiles within the limits of no viscous crossflow and viscous crossflow equilibrium for the $M_{F,HS} < 1 < M_{F,LS}$ mobility-ratio case for a convective secondary LSWF..... 194
Fig. 7.11: Water saturation and salinity profiles within the limits of no viscous crossflow and viscous crossflow equilibrium for a secondary LSWF with significant dispersion..... 195
Fig. 7.12: Change in recovery efficiency due to gravity-assisted crossflow as a function of crossflow amount in comparison to that without gravity (i.e. viscous-dominated) in a secondary LSWF for a convective flow regime and under dispersion (*Pe* of 2.0% of the model-length) 196
Fig. 7.13: Mid-time recovery efficiency as a function of shape factor at different levels of physical mixing with and without transverse dispersion for the no crossflow limit. Change in recovery efficiency due to VC as a function of crossflow amount at different shape factor and performance times 198
Fig. B.1: A schematic of the 2D-model used for the evaluation of transverse dispersion..... 230
Fig. B.2: An example of a concentration map showing the effect of transverse dispersion 230
Fig. C.1: Relative permeabilities for the various shock-front mobility-ratio cases under different wettability conditions 232
Fig. D1: Change in recovery efficiency due to crossflow as a function of crossflow amount for various shock-front mobility-ratio cases in a secondary LSWF under dispersion (*Pe* of 1.0% of the model-length)..... 233
Fig. D2: Change in recovery efficiency due to crossflow as a function of crossflow amount for various shock-front mobility-ratio cases in a secondary LSWF under dispersion (*Pe* of 3.5% of the model-length)..... 234
Fig. D3: Change in recovery efficiency due to crossflow as a function of crossflow amount for various shock-front mobility-ratio cases in a secondary LSWF under dispersion (*Pe* of 5.0% of the model-length)..... 235
Fig. E1: Change in recovery efficiency due to gravity-assisted crossflow as a function of crossflow amount in comparison to that without gravity (i.e. viscous-dominated) in a secondary LSWF under a convective flow regime and under dispersion (*Pe* of 1.0% of the model-length) 236
Fig. E2: Change in recovery efficiency due to gravity-assisted crossflow as a function of crossflow amount in comparison to that without gravity (i.e. viscous-dominated) in a secondary LSWF for a convective flow regime and under dispersion (*Pe* of 3.5% of the model-length) 237
Fig. E3: Change in recovery efficiency due to gravity-assisted crossflow as a function of crossflow amount in comparison to that without gravity (i.e. viscous-dominated) in a secondary LSWF under a convective flow regime and under dispersion (*Pe* of 5.0% of the model-length) 238

List of Tables

Table 2.1: Conditions for transitions between the dominated regions (Zhou et al., 1994) 49
Table 4.1: Description of the 1D-System 67
Table 4.2: Descriptions of the 1D and 2D models 88
Table 5.1: Description of the 2D-System 100
Table 5.2: Summary of the variables used in the simulations in this chapter 106
Table 5.3: Summary of the nominal optimization results for the threshold strategy 113
Table 6.1: Description of the 2D and 3D models 132
Table 6.2: Summary of the variables used in the simulations in this chapter 136
Table 6.3: Mean and standard deviation of the computed ultimate recovery factor, URF 148

1 Introduction

Traditional oil recovery processes often leave at least 50% of the oil trapped in petroleum reservoirs (Lake et al., 2014). This has shifted most investment decisions during a period of oil price volatility and increasing global energy demand towards maximizing recovery from these reservoirs. Enhanced Oil Recovery (EOR) processes are key to improve petroleum recovery from conventional primary recovery and waterflooding. They target a wide range of crude oils with different physical and chemical properties – but, previously, were not applied widely due to their high cost and complexity.

Of these processes, Controlled/Low Salinity Waterflooding (LSWF) has the advantage of being low-cost and environmentally-friendly (Sheng, 2010). It is an emerging method for both clastic and carbonate reservoirs that has caught the attention of researchers (Tang and Morrow, 1999; Lager et al., 2007; Jerauld et al., 2008; Austad et al., 2010; Puntervold et al., 2015; McMillan et al., 2016; Al-Shalabi and Sepehrnoori, 2016; Mahmoudpour and Pourafshary, 2021). LSWF is defined as an augmented or engineered waterflooding where the ionic concentrations and/or compositions of the injected water is modified relative to the *in situ* brine to improve oil recovery. For sandstones, it is widely regarded to typically involve desalinating or lowering the total salinity of the injected brine.

Despite increasing interest over the past decades, uncertainty concerning the exact mechanism(s) of LSWF has contributed to limiting its field deployment. Wettability alteration making the pore surfaces more water-wet is now widely accepted as the primary cause of the associated improved recovery from the low salinity effect (LSE) (Jerauld et al., 2008; Dang et al., 2015; Bartels et al., 2019; Katende and Sagala, 2019; Liu and Wang, 2020). This causes a change in the relative permeabilities which manifests, at the macroscale, by a connate water-oil bank signature that has been observed in core and field tests.

The size of the connate water or oil bank influences the improved displacement efficiency from the injected low-salinity (LS) brine. However, mixing of the injected LS brine with connate or *in situ* brine and/or active ion transport can compromise its integrity to delay or even suppress the LSE particularly if limited (i.e. slug injections). Besides, such interaction between the distinct brines is enhanced when the flood front becomes distorted by other physical effects such as reservoir heterogeneity and crossflow. Therefore, this becomes crucial since slug injection schemes are usually favoured by field economics with less injected chemical, and often greater displacement stability and sweep efficiency.

Reservoir complexity introduces uncertainty in the exact magnitude of these physical effects on the flood displacement, which makes it difficult to design an effective injection strategy. Even though

finding the optimal slug injection that maximizes the flood performance criteria while justifying related capital and ongoing costs may be difficult and challenging, it is a key factor for its successful field-scale application.

There were a few attempts to evaluate the optimal amounts of low-salinity brine to inject considering the effects of mixing and heterogeneity in clastic reservoirs (Jerauld et al., 2008; Attar and Muggeridge, 2018). However, the impact of their uncertainties at inter-well scales was not or only poorly considered in these works. Meanwhile, it remains important to guarantee a return on investment through the selection of a suitable injection strategy for optimal performance and/or reduced risks from physical mixing. Where the influence of geological uncertainty was investigated (Dang et al., 2017), the dependence of the optimal injected LS slug amount on flood or well pattern was not examined in the presence of mixing.

Crossflow is a major factor affecting recovery efficiency in heterogeneous permeable media. Improved oil recovery efficiency due to viscous-dominated crossflow has been proposed relative to no-crossflow. While this was suggested to be dependent on the displacement shock-front – sharpening or spreading (Zapata and Lake, 1981), or the mobility ratio across it (Debbabi et al., 2017), the literature has been on mainly typical water-oil displacements. Hence, crossflow effects are not fully understood for augmented or engineered waterfloods.

To analyse the impact of the different physical phenomena on recovery from LSWF, a detailed reservoir simulation study is needed. Unfortunately, simulation results from existing LSWF models are erroneously affected by numerical dispersion especially in conventional numerical grids that are computationally practical. Since this problem cannot be readily addressed with higher-order numerical schemes or fine-grid resolution, the use of 'pseudo or effective' salinity-thresholds were proposed to capture the displacement fronts accurately (Jerauld et al. 2008; Muggeridge and Hongtong, 2014; Al-Ibadi et al., 2018a). However, discrepancies between the coarse- and (reference) fine-scale results were still seen with these methods.

Given the information above, this research explores primarily the modelling and the impact of mixing on LSWF efficiency and optimal field-scale injection design under geological uncertainties. Four main areas of objective are focussed on in this thesis using detailed simulation investigations: (i) Control of numerical dispersion effects in LSWF simulations; (ii) Evaluate how the interaction between inter-well mixing and geological heterogeneity affects the optimal LS slug injection considering uncertainty; (iii) Examine the influence of flood or well pattern and geological uncertainty on the impact of physical mixing on the optimal slug injection design; and (iv) Explore crossflow effects on displacement during LSWF in stratified heterogeneous permeable media, to aid its injection design.

In this thesis, we propose a methodology to allow accurate and representative field-scale simulations of LSWF accounting for the effect of physical mixing amidst numerical influence. This is then combined with a detailed quantitative analysis of the uncertainty in the magnitude of the physical effects on LS displacement. Following that, the optimal slug injection design for flow predominantly along homogeneous inter-well paths is evaluated. Additionally, this thesis considers the sensitivity of the optimal slug injection to heterogeneity for its scale-up under uncertainty in the effects of both physical mixing and geological heterogeneity for different flood patterns. The significance of transverse mixing when heterogeneity impacts the areal sweep is also investigated to understand their critical effects on slug exposure and performance. A more comprehensive treatment is presented for crossflow effects on displacement efficiency in LSWF considering physical mixing – for different mobility ratios with the more realistic non-piston-like displacement shock-front.

Analyses in this study are limited to only technical uncertainty – which refers to uncertainty in the realization of some reservoir and LSE-controlling spatial and parametric properties respectively – associated with mixing. Injection optimization and performance uncertainty are assessed through validated experimental designs and response surfaces, in addition to a practical and effective approach to select representative geological realizations to minimize computational resources.

Chapter 2 begins with an overview of the low salinity waterflooding process – including a discussion of the uncertainty surrounding the proposed (pore-scale) mechanisms governing the LSE. We review evidence that shows that LSWF can be a promising EOR process. Existing approaches to model LSWF are then discussed, while presenting the commonly used numerical simulators and their conventional limitations to capture the physical effects reliably amidst numerical errors. Following that, a review of the influence of some geo-physical reservoir interactions – mixing between the distinct brines, reservoir heterogeneity, and crossflow – on the improved displacement from the flood is presented.

A review of the uncertainties in the exact magnitude of these physical reservoir effects and some LSE-controlling parameters associated with mixing is presented in Chapter 3. The chapter concludes with the discussion on the techniques to assess the flood performance and optimize its injection design in the presence of these uncertainties.

Chapter 4 presents the methodology to constrain numerical dispersion for representative simulations of LSWF with physical mixing. This is very important as numerical influence can completely obscure the low salinity effect in simulations: without this correction, field-scale evaluations of the flood performance would be of doubtful accuracy. The limitations of existing methods to control numerical dispersion effects with the concept of ‘pseudo or effective’ threshold solute-component concentrations as suggested by Jerauld et al. (2008) are examined. A new simple-to-implement

approach to handle these limitations is then discussed and validated with examples. Later, the effects of pseudo (effective) thresholds on the transverse component of mixing in simulations are investigated. We finally discuss how to model physical mixing reliably in multidimensional coarse simulation grids amidst the inherent numerical component. This chapter consists of some material that was published as a journal article (Ladipo et al., 2020a).

Chapter 5 investigates the effect of physical mixing on the optimal slug amount (or size) for the flood considering flow uncertainties under a line-drive flood pattern in two-dimensions. The evaluation in this chapter excludes geological uncertainty in the description of reservoir heterogeneity. The impact of LS injection start-time on recovery and the effective displacement mode of the flood is initially presented. We then discuss the sensitivity of its optimal slug injection to injection start-time followed by heterogeneity. This chapter shows the significance of transverse mixing on how the interaction between inter-well mixing and areal heterogeneity can affect LS slug performance.

Geological uncertainty is introduced in Chapter 6 for line-drive and quarter five-spot well patterns. In 2D, we first examine how flood pattern influences the interaction between mixing and heterogeneity and its effects on LS slug performance, its displacement stability, and the optimal amounts to inject. The generality of the sensitivity of the optimal injected amounts to heterogeneity for quarter five-spot flood pattern is later tested in 3D models with more representative heterogeneous reservoir connectivity.

Chapter 7 presents the effects of crossflow on recovery or displacement efficiency along stratified media of contrasting properties during an engineered waterflood or LSWF. This transcends the no-crossflow, viscous- and gravity-dominated crossflow regimes in the presence of physical mixing. This is critical as LSWF has two distinct displacement shock-fronts – unlike the standard waterflood – that are potentially influenced by mixing of the brines which further complicates the crossflow behaviour. The chapter first examines the influence of property contrasts and mobility-ratios across the two shock-fronts on the viscous crossflow (VC) behaviour in a LSWF for non-piston-like displacements. The sensitivity of VC recovery and chemical-sweep efficiency to mobility-ratios is then evaluated relative to no-crossflow displacement to identify unfavourable mobility-ratios. The control of unfavourable displacements with VC is later discussed to aid better flood design. This chapter consists of some material that has been published as a journal article (Ladipo et al., 2022).

Chapter 8 summarizes this thesis by discussing its main findings from each chapter and the recommendations for future work.

2 Enhanced Oil Recovery: Low Salinity Waterflooding

Research interest on the EOR technique known as LSWF has increased sharply in recent years. The main motivation for its field application is the improvement in oil recovery by delayed water breakthrough and accelerated oil production, through improved microscopic displacement, compared to conventional high-salinity (HS) brine injection. This research aims to evaluate the impact of the interactions between physical mixing and reservoir heterogeneity on the optimal field-scale injection design or implementation of the flood considering uncertainty. To effectively conduct this, a critical review of the literature is therefore essential to identify research gaps on the effects of mixing and geological heterogeneity on the flood performance in existing studies.

This chapter first describes the low salinity waterflooding process – the pore-scale mechanisms that are largely believed to govern the low salinity effect (LSE) which improves oil recovery, and evidential demonstrations from laboratory experiments and field-scale trials that show LSWF as a promising EOR process. Existing approaches to model LSWF are then discussed, while presenting the commonly used numerical simulators and their conventional limitations to capture the physical effects reliably amidst numerical errors. We later examine the influence of some geo-physical reservoir interactions – which are significant to the performance response from an injection design – on the improved displacement from the flood.

2.1 Description of the Local Displacement Process

Controlled/Low Salinity Waterflooding (LSWF) is generally described as a process to improve oil recovery by modifying the ionic compositions or concentrations of the injected brine relative to the *in situ* brine during waterflooding. This is otherwise referred to as engineered water injection (EWI) for carbonates, where only the ionic compositions are modified to harden or soften the injected water (Al-Shalabi and Sepehrnoori, 2016; Adegbite et al., 2018) or both the concentrations and compositions are adjusted, as typical for carbonates and clastic (sandstone) reservoirs (Mahmoudpour and Pourafshary, 2021). While carbonates could give incremental oil even at high salinity, the LSE is now widely accepted to typically involve lowering the total salinity of the injected brine for clastic reservoirs which is the focus in this research.

Earlier coreflooding experiments on outcrop and reservoir sandstones by Tang and Morrow (1999) suggested that the salinity of the injected water should be in the range of $1{,}000$ - $7{,}000$ ppm compared to the injection of seawater – $30{,}000$ - $54{,}000$ ppm (Nasralla et al., 2013). Other studies have demonstrated the LSE only for salinities below $5{,}000$ ppm relative to injecting higher salinity

formation brine (Webb et al., 2004; McGuire et al., 2005; Morrow and Buckley, 2011; Suman et al., 2013). However, there remains a difference of observations and opinion about this effective salinity range as it is clear from the literature that it is thought to vary with a number of factors. Zhang and Morrow (2006) suggested that the salinity range varies from one reservoir to another, and depends on the rock type, reservoir fluid and mineral compositions, and importantly, the LSE mechanism(s) at play, which may also vary within a system.

2.2 Mechanisms Governing the Low Salinity Effect

While this thesis explores primarily the modelling and the impact of mixing on LSWF efficiency and optimal injection design under geological uncertainties, some attention is given to review the different theories and uncertainty surrounding the proposed pore-scale mechanisms governing the LSE. This is essential as it informs how the flood displacement is being generally modelled at the Darcy-scale, upon which our evaluations and findings on mixing effects in this work are based.

In addition to the significant reduction in injected brine salinity relative to that of formation water present, for example in sandstones, other necessary conditions for the LSE may include a significant clay fraction, presence of multivalent ions in the connate water, and exposure to crude-oil containing acid or basic polar components to create initially mixed- or oil-wet conditions (Bernard, 1967; Tang and Morrow, 1999; Lager et al., 2007; Morrow and Buckley, 2011; Alotaibi et al., 2011). However, these conditions remain qualitative and not necessarily sufficient, with the supporting evidence often far from overwhelming (Jackson et al. 2016). Furthermore, the exact mechanism that gives rise to incremental oil recovery by LSWF is still under debate due to the complexity of rock-oil-brine interactions in reservoir pores (Shaddel and Tabatabae-Nejad, 2015; Dang et al., 2016; Jackson et al., 2016). Nonetheless, several mechanisms have been suggested to explain the LSE: clay swelling and fines migration (Tang and Morrow, 1999), *pH* increase and surfactant generation or saponification (McGuire et al., 2005), multi-ion exchange (Lager et al., 2009), local increase in *pH* (RezaeiDoust et al., 2009; Austad et al., 2010), and double layer expansion (Ligthelm et al., 2009), salting-in (RezaeiDoust et al., 2009), or osmosis (Sandengen and Arntzen, 2013) amongst others. These remain topics of active research (Zeinijahromi et al., 2015; McMillan et al., 2016), alongside some contrary observations which are discussed briefly below.

Many studies have observed the LSE with no fines production or reduction in permeability (Zhang et al., 2007; Alagic and Skauge, 2010; Pu et al., 2010; Robertson, 2010; RezaeiDoust et al., 2011), while fines production in the effluent fluids and/or permeability decrease has been reported by others with no LSE (Cissokho et al., 2010; Cissokho et al., 2012; Nasralla et al., 2014). Therefore, fines migration

cannot be considered as the sole pore-scale mechanism for improved recovery from the LSE. Zhang and Morrow (2006), Boussour et al. (2009), and RezaeiDoust et al. (2011) observed the LSE with crudes of lower acid number than that required for saponification reactions ($pH > 9$) which is unlikely at reservoir conditions, owing to the presence of CO_2 and other *pH* buffers (Jackson et al., 2016). Lager et al. (2006) observed no relationship between the LSE and acid number. Moreover, further investigation by Zhang et al. (2007) found no correlation between the LSE and effluent *pH*. All these are inconsistent with the hypothesis that the LSE is conditional on *pH* increase and saponification.

Cation exchange with protons (H^+) at the clay surface is reflected by a local increase in *pH* as reported by Austad et al. (2010). Whereas, the proposed adsorption of Ca^{++} and Mg^{++} at low-salinity under the multi-ion exchange (MIE) mechanism does not cause a change in *pH*. Kaolinite with relatively low cation exchange capacity (CEC) has been closely associated with the LSE (Seccombe et al., 2008). In contrast, the MIE mechanism as proposed by Lager et al. (2008a) suggests high CEC for optimal LSE since clay minerals act as the ion exchangers. Therefore, MIE as a mechanism alone does not sufficiently describe the LSE regardless of its wide observation in field and laboratory experiments.

pH increases have been observed in the effluent profile of several unbuffered experiments without any associated LSE (Cissokho et al., 2010; RezaeiDoust et al., 2010). The retention of Mg^{++} in aged samples during successful LS corefloods by Alagic and Skauge (2010) is inconsistent with the desorption of surface-active cations from clay mineral surfaces proposed by Austad et al. (2010), RezaeiDoust et al. (2011) and Aksulu et al. (2012). The mechanism of local increase in *pH* does not explain those coreflooding experiments (e.g. Cissokho et al., 2010; RezaeiDoust et al., 2010) where no LSE is reported in the presence of the required conditions and *pH*-change.

Electrostatic forces are assumed central to the LSE by double layer expansion (DLE). The adsorbed polar oil components and/or the brine-oil interface need be of same polarity as the mineral surfaces at reservoir *pH* to repel and yield desorption with decreasing salinity. While this is consistent with many plug-scale measurements of wettability as a function of brine salinity (e.g. Anderson, 1986), contrary observations have been reported by mineral-surface-scale adhesion tests (Buckley and Morrow, 1990; Drummond and Israelachvili, 2004; Lebedeva and Fogden, 2010) that suggested increased adhesion of oil as salinity decreases at fixed *pH*. Moreover, DLE fails to explain why the LSE is not always observed with reduced ionic strength. Austad et al. (2010) indicated no significant difference in the desorption development between high- and low-salinity water injection, unless associated with local increase in *pH*, which clearly contradicts the salting-in mechanism of RezaeiDoust et al. (2009, 2011). Ashraf et al. (2010) reported improved oil recovery in neutrally-wet cores during LSWF which suggests that osmosis (Sandengen and Arntzen, 2013) cannot solely describe the LSE.

2.3 Wettability Alteration

As discussed previously, the exact mechanism(s) that drives the LSE is yet to be established and remains uncertain. However, it is widely accepted from available evidence that wettability alteration making the pore surfaces more water-wet, or perhaps just less oil-wet, is the primary cause of its associated core- to reservoir-scale improved oil recovery (Jerauld et al., 2008; RezaeiDoust et al., 2009; Dang et al., 2015; Ding and Rahman, 2017; Tian and Wang, 2017; Bartels et al., 2019; Katende and Sagala, 2019; Liu and Wang, 2020). Such alteration affects the oil displacement efficiency of brine, by releasing oil initially adsorbed to mineral surfaces, allowing water invasion of oil-filled pores that hitherto would be bypassed, or reducing oil-trapping by snap-off (Jackson et al., 2016). Although, a change from water-wet to neutral-wet conditions has been associated with improved oil recovery in a few LS coreflooding experiments (Ashraf et al., 2010), it could be that in other cases we see a transition from unfavourable oil-wet states to more favourable neutral or mixed-wettability. Fogden et al. (2011) argued that as clay minerals that initially were oil-wet, and the detachment of oil and its mobilization during LSWF revealed more water-wet pore surfaces. A similar mechanism might also have operated in other studies (Berg et al., 2010; Cense et al., 2011).

Wettability is a measure of the rock surface preference for one fluid in the presence of others (Nasralla et al., 2013). It is generally evaluated by averaged properties indirectly, such as the Amott-Harvey method (Amott, 1959), and the USBM method (Donaldson et al., 1969), or by contact angle measurements on flat surfaces of representative mineralogy outside the rock (Anderson, 1986; Bortolotti et al., 2010). More recently, high-resolution imaging has allowed contact angles to be measured *in situ*, inside the pore space of the rock (Andrew et al., 2014; Blunt et al., 2019).

When reservoir pore surfaces become more water-wet during LSWF, the associated improved recovery results from its favourable modification of the fluids' mobilities relative to a HS water injection. At the Darcy scale these effects are encapsulated in changes in relative permeabilities as a function of fluid saturation (illustrated in **Fig. 2.1**) rather than in the displacing fluid viscosity seen in polymer floods (Callegaro et al., 2013; Bartels et al., 2019). Thus, oil mobility improves with reduced residual saturation as water displacement is retarded under LS conditions. The extent to which each fluid mobility is favourably modified is controlled by how more water-wet the system becomes (**Fig. 2.1**), and this is influenced by mixing of the distinct brines. This would be discussed later in this Chapter.

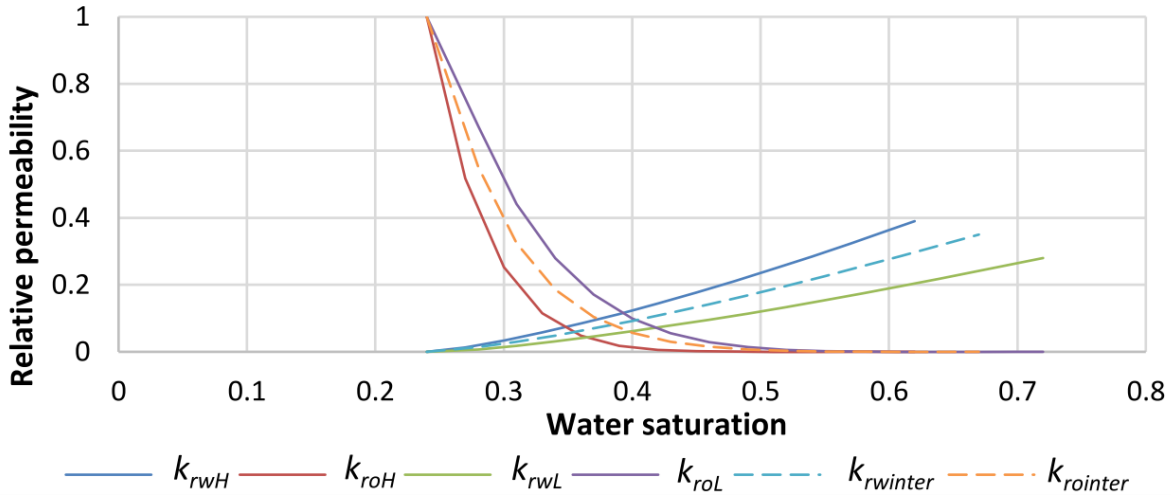


Fig. 2.1: Relative permeabilities for different stages of more water-wetness of pore surfaces with LS water in comparison to a HS brine (reproduced from a core experiment by Callegaro et al., 2013). k_{rwH} and k_{roH} are the water and oil relative permeabilities for HS waterflooding. ($k_{rwinter}$, $k_{rointer}$) and (k_{rwL}, k_{roL}) are the water-oil relative permeabilities pairs for increasingly more water-wetness respectively with LS water injection.

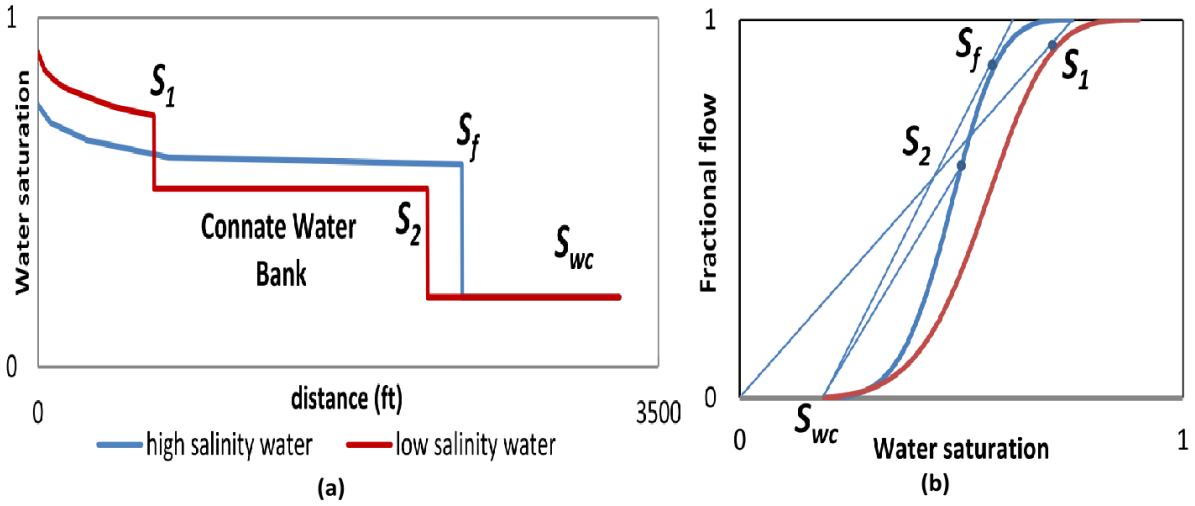


Fig. 2.2: Typical one-dimensional Buckley Leverett water saturation and fractional flow profiles for secondary-mode LSWF in comparison to conventional HS waterflood (reproduced from Jerauld et al., 2008). (a) Water saturation. (b) Fractional flow curves showing the estimation of water saturation and watercut for the shock-fronts. LSWF has two displacement fronts leading to three profile-regions: oil saturated (front), connate water-oil bank (middle), and injected LS displacement (rear); S_1 and S_2 are its trailing and leading shock-fronts' saturations. HSWF consists of just one displacement front with water saturation S_f. S_{wc} is the connate water saturation.

In contrast to conventional HS waterflood with only one displacement shock-front, LSWF consists of two shock-fronts (as shown for a one-dimensional displacement in **Fig. 2.2**a) similar to other EOR-engineered water injections including polymer and surfactant floods (Pope, 1980; Jerauld et al., 2008). The (oil saturated) HS zone lies ahead of the leading (first) shock while the injected LS brine is behind

the trailing (second) shock. A connate water-oil bank is formed between these two shock-fronts regardless of the injection mode – secondary or tertiary (Jerauld et al., 2008). This arises because the injected LS water, which displaces the HS formation or connate water, has a different fractional flow from that associated with a displacement of the oil by HS formation water (**Fig. 2.2**b).

Evidence of connate water or oil bank during LSWF has been reported for both corefloods (Jerauld et al., 2008; Korrani et al., 2014) and field trials (Vledder et al., 2010; Law et al., 2014; Korrani et al., 2014), as presented in **Fig. 2.3**. Its size depends on the relative mobilities of the fluids in both wettability states and influences the displacement efficiency of the injected LS water particularly if limited (i.e. slug injections). The analytical solution for secondary-mode displacement is shown in **Fig. 2.2** (modified from Jerauld et al., 2008), and this will be further discussed later in this Chapter. The derivation of the analytical solution of LSWF is presented in Chapter 4.

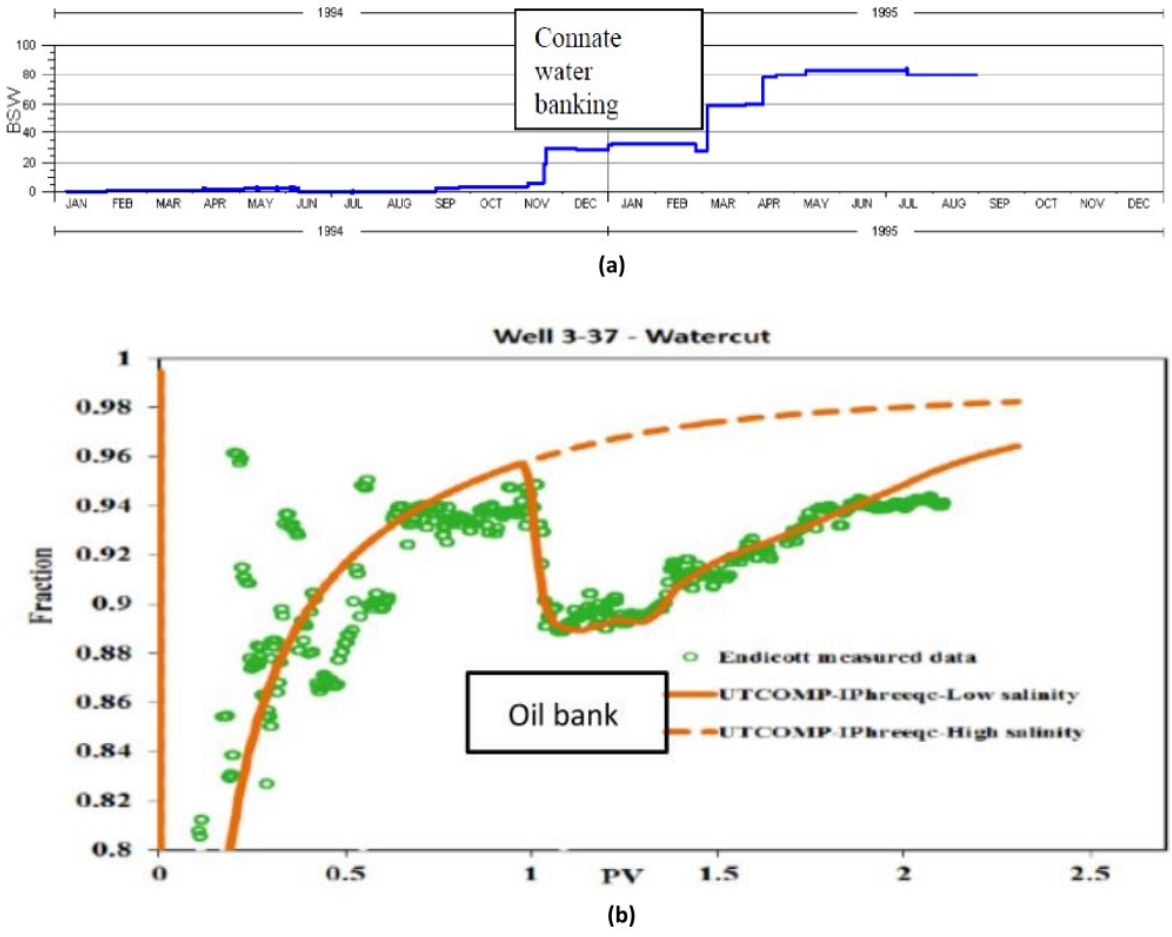


Fig. 2.3: Produced water during field-scale LSWF from (a) the Omar field in Syria (reproduced from Vledder et al., 2010). (b) Endicott field in Alaska (reproduced and modified from Korrani et al., 2014). A connate water bank was formed during secondary displacement in the Omar field with the produced water cut staying roughly constant for some time. During tertiary LS displacement in the Endicott field, the produced water cut dropped for some time indicating the arrival of an oil bank – which demonstrated improved oil displacement (or recovery) relative to a HS-brine injection.

2.4 Low Salinity Effect (LSE) and Wettability Alteration: Experimental and Field Tests

Improved oil recovery from LSWF has been confirmed by several coreflooding experiments and field-scale trials in both secondary (i.e. immediate LS injection at initiation of displacement) and tertiary (i.e. injection post initial displacement with HS brine) modes. This section reviews the findings of these studies in relation to the significance of wettability alteration and the influence of some proposed necessary conditions on the LSE in clastic reservoirs.

For corefloods where the LSE potential has been demonstrated in secondary- and/or tertiary-mode displacement (e.g. Zhang and Morrow, 2006; Seccombe et al., 2008; Agbalaka et al., 2009; Cissokho et al., 2010; Austad et al., 2010; Hadia et al., 2011; Hadia et al., 2012; Robbana et al., 2012; Callegaro et al., 2013), variations in the recovered additional oil are probably related to the initial wettability of the cores, salinity of the injected brines, relative compositions of the *in situ* and injected brines, divalent ions or cations presence in the distinct brines, as well as clay content. Improved recovery efficiency with LSWF appears largely dependent on the initial state of the pore wettability – the more oil- or intermediate-wet the system is, the more likely the LSE (Skrettingland et al., 2011; Hadia et al., 2012). Whereas a significant reduction in the injected brine salinity still improved the oil recovery in some cores even in the absence of divalent ions – Ca^{++} and Mg^{++} (Agbalaka et al., 2009; Cissokho et al., 2010; Hadia et al., 2012; Callegaro et al., 2013). This suggests that the LSE is more related to the brine salinity than necessarily the presence of divalent ions in the resident and injected brines. While a higher clay content may be beneficial to a more favourable LSWF (e.g. Austad et al., 2010; Thyne and Gamage, 2011), the LSE potential does not always depend on clay content (e.g. Skrettingland et al., 2011).

Observations from coreflooding experiments were generally affirmed in reported field trials, where the LSE potential appears influenced by the initial wettability and clay content. A higher clay content (20%) in sandstones of the Endicott formation (Seccombe et al., 2010) seems more favourable to LSWF with additional oil recovery (10%) compared to the low clay content (<2%; mostly illite) in fields within the Minnelusa formation (Thyne and Gamage, 2011) with no improved recovery from LSWF (<<10% of connate salinity). On the other hand, LSWF (<<5% of connate salinity) failed to improve recovery in the Snorre North field (Skrettingland et al., 2011) despite its relatively high clay content (5-35%; mostly kaolinite), indicating its independence on clay presence.

For an initially oil-wet Omar field (Vledder et al., 2010), injecting LS brine (<<10% of connate salinity) resulted in an additional oil recovery (10-15%). Contrarily, LS water injection (<<5% of connate salinity)

in the Snorre North field with weakly water-wet initial conditions failed to improve the oil recovery considerably (Skrettingland et al., 2011). They suggested that such initial pore wettability was near-optimal for oil recovery hence, showed little or no improvement with LSWF relative to conventional seawater injection. This seems to agree with Jadhunandan and Morrow (1995) who showed in corefloods that the optimum oil recovery is usually at mixed-wet conditions, with low water relative permeability and residual oil saturation. Thus, a shift to more water-wet conditions during LSWF may not always favour improved recovery (Li, 2011). However, this remains a subject of interest for future studies.

2.5 Approaches to Modelling Low Salinity Waterflooding (LSWF)

Despite the differences of opinion on the exact mechanism(s) of the LSE, it is generally accepted that the process should be modelled primarily as a wettability alteration effect represented through a change of mobility, quantified through active solute concentration-dependent relative permeabilities. Nonetheless, different considerations are often adopted to capture the influence of other identified necessary conditions – discussed in the previous section – on the wettability alteration effect.

Three main methods are currently, broadly used to model LSWF: the standard tracer-component model, the mechanistic model, and the hybrid model that considers a combination of different pore mechanisms of the LSE. In all the three methods, the change in wettability resulting from injecting LS water is modelled by modifying the relative permeabilities, as illustrated earlier in **Fig. 2.1**. Even those who suggested mechanisms such as fines migration and changes to interfacial tension have adjusted the relative permeabilities to match their experimental data (Aladasani et al., 2012; Chequer et al., 2019; Nguyen et al., 2020). The relative permeability function is itself a proxy model for the average of complex pore scale behaviour, thus this approach seems reasonable.

For the standard tracer-component approach, a single-component tracer such as solute concentration or salinity is adopted to change the relative permeabilities from HS mobilities to LS behaviour to control wettability alteration towards more water-wetness. This involves using more water-wet (or less oil-wet) relative permeabilities as brine salinity decreases below some specified threshold or effective salinity. Mechanistic models consider other geo-chemical and intra-aqueous reactions, associated with their proposed active ion-exchange processes between brine and pore-mineral surfaces, to modify the relative permeabilities as a function of selected adsorbed ion(s).

2.5.1 Standard Tracer-component Model

Jerauld et al. (2008) introduced the tracer-component model for LSWF based on standard approaches to modelling chemical EOR processes, which is currently in-use in many black oil simulators.

Approximations also exist in some compositional simulations to accommodate this method. The black oil model basically consists of the standard mass conservation equations reduced to oil and water phases along with dynamic modifications of relative permeabilities and capillary pressures corresponding to high- and low-salinity behaviours. Salinity is treated as a single-component conservative tracer being tracked to modify the relative permeabilities and capillary pressures in grid-blocks at each time step. Threshold aqueous phase salinities are attached to the high- and low-salinity relative permeabilities and capillary pressures. The high-salinity relative permeabilities are used when the aqueous phase salt concentration exceeds the upper threshold and vice versa for the lower threshold. The change in salinity is modelled using a mass conservation equation and depends on the oil and water velocities.

After normalizing the saturation dependence of the two pairs of relative permeabilities, the relative permeabilities and capillary pressures when intermediate concentrations exist are interpolated between the high- and low-salinity values using

$$k_{ri}(S_w^*, \theta) = \theta k_{riHS}(S_w^*) + (1-\theta)k_{riLS}(S_w^*) \tag{2.1}$$

$$P_{ci}(S_w^*, \theta) = \theta P_{ciHS}(S_w^*) + (1-\theta)P_{ciLS}(S_w^*) \tag{2.2}$$

where $k_{riHS}(S_w^*)$ and $k_{riLS}(S_w^*)$ are the effective high- and low-salinity relative permeabilities and capillary pressures at the upper and lower threshold salinities (or solute concentrations) respectively for phase i at normalised water saturation S_w^*.

$$S_w^* = \frac{S_w - S_{w,r}}{1 - S_{w,r} - S_{o,r}} \tag{2.3}$$

where S_w and $S_{w,r}$ are the water and connate (residual) water saturations. $S_{o,r}$ is the residual oil saturation at the intermediate brine salinity and is interpolated between the high-salinity residual oil saturation ($S_{o,rHS}$) and the low-salinity residual oil saturation ($S_{o,rLS}$) as

$$S_{o,r} = S_{o,rLS} + \theta(S_{o,rHS} - S_{o,rLS}) \tag{2.4}$$

The interpolant that defines the concentration weighting function, θ is given as

$$\theta = \frac{c - c_{LS}}{c_{HS} - c_{LS}} \; for \; c_{LS} < c < c_{HS} \tag{2.5}$$

where c is the salinity or solute concentration in a grid-block, c_{LS} and c_{HS} are the low- and high-salinity thresholds respectively. $0 \leq \theta \leq 1$: $\theta = 1 \; for \; c \geq c_{HS}$ and $\theta = 0 \; for \; c \leq c_{LS}$. This provision for

intermediate solute-component concentrations makes considering the effect of physical mixing or dispersion between the distinct brines, which is investigated in this thesis, possible with this method.

Despite the linear salinity weighting function (as presented above in equation 2.5) being generally accepted, it remains a subject of debate (Al-Ibadi et al., 2019). The use of two different weighting factors, reflecting different effects on oil and water, has been suggested by Al-Shalabi et al. (2015) to simulate the wettability alteration during LSWF. Others (e.g. Shojaei et al., 2015) have proposed adjusting only the oil relative permeabilities for the LSE while the water relative permeabilities are left unchanged. A wide practice is to adjust both relative permeabilities (and/or capillary pressures) to fit laboratory results (Jerauld et al., 2008; Brodie and Jerauld, 2014).

A very similar model was proposed by Tripathi and Mohanty (2008). They considered Corey exponents (Brooks and Corey, 1966; Delshad and Pope, 1989) to define the different characteristic shapes for the relative permeabilities that are representative of either low- or high-salinity water. The exponents can be interpolated linearly using a similar function as equation 2.5 to scale the relative permeabilities and capillary pressures to intermediate wettability changes accordingly.

The standard salinity-dependence approach considers wettability alteration with reduced residual oil saturation and modified mobility as the main cause of the improved recovery from the LSE. It does not elaborate on the putative pore scale mechanisms. While it has been reported that it is not just the brine salinity itself that controls the mobility change, the salinity mechanism could be adopted to represent other specific solute(s) such as Ca^{++} or Mg^{++} (Puntervold et al., 2015). Hence, Jerauld et al. (2008) validated this tracer model in agreement with experimental data. Furthermore, the model has been used to evaluate field behaviour and the optimal injection strategy (Mahani et al., 2011; Brodie and Jerauld, 2014; Callegaro et al., 2015; Spagnuolo et al., 2016; Attar and Muggeridge, 2018).

The model described here is available in commercial simulators such as ECLIPSE and CMG STARS: in this work we will use the model in CMG STARS.

2.5.2 Ion Exchange (Mechanistic) Model

Dang et al. (2015, 2016) introduced a mechanistic model based on multicomponent ion exchange (MIE) that captures the geo-chemical interactions leading to the LSE for its compositional simulation. This was a sequel to earlier studies by Omekeh et al. (2012) and Korrani et al. (2013). Three main crude oil-brine-rock (COBR) geo-chemical interactions are usually assumed to occur during LSWF (Dang et al., 2015): ion-exchange (Appelo, 1994; Lager et al., 2008a, 2008b; Suijkerbuijk et al., 2012), intra-aqueous reactions and mineral dissolution (Zhang et al., 2006; Fathi et al., 2010). While the possible influence of reactive interactions on the injected LS brine and the flood displacement is considered

through mineral dissolution and intra-aqueous reactions, the two primary ion exchange processes governing the LSE in this model are defined as

$$Na^{+} + \frac{1}{2}(Ca - X_2) \leftrightarrow (Na - X) + \frac{1}{2}Ca^{++} \tag{2.6}$$

$$Na^{+} + \frac{1}{2}(Mg - X_2) \leftrightarrow (Na - X) + \frac{1}{2}Mg^{++} \tag{2.7}$$

where X is the clay mineral in the rock, with subscript 1 when attached to a single positive charge (Na^{+}) and 2 if attached to a divalent positive ion (Ca^{++} or Mg^{++}). In addition, the cation exchange capacity (CEC) of the clay minerals controls the rate of the ion exchange reaction between their surfaces and the injected LS brine for the LSE.

This mechanistic model has been demonstrated with commercial simulators such as coupled modelling using UTCOMP and IPhreeqc to validate LS experimental data and field trials (Korrani et al., 2014; Kazemi et al., 2016). Dang et al. (2016, 2017) and Adegbite et al. (2018) extended this model with CMG GEM to assess the impact of intra-aqueous reactions and mineral dissolution on the flood efficiency in sandstones and carbonates respectively.

2.5.3 Hybrid (Mechanistic) Model

Kuznetsov et al. (2015) developed an approach to model the LSE where two pore scale mechanisms are considered – multicomponent ion exchange (MIE) and double layer expansion (DLE). The model analyses the type of force – van der Waals, ligand exchange or cation bridging – that binds the adsorbed multivalent ion(s) to the clay mineral surfaces. It was primarily built and validated with LS coreflood data from the literature. Further validation with field data is still required; thus, it is currently not adopted in any commercial simulator to model the LSE. Recently, Gorucu et al. (2019) incorporated fines transport with the MIE mechanism to model the LSE. The proposed model was only validated with a LS coreflood experiment conducted with a non-polar oil thereby questioning its combined effects of fines migration and MIE. While the model has been demonstrated with CMG GEM for simulation studies (Nguyen et al. 2020), further validation with tests data showing both mechanisms across length scales is still required.

In this thesis, the standard tracer-component model is used to evaluate the LSE in CMG STARS which implements a finite-difference approach to discretize the governing equations. Salinity will be treated as the 'proxy' single-component tracer to control wettability alteration towards more water-wet conditions, and the linear weighting function is adopted for mobilities at intermediate salinities.

2.6 Numerical Dispersion in Conventional LSWF Simulations

When LS brine is injected into the reservoir, it either fully displaces all the HS connate (or resident formation) brine or mixes with it to form brine with intermediate-salinity or -solute concentration. Either way, a connate water-oil bank will be formed ahead of the displacing injected LS water (Jerauld et al., 2008; Vledder et al., 2010; Korrani et al., 2014; Law et al., 2014), as shown in **Fig. 2.3**. Besides, the flood displacement efficiency (particularly for limited or slug injections) is influenced by the effective size of its connate water-oil bank which depends on the relative mobilities of the fluids in the active wettability states.

Since successful reservoir management relies on accurate simulation of proposed displacements, it is therefore important to represent the connate water-oil bank displacement reliably in LSWF simulations. Unfortunately, it is well established that numerical models of multi-component flow suffer from numerical dispersion that smears the displacement shock-fronts erroneously (Lantz, 1971; Saad et al., 1990; Solano et al., 2001; Jessen et al., 2001). Such dispersion is more excessive and dissimilar to that observed in conventional waterflooding applications where it is due to truncation errors from discretization (Peaceman, 1977; Thomas, 1982; Mattax and Dalton, 1990; Ertekin et al., 2001), and its effect is controlled with few more grid-blocks as the Buckley-Leverett shock is typically self-sharpening. In augmented or engineered waterfloods such as LSWF, the fractional flow is coupled with the solute-component concentration (and often with its compositional physical dispersion) to modify it for the LSE. Errors in the concentration profile affect the fractional flow and lead to incorrect wavespeeds and the excessive smearing of shock-fronts that bound the connate water-oil bank hence, misrepresenting it (AlSofi and Blunt, 2012). This exacerbates the numerical dispersion effects despite that such simulations fundamentally adopt a black oil model. These are further discussed in Chapter 4 where this thesis focuses on controlling numerical dispersion effects in LSWF simulations.

Improved or higher-order discretization schemes have been proposed to reduce numerical dispersion effects and enable the use of coarser grids for multi-component flows (Gupta et al., 1991; Blunt and Rubin, 1991; Liu et al., 1995; Mallison et al., 2005). Higher-order schemes may resolve numerical dispersion effects in LSWF simulations since they essentially use an extended black oil model. However, results from their applications specifically to LSWF are scarce (if available at all) in the literature, perhaps due to its recent and emerging status as an EOR technique. Nonetheless, Liu et al. (1995) employed a third-order total variation diminishing scheme to control numerical dispersion effects in augmented waterflooding simulations but limited to only polymer floods. Implementing these schemes requires upgrading existing codes which may become more computationally-demanding to run in some cases, thus discouraging their wide consideration in commercial simulators.

AlSofi and Blunt (2012, 2013) suggested a method to minimize numerical dispersion in augmented waterfloods – polymer and LSWF. Promising results from streamline simulation of the floods were presented, using a segregated flow scheme where the injected and resident compositions were transported separately. Babaei and King (2013) extended the segregated flow scheme of AlSofi and Blunt (2012) to a static modified nested-gridding algorithm for coarse-grid simulations of processes such as polymer, surfactant and thermal EOR. The constraint of reconstructing the fine pressure distribution was eliminated in its downscaling framework, allowing the composite scheme to capture the more challenging trailing shock with reduced computational requirements. However, further developments of existing simulators would be required to implement either of these approaches.

Jerauld et al. (2008) investigated the effects of numerical dispersion on LSWF simulations. They observed increasing degradation of the injected LS slug effectiveness with higher levels of numerical dispersion. This resulted from numerically-induced 'artificial' interactions between the connate water-oil bank and the injected LS water in the simulations, which appears similar to actual reservoir physical mixing when considering the effect of dispersion. Since numerical dispersion seems inevitable in most computationally-efficient conventional coarse grids, Jerauld et al. (2008) instead proposed the use of numerical dispersion to mimic physical mixing in LSWF. However, this approach is limited by the coarseness of the simulation grids, as the numerical dispersion associated with a large simulation grid-size may be too large for the physical mixing desired. Indeed, this is what we show later in Chapter 4, unless care is taken to reduce numerical errors.

They suggested using 'pseudos' for the threshold salinities (or solute-component concentrations) and relative permeabilities for the LSE in coarse-grids to reduce their large numerical dispersion when matching test data. No definitive method was proposed to evaluate the appropriate pseudo or effective threshold salinities for a coarse grid. They rather suggested varying the salinity-thresholds in the coarse grid till a match is obtained with the test or reference fine-grid results.

Muggeridge and Hongtong (2014) and Al-Ibadi et al. (2018a) also identified the need to replace the initial or reference salinity-thresholds for LSWF with upscaled or effective thresholds in coarse grid simulations. This is to correct numerical dispersion effects on the velocities of the water fronts in such grids. Simulation- and analytical-based methods were suggested to evaluate the appropriate effective threshold-salinities for coarse-grid simulations. In their simulation-based approach, Muggeridge and Hongtong (2014) compared the salinity versus distance plots obtained from the coarse-grid and the reference fine-grid simulations to read-off the upscaled thresholds at locations in the coarse grid output corresponding to where the initial or reference thresholds exist in the fine grid output. Its

accuracy is questionable since different upscaled thresholds are read-off from plots obtained at different injected volumes of low-salinity water in the same coarse simulation.

Alternatively, they proposed calculating the effective thresholds with the analytical solution to the advection-dispersion equation for miscible displacement from Aronofsky and Heller (1957) – equation (A.1) in Appendix A. Therein, the salt-front profiles are predicted for the coarse grid and its reference fine grid with the analytical solution. While the numerical dispersion coefficient of each salt front is a function of its simulation grid, a constant single-phase advection velocity is assumed for the salt-front transport in all simulation grids. The effective salinities for the coarse grid are then evaluated as the salinities – along its predicted salt front – with equal velocities as the initial salinity-thresholds – along the predicted salt front for its reference fine grid. In comparison with the reference fine-grid solutions, large discrepancies were still observed in the coarse-grid results for the watercut in the region of the connate water bank as well as the recovery profile. This implies that the velocities of the water fronts were not adequately corrected in the coarse-grid simulations.

In contrast, Al-Ibadi et al. (2018a; 2018b; 2018c) observed that the advection velocity of the salt front is not constant but increases with numerical dispersion. Later in Chapter 4.3, we will also observe the same effect. Al-Ibadi et al. (2018a, 2018b) defined the salt front velocity as a function of the analytical velocities of the leading and trailing water fronts, Peclet number (*Pe*), and the mid (average) salinity-threshold, see equations (A.7) – (A.9). The mid salinity-threshold is the midpoint between the high and low salinity-thresholds. Al-Ibadi et al. (2018a) used this idea to define a pseudo or effective midpoint salinity-threshold to control the impacts of numerical solute dispersion on the velocities of water fronts in coarse grids. With a fixed effective midpoint, the upper and lower bounds were adjusted together with the relative permeabilities to improve the precision of the simulation results. However, discrepancies between the upscaled and reference fine-scale results were still seen, and the method only appears to assign a given effective salinity-thresholds midpoint: this still leaves ambiguous the appropriate values of the lower and upper effective thresholds.

Meanwhile, the impact of transverse mixing or dispersion on LSWF has been demonstrated with reservoir simulations (Brodie and Jerauld, 2014; Attar and Muggeridge, 2018). Numerical dispersion also exaggerates the modelling of transverse mixing in simulations, similar to longitudinal mixing (Attar and Muggeridge, 2016). However, the effects of upscaled or effective salinity-thresholds on modelled transverse component of mixing in simulations have not been investigated. Furthermore, the accuracy of existing commercial simulators is limited when multidimensional grids are considered. The presence of multidirectional flows, transverse to the principal flow direction, makes the simulator model longitudinal dispersion with the input transverse dispersivity and vice versa. This is because the

dispersion tensor is diagonal and mechanical dispersivities are defined for the flow axes along fixed coordinate directions in most commercial codes.

The truncation error from discretization is a function of time step size as well as mesh resolution (grid-size). From the analysis based on a Taylor series expansion given by Lantz (1971), Sorbie and Mackay (2000) suggested that the numerical dispersion in a first-order discretization scheme under controlled time step (or implicit) can be approximated using

$$\alpha_{L,num} = \frac{\Delta x}{2} + v\frac{\Delta t}{2} \tag{2.8}$$

where $\alpha_{L,num}$, Δx, Δt, and v are the equivalent inherent numerical diffusivity or dispersivity, discretized grid-size in flow direction, time-step, and solute front velocity respectively. In dimensionless terms normalized relative to the system or model length (L) in the flow direction,

$$D_{L,num} = \frac{\Delta x_D + \Delta t_D}{2} = \frac{\Delta x_D}{2}(1 + CFL) \tag{2.9}$$

$$D_{L,num} = \frac{\alpha_{L,num}}{L}, \qquad \Delta x_D = \frac{\Delta x}{L}, \qquad \Delta t_D = \frac{q_t \Delta t}{\varphi L} \tag{2.10}$$

where $v = \frac{q_t}{\varphi}$: q_t and φ are the total Darcy velocity and porosity respectively. The Courant-Friedrichs-Lewy (CFL) criterion or Courant number is defined as

$$CFL = \frac{\Delta t_D}{\Delta x_D} \tag{2.11}$$

such that using controlled time-step equal to that given by a CFL, numerical dispersivity varies linearly with grid-size.

To summarize this section, numerical dispersion is a very serious problem for LS simulations which cannot be readily addressed with higher-order numerical schemes or fine-grid resolution. Instead, as discussed in Chapter 4, a new approach, based on effective salinity-thresholds, is required to capture the behaviour of the displacement fronts accurately and to constrain numerical dispersion to be no greater than physical dispersion due to small-scale heterogeneity. Without this correction, simulations, especially at the field scale, would be of uncertain accuracy and dubious reliability.

2.7 Impact of Reservoir Interactions and Mechanisms on Field-scale LSE Potential

The LSE potential to improve oil recovery can be affected by various possible interactions and mechanisms whose impacts should be carefully considered and evaluated when designing the flood, especially for field-scale implementation. However, the differences of opinion on the exact mechanism(s) of the process have engendered diverse contributions on these anticipated performance-influencing reservoir effects and are still subjects of debate. For example, the influence of geo-chemical reactive interactions on the injected LS brine effectiveness and the flood displacement, as considered by Dang et al. (2016) and Kazemi et al. (2016), varies largely with localized factors that are dissimilar, and remains inconclusive. Nevertheless, the interaction between the injected LS water and the connate water-oil bank during displacement has been shown to be critical to the overall flood efficiency. In existing approaches to model LSWF, coupling the fractional flow with the tracked concentration of active solute-component or adsorbed-ion allows for intermediate wettability alteration effects. This provision makes it possible to consider the impact of the brine-brine interaction on the LS displacement in simulations. In this section, mechanisms such as mixing between the distinct brines, reservoir heterogeneity and crossflow, with direct influence on such interaction are discussed.

2.7.1 Mixing

The LSE is largely conditional on a significant reduction of the injected brine salinity (or active solute-component or adsorbed-ion concentration) relative to that of the resident formation brine (Tang and Morrow, 1999; Webb et al., 2005; Zhang and Morrow, 2006; Lager et al., 2008a; 2008b). This is a crucial consideration where the improved recovery depends on the stability of the flood fronts and the LS displacement, especially when limited LS injections are considered for field economics. Mixing of the injected LS brine with HS formation brine and/or active ion transport can compromise the flood efficiency – the mixed brine has a composition which may no longer provide the LSE. Such interaction between brines, with different but active solute or ion concentrations and/or compositions, is apparent from various effluent concentration profiles reported of LSWF (Jerauld et al., 2008; Vledder et al., 2010; Seccombe et al., 2010; Thyne and Gamage, 2011; Fjelde et al., 2012; Callegaro et al., 2013; Korrani et al., 2014; Law et al., 2014; Korrani et al., 2016; ; Dang et al., 2016; Nguyen et al., 2020) and can influence the improved recovery significantly (Jerauld et al., 2008; Mahani et al., 2011; Erke et al., 2016; Attar and Muggeridge, 2018; Chávez-Miyauch et al., 2020).

Mixing between the injected low-salinity and resident high-salinity brines depends primarily on molecular diffusion and advective dispersion of solute or ions. While studies on EOR processes have discussed the concept of mixing in miscible gas flooding extensively, little has been reported for LSWF. During diffusion, molecules move (spread) randomly from regions of higher concentration to regions with lower concentration when two fluids with different concentrations are in contact. Subsequently, a mixed region with intermediate concentration(s) is formed, and the concentration later becomes uniformly distributed across the two fluids (Perkins and Johnston, 1963). Fick's law relates the flux J of the diffusive fluid component to its concentration as

$$J = -D_o \frac{\partial c}{\partial x} \tag{2.12}$$

where J is the diffusion flux (mol/L^2T), D_o is the molecular diffusion coefficient (L^2/T), c is the concentration (mol/L^3), and x is the position (L).

In the presence of advective dispersion, their combined effects on mixing are well characterized as consisting of additive contributions of diffusion and convection given by Perkins and Johnston (1963):

$$K_l = D^* + \alpha_l v \tag{2.13}$$

$$K_t = D^* + \alpha_t v \tag{2.14}$$

where K_l and K_t are the longitudinal and transverse dispersion coefficients respectively (L^2/T). $D^* = D_o/\tau$, $\tau = F\varphi$: τ is the pore space tortuosity (dimensionless) and F is the formation electrical resistivity factor (dimensionless) and often assumed to be 1. α_l and α_t are the mechanical (advective) longitudinal and transverse dispersivities respectively (L), and are function of average particle size and local heterogeneity. v is the displacement front velocity (L/T).

Physical dispersion or mixing of fluids in a porous medium may result from molecular diffusion and variations in fluid velocity within and between pores. However, diffusivity is usually lower than it would be in a bulk fluid as the random movement of the molecules is restricted within the pores. At a velocity above about $0.1\ ft/D$ ($0.35\ \mu m/s$) the convection term dominates the total physical dispersion, and for practical displacement – about $1\ ft/D$ ($3.5\ \mu m/s$) – mixing depends mainly on advective (velocity-dependent) dispersion (Lake and Hirasaki, 1981). Besides, mixing within the flowing wetting phase in multiphase flow is velocity-dependent, thus mostly governed by dispersion not diffusion (Salter and Mohanty, 1982; Wang, 1988). The effect of molecular diffusion is therefore typically small in porous media and is probably further reduced if the pore is only partially occupied by the diffusing or mixing phase (Hu and Wang, 2003).

At the pore-scale during LS injection, component-transport is advection-controlled in the flowing region – with wettability alteration to more water-wet conditions, while the diffusion-controlled transport observed in the stagnant region is very slow (Aziz et al., 2019). At the reservoir scale, the effect of molecular diffusion is negligible compared to dispersion due to advective spreading caused by small-scale heterogeneity (Lake and Hirasaki, 1981), hence velocity-dependent dispersion is often mainly considered in multiphase flow in porous media. Brodie and Jerauld (2014) and Attar and Muggeridge (2018) showed, through simulation studies, that the impact of diffusion on mixing during LSWF is significant only in inter-bedded heterogeneity with thick shale or low-permeability layers. In this thesis, more emphasis is therefore placed on the impact of physical mixing from advective dispersion rather than diffusion.

In layered heterogeneity, for example, where the coefficients (or components) of physical dispersion may be both active, K_l and K_t are scaled respectively to the system geometry along the principal flow direction with dimensionless Peclet number (Pe) given by

$$Pe = \frac{vL}{K_l}, \qquad (Pe)_t = \left(\frac{vH}{K_t}\right)\frac{H}{L} \tag{2.15}$$

where L is the longitudinal measurement scale or system-length travelled along the principal flow direction, and H is the measurement scale transverse to the principal flow direction. The dimensionless *Pe* is adopted later in this thesis to characterize physical dispersivity in terms of the measurement- or length-scale of the reservoir models explored.

Active transverse dispersion and longitudinal bulk flow in layered heterogeneity can manifest themselves as enlarged effective longitudinal dispersion, further compromising the effectiveness of the injected fluid with lower solute concentration. This was earlier identified by Taylor (1953; 1954) as an increased longitudinal diffusion phenomenon if a certain criterion is met. Taylor (1953; 1954) showed analytically that when a soluble substance is added to a solvent that is moving slowly in a tube, the solute dispersion along the tube is controlled by increased longitudinal diffusion. This is known as Taylor dispersion. Lake and Hirasaki (1981) later showed increased longitudinal dispersion resulting from a combination of transverse dispersion and layering in porous media (**Fig. 2.4**), based on Taylor's work. For a horizontal two-layer porous medium with contrasting permeabilities, they scaled the importance of advective transverse dispersion to the total mixing with a dimensionless transverse dispersion number (N_{TD}) defined as

$$N_{TD} = \frac{LK_t}{H^2 v_1} \tag{2.16}$$

where v_1 is the displacement front velocity in the high-permeability layer. Attar and Muggeridge (2018) adopted the dimensionless N_{TD} in simulations to suggest that transverse mixing is relevant in LSWF when heterogeneity affects the vertical sweep. However, it remains unclear the significance of the transverse component of physical dispersion on the LSE when the heterogeneity impacts the areal sweep. This is considered and investigated in Chapter 5.

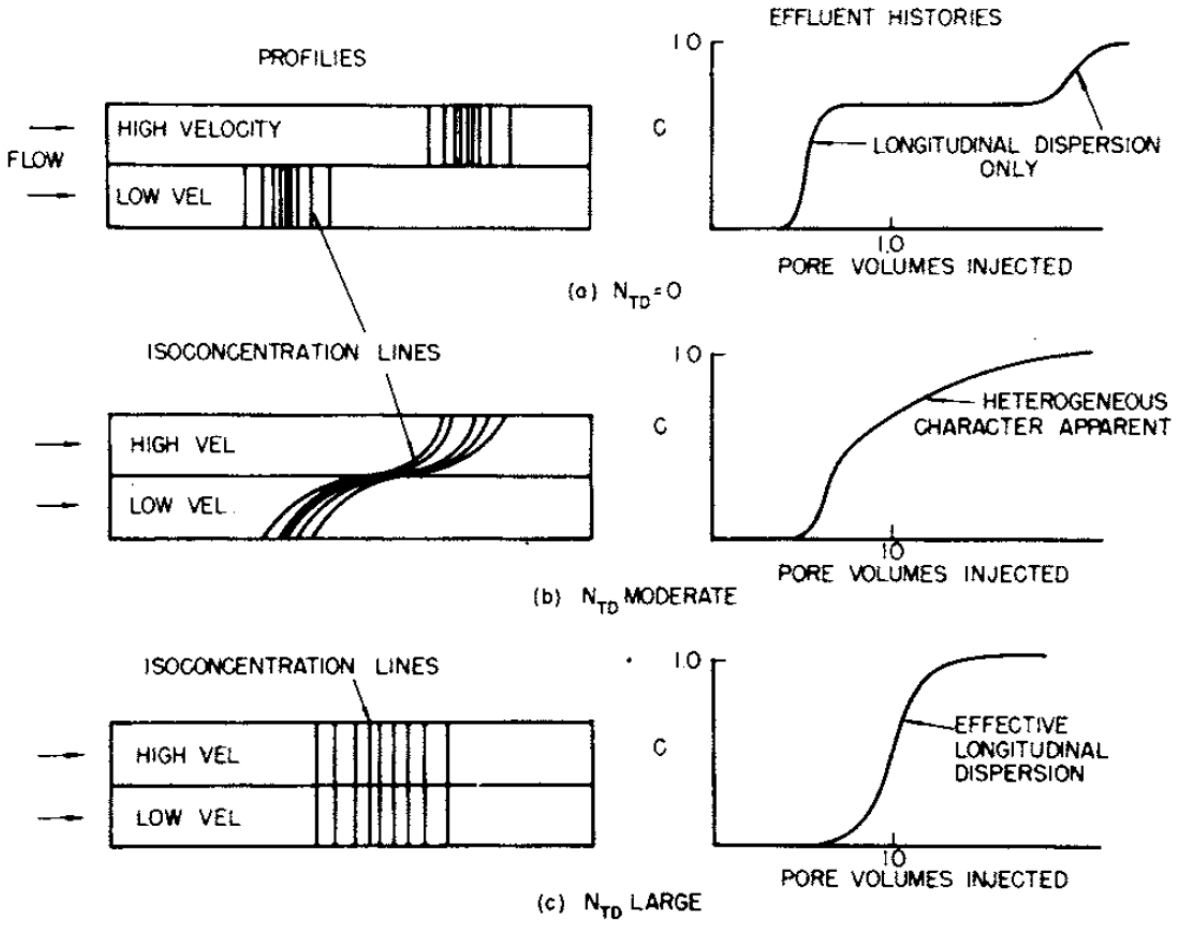


Fig. 2.4: Schematic illustration of Taylor dispersion in two-layer porous media showing the limits toward which transverse dispersion will drive a miscible displacement as a function of N_{TD} (reproduced from Lake and Hirasaki, 1981). For small N_{TD} (**a**), transverse dispersion is negligible, so the produced concentration profile depends on the longitudinal dispersion of each layer and their permeability contrast – the medium behaves as a two-layer system. At moderate N_{TD} (**b**), inter-layer fluid flow due to transverse dispersion distorts the isoconcentration lines. Resulting concentration profile is influenced by both heterogeneity and transverse dispersion. Under large N_{TD} (**c**), transverse dispersion causes the isoconcentration lines to be vertical across the width or thickness of the system. This results in having an effluent concentration profile that reflects enlarged effective longitudinal dispersion with larger isoconcentration lines relative to the actual longitudinal dispersion of each layer. The medium behaves as a single-layer system with increased longitudinal dispersion.

Mixing is also enhanced when the flood front becomes distorted by heterogeneity and crossflow as this increases the surface area over which diffusion and/or advective-dispersion occur (Zapata and Lake, 1981; Yortsos, 1995). In miscible floods, small scale heterogeneity at the pore-scale is believed

to cause additional mixing between the displacing and displaced fluids – due to the disturbed front between them – as length-scale increases (Perkins and Johnston, 1963; Alkindi et al., 2011; Mahadevan et al., 2003). In contrast, Coats et al. (2009) argued that such an apparent increase in dispersion observed in production effluent profiles purely results from 'conformance' of fluids from different layers in the wellbore rather than actual physical mixing in the reservoir. The uncertainty in the level of physical dispersion with length-scale in heterogeneous porous media is discussed in Chapter 3.

Physical dispersion in porous media is usually evaluated from the effluent concentration profiles obtained during tracer displacement tests. The longitudinal dispersivity is fitted by matching the effluent concentration profile with the analytical solution to the 1D advection-dispersion equation for miscible displacement in a homogeneous porous medium given by Aronofsky and Heller (1957):

$$c = \frac{1}{2} erfc\left(\frac{x - vt}{2\sqrt{\alpha_l vt}}\right) + \frac{e^{\frac{x}{\alpha_l}}}{2} erfc\left(\frac{x + vt}{2\sqrt{\alpha_l vt}}\right) \tag{2.17}$$

where c is the solute or tracer concentration (fraction of 1), $erfc(x) = 1 - erf(x)$, x is the position in the system along the longitudinal direction of flow and equals L at the end of the model, t is the displacement or injection time, v is the advection velocity of the displacement or concentration front, and α_l is the longitudinal dispersivity.

Brigham et al. (1961) developed an approximate solution to equation (2.17) to fit the longitudinal dispersivity (in dimensionless *Pe*) from the profile of effluent concentration as a function of total pore volumes injected:

$$P_e = \left(\frac{2.380}{U_{80} - U_{20}}\right)^2 = \left(\frac{3.625}{U_{90} - U_{10}}\right)^2 = \left(\frac{4.65}{U_{95} - U_5}\right)^2 \tag{2.18}$$

where U is a volume modifying function calculated at different percentiles of the effluent concentrations (c) given as

$$U = \frac{(Q_D - 1)}{\sqrt{Q_D}} \tag{2.19}$$

and Q_D is the dimensionless total pore volumes injected at the percentile point of the reference U. Further details on evaluating longitudinal dispersivity are presented in **Appendix A**.

Permeability contrasts affect the effluent concentration profiles in stratified reservoirs with layered heterogeneity. Thus, the analytical solution of the effluent concentration profiles given by the Muskat method (Muskat, 1949) is applicable:

$$c(Q_D) = \frac{\int_0^H F(Q_{DZ})k(z)\,dz}{\bar{k}\,H} \tag{2.20}$$

$$Q_{DZ} = \frac{k(z)}{k}Q_D\,, \qquad \bar{k} = \frac{\int_0^H k(z)\,dz}{H} \tag{2.21}$$

where $c(Q_D)$ is the concentration (fraction of 1), Q_{DZ} is the pore volumes injected into a given layer z (dimensionless), $F(Q_{DZ})$ is any function that defines the concentration profiles in each layer, $k(z)$ is the permeability as a function of layers (md), and H is the reservoir thickness. $F(Q_{DZ})$ is a step function from 0 to 1 at $Q_{DZ} = 1$ for a zero-physical longitudinal dispersivity (α_l). For a non-zero α_l, $F(Q_{DZ})$ is represented by equation (2.17).

Measurements of physical transverse dispersivity are much less common than the longitudinal component (Lake and Hirasaki, 1981). Nonetheless, a few experiments evaluating transverse dispersion have been reported (e.g. Blackwell, 1962; Alkindi et al., 2011). A typical description of such experiments as it may relate to a low-salinity displacement is presented in **Appendix B**. The concentration profile taken transversely (perpendicular to the principal flow direction) at any reference longitudinal point x (away from the injection face of the porous medium) is fit to the transverse dispersivity using the analytical solution of Hiby (1962):

$$c = \frac{1}{2}erf\left(\frac{y+b}{2\sqrt{\alpha_t x}}\right) - \frac{1}{2}erf\left(\frac{y-b}{2\sqrt{\alpha_t x}}\right) \tag{2.22}$$

where α_t is the transverse dispersivity, y is the position in the system along the transverse direction, and b is the position of the reference longitudinal evaluation point x along the transverse direction. Further details on evaluating transverse dispersivity in porous media are presented in **Appendix B**. These methods are adopted in Chapter 4 to evaluate the magnitude of both components of physical dispersion – longitudinal and transverse – as represented during numerical simulations.

In numerical simulations of LSWF, mixing can be modelled either explicitly through input physical dispersion or approximating representative physical dispersion with numerical dispersion as discussed in the previous section. Jerauld et al. (2008) conducted a simulation study on LS water injection to establish that numerical dispersion can model physical dispersion. They demonstrated the use of grid-size to model numerical dispersion to mimic physical mixing effects. Slugs of LS water were injected in tertiary mode in a $2D$ quarter-five-spot model using isotropic fine and coarse simulation-grids separately. The inherent numerical dispersivity (dimensionless) at each discretized grid-size was estimated using

$$D_{L,num} = \frac{1}{2\,N} \tag{2.23}$$

where N is the number of horizontal grid-blocks.

Input physical dispersivity was used to balance the total physical dispersion in the fine grid with that of the coarse grid, since the latter – with fewer grid blocks, N – is of a larger inherent numerical component based on equation (2.23). The predictions showed good agreement between the coarse- and fine-grid simulations over the range of slug sizes and total pore volumes of injected water considered (**Fig. 2.5**). This confirms that numerical dispersion in coarse-grid models can approximate representative physical dispersion. As we presented in the previous section, this approach is limited by the fact that in almost all field-scale simulations the uncorrected numerical dispersion far exceeds the physical value. The numerical dispersion associated with a realistic but large simulation grid-size may be too large for the physical mixing desired. This challenge is considered extensively in Chapter 4.

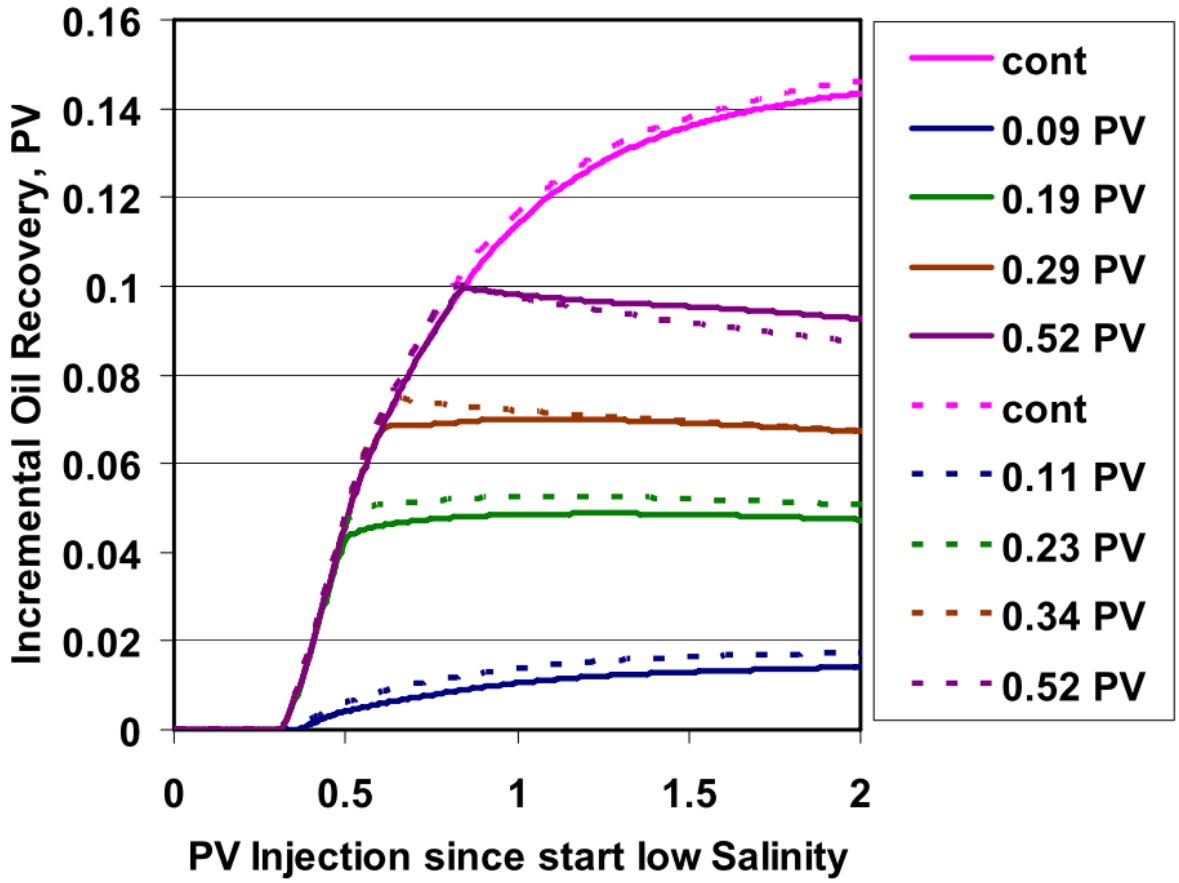


Fig. 2.5: Simulation results demonstrating the use of numerical dispersion to approximate physical dispersion effects in a tertiary mode LSWF (reproduced from Jerauld et al., 2008). Results for a coarse-grid model (25×25) dominated by numerical dispersion (dashed lines) are compared with those for a fine-grid model (162×162) where mixing is dominated by dispersion explicitly defined with input physical dispersivities (solid lines). The predictions from both models are in very good agreement.

2.7.2 Reservoir Heterogeneity

Heterogeneity is a major factor to consider when evaluating the prospect and performance of recovery processes designed for hydrocarbon reservoirs. Its effects have been extensively investigated and perhaps reasonably understood for conventional waterflooding (Osman and Tiab, 1981; Sorbie et al., 1987; Cinar et al., 2004). Its influence on recovery from EOR chemical floods is well-recognized (Kossack and Bilhartz, 1976; Brown and Smith, 1984; Hankins and Harwell, 1996; Cheng et al., 2012). Generally, heterogeneity effects tend to reduce the displacement efficiency especially if flow is viscous-dominated with large injection rates and permeability contrast – **Fig. 2.6** (Baker, 1998; Coll et al., 2000; Wang et al., 2012). Brodie and Jerauld (2014), Attar and Muggeridge (2018) and Adegbite et al. (2021) showed significant impact of heterogeneity on the volumetric sweep efficiency of LSWF. Plausible efficiency-limiting influence of clay-minerals heterogeneity on the microscopic displacement from the LSE in clastic reservoirs has been reported by Dang et al. (2017).

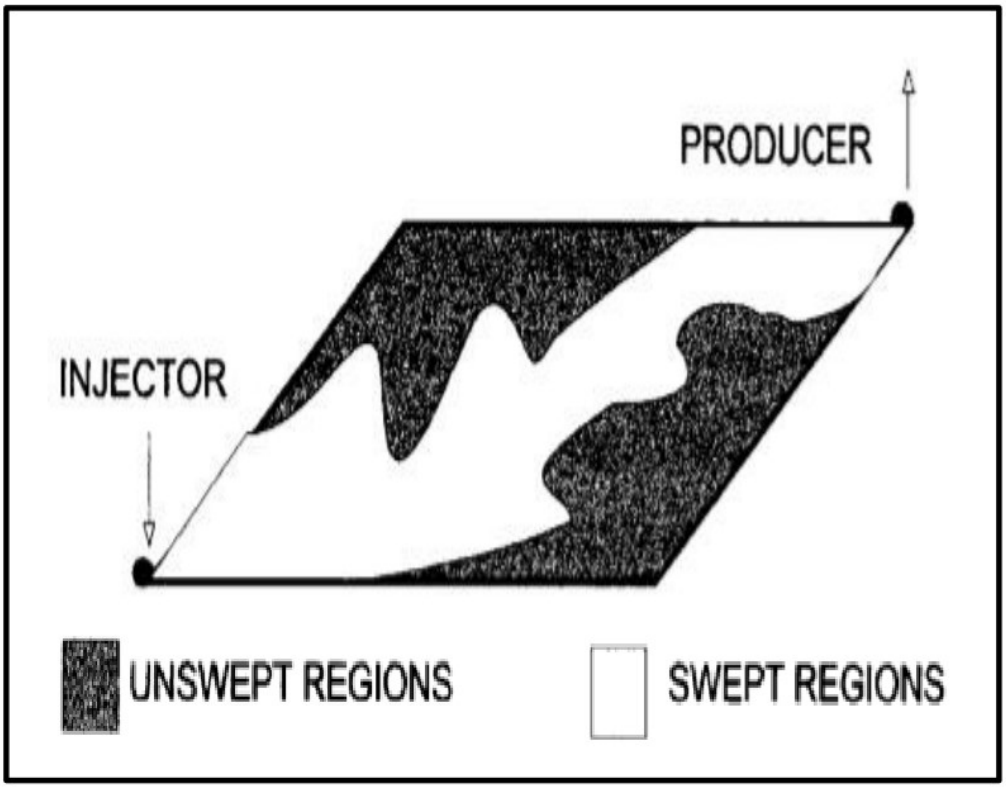


Fig. 2.6: Displacement channelling through high permeability areas in fluvial sands leads to a huge amount of oil bypassed in the low permeability areas, and a poor sweep is achieved (reproduced from Baker, 1998).

The influence of reservoir heterogeneity on macroscopic sweep during LSWF is anticipated to be similar to conventional HS waterflooding if it involves a similar gravity contrast between the fluids. However, fines migration as a potential mechanism or consequence of the LSE has been suggested to alter the reservoir sweep compared to HS waterflood (Chequer et al., 2019; Nguyen et al., 2020).

Besides, the reduced mobility of the displacing injected brine during LSWF may limit the effect of viscous fingering on the volumetric sweep relative to HS waterflood. Nonetheless, a general complication to LSWF is that mixing between the injected LS brine and the HS resident or formation brine is enhanced when the flood front becomes distorted by heterogeneity and crossflow – as seen in other EOR chemical or augmented waterfloods (Zapata and Lake, 1981; Yortsos, 1995). The brine-brine interaction increases as the surface area over which physical dispersion occurs enlarges with heterogeneity, thereby reducing the microscopic displacement potential of the LSE by forming brines with intermediate wettability alteration effects (Jerauld et al., 2008; Mahani et al., 2011; Erke et al., 2016; Chávez-Miyauch et al., 2020). Unlike previous studies, the impact of this on the optimal amount of LS brine to inject is investigated later in this thesis considering geological uncertainties.

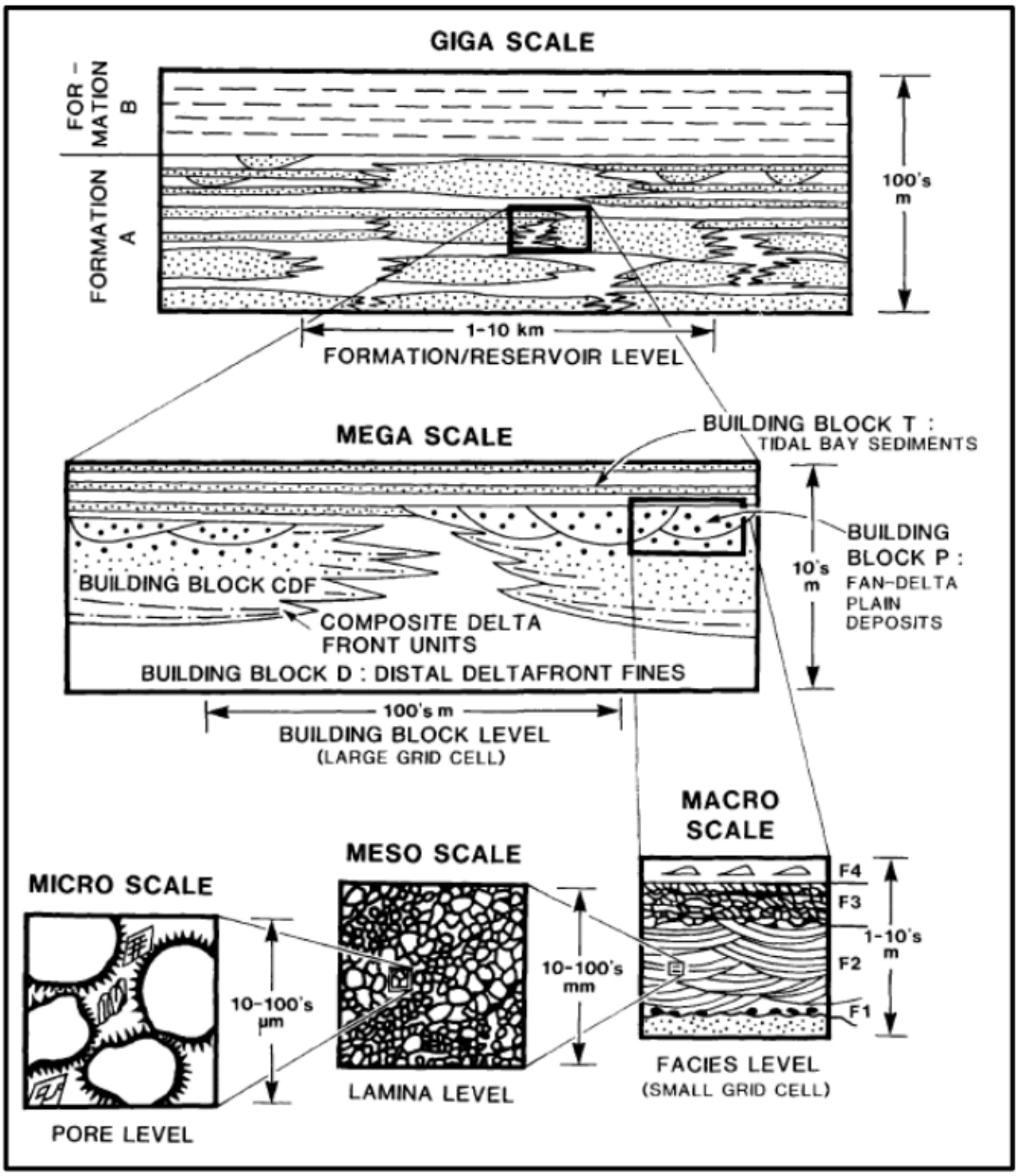


Fig. 2.7: Scales of subsurface geological heterogeneity (reproduced from Henson et al., 2002).

A reliable evaluation of the impact of heterogeneity on recovery processes requires quantifying, characterizing, and representing it appropriately in reservoir models. This is because geological heterogeneity cuts across all scales – from the pore- or micro-scale to the depositional- or mega-scale – as illustrated in **Fig. 2.7**, with distinct effects on fluid displacement and recovery (Jones et al., 1995; Henson et al., 2002). In addition to altering the microscopic displacement potential of the LSE, permeability contrast and crossflow between layers can affect the volumetric sweep efficiency at large scales (Kjonsvik et al., 1994). In contrast, laminations cause trapping of oil at small scales (Jones et al., 1995).

Heterogeneity in a given reservoir is mainly characterized with static and dynamic indices. Static indices quantify reservoir heterogeneity without modelling any flow in the model. The dimensionless Dykstra-Parsons coefficient (Dykstra and Parsons, 1950) is one of the earliest static parameters suggested to quantify heterogeneity. Others include the improved Dykstra-Parsons coefficient (Jensen and Lake, 1988; 1989; Jensen and Currie, 1990) and the Lorenz coefficient (Schmalz and Rhame, 1950). The heterogeneity factor (Koval, 1963), dynamic Lorenz coefficient (Shook and Mitchell, 2009), and vorticity heterogeneity index (Rashid et al., 2012) are some of the proposed dynamic indices. However, these indices only quantify the heterogeneity of fully-represented spatial distribution of the geological property in reservoir models assuming it is certainly accurate. Whereas in real sense, a very few data points are known while others are either interpolated, correlated or kriged. They do not represent or model the absolute heterogeneity of the reservoir geology, thus are post-representation parameters and are often less-adopted for field-scale reservoir descriptions.

The spatial distribution of properties – facies (discrete) and petrophysical (continuous) – between available wells or known data points is generally represented or populated through geostatistical modelling while preserving the realistic reservoir heterogeneity and geological trends. It can be deterministic or stochastic, to account for the uncertainty associated with reservoir geological descriptions. The interpolation between well or data points is constrained with property histograms and variograms to improve the representation of the real case (Tran, 1994; Kelkar et al., 2002). A variogram analysis simply involves a plot of variability of data points in terms of semi-variance against their separation distance in a specific direction (**Fig. 2.8**). Different variogram types or methods can be used when constructing variograms from available data. For example, the classical variance measure (Deutsch and Journel, 1998) is defined as half of the average squared difference between the paired data values, given by

$$\gamma(h) = \frac{1}{2N(h)} \sum_{i=1}^{N(h)} (x_i - y_i)^2 \tag{2.24}$$

where $\gamma(h)$ is the variogram value at separation or lag distance h, $N(h)$ is the number of pairs, x_i and y_i are the tail and head value of the pair i.

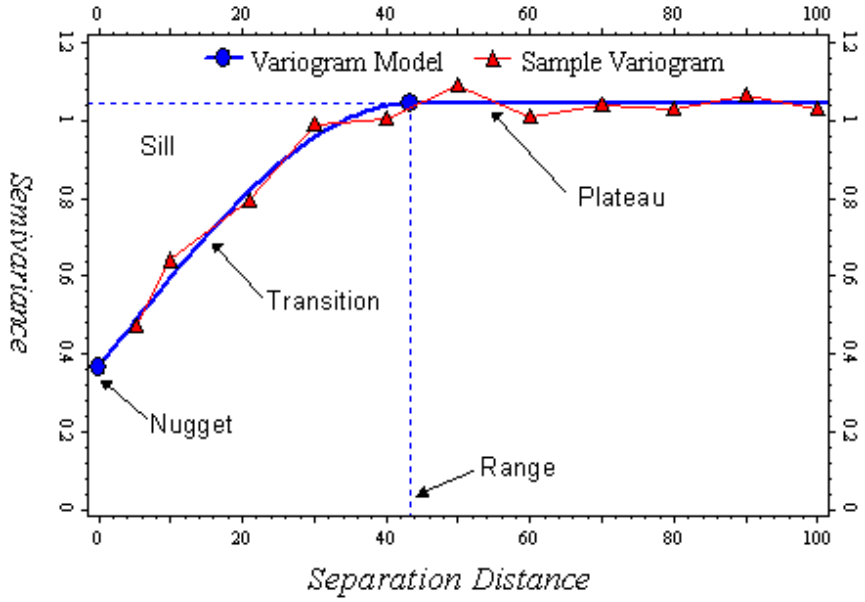


Fig. 2.8: Experimental and model variogram key parameters (reproduced from Schlumberger, 2020).

Variograms are also fitted unconditionally – in the absence of data points – as adopted in this thesis to characterize reservoir heterogeneity. Such a variogram model is defined by its type, nugget, sill, and ranges (**Fig. 2.8**). The range describes where the variogram model reaches its plateau – the separation distance where there is no longer any change in the degree of correlation between pairs of data values. The sill is the semi-variance where the separation distance is greater than the range (on the plateau) and describes the variation between two unrelated samples. The nugget is the semi-variance where the separation distance is zero and describes the short scale variation in the data. In an ideal case, the variograms calculated for a particular property in a particular zone should have the same sill and nugget but different ranges in the major and minor directions which, in turn, describes the "geometrical anisotropy" exhibited by geological phenomena (Isaaks and Srivastava, 1989).

Spherical, Exponential and Gaussian variograms (schematics presented in **Fig. 2.9**) are the three commonly used transition models when constructing or fitting a variogram model (Isaaks and Srivastava, 1989). The spherical model produces linear behaviour at small separation or lag distances (h) and reaches the sill at the effective range (a). The effective range equals the actual range.

If $h \leq a$:

$$\gamma(h) = c\left[1.5\frac{h}{a} - 0.5\left(\frac{h}{a}\right)^3\right] \tag{2.25}$$

else:

$$\gamma(h) = c \tag{2.26}$$

where $c = Sill - Nugget$. The curve is linear at shorter distances and then makes a sharp transition to a flat sill.

The exponential model reaches its sill (c) asymptotically and the effective range (a) is defined as the distance at which $h = 0.95c$.

$$\gamma(h) = c\left[1 - exp\left(-\frac{3h}{a}\right)\right] \tag{2.27}$$

where $c = Sill - Nugget$. The curve has an exponential behaviour, with a rapid variation at shorter distances (i.e. the variation is rapid for small lags). It reaches the sill with an asymptotic approach.

The Gaussian model reaches its sill (c) asymptotically and the effective range (a) is defined as the distance at which $h = 0.95c$. This model has a parabolic behavior near the origin and is the only model that has an inflection point.

$$\gamma(h) = c\left[1 - exp\left(-\frac{3h^2}{a^2}\right)\right] \tag{2.28}$$

where $c = Sill - Nugget$. The curve has a zero slope near the origin. For shorter lag distances, the variation is very slow and then rapidly increases at larger lag distances.

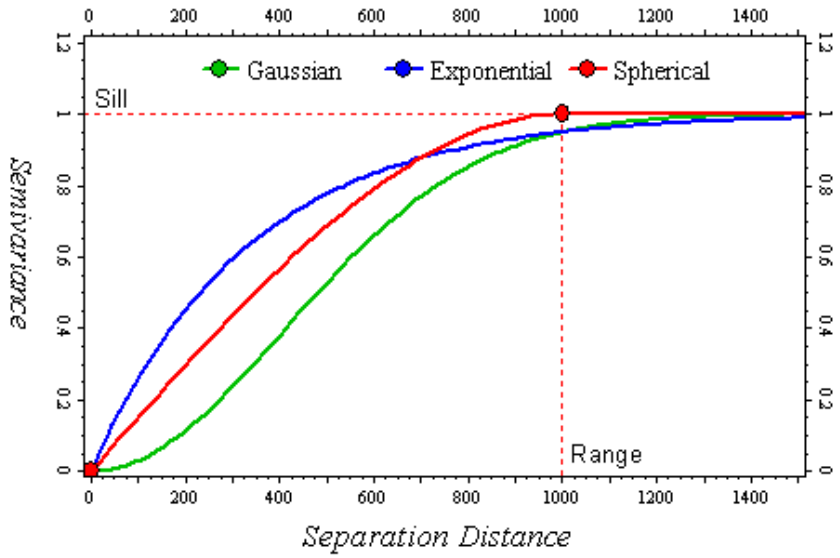


Fig. 2.9: Typical transition variograms for constructing a variogram model (reproduced from Schlumberger, 2020).

Several algorithms are available in commercial simulators such as Schlumberger PETREL, CMG BUILDER, and Paradigm GOCAD™ for both conditional and unconditional deterministic or stochastic geostatistical property modelling. These include but not limited to Sequential Gaussian Simulation (SGS), Gaussian Random Function Simulation (GRFS), Kriging, Moving Average, Neural network etc.

A Gaussian variogram will give a more continuous look within shorter distances, whereas the exponential variogram will give more variation within shorter distances. The output of a model with an exponential variogram will show a more unclear picture than an output from a model with a Gaussian variogram (Isaaks and Srivastava, 1989). The variogram range is the distance within which data can be correlated – correlation length. If A is the range for a variable in a particular direction, a data point at location X can be correlated to a maximum distance of A from that location. Beyond the range, the two points bear no relation to each other. Hence, large range means greater continuity, small range means less continuity, and the larger the range the smaller the heterogeneity (Deutsch and Journel, 1998). Nonetheless, channelling phenomena or flow patterns can be initiated when the permeability field is of a large range or correlation length (Chang et al., 1994). If the nugget is high, then the spatial variation or distribution of the property modelled will give a heterogeneous result even with a large range. Moreover, the spatial heterogeneity result varies with the statistical moments – e.g. mean and standard deviation – of the considered variable property values and their histogram or probability distribution range or limits (Chiles and Delfiner, 1999; Kelkar et al., 2002).

In this thesis, the geostatistical reservoir heterogeneity description is characterized comparatively with the Gaussian and exponential variogram models to evaluate the influence of heterogeneity on the LSE potential considering mixing. Both models are used because they present the extreme cases of spatial variability within a lag distance or correlation length relative to a spherical variogram. In addition, the representative heterogeneity in the reservoir models adopted is varied using different correlation lengths and histograms – defined by the statistical mean and standard deviation – of the variable property. The geostatistical models are simulated with the Gaussian Random Function Simulation (GRFS) algorithm in PETREL.

2.7.3 Crossflow

Crossflow across strata in directions other than that of the bulk flow is among the factors influencing fluid flow in heterogeneous permeable media. While extensive research has been conducted on crossflow effects in conventional waterfloods (Goddin et al., 1966; Osman and Tiab, 1981; Zapata and Lake, 1981; Ahmed et al., 1988; Yortsos, 1995; Cinar et al., 2006; Datta and Weitz, 2013; Debbabi et al., 2017) and EOR polymer floods (Zapata and Lake, 1981; Wright et al., 1987; Sorbie et al., 1987), a few (if any) have investigated its impact on the displacement efficiency in the presence of mixing in LSWF. Experimental studies have shown that crossflow effects can be significant in heterogeneous media where high- and low-permeability zones exist (Richardson and Perkins, 1957; Dawe et al., 1992; Wylie and Mohanty, 1997; Orr, 2004). This induces differences in the displacement-front velocity, distinguishing high-velocity (fast) from low-velocity (slow) layers or zones.

The influence of crossflow on the displacement efficiency of recovery processes is therefore controlled by the property contrasts of the layers (Zhou et al., 2019), and the driving forces present – viscous, capillarity, gravity, and dispersion or dilution (Kereluk and Crawford, 1968; Lake and Hirasaki, 1981). Crossflow affects the displacement of oil by the injected fluid depending on which of the forces present dominate(s), and this is determined by the balance between them (Shook et al., 1992; Haq and Reis, 1993; Tchelepi, 1994; Cinar et al., 2004).

The relevant scaling groups for dominance of one driving force in the presence of another, for example during displacement of oil by water in systems that contain some simple heterogeneity such as layers, are the transverse gravity and capillary numbers, which are given by (Tchelepi, 1994; Zhou et al., 1994):

$$N_{gv} = \frac{\Delta\rho g L k_{av}}{H v \mu_o} \tag{2.29}$$

$$N_{cv} = \frac{L p_c^* k_{av}}{H^2 v \mu_o} \tag{2.30}$$

$$p_c^* = \int_{S_{wc}}^{1-S_{or}} \frac{p_c(S_w)}{(1 - S_{or} - S_{wc})}\, dS \tag{2.31}$$

$$R_l^2 = \left(\frac{L}{H}\right)^2 \frac{k_{av}}{k_{ah}} \tag{2.32}$$

$$N_B = \frac{N_{gv}}{N_{cv}} = \frac{\Delta\rho g H}{p_c^*} \tag{2.33}$$

where N_{gv} and N_{cv} are the ratios of characteristic times for fluid to flow in the transverse direction caused by gravity or capillary forces, respectively, to those in the horizontal direction caused by viscous forces, and p_c^* is a characteristic capillary-pressure difference in the direction transverse to the main flow direction. R_l characterizes the relative impacts of vertical and horizontal viscous-dominated flow. N_B is the Bond number – ratio of gravity to capillary forces. $\Delta\rho$ is the density difference between oil and water, $v = \frac{q_t}{\varphi}$ and q_t is the total Darcy velocity, φ is the porosity, μ_o is the oil viscosity, g is the gravitational constant, and k_{av} is the average absolute permeability in the transverse direction across the layers.

Zhou et al. (1994) used simulation and experimental results in the literature to delineate when capillary forces dominate displacement performance as well as when gravity or viscous forces do. In terms of the mobility ratio across the displacement front M, they defined transitions between different regimes described as gravity-capillary, viscous-capillary, and viscous-gravity equilibrium –

summarized in **Table 2.1**. These have been reported consistent with experimental and numerical observations on the displacement of oil by water in systems that contain some simple layered heterogeneity (Cinar et al., 2006).

Table 2.1: Conditions for transitions between the dominated regions (Zhou et al., 1994).

Flow region	Condition
From viscous- to capillary-dominated	$0.2 < \frac{N_{cv}M}{1+M} < 5.0$
From viscous- to gravity-dominated	$0.2 < \frac{N_{gv}M}{1+M} < 5.0$
From capillary- to gravity-dominated	$0.2 < N_B < 5.0$
Viscous-dominated	$\frac{M(N_{cv}+N_{gv})}{1+M} \ll 1.0$

Early work (Richardson and Perkins, 1957; Gaucher and Lindley, 1960) examined crossflow effects on waterflood performance in layered models with vertical communication. It was reported that, as the flow rate and mobility ratio decreased, the oil recovery increased considerably. They suggested this was because at faster flow rates – viscous-dominance, water tendency to channel through the more permeable layers increased, resulting in early breakthrough. Higher recoveries were also obtained from models with the more permeable layer at the top. However, improved oil recovery efficiency due to viscous-dominated crossflow (VC) has been proposed by Zapata and Lake (1981) and Debbabi et al. (2017).

Crossflow effects on fluid displacements along parallel layers of contrasting property have also been reported in laboratory experiments focussing on capillary forces (Bertin et al., 1990; Dawe et al., 1992; Cinar et al., 2006; Alhamdan et al., 2012; Datta and Weitz, 2013). The more likely dominance of flow by viscous forces at larger scales makes the results less applicable to field settings. Using theoretical models, Zapata and Lake (1981) and Yortsos (1995) investigated the individual effect of viscous forces on flow along layers of contrasting absolute permeability, assuming layer properties are otherwise identical.

Zapata and Lake (1981) suggested VC to be important only for sharpening or piston-like non-unity mobility-ratio displacements, in which the entire saturation change occurs at the shock-front, for both typical waterflood and engineered waterfloods such as EOR-polymer and -surfactant injections. Unlike the former which has only one shock-front during flow along each layer, the later are similar to LSWF

with two distinct displacement shock-fronts – a leading chemical-free (connate) water-oil bank front and a trailing EOR-chemical front (**Fig. 2.2**). They identified dilution (dispersion) of the displacing chemical front in the fast layer by the chemical-free water-oil bank crossflow from the adjacent slow layer as threat to the EOR-chemical sweep efficiency and effectiveness, but not the improvement in oil recovery efficiency due to VC when compared to the no-crossflow (NC) displacement.

Nonetheless, VC recovery efficiency was suggested to be generally better than NC displacement, at least for much of the injection time irrespective of the mobility ratio across the shock-fronts. Increasing the displacing chemical-front velocity or mobility in the slow layer such that its chemical-free water-oil bank front moves ahead of the chemical front in the fast layer was proposed to reduce the unfavourable chemical-free crossflow dilution effect on the chemical sweep efficiency. However, they considered only piston-like displacements with mobility-ratios that are favourable across the chemical front and unfavourable across its leading chemical-free water-bank front. While such mobility-ratios case may be typical of polymer floods because of the increased viscosity of the displacing phase, their application may be limited for LSWF. This is because there is often no significant change between the *in situ* and injected viscosity of the displacing-phase as reported for typical LSWF (Bartels et al., 2019), hence the shock-front mobility-ratios will be different from polymer flooding. Moreover, many displacement processes are not piston-like, in which some of the saturation change occurs over the shock-front, and some occurs over a rarefaction wave following the shock-front. This becomes more prominent around the displacing EOR-chemical front in the presence of dispersion as shown later in Chapter 7.

Debbabi et al. (2017) extended the analysis of VC to different mobility-ratios with more realistic non-piston-like displacements associated with many geologic systems using two-layer models, in addition to considering layers with contrasting porosity and relative permeabilities. They observed a significant influence of VC on displacement processes that are not piston-like. The impact of VC on recovery efficiency was suggested to depend on the mobility ratio across the shock-front in the fast layer and on the time at which the efficiency is measured. VC was observed to be unimportant at late injection times regardless of the mobility ratio across the shock-fronts. However, this is limited to typical water-oil displacements with single shock-front along each layer.

In this thesis, a more general treatment is presented for crossflow effects on recovery efficiency in engineered or low-salinity waterflood considering physical dispersion in Chapter 7. This transcends the no-crossflow, viscous- and gravity-dominated crossflow regimes, for different mobility ratios with the more realistic non-piston-like (or non-sharpening) displacement shock-front often seen in geological systems.

3 Optimization of Injection Design under Uncertainty

Reservoir complexity introduces uncertainty in the exact magnitude of the physical effects on displacement, as discussed in the previous chapter, and this requires adequate considerations when evaluating the optimal injection strategy for the flood. Such optimal design or strategy could be in terms of the injection time, the injected EOR-slug size or LS-brine amount, and the well placement or arrangement. In this chapter, these uncertainties are discussed while techniques to assess the flood performance and optimize its injection design in their presence are reviewed.

3.1 Sources of Uncertainty

As mentioned earlier, LSWF performance varies between laboratory and field tests (Agbalaka et al., 2009; Seccombe et al., 2010; Vledder et al., 2010; Thyne and Gamage, 2011; Skrettingland et al., 2011; Callegaro et al., 2013). This can be associated with uncertainty in the scale-up process from laboratory to field applications. Since LSWF can achieve negligible improved recovery in some circumstances (Thyne and Gamage, 2011; Skrettingland et al., 2011), uncertainty can be detrimental to the success of its wide-scale optimal injection design or strategy. The existence of these uncertainties could imply an inability to predict variable interactions or behaviour in the reservoir (Lowry et al., 1986). Furthermore, uncertainty may prevent field-scale application with significant capital and ongoing costs.

In the field, the level of mixing from dispersion is not accurately known and it is expected to vary between fields because of their different geological heterogeneities and geometries. Results from tracer displacements observed on a range of scales up to $100\ km$ by Mahadevan et al. (2003) suggested that the value of longitudinal dispersivity (α_l) increases with length scale (**Fig. 3.1**). They attributed this to the Taylor dispersion resulting from heterogeneity on a range of length scales. For the inter-well distances which are important to field-scale low-salinity flood design, the dispersivity is roughly $2-5\%$ of the length travelled. While this was corroborated by BP data from Jerauld et al. (2008) – indicated with red dots in **Fig. 3.1**, uncertainty remains in the level of physical dispersion from inter-well tests unlike SWCTT. The reported large inter-well dispersivities remain controversial because contributions from 'conformance' in the well bore are not distinguished from true mixing in the reservoir (Coats et al., 2009). For example, the commingling of fluids in the wellbore – from layered heterogeneity or streamlines of different lengths – is an apparent mixing and does not necessarily mean that actual physical mixing occurs within the pore space.

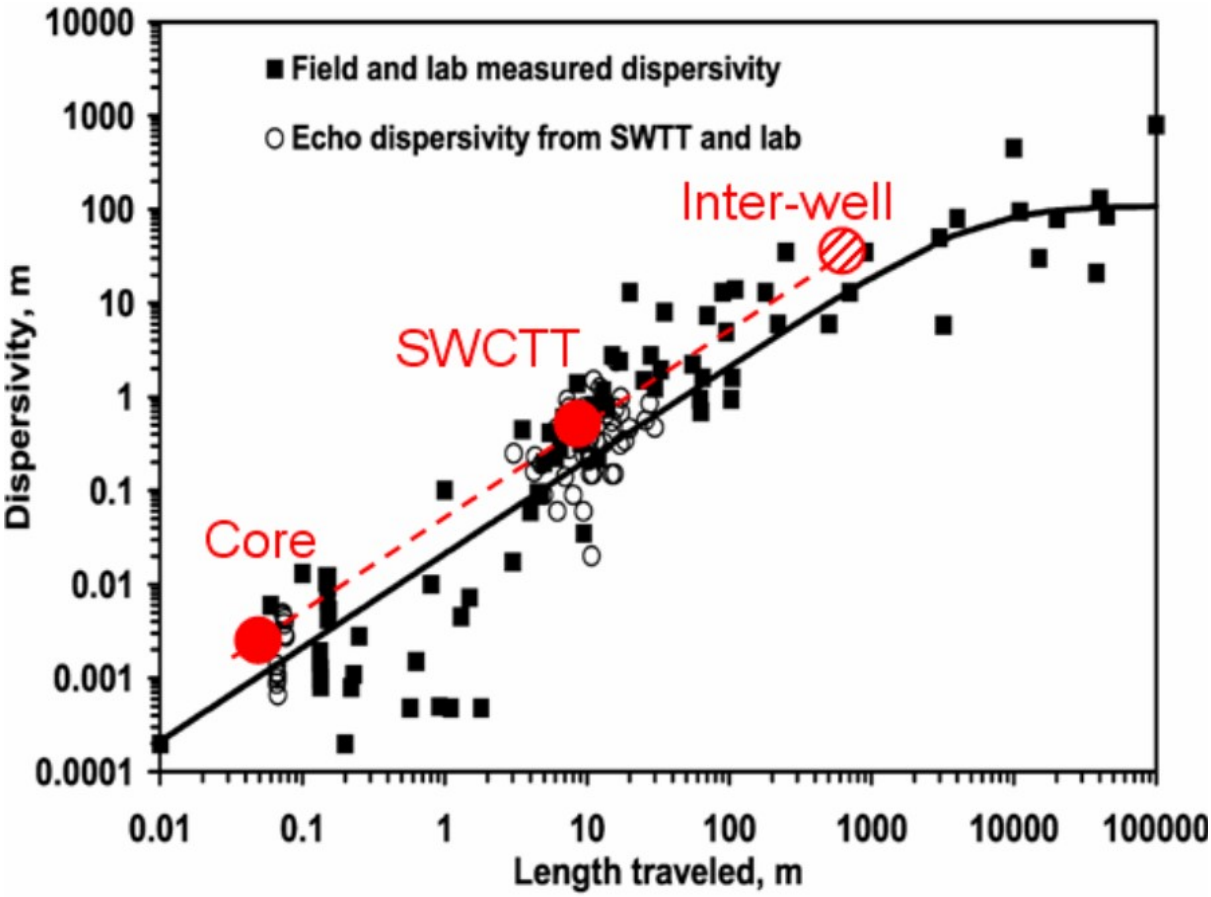


Fig. 3.1: Dispersivity as a function of length travelled from Mahadevan et al. (2003). BP data from corefloods, single-well chemical tracer tests (SWCTT), and inter-well tests are indicated in red dots (reproduced from Jerauld et al., 2008).

Coats et al. (2009) used the analytical method of Muskat (1949) discussed in Chapter 2.7.1 to fit the effluent concentration profile of a transmission test in layered heterogeneity taken from Mahadevan et al. (2003). It was suggested that matched dispersion is the sum of apparent dispersivity (due to conformance or heterogeneity) and the actual physical dispersivity. They argued that physical dispersivity is scale-independent and is always a constant value of $0.003\,m$. Whereas, larger dispersivities have been matched by Jerauld et al. (2008) and Seccombe et. al (2008) from corefloods and reliable SWCTT which does not reflect differences in streamline speeds the way inter-well tracers do. This issue has been well recognized in the literature but no simple ways of addressing it have been suggested (Jerauld et al., 2008).

Measurements of physical transverse dispersivity (α_t) are much less common than α_l but they indicate that $\alpha_t \cong \alpha_l/30$ (Grane and Gardner, 1961; Perkins and Johnston, 1963; Lake and Hirasaki, 1981; Coats et al., 2009). Therefore, the magnitude of both transverse and longitudinal dispersion at inter-well and inter-layer length scales remains highly uncertain (Gelhar et al., 1992).

Reservoir heterogeneity generally tends to reduce the displacement efficiency of floods (Baker, 1998; Coll et al., 2000; Wang et al., 2012). The effect of mixing on brine-brine interactions and the LS displacement is further enhanced when the flood front becomes distorted by heterogeneity and crossflow. For accurate field-scale prediction of LSWF performance, both mixing and heterogeneity need to be adequately captured. Since the spatial distribution of geological heterogeneity between the few known well or data points is either interpolated, correlated or kriged in reservoir models (Isaaks and Srivastava, 1989; Deutsch and Journel, 1998; Kelkar et al., 2002), uncertainty is introduced into the represented reservoir descriptions.

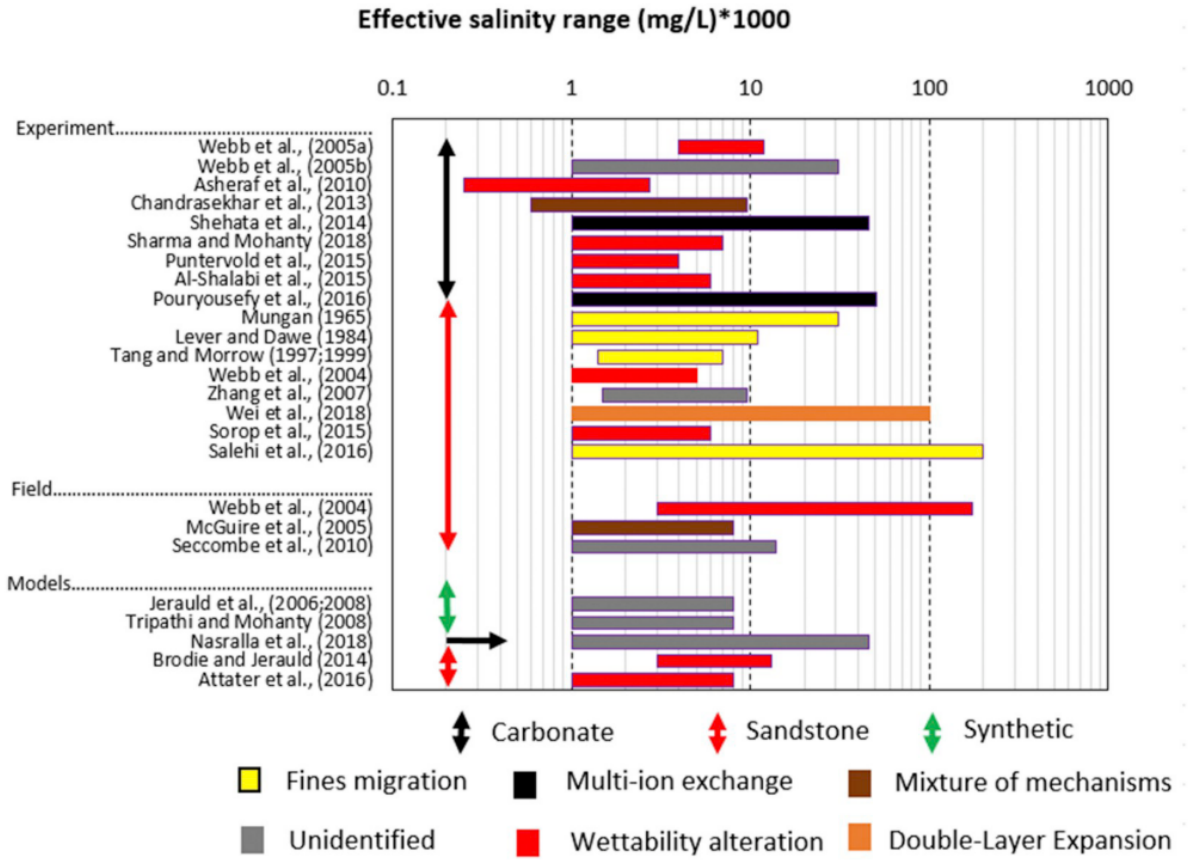


Fig. 3.2: Reported salinity-thresholds for the LSE, indicating on a log-scale where the effect of salinity is variable (reproduced from Al-Ibadi et al., 2019). Salinity changes outside of the range had no further noticeable effect. Arrows indicate group of rock types. Bars are colour-coded for the identified LSE mechanisms.

It is evident from the literature that the change in flow behaviour and fluid mobility from LSWF is dependent on certain concentrations of the active solute-component or adsorbed-ion. As we also show later in Chapter 4, these solute-concentration thresholds are a crucial factor in modelling the process and the impact of physical dispersion on the effectiveness of the injected LS brine. However, just as there are disagreements about the LSE mechanism and the level of mixing across length scales,

there remains a difference of observations and opinion about the threshold salinities. The evidence of this is available on a range of scales – from laboratory experiments to field observations, and various data that have been used to model LSWF (**Fig. 3.2**). For sandstones which is our focus, it is generally accepted that incremental oil can be obtained when the injected brine salinity was $< 10{,}000\ ppm$, though this may not always be the case (Al-Ibadi et al., 2019). Nonetheless, the LSE appears to be largely reported for injected salinity $< 3{,}000\ ppm$ across the studies presented in **Fig. 3.2**.

Residual oil saturation to EOR floods is considered as a significant factor when assessing the uncertainty in their improved oil recovery during scale-up to field applications (Brown and Smith, 1984; Dang et al., 2011; Solairaj et al., 2012; Dang et al., 2017). The dependence of the residual oil saturation to the LSE on local lithology and mineralogy (Jerauld et al., 2008; Aladasani et al., 2014; Bartels et al. 2019) further compounds the performance uncertainty in reservoirs with a spatial distribution of mineral content and heterogeneity.

Due to the significant impact of these reservoir properties on LSWF performance, the optimal injection design obtained based on a single realization may deviate severely from the actual optimality. This forms a major part of the objectives of this thesis which is to investigate how the optimal injection design is influenced by these physical phenomena and their interactions under uncertainty.

3.2 Optimal Injection Design or Strategy

Optimization of low-salinity water injection in clastic reservoirs has received little attention in the literature, with most research concentrated on core-scale experiments (Katende and Sagala, 2019). Early commencement of an EOR process conventionally favours recovery performance with respect to stable displacement of the injected chemical particularly if limited (i.e. slug injections). However, the possible reduction of uncertainty with time has been identified as a likely benefit of delayed injection (Alkhatib and King, 2014; Ladipo and Ogbe, 2015).

Jerauld et al. (2008) considered the reported distance-dependent physical dispersivity data of Mahadevan et al. (2003) and Lake (1989) to evaluate the impact of physical dispersion on LS slug injections using the standard salinity-dependence model. They suggested a minimum slug size of $0.4\ PV$ to contact most of the available residual oil target under homogeneous reservoir conditions. Under geological heterogeneity and in the presence of an aquifer, Attar and Muggeridge (2018) proposed at least $0.6\ PV$ slug size to achieve 95% of the recovery from continuous LS water injection. The effect of the uncertainties associated with mixing and other interacting process-controlling reservoir properties at field or inter-well scales is not or only poorly considered in existing works to

estimate optimal slug size for LSWF designs. This is examined through representative heterogeneous reservoir models in Chapters 5 and 6.

To address this issue, Dang et al. (2017) proposed an optimization scheme for LSWF with a mechanistic model. They only considered the influence of geological uncertainties on the optimal well placement in a continuous LS brine injection. The same scheme was extended by Gorucu et al. (2019) but in the presence of fines transport to optimize well placement in a continuous LS injection excluding geological uncertainties. However, no study has investigated the dependence of the optimal injected LS slug amount on well arrangement or flood pattern in the presence of physical mixing until now. This will be discussed in Chapter 6.

3.3 Recovery Uncertainty Assessment and Injection Design Optimization

Quantification of uncertainty in performance predictions of recovery processes – which stems from the uncertainties of various model input parameters (or state variables) as previously discussed – is an important aspect of reservoir simulation studies. Optimizing the injection design or strategy considering this risk is fundamental to reliably balance the technical and financial performance of such processes. Some of the existing techniques or methods to assess performance (or objective function) variability – in form of probability density or distribution functions – and optimize injection designs (or control variables) for recovery processes in the presence of uncertainties are reviewed here.

3.3.1 Uncertainty Quantification (UQ)

Unlike the traditional one-parameter-at-a-time method, systematic approaches have emerged to quantify the uncertainty associated with various model input parameters based on experimental design (ED) and response surface generation (RS) techniques (Friedmann et al., 2001; Kabir et al., 2002; Peake et al., 2005; Kalla and White, 2005). ED is the science of designing a minimum number of experiments (simulations) in such a way that sufficient information about the system response or objective function can be obtained (Yang et al., 2007). The ED technique arranges simulation runs according to statistically predefined patterns or design matrices in which several parameters are varied simultaneously. Hence, it becomes possible to understand linear, nonlinear and interaction effects of uncertain parameters on the response, while minimizing the number of simulations.

Satterthwaite (1959) proposed random design – one for which a random sampling process (with replacement), as seen in stochastic Monte Carlo, is used to choose all or some of the elements of each variable in the design matrix. Significant correlations can exist between columns of the design matrix,

with biased estimators of the coefficients in the resulting response model (Youden et al., 1959). McKay et al. (1979) developed the Latin hypercube sampling method to improve upon random designs by using the ideas from 'quota sampling'. In Latin hypercube sampling, the input variables are considered to be random variables with known distribution functions. For each input variable x_k, all portions of its distribution are represented by input values by dividing its range into n strata of equal marginal probability $\frac{1}{n}$, and sampling once from within each stratum. Latin hypercube (Tang, 1993) is a common variant of the design obtained by Latin hypercube sampling, in which an $n \times k$ Latin hypercube consists of k permutations of the vector $\{1,2,\dots,n\}^T$. The input values are therefore predetermined and there is no sampling within strata. As with Latin hypercube sampling, there are no restrictions on how the different variable columns are combined to form the design matrix. Therefore, Latin hypercube designs can have significant correlations between the columns of the design matrix.

Ye (1998) introduced orthogonality into Latin hypercubes to enhance the use of Latin hypercube designs for regression analysis and response surface generation. Orthogonality is a measure of the maximum pair-wise correlation between columns of input parameters at the sampling points of a design matrix. For example, the orthogonality of two columns in a design matrix: $\vec{a} = (a_1, a_2, \dots\dots, a_n)$ and $\vec{b} = (b_1, b_2, \dots\dots, b_n)$ with mean values, $\bar{a}$ and $\bar{b}$ respectively, is measured by the correlation between the two column vectors as follows:

$$\frac{\sum_{i=1}^{n}\left[(a_i - \bar{a})\left(b_i - \bar{b}\right)\right]}{\sqrt{\sum_{i=1}^{n}(a_i - \bar{a})^2 \sum_{i=1}^{n}\left(b_i - \bar{b}\right)^2}} \tag{3.1}$$

Two columns are orthogonal if they have zero correlation. A design is orthogonal if all its matrix-columns are orthogonal. This implies that every pair of columns in an orthogonal Latin hypercube has zero correlation. Furthermore, the elementwise square of each column has zero correlation with all other columns, and the elementwise product of every two columns has zero correlation with all other columns. These properties ensure the independence of estimates of linear effects of each variable, and the estimates of the quadratic effects and bilinear interaction effects are uncorrelated with the estimates of the linear effects (Ye, 1998). However, absolute orthogonal designs may exhibit poor space-filling which is desirable for data analysis methods such as residual plots in regression diagnostics and nonparametric surface fitting (Ye, 1998; Cioppa, 2002). A good space-filling means the design points are scattered throughout the experimental region or parameter uncertainty space – all possible realizations for a given distribution space of the random input variables – with minimal unsampled regions (i.e. voided regions are relatively small).

Fang et al. (2000) later defined uniform designs where experimental points are uniformly scattered on the domain parameter uncertainty space unlike two-level factorial designs (**Fig. 3.3**). They do not require orthogonality and are space-filling. Space-filling designs provide coverage of the entire uncertainty space, and this facilitates its broad exploration (Fang and Wang, 1994; Ye, 1998).

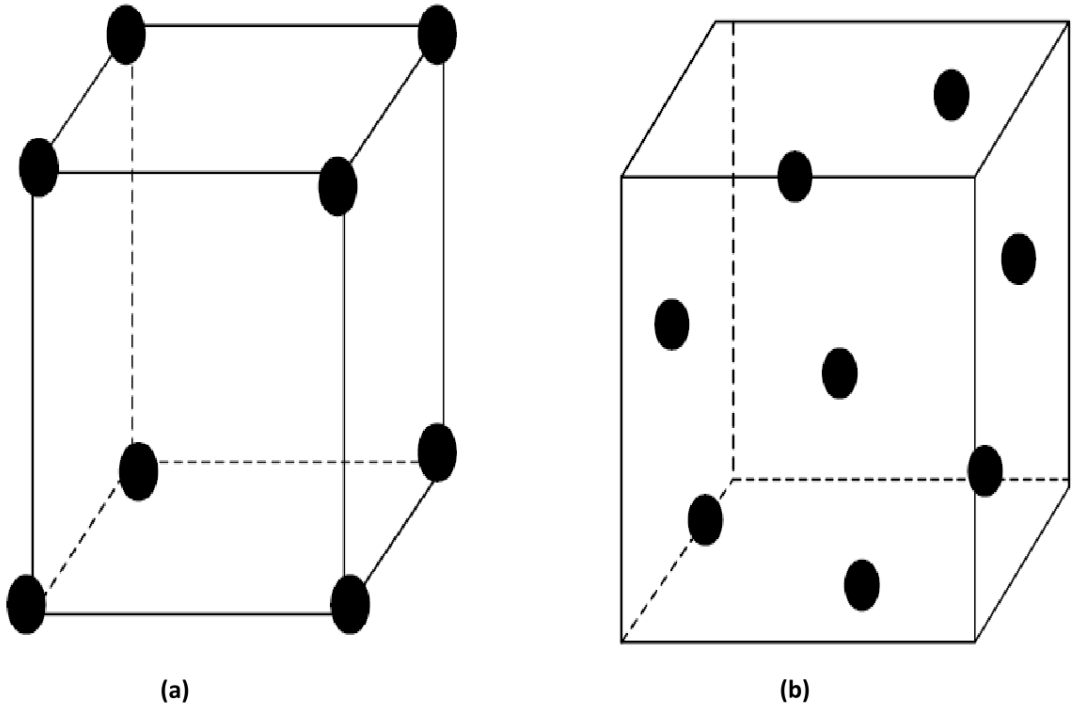
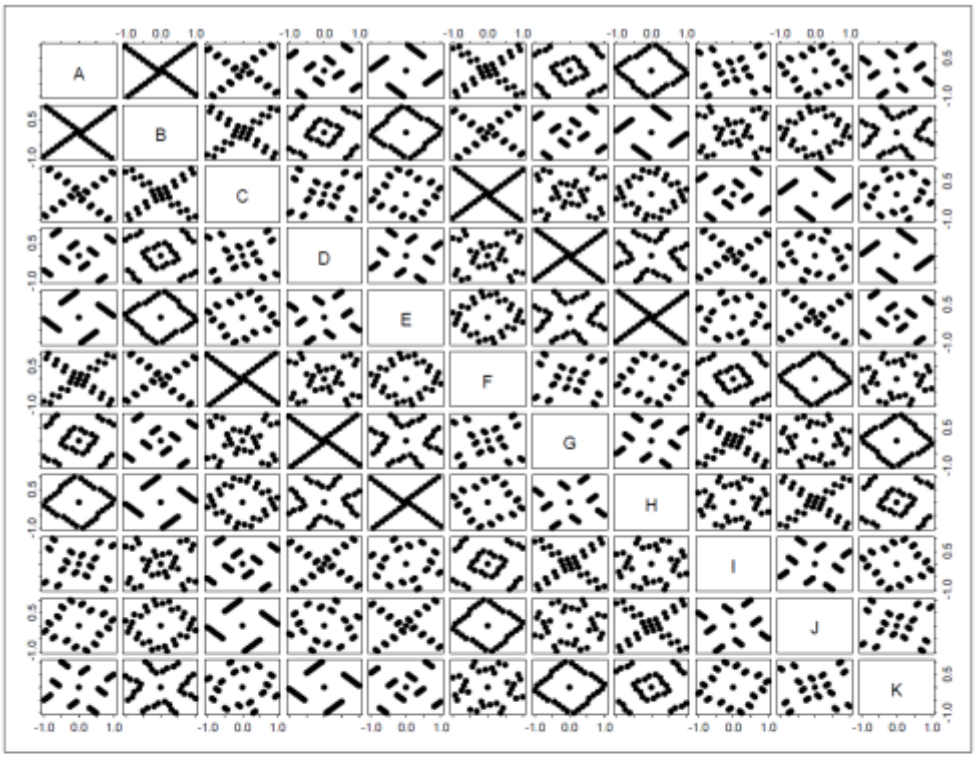
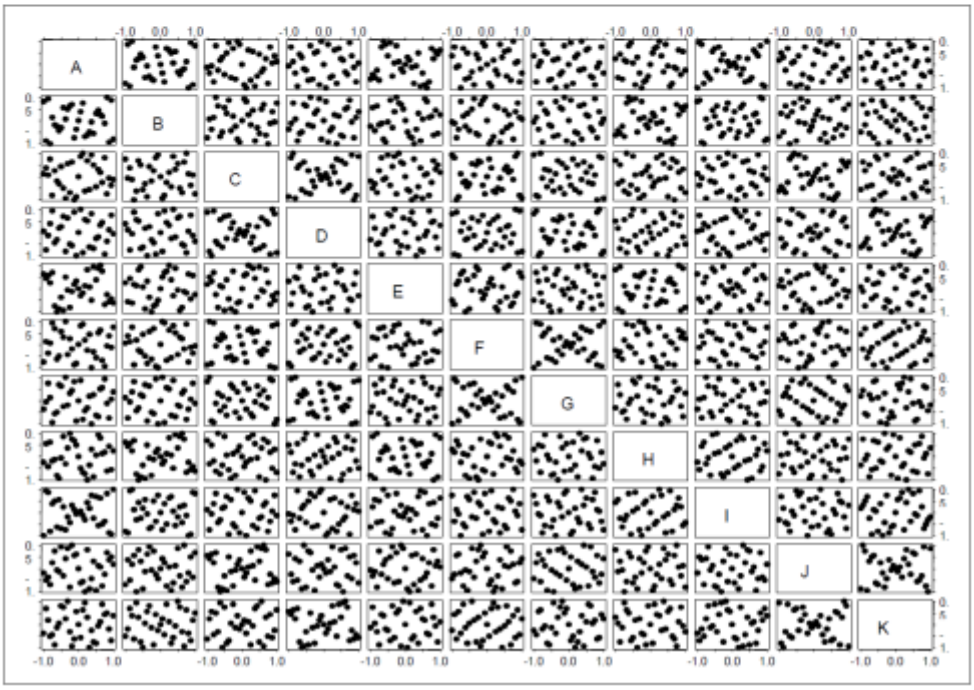


Fig. 3.3: Experimental design points of (a) a traditional 2^3 factorial design compared to (b) a uniform design illustrating their dispersion or better space-filling in the latter.

The most critical and desirable characteristics of an experimental design are orthogonality and space-filling. Cioppa (2002) melded together the concepts of orthogonal Latin hypercube and uniform designs to create a new design – near-orthogonal Latin hypercube design – that performs well on both of these characteristics. Algorithms that improve the space-filling capabilities may do so while compromising orthogonality – the goal is an effective trade-off between the concepts of near orthogonality and space-filling (Cioppa, 2002). A candidate near-orthogonal Latin hypercube design for 11 input variables with 33 simulation-runs $(N_o)_{11}^{33}$ showed better space-filling with higher orthogonality value (< 0.1) than corresponding absolutely orthogonal Latin hypercube design $(O)_{11}^{33}$ (Cioppa, 2002) – **Fig. 3.4**. A good design for sensitivity analysis and uncertainty assessment should have an orthogonality value < 0.2 (CMG, 2019). In this thesis, an orthogonality value less than 0.1 is rather adopted as good for response surface generation or proxy modelling to assess performance uncertainty. The Latin hypercube sampling under several variants has been used to design experiments to quantify performance uncertainty in many EOR studies (Yang et al., 2011; Spagnulo et al., 2015).



(a)



(b)

Fig. 3.4: Two-dimensional projections of columns for sampled input variable-pairs over discretized experimental region or parameter uncertainty space for (a) $(O)_{11}^{33}$ design. (b) $(N_o)_{11}^{33}$ design. Although (**a**) is orthogonal, its space-filling is poor (reproduced from Cioppa, 2002).

There are also lower-level but deterministic classical experimental designs for sensitivity analysis – such as two-level fractional factorial, full factorial, and Plackett-Burman designs – and uncertainty

quantification – such as three-level Box-Behnken and central composite designs. While these lack the flexibility of handling mixed levels (i.e. different numbers of sampling values) of input variables compared to Latin hypercube design, they can be informative for response surface generation.

The response surface generated from an experimental design explores the relationships between the input variables (parameters) and the performance response (objective function) to assess its uncertainty (variability) within the defined parameter space. The main idea of response surface is to use a set of designed experiments to build a proxy (approximation) model to represent the original complicated reservoir simulation model (Cullick et al., 2006; Yang et al., 2009; Yang et al., 2011). The most common proxy models take either a linear or quadratic form of a polynomial function determined by a least-square fit between the polynomial response and the supplied training data.

The linear proxy model is defined as

$$y = a_0 + a_1x_1 + a_2x_2 + \ldots + a_kx_k \tag{3.2}$$

where y is the response (objective function), and $a_1, a_2, \ldots, a_k$ are the coefficients of the proxy model otherwise referred to as the linear effects or, in some statistics references, parameter estimates or unknown parameters. $x_1, x_2, \ldots, x_k$ are the input variables (parameters).

The second-order (quadratic) polynomial model is given as

$$y = a_0 + \sum_{j=1}^{k} a_j x_j + \sum_{j=1}^{k} a_{jj} {x_j}^2 + \sum_{i<1} \sum_{j=2}^{k} a_{ij} x_i x_j \tag{3.3}$$

where a_0 is the intercept, $a_1, a_2, \ldots, a_k$ are the coefficients of linear terms, a_{jj} are the coefficients of quadratic terms, a_{ij} are the coefficients of cross (interaction) terms.

For a polynomial regression proxy model, the statistical significance of each term and the model can be analysed using equations given by Sall (1990). Statistically insignificant response surface term(s) are removed from the proxy model to simplify and improve the model. Proxy model verification or validation is by comparing some predicted response (from generated response surface) with the actual (from original reservoir model simulation).

The latest developments on response surface generation have engaged the use of artificial neural networks to train (polynomial) proxy models from experimental design results (Haykin, 1999; Dang et al., 2018). Neural networks often capture the interaction effects better for highly multi-level non-linear multidimensional problems, with improved proxy predictions relative to typical polynomial

regression (Cullick et al., 2006; Zubarev, 2009; Aifa, 2014). The literature is rich and still evolving on this subject.

In this thesis, the near-orthogonal Latin hypercube and neural networks are adopted to design experiments and generate response surfaces (or proxy models) respectively to quantify performance uncertainty in LSWF.

3.3.2 Optimization

Optimization aims to improve a model by varying controllable parameters to create the best possible objective – to identify the maximum objective function value possible at a desired 'level of confidence'. Optimization problems affected by uncertainty in model input data have long been a focus of optimization studies (Beyer and Sendhoff, 2007). Solutions to optimization problems can exhibit significant sensitivity to perturbations in input data uncertainty, thus rendering a computed solution suboptimal, or even potentially worthless (Yang et al., 2011).

When uncertainty is included in the optimization process, a single objective function evaluation is composed of the outcomes of a number of 'realizations' sampled from the inherent input data uncertainty space. Each realization is based on a particular configuration of the uncertain variables and requires an individual simulation evaluation. In addition, the combined objective function F (to be maximized in most cases) at a desired utility or confidence level is generally given by:

$$F(X;R,\lambda) = \mu(X;R) - \lambda \cdot \sigma(X;R) \quad , \qquad \mu(X;R) = \frac{1}{S}\sum_{i=1}^{S} f_i \quad ,$$

$$\sigma(X;R) = \sqrt{\frac{1}{S}\sum_{i=1}^{S}(f_i - \mu)^2} \quad , \qquad f_i = F(X;r_i) \tag{3.4}$$

where X is the set of N control variables, R is the set of S realizations (r_i), and μ and σ represent the mean and standard deviation of F from each X over all S realizations respectively. All S realizations share one unique configuration of the control variables X. λ is the 'risk aversion factor' indicating the desired level of confidence with which to optimize the objective function. Its role is to control the coupling of the two optimization goals: maximizing μ and minimizing σ. The greater the value of λ selected, the greater the risk aversion and therefore the lower the degree of variability sought in the result.

Several algorithms have been suggested to explore the search and solution space in optimization problems. Meanwhile, population-based search algorithms maintain knowledge of several promising

regions of the search space at once and provide candidate solutions in large batches. Thus, they are less trapped in a local optimum and are often preferred to local gradient-based methods including simplex and simplex non-linear optimizers (e.g. Nelder and Mead, 1965; Couët et al., 2000). They include the Particle Swarm Optimization (Kennedy and Eberhart, 1995), Multiple Objective Particle Swarm Optimizer (Coello et al., 2004), Differential Evolution (Storn and Price, 1995; Beyer and Schwefel, 2002), DECE – Designed Exploration and Controlled Evolution (Yang et al., 2009) etc. In the literature, a number of optimization studies on EOR processes have been conducted with these algorithms (Egermann et al. 2001; Yang et al., 2007; Peterson et al., 2010; Dang et al., 2017; Dang et al., 2018; Gorucu et al., 2019). DECE implements CMG's proprietary optimization method and imitates the process which reservoir engineers commonly use to solve history matching or optimization problems. It is a robust process that has been used to optimize LSWF in a few studies (Dang et al., 2017; Gorucu et al., 2019).

DECE can be simply described as an iterative optimization process that first applies a designed exploration stage and then a controlled evolution stage using a specific objective function. In the designed exploration stage, the goal is to explore the search space in a designed random manner such that maximum information about the solution space can be obtained. In this stage, experimental design and Tabu search techniques are applied to select parameter values and create representative simulation datasets. In the controlled evolution stage, statistical analyses are performed for the simulation results obtained in the designed exploration stage. Based on the analyses, the DECE algorithm scrutinizes every candidate value of each parameter to determine if there is a better chance to improve solution quality if certain candidate values are rejected (banned) from being picked again. These rejected candidate values are remembered by the algorithm and they will not be used in the next controlled exploration stage. To minimize the possibility of being trapped in local optimum, the DECE algorithm checks rejected candidate values from time to time to make sure previous rejection decisions are still valid. If the algorithm determines that certain rejection decisions are not valid, the rejection decisions are recalled, and corresponding candidate values will be activated again.

However, these algorithms become computationally costly to apply in the presence of geological uncertainties. For example, in a LSWF where reservoir heterogeneity impacts performance significantly, the optimal solution obtained based on a single realization may deviate substantially from the actual optimality. Hence, a valid solution may require considering all realizations for the (iterative) optimization process which can be computationally impractical. Robust optimization is a recent approach for solving such optimization problems under uncertainty, including geological uncertainties (Yeten et al., 2003; van Essen et al., 2009; Hasan et al., 2009; Yang et al., 2011; Dang et

al., 2017). In robust optimization, the objective is an optimal risk-weighted solution that is most likely to give good performance for any realization of the uncertainty in a given set (Yang et al., 2011). This is achieved by first ranking the entire set of geological realizations (≥ 100) and then selecting a small set of representative realizations to be used in the robust optimization procedure. It involves discretizing the uncertainty space R into a finite number of realizations r_i as discussed previously in equation (3.4), such that (Van Essen et al., 2009):

$$r_i = \{r_1, r_2, \cdots, r_S\} \in R\ , \qquad F = F(X, r_i)\ , \qquad F_{RO} = \mu_{r_i}[F(X, r_i)] - \lambda \cdot \sigma[F(X, r_i)] \tag{3.5}$$

where S is the total number of realizations (e.g. geostatistical spatial reservoir descriptions), F is the performance measure (objective function) which is a function of optimization parameters (control variables) X and realizations r_i, and F_{RO} is the objective function in robust optimization.

Assuming all realizations are equiprobable, F_{RO} can be further defined as

$$F_{RO} = \bar{F} - \lambda \cdot \sqrt{\frac{1}{S}\sum_{i=1}^{S}(F(X, r_i) - \bar{F})^2}\ , \qquad \bar{F} = \frac{1}{S}\sum_{i=1}^{S} F(X, r_i) \tag{3.6}$$

Choosing the small set of geological realizations randomly will not accurately represent the uncertainty (Yang et al., 2011). Several ranking methods have been investigated for the purpose of selecting representative realizations that span recovery uncertainty in EOR processes (McLennan and Deutsch, 2005; Fenik et al., 2009). After accurately ranking these S realizations, a small set S_R is chosen for robust optimization such that:

$$r_R = \{r_1, r_2, \cdots, r_{S_R}\} \in r_i = \{r_1, r_2, \cdots, r_S\} \in R \tag{3.7}$$

$$F_{RO} = \bar{F} - \lambda \cdot \sqrt{\frac{1}{S_R}\sum_{i=1}^{S_R}(F(X, r_R) - \bar{F})^2}\ , \quad \bar{F} = \frac{1}{S_R}\sum_{i=1}^{S_R} F(X, r_R) \tag{3.8}$$

To further reduce the number of required simulations in a robust optimization process, Yang et al. (2011) suggested a Latin Hypercube plus Proxy Optimization procedure. The algorithm has four key steps: (i) Experimental design with Latin hypercube; (ii) Response surface generation or proxy modelling with polynomial regression or neural network; (iii) Proxy-based optimization, to generate a pre-defined number of possible optimum solutions to increase the chance of finding the global optimum solution; and (iv) Validation and iteration of possible optimum solution(s) from proxy optimization with actual reservoir simulation, to further improve both the proxy prediction(s) and the optimal solution found.

Most of the algorithms discussed in this section are readily available in the uncertainty assessment and optimization packages of some commercial simulators such as Schlumberger PETREL and CMG CMOST. For the optimization problems in this thesis, we consider the DECE and the Latin hypercube plus proxy optimization procedure comparatively.

3.4 Concluding Remarks and Research Contributions

The literature has shown LSWF to be an emerging but largely promising improved oil recovery process at different length scales. Due to the complex crude-oil/brine/rock-mineral (COBR) interactions during LSWF, the actual pore mechanism driving its LSE remains a subject of debate. However, it is widely accepted that wettability alteration causes a change in the relative permeabilities which manifests, at the macroscale, by a connate water-oil bank signature that has been observed in core and field tests.

It is difficult to represent the connate water-oil bank displacement accurately in existing models using conventional numerical grids that are computationally practical. Consequently, this will be further examined in this research to propose a simple-to-implement method – relative to the limitations of existing approaches – to capture the displacement reliably. This is presented in Chapter 4 and is a necessary first step before the presentation of field-scale simulations of LSWF.

The literature has shown that the interaction between the injected LS water and the connate water-oil bank during displacement is critical to the overall flood efficiency. It is anticipated that this can be significantly influenced by reservoir mechanisms such as mixing between the distinct brines, reservoir heterogeneity and crossflow. While transverse mixing is reportedly relevant when heterogeneity affects the vertical sweep, its significance on the LSE when the heterogeneity impacts the areal sweep remains unclear. This research aims to investigate this conclusively using a detailed simulation study which is presented in Chapters 5 and 6.

The effects of mixing and heterogeneity on the LS displacement and the flood performance in clastic reservoirs have been evaluated through different approaches in a few studies. However, the uncertainties in the exact magnitude of these physical effects and other interacting process-controlling reservoir properties at field or inter-well scales are not or only poorly considered in these works. In this thesis, a simulation study is conducted to explore these areas through representative heterogeneous reservoir models and investigate how the optimal injection design can be influenced by these physical phenomena and their interactions under uncertainties. Furthermore, the dependence of the optimal injected LS slug amount on well arrangement or flood pattern is evaluated in the presence of physical mixing unlike any previous work. This is presented in Chapter 6.

Crossflow effects on recovery efficiency have been examined in the literature but have been focussed on typical water-oil displacements. This thesis will present a more general approach for engineered or low-salinity waterflood to aid its design considering physical dispersion. This is presented in detail in Chapter 7.

Overall, this thesis presents a methodology to allow accurate and representative field-scale simulations of LSWF, combined with a detailed quantitative analysis of the effect of different physical mechanisms on recovery. We finally demonstrate a workflow for LSWF optimization under uncertainty.

4 Controlling Numerical Dispersion Effects in Low Salinity Waterflooding Models

4.1 Introduction

Successful reservoir management design relies on accurate simulation of the proposed displacement processes. For an augmented or engineered Enhanced Oil Recovery (EOR) waterflood such as Controlled/Low Salinity Waterflood (LSWF), the size of the high-salinity (HS) connate water-oil bank formed ahead of the displacing injected low-salinity (LS) water (**Fig. 4.1**a) – due to the different fractional flow for the distinct brines in the presence of oil (**Fig. 4.1**b) – significantly influences the flood displacement efficiency. Furthermore, interaction in the form of actual reservoir mixing between the injected LS water and the HS connate water-oil bank impacts the effectiveness of the LS brine. This is demonstrated in the effluent concentration profiles reported from various experimental and field demonstrations of LSWF (Jerauld et al., 2008; Vledder et al., 2010; Seccombe et al., 2010; Mahani et al., 2011; Thyne and Gamage, 2011; Fjelde et al., 2012; Callegaro et al., 2013; Korrani et al., 2014; Law et al., 2014; Erke et al., 2016; Kazemi et al., 2016; Dang et al., 2016). It is therefore important to represent the connate water-oil bank displacement reliably in LSWF simulations as discussed in Chapters 2 and 3.

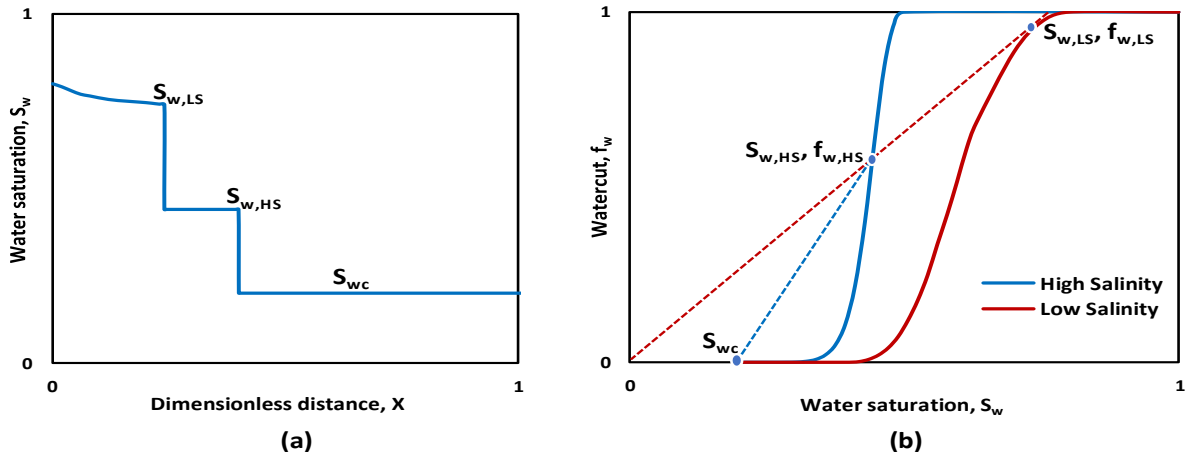


Fig. 4.1. Analytical water saturation and fractional flow profiles for a 1D-homogeneous secondary-mode low-salinity waterflood. (a) Water saturation profile with two displacement shock-fronts – oil saturated zone lies ahead of the leading shock ($S_{w,HS}$) while injected low-salinity brine lies behind the trailing shock ($S_{w,LS}$), with a connate water-oil bank formed between the shocks. (b) Low-salinity and high-salinity fractional flow curves showing the estimation of the water saturation and watercut for the shock-fronts.

In numerical models of this flood (Jerauld et al., 2008; Dang et al., 2015; 2016), the fractional flow is coupled with the solute-component concentration (and often, the compositional physical dispersion)

to modify it for the low salinity effect (LSE), see equations (2.1) – (2.5). Relative permeabilities and capillary pressures are interpolated between set threshold values for high- and low-salinity effects when intermediate concentrations exist, to model wettability alteration with a smooth change in multiphase flow properties. This often results in interactions between the injected LS brine and the associated connate water-oil bank – potentially through tracked concentration of the active solute or adsorbed-ion that defines the LSE in the model. Such provision for intermediate solute (or salt) concentrations makes consideration of the impact of physical mixing or dispersion possible with this approach.

In numerical solutions, numerical dispersion has a significant influence through transporting intermediate concentrations at erroneous phase velocities, as we show later in this chapter. The numerical scheme introduces errors in the solutions either with or without any input physical (reservoir) mixing, resulting in artificial additional mixing in simulations. This also makes it difficult to evaluate advective flow effects with most computationally efficient coarse grids because the active solute-component or adsorbed-ion mixes uniformly within each grid-block (Lantz, 1971). As discussed in Chapter 2.6, earlier studies have proposed methods to constrain numerical dispersion to desired representative effects of physical mixing using 'pseudo or effective' threshold solute-component concentrations (or salinities). However, discrepancies between the (upscaled) coarse- and reference fine-scale results were still seen with these methods. This chapter focuses on how to handle these limitations rather than implementing an improved discretization scheme. We show how a simple scheme allows accurate solutions with a modest number of grid blocks, applicable to full-field simulation.

The impact of numerical mixing in numerical solutions of LSWF is first analysed critically based on the modelling work of Jerauld et al. (2008). We then examine the limitations of existing methods to evaluate effective threshold salinities to correct numerical dispersion effects. A new approach is thereafter proposed to evaluate these effective thresholds: it involves a simple-to-implement method, which can then be directly incorporated into conventional simulators without further modification and which does not require a fine-grid numerical solution. The proposed approach is validated for a 1D homogeneous model and its effectiveness in multidimensional grids is illustrated. The use of effective thresholds to control the inherent numerical dispersion effects in a coarse simulation grid to desired representative levels is later demonstrated for a 1D problem. Upon investigating the effects of effective salinity-thresholds on transverse mixing in higher dimensions, we propose a method to model transverse dispersion in simulations whose longitudinal component is controlled with effective thresholds. Finally, we discuss the use of this method to handle current limitations in the explicit modelling of physical dispersion in systems with multidirectional or transverse flows.

4.2 Numerical Dispersion in LSWF Simulations

4.2.1 Model Description

The 1D-homogeneous system considered is described in **Table 4.1**. The analytical solution to a LSWF is used in this work as its reference for advection-controlled non-dispersive simulation results. **Fig. 4.2** shows the relative permeabilities and fractional flows for both high-salinity and low-salinity brines. They are taken from a template input file of a commercial simulator (Schlumberger, 2015).

Table 4.1: Description of the 1D-System.

Property (unit)	**Value**
Model dimensions (x, y, z) (m)	304.8 x 30.48 x 1.52
Porosity	0.2
Initial water saturation	0.2
Permeability (x, y, z) (mD)	(500, 500, 500)
Initial reservoir pressure (Pa)	4.10×10^{7}
Formation compressibility (1/Pa)	1.93×10^{-8}
Water compressibility (1/Pa)	1.89×10^{-8}
Oil density (kg/m^3)	786
Water density (kg/m^3)	1000
Oil and water viscosity (Pa.s)	4.00×10^{-4}
Oil formation volume factor (rm^3/sm^3)	1.98
Water formation volume factor (rm^3/sm^3)	1.01

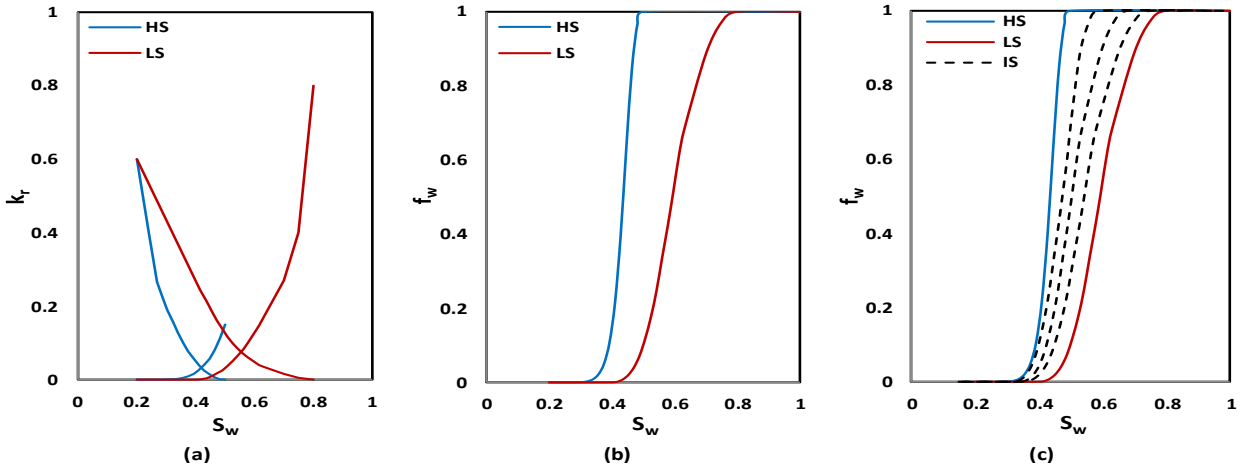


Fig. 4.2. Flow properties of systems used in this work: high-salinity (HS) in blue, low-salinity (LS) in red, and intermediate-salinities (IS) in black. (a) Relative permeabilities. (b) Fractional flows. (c) Intermediate fractional flows.

4.2.2 Analytical and Numerical Solutions

In a 1D low-salinity water displacement for incompressible fluids with no physical dispersion, the Buckley-Leverett analytical solution has two equations for conservation of mass (or volume for the incompressible case considered here): one for the water phase and one for its salt component. These are:

$$\frac{\partial S_w}{\partial t} + \frac{q_t}{\phi}\frac{\partial f_w}{\partial x} = 0 \tag{4.1}$$

$$\frac{\partial (S_w C_i)}{\partial t} + \frac{q_t}{\phi}\frac{\partial (f_w C_i)}{\partial x} = 0 \tag{4.2}$$

where C_i is the amount of salt dissolved in the brine, which is either that of resident high-salinity brine or injected low-salinity brine as there are no intermediate salinities in the absence of diffusion or dispersion. For a constant-salinity displacement, C_i is constant, and equation (**4.2**) becomes equation (**4.1**). S_w is the water saturation (dimensionless). q_t is the total Darcy velocity (L/T). ϕ is the porosity (dimensionless). L is the model length (L).

The fractional flow of the water phase, ignoring gravity, is defined as:

$$f_w = \frac{1}{1 + \frac{k_{ro}}{\mu_o}\frac{\mu_w}{k_{rw}}} \tag{4.3}$$

where k_{ro}, k_{rw}, μ_o, μ_w are the oil relative permeability, water relative permeability, oil viscosity and water viscosity respectively. Crucially for low-salinity waterflooding, the relative permeabilities are also functions of the salinity.

The water saturation $(S_{w,LS})$ and flowing watercut $(f_{w,LS})$ at the trailing shock front with no dispersion are determined by drawing a tangent line from $S_w = 0$ to the fractional flow curve of the low-salinity brine. The intersection of this tangent line with the fractional flow curve of the high-salinity brine is used to determine the water saturation $(S_{w,HS})$ and flowing watercut $(f_{w,HS})$ at the leading shock front. A typical description is shown on **Fig. 4.1**b. S_{wc} is the connate water saturation. The wavespeed and position of any water saturation – $S_{w,HS}$, $S_w \geq S_{w,LS}$ – are estimated from the slope of its tangent line, $\frac{df_w}{dS_w}_{S_w}$.

The numerical evaluation is performed with the low-salinity simulation package of ECLIPSE-100. This is an extended black oil simulator which uses the standard tracer-component approach described in Chapter 2.5.1 to model the LSE. It implements a first-order finite-difference approach to discretize the governing equations. Salinity is treated as the 'proxy' single-component tracer that controls

wettability alteration towards more water-wetness (or less oil-wet). This could also represent other active solute-component or adsorbed ion such as Ca^{++} or Mg^{++} (Puntervold et al., 2015). Simulations are run fully implicit with a range of 10 to $10{,}000$ equally-sized grid-blocks. The injector and producer wells are in the first and last grid-cells respectively, with the injection and production rates kept constant and equal. The same rate is used for the analytical evaluation.

The injected and connate brine salinities are $1{,}000$ ppm and $30{,}000$ ppm respectively, with thresholds for LSE set at $1{,}000 - 7{,}000$ ppm. These thresholds are chosen as they represent realistic thresholds as confirmed by previous experiments (Tang and Morrow, 1999; Jerauld et al., 2008). A linear interpolation is adopted for the relative permeabilities at intermediate salinities. These are as defined by Muggeridge and Hongtong (2014). The effect of capillary pressure is ignored by setting it to zero. This is generally valid for field-scale simulations where the pressure difference from capillary forces is negligible compared to the viscous pressure drop between wells.

4.2.3 Discussion of Results

Fig. 4.3a illustrates the water saturation profiles of the analytical and numerical solutions, with different numbers of grid-blocks, at 0.2 PV (pore volumes) of injected LS brine. **Fig. 4.3**b shows the effluent concentration front with different numbers of grid-blocks. For convenience, the salinity limits are shown from 0 to 1. 1 is used for the salinity of the brine initially in place, and 0 for the salinity of the displacing injected brine. Significant smearing of the shock-fronts is observed in the numerical solution due to numerical dispersion. While the leading HS-brine shock is better resolved after a few grid-blocks, the trailing LS-brine shock remains smeared even with 10,000 grid-blocks. Its persistent smearing noticeably impacts the velocity of the leading shock.

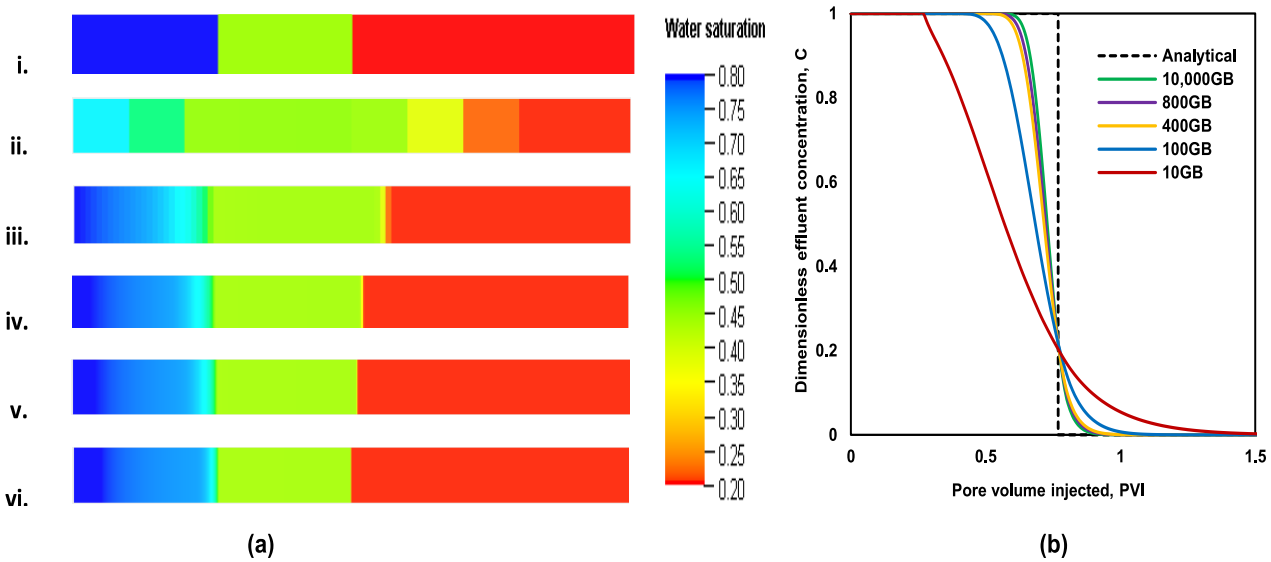


Fig. 4.3. Simulated profiles with different numbers of grid-blocks (GB) in comparison to the reference (analytical) solution. (a) Water saturation profile for the 1D-system at 0.2 PV injected low-salinity brine (i: analytical, ii: 10GB, iii: 100GB, iv: 400GB, v: 800GB, vi: 10,000GB). (b) Effluent concentration *(C)* as a function of pore volumes injected (PVI).

The unresolved trailing LS-brine shock experiences numerical mixing characterized by varying salt compositions across the shock. The numerical solution combines compositional dispersion with the fractional flow to model the LSE as a function of salt concentration (salinity). This renders the saturation wavespeeds across the trailing shock defined by the intermediate fractional flow curves rather than the LS curve (**Fig. 4.2**c) (AlSofi and Blunt, 2013). The wavespeed therefore decreases with increasing saturation, resulting in an erroneous unstable fractional flow with significant smearing or spreading of the displacement. The trailing shock becomes difficult to resolve completely even at unfeasibly fine grid resolutions. This is a general simulation problem in compositional displacements (Thiele et al., 2010; AlSofi and Blunt, 2013), as discussed in Chapter 2.6.

The saturation wavespeeds across the leading Buckley-Leverett shock are defined by only the HS fractional flow curve and hence it is better resolved after a few grid blocks. However, the trailing shock's excessive artificial smearing makes its wavespeeds too high until well over 100 grid blocks are used in the simulation (**Fig. 4.3**b). We note that typically there are only a few grid blocks between wells in full-field simulation, and furthermore, we have a heterogeneous system. Heterogeneity tends to physically smear out the saturation fronts; therefore, a small amount of numerical dispersion should ordinarily not substantially influence the numerical solution. In a LSWF, however, the movements of the concentration and water fronts are interdependent. A small spread of the concentration front initiates erroneous velocity changes for the water fronts, especially if flow is advection-controlled or less dispersion-dominated. Therefore, solutions from a combination of coarse

grid and heterogeneity are influenced significantly by numerical errors. These errors can be large even for grids which are sufficiently refined to model normal waterflooding accurately.

The numerical (unphysical) mixed zone across the smeared trailing shock consists of both the injected LS and *in situ* HS brines. The mixed section of the injected brine assumes concentrations within and above the salinity-thresholds. This increases the water saturation ($S_{w,HS}$) and flowing watercut ($f_{w,HS}$) at the leading shock. Consequently, the leading shock accelerates while the trailing LS front is retarded (Al-Ibadi et al., 2018c). This is manifested in the simulated performance as early water breakthrough, high watercut in the connate water-oil bank, and subsequent reduced watercut after breakthrough of injected brine. **Fig. 4.4** shows these erroneous signatures in the numerical solutions to the watercut (*WC*)-pore volumes injected (*PVI*) production performance at different grid numbers.

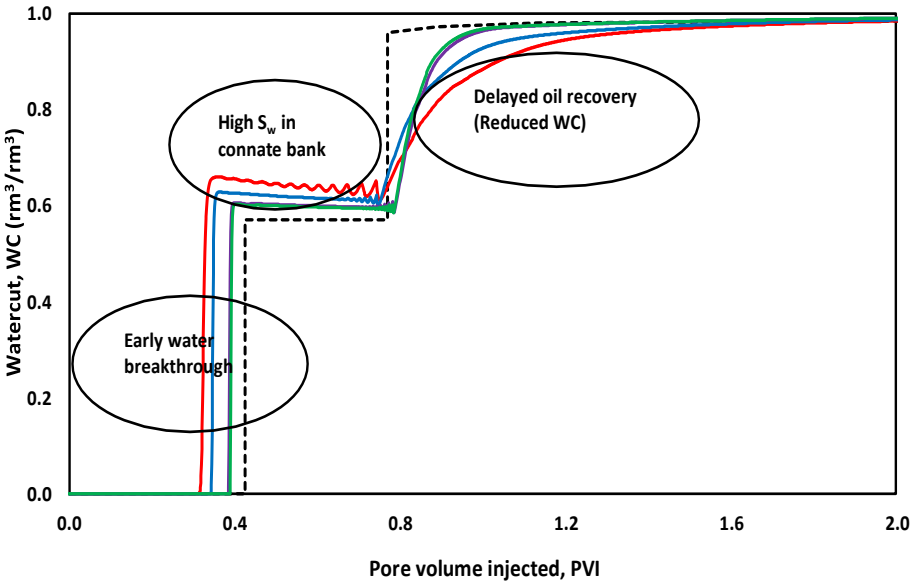


Fig. 4.4. Watercut as a function of pore volumes injected showing the characteristic signatures of numerical dispersion in LSWF simulations with different numbers of grid-blocks (GB) in comparison to the analytical solution (black dashed line analytical; red line 50GB; blue line 200GB; purple line 800GB; green line 1,000GB).

The inability of conventional grid refinement to represent these fronts adequately is analysed using the convergence of the numerical solutions to the reference (analytical) solution. Root-mean-square errors (*RMSEs*) are evaluated for the WC-PVI profiles. These are compared with those of high- and constant-salinity waterflooding. The efficiency of grid refinement on the precision of the numerical solutions of both processes can then be statistically distinguished. **Fig. 4.5** presents this comparative evaluation.

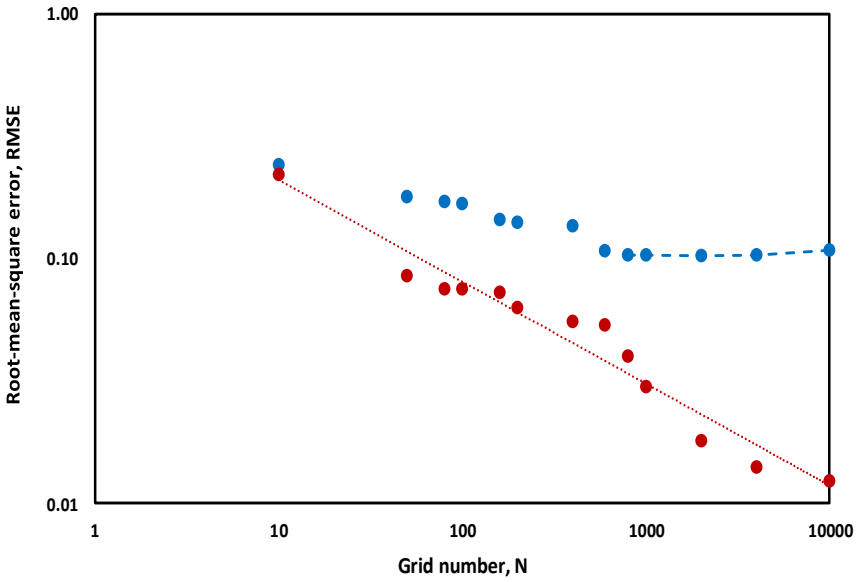


Fig. 4.5. Error evaluation of the predicted watercut as a function of pore volumes injected (*PVI*) (blue low-salinity; red constant-salinity) for different grid-numbers. The constant-salinity (the normal Buckley-Leverett profile) simulation displays convergence of order 0.42 while the low-salinity simulation shows an apparent zero order for 800GB and above.

Even the constant-salinity numerical solution demonstrates a rather poor rate of convergence (average slope of 0.42) to its analytical solution. This is typical of conventional first-order numerical schemes when used to solve the Buckley-Leverett equations and represents the difficulty in resolving the shock front accurately (Hoteit and Firoozabadi, 2008). However, the LS case is even worse and indeed appears not to converge any further beyond 800 grid-blocks. This is due to the smearing of the trailing shock which incorrectly introduces mixed-zone signatures into the numerical solution. At around 800 grid-blocks, these errors dominate the total solution for the example case considered here. An apparent zeroth order of convergence is therefore established, thereby limiting the improvement in solutions from further grid refinement.

4.3 Correctional Procedure: Representing Advective (Non-Dispersive) Flow Effects in Simulations

In this section, we examine the limitations of existing methods to correct for numerical dispersion in LSWF and propose a simple approach to evaluate effective salinity-thresholds.

As discussed in Chapter 2.6, both the methods of Al-Ibadi et al. (2018a) and Muggeridge and Hongtong (2014) calculate effective salinity-thresholds based on predicted movement of the LS front – the trailing shock in **Fig. 4.1**. To examine the accuracy of their predicted salt fronts, we apply both methods to the 1D system of **Table 4.1** to predict the effluent profiles at different levels of dispersion (*Pe*) in comparison with the simulated profiles. These are shown in **Fig. 4.6**. The profiles from both methods are generated using the analytical solution to the advection-dispersion equation from Aronofsky and Heller (1957) – equation (A.1) in **Appendix A**, but different advection velocity terms. The modified advection velocity term of Al-Ibadi et al. (2018a) – equation (A.7) – is used to calculate the advection velocity of their predicted profile at each level of dispersion. A constant advection velocity of the trailing LS water front, $\frac{df_w}{dS_w}_{S_{w,LS}}$, is used for the predicted profiles from the method of Muggeridge and Hongtong (2014). This is estimated analytically from its fractional flow curve as described in Section 4.2.2. The relative permeabilities are as presented in **Fig. 4.2**. Dispersion is modelled numerically with equations (2.8) – (2.10) from the method of Sorbie and Mackay (2000), which is re-presented in **Appendix A**.

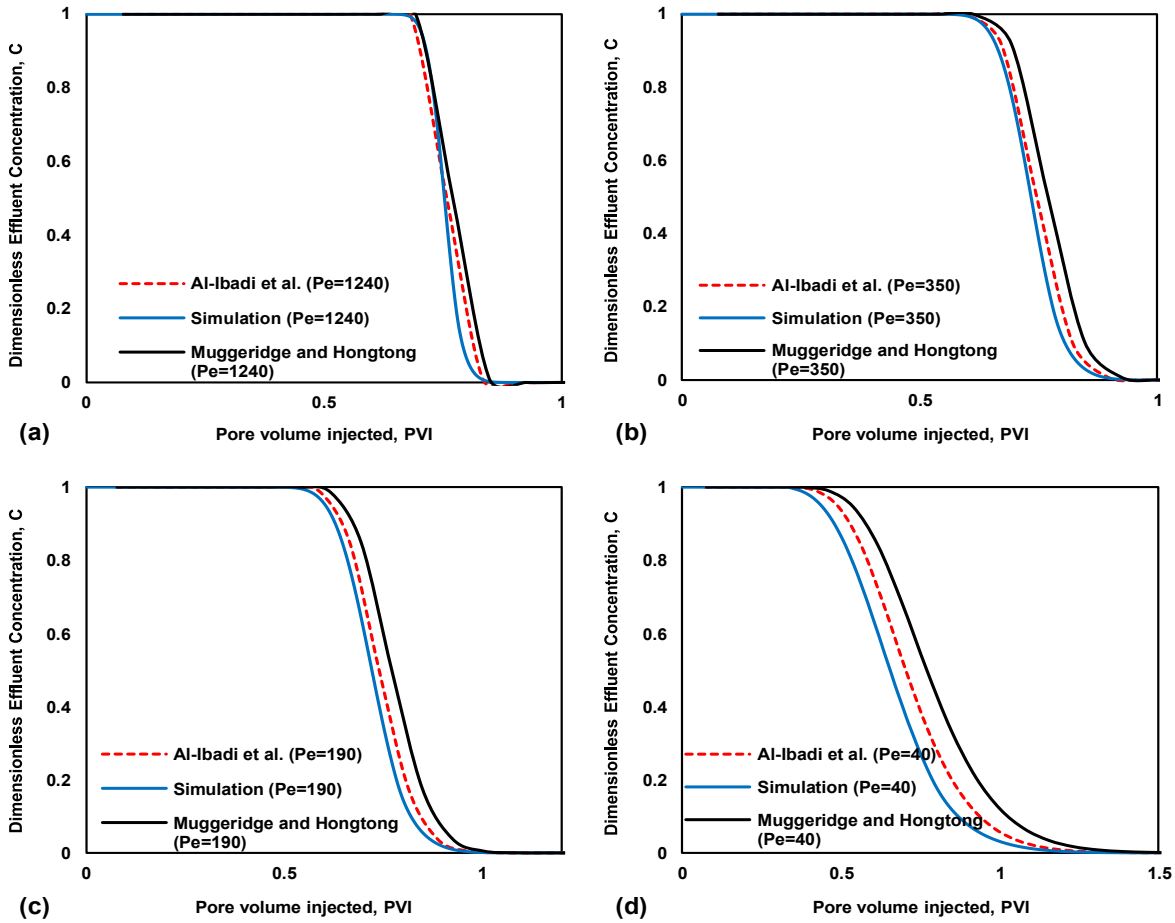


Fig. 4.6. A comparison of predicted normalized effluent profiles from the method of Muggeridge and Hongtong (2014), the method of Al-Ibadi et al. (2018a), and simulation results at different levels of dispersion (*Pe* – Peclet number).

As illustrated in **Fig. 4.6**, the advection velocity of the salt front in simulations increases with dispersion as noted by Al-Ibadi et al. (2018a, 2018b). Muggeridge and Hongtong (2014), however, assume that this speed is fixed and hence underestimate the speed of the water and salt fronts. We suggest this explains the discrepancies observed in their coarse simulation results. The method of Al-Ibadi et al. (2018b) captures the salt front movement better at high *Pe,* but the precision degrades as flow becomes more dispersive (low *Pe*). Al-Ibadi et al. (2018a) also observed this mismatch in dispersion-dominated flows and suggested that predictions from their modified form seem less reliable for these flows. They attributed the imprecision to numerical instabilities characterized by a deformed shape of the solute front as dispersion increases. However, the system-length of our model is much longer than the considered lengths of its dispersed or mixed section in this analysis. This is to avoid any boundary-induced deformation of the front-shape from the analytical solution to the advection-dispersion equation in dispersive flows as suggested by Brigham et al. (1961). In addition, the numerical solution is stable for all the *Pe* studied. This is observed in the salt-front shapes of dispersion-dominated flows (**Fig. 4.6**c and d) from simulation if compared with their analytical predictions (i.e. Muggeridge and

Hongtong). A predominant 'bodily shift' of the salt front is indicative of the mismatch between predictions of Al-Ibadi et al. (2018a, 2018b) and simulations of dispersive flows as observed in **Fig. 4.6**. We suggest this signifies amongst other possible reasons an incorrect advection velocity of the front, as could also be inferred of the predictions of Muggeridge and Hongtong (2014). Generally, both methods show inaccurate predictions of the salt front movement especially in dispersive simulation grids.

We apply the method of Al-Ibadi et al. (2018a) to correct numerical dispersion effects in a coarse grid simulation of the 1D system of **Table 4.1**. The analytical solution of a LSWF is considered here as the reference fine-grid solution. The predicted salt front is used to evaluate the effective mid salinity-threshold to correct the velocities of the water fronts in a simulation with 100 grid-blocks. Around 13,300 ppm is evaluated as the effective mid threshold for the grid. The effective salinity-threshold range is widened to improve the precision of the simulation results as suggested by Al-Ibadi et al. (2018a). The relative permeabilities are not adjusted. The simulated watercut profile is compared with the reference solution in **Fig. 4.7**. The velocities of the water fronts are inadequately corrected as shown in **Fig. 4.7**. The main discrepancies occur around the breakthrough of the water fronts that bound the connate water-oil bank, indicating an inaccurate upscaled recovery profile if compared to the reference solution.

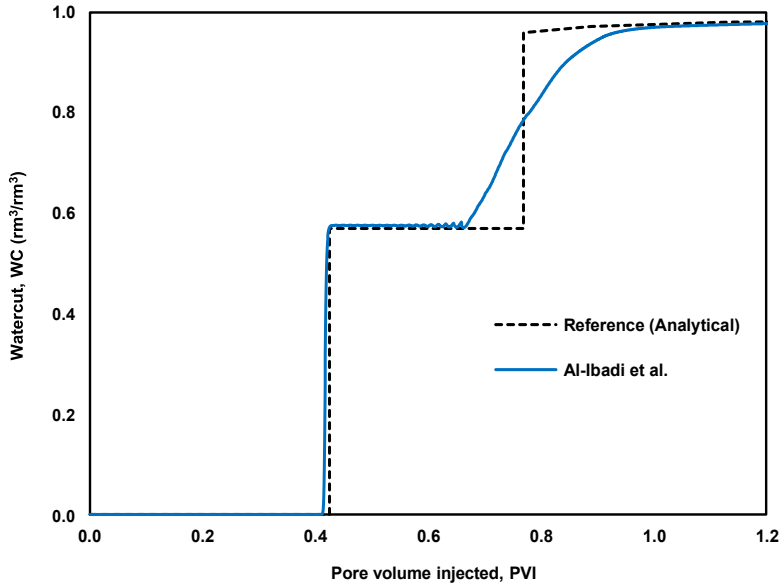


Fig. 4.7. Watercut as a function of pore volumes injected showing the simulated performance from the method of Al-Ibadi et al. (2018a) using a 100 grid-block model and effective salinity-threshold range of 10,000-16,600 ppm, in comparison with the reference (analytical) solution for the 1D system of Table 4.1.

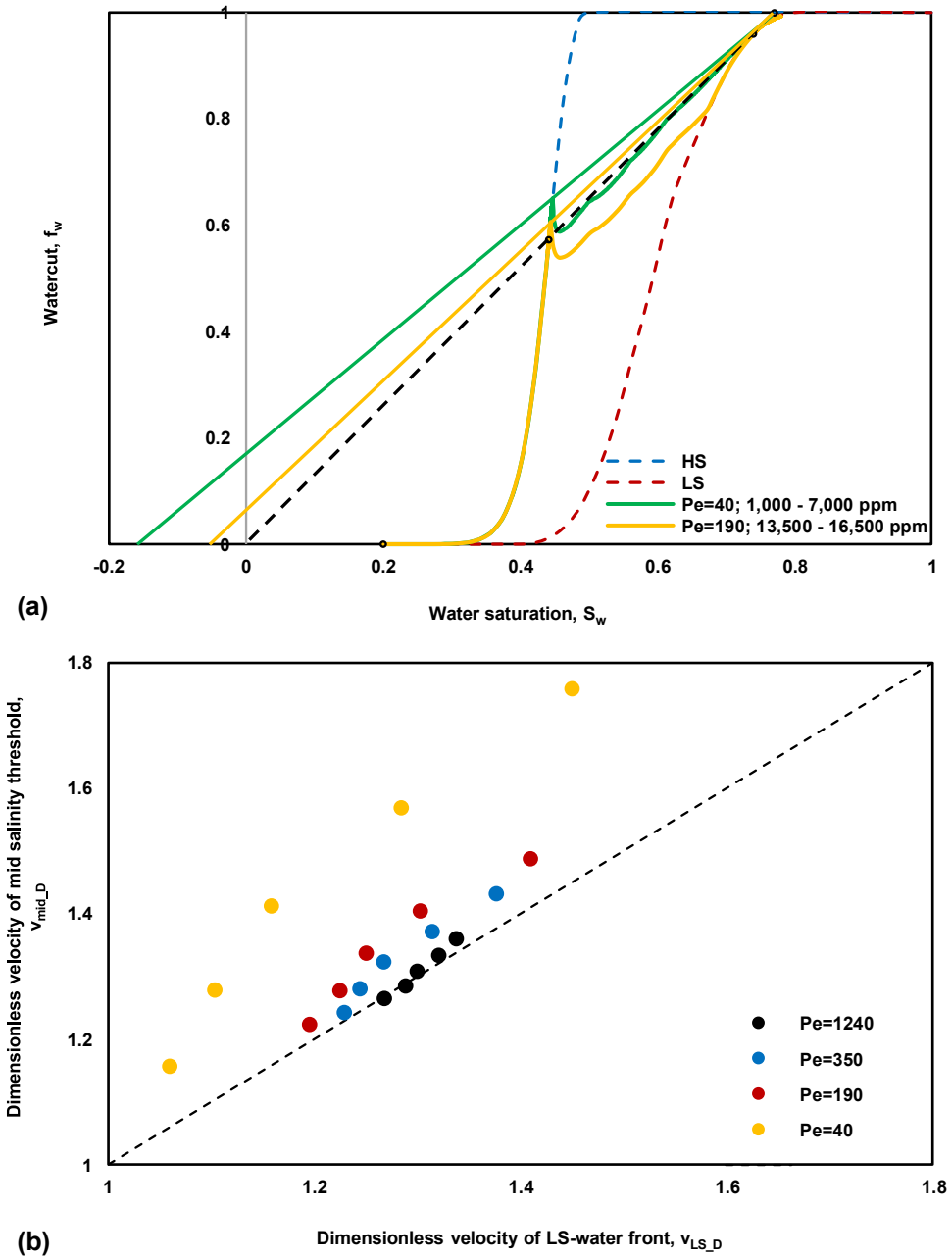


Fig. 4.8. (a) Typical evaluations of the LS water front velocity at different combinations of dispersion (Pe) and salinity-thresholds using simulator output fractional flow at the end of the model (solid green and orange) in comparison with the evaluation of the analytical LS water front velocity (dash black). (b) Comparison between the velocities of the mid salinity-threshold and the low-salinity water front at the producer-end of the model at different levels of dispersion (*Pe*) and salinity-thresholds. The velocities show significant inequalities as dispersion increases.

We investigate the difference between the speed of the midpoint salinity-threshold and the LS water front in the simulations which are hitherto assumed to be equal by Al-Ibadi et al. (2018a). Both parameters are evaluated from simulation results at different levels of dispersion and salinity-thresholds. The velocity of the LS water front is evaluated from the simulator output fractional flow profile of the resident and injected brines at the producer-end of the model. We consider the

retardation and acceleration effects of dispersion on frontal velocity as presented by Pope (1980) for augmented waterflooding and Al-Ibadi et al. (2018c) for LSWF. The watercut is plotted as a function of the water saturation for each combination of dispersion and salinity-thresholds. The velocity of the LS water front is evaluated as the slope of the tangent line at its analytical watercut and water saturation $(f_{w,LS}, S_{w,LS})$ to the dispersion-induced saturation of the high-salinity water front. This can be compared with the zero-dispersion analytical fractional flow profile in **Fig. 4.1**b. A typical demonstration of this is illustrated in **Fig. 4.8**a at different dispersion and salinity-thresholds.

The velocity of the mid salinity-threshold is evaluated from a plot of effluent concentration (*C*) as a function of pore volumes injected (*PVI*) using equation (A.11). This is as proposed by Al-Ibadi et al. (2018a) and presented in **Appendix A**. Both parameters are normalized by the total interstitial velocity, $\frac{q_t}{\phi}$. **Fig. 4.8**b shows the comparison between these velocities as dispersion increases. The velocity of the LS water front is distinctly different from that of the mid salinity-threshold in dispersive grids. The effective position of the LS water front lies behind that of the mid salinity-threshold. We suggest this relationship between the parameters explains the limited accuracy of the method of Al-Ibadi et al. (2018a) to adequately correct for dispersion at low *Pe*.

As we show later, a salinity cut-off can correct the effect of numerical dispersion in LSWF simulations. The challenge is to estimate the effective salinity-thresholds suitable for a reference solution. Numerical dispersion mimics the physical mixing of the brines where a mixed zone is created that alters the movement of the water fronts, misrepresenting the connate water-oil bank size. We propose a simple simulation-based approach to evaluate thresholds to have the correct amount of injected and resident brines around the water bank region. This is used to correct the movement of the fronts in coarse-grids to model either advective or dispersive flow effects for history-matching and predictions. Effective threshold salinities are initially evaluated for advective flow effects, described below, and subsequently modified to model desired dispersive effects in Section 4.4.

The procedure involves a simulation of the low-salinity process with the initial or reference salinity-thresholds. The simulation grid should be suitable to reasonably resolve the leading shock. The effluent concentration (*C*) and cumulative water produced (*WP*) are plotted as a function of pore volumes injected (*PVI*). The initial high-salinity resident brine volume is displaced ahead of the injected low-salinity brine. The *PVI* to produce this bank of initial brine is found from the *WP-PVI* function, and the corresponding effluent concentration at this *PVI* is evaluated from the *C-PVI* function. This value is taken as the maximum effective salinity-threshold at which the breakthrough of the injected low-salinity brine should be first evident. In theory, this ought to correspond to the minimum effective salinity-threshold to ensure no zone with intermediate fractional flow curves is created in the

advective flow such as the reference LSWF-analytical solution. It is, however, necessary to have a different value for the minimum effective threshold salinity. Moreover, a salinity-threshold range needs to be defined for the simulator. For our analysis in this work, we select a concentration within 1% of cumulative water produced (*WP*) after the production of the initial resident brine. This is also graphically evaluated from the plot of the *C-PVI* and *WP-PVI* functions. Furthermore, we observe negligible numerical instabilities in the simulations following this selection. The evaluated effective thresholds can then be applied to correct numerical dispersion effects in the coarse grid. We demonstrate this procedure in an example in the next section.

4.3.1 1D Validation of the Correctional Approach

Our procedure is demonstrated using the 1D system in **Table 4.1** and its analytical solution as reference. The initial resident brine salinity is 30,000 ppm; injected brine salinity, 1,000 ppm; and an initial salinity-threshold range of 1,000-7,000 ppm. We separately consider simulation grids of 50 and 800 grid-blocks, both with 0.2 PV initial HS resident formation brine volume. **Fig. 4.9** illustrates the evaluation of 15,900 ppm and 14,500 ppm as the maximum effective threshold salinities at the production of the bank of initial brine for the 50 and 800 grid-block cases respectively. The *C-PVI* and *WP-PVI* functions are from simulations run with the initial salinity-thresholds. Minimum effective salinities of 14,800 ppm and 12,800 ppm are also evaluated for the 50 and 800 grid-block simulations respectively at the selected 1% of cumulative water produced (*WP*) after producing the bank of initial resident brine.

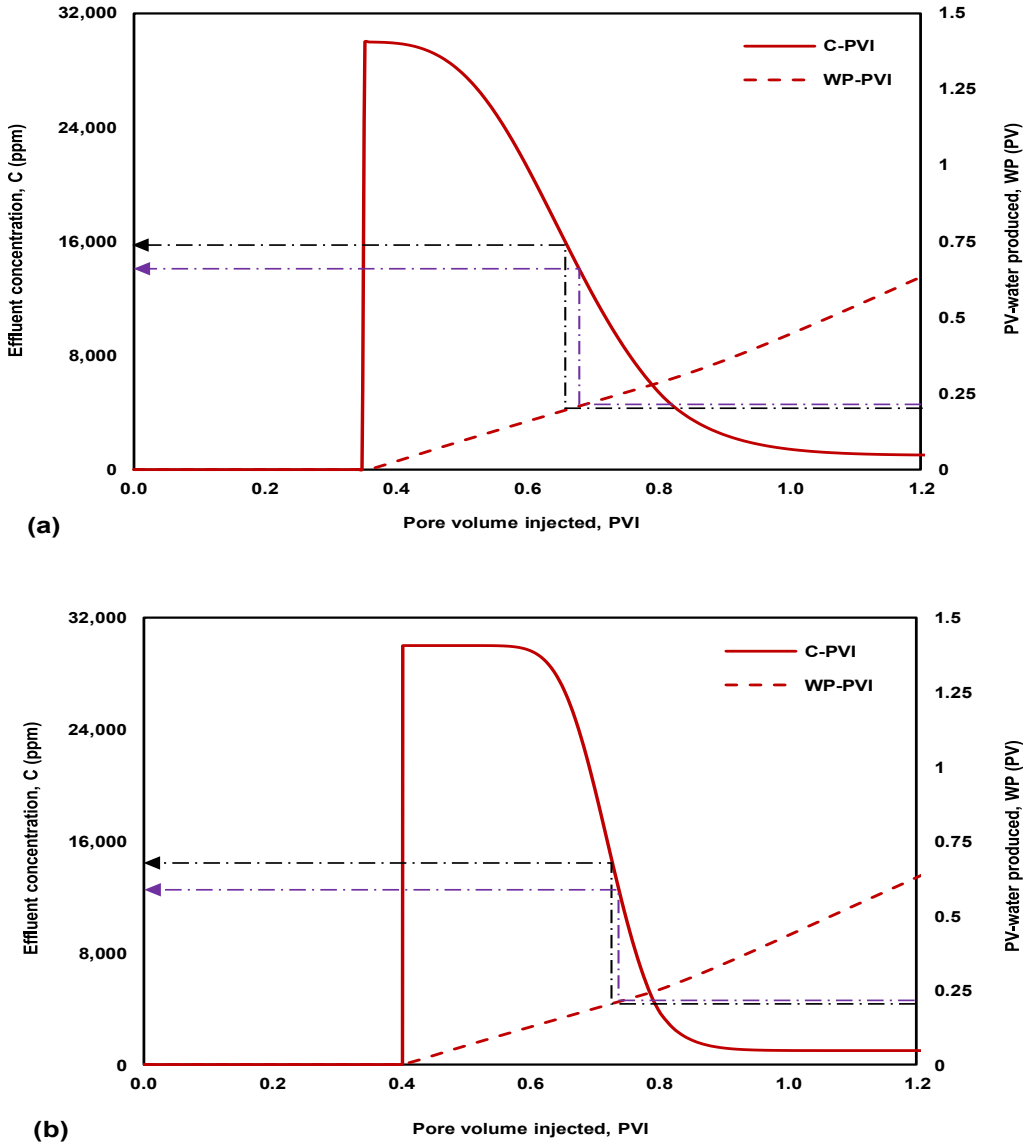


Fig. 4.9. (Step 1) Evaluation of effective salinity-thresholds for zero-dispersion (advective) effect at an initial brine volume of 0.2 PV (black dashed line: maximum threshold, purple dashed line: minimum threshold), using the *C-PVI* (solid line) and *WP-PVI* (dashed line) functions from simulation run with an initial salinity-threshold range of 1,000-7,000 ppm. (a) 50 grid-blocks. (b) 800 grid-blocks.

Fig. 4.10 shows the adjustments in the *C-PVI* and *WP-PVI* functions after the effective threshold salinities are used for both simulation grids. The produced water volumes at the breakthrough of the salinity-thresholds are reduced to approximately the initial brine volume. This reflects an acceleration of the LS water front compared to simulations with the initial salinity-thresholds. The size of the mixed zone, the velocity and spread of the salt front are also reduced. In addition, effective threshold salinities are evaluated and applied to a 20-block simulation grid. The improvement in simulated performance compared to the reference solution is presented in **Fig. 4.11**. We consider the water saturation and produced watercut profiles for this. In this case, with the effective threshold salinities and no adjustment to the relative permeabilities, the analytical or reference production performance is reliably predicted with an upscaled simulation of 50 grid-blocks: the order of convergence is now

similar to that achieved for the standard (constant-salinity) waterflood Buckley-Leverett problem. However, the convergence of the corrected LS case is peculiarly slow especially between 50 to 400 grid-blocks (**Fig. 4.11**c). We suggest this might have resulted from the performance profile considered (i.e. production watercut). This often has more solution (data) points in the LS case, especially around the connate water-oil bank, which could have influenced its root-mean-square errors compared to the constant-salinity scenario. Meanwhile, for the coarsest grid considered – with only 20 grid-blocks – numerical instabilities persist. These are associated with fluctuating production profile (**Fig. 4.11**b) – and not water saturation profile (**Fig. 4.11**a) – just before LS-water breakthrough and around when the produced salinity drops to the threshold range (**Fig. 4.10**). We suggest they probably result from unstable solute (or salinity) displacement which causes rapid changes in mobility or relative permeability.

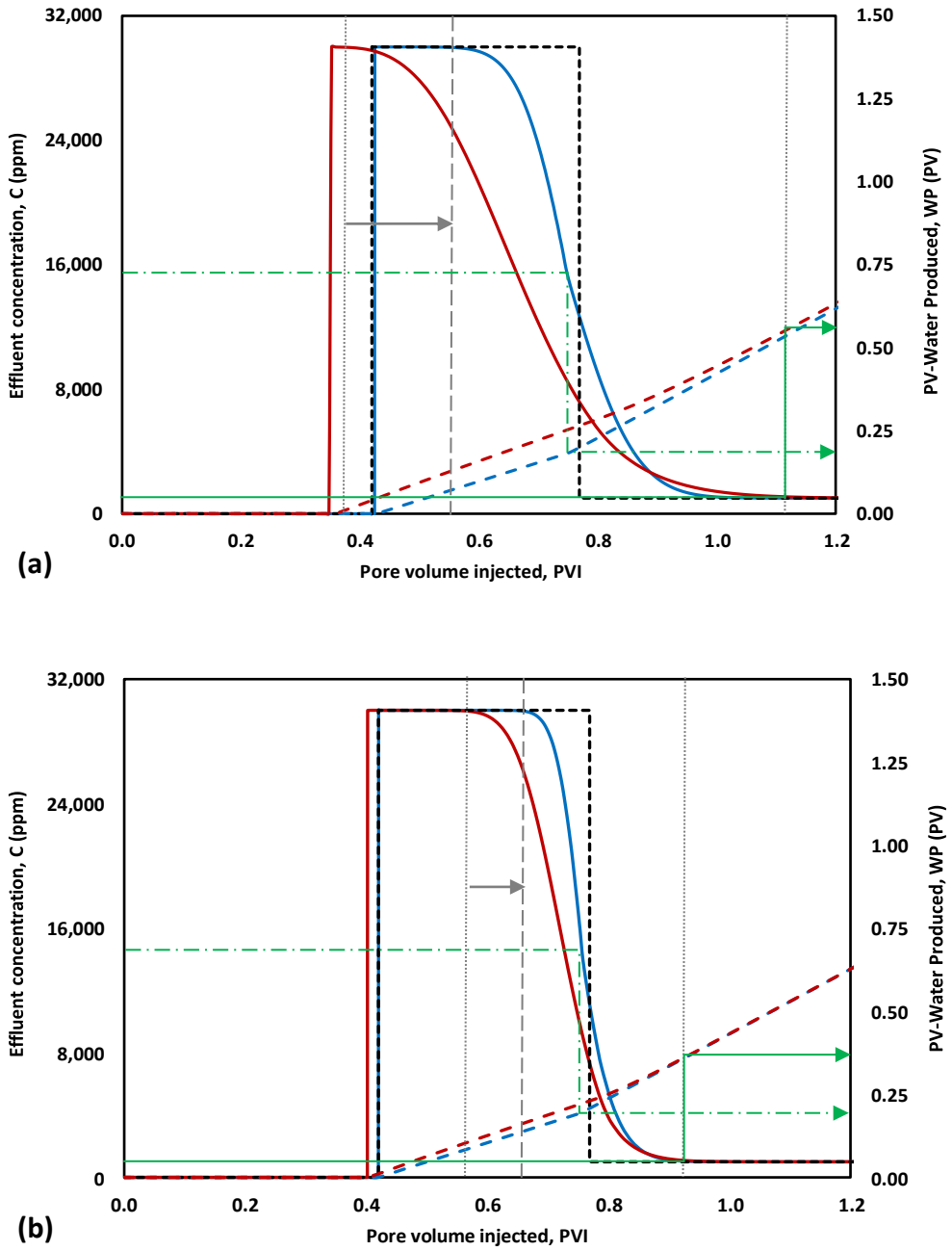


Fig. 4.10. (Step 2) Simulation results with (blue) and without (red) the effective threshold salinities. (a) 50 grid-blocks. (b) 800 grid-blocks. The figure also shows the cumulative pore volumes of water produced with (green dashed line) and without (green solid line) the effective threshold salinity procedure at the breakthrough of their respective salinity-thresholds. The net change in the size of the mixed-zone, the average velocity and spread of the salt front is illustrated with the vertical dashed lines and the arrow.

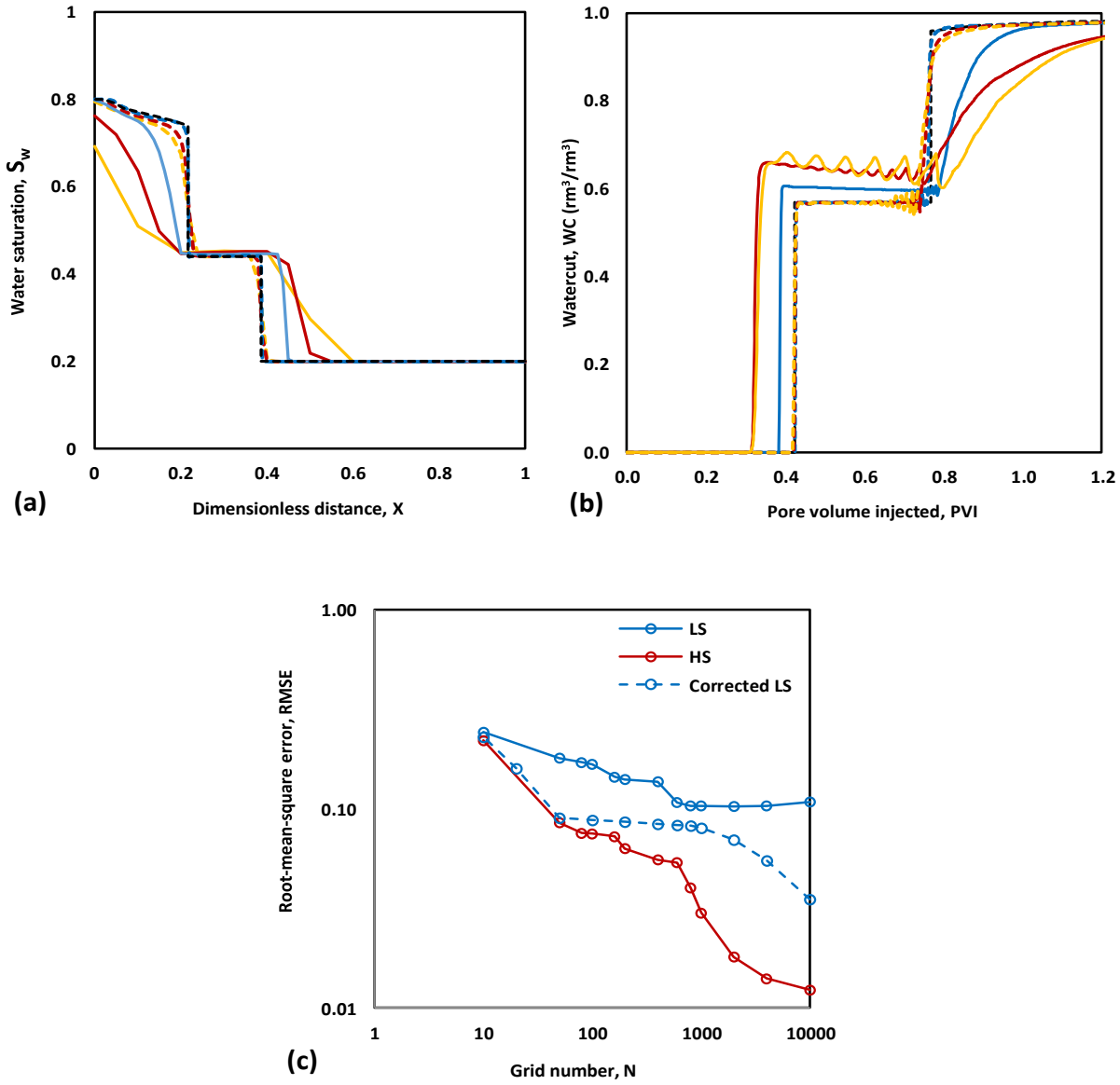


Fig. 4.11. Simulation results with (dashed lines) and without (solid lines) the effective threshold salinity procedure at different numbers of grid-blocks (yellow 20, red 50, blue 800) in comparison with the analytical solution (black dashed line). (a) Water saturation profiles at 0.165 pore-volumes of the injected LS brine. (b) Watercut as a function of pore volumes injected. (c) Convergence of the root-mean-square error in the simulated watercut performance before (blue solid line) and after (blue dashed line) changing the thresholds in comparison to that of high- and constant-salinity case (red).

4.3.2 Extension to multidimensional systems

In this section, we use effective threshold salinities to correct the effect of numerical salt front dispersion on the velocities of the water fronts in upscaled simulations of multidimensional systems. The systems are heterogeneous with no defined analytical or reference solutions. However, we consider solutions from highly refined grids with the initial salinity-thresholds as reference for the upscaled simulations with effective threshold salinities. Homogeneous coarse grids are used to evaluate the effective threshold salinities with our approach. We assume the equivalent

homogeneous grid distinguishes the effects from numerical dispersion from those from heterogeneity.

4.3.2.1 2D-System

The 2D heterogeneous system from the SPE10 Model 1 dataset (Christie and Blunt, 2001) is used with an upscaled permeability distribution (**Fig. 4.12**a). The dimensions of this model are 762 x 7.62 x 15.24 m. The coarse grid considered is 100 x 1 x 20 with uniform grid-block size of 7.62 x 7.62 x 0.76 m. The model is initially saturated with oil and 0.2 PV connate water. Porosity is constant at 0.2. Injection and production rates are equal at the left and right faces of the model respectively. Fluid properties and relative permeabilities are shown in **Table 4.1** and **Fig. 4.2**a respectively.

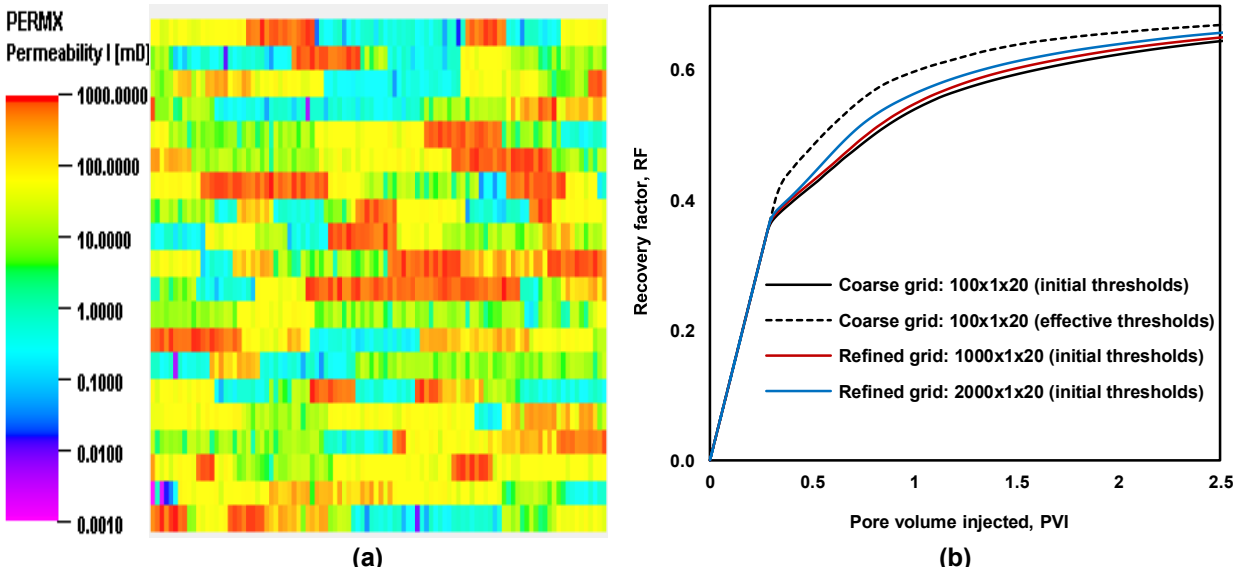


Fig. 4.12. (a) 2D permeability map. (b) Simulated performance from a coarse grid (100x1x20 grid-blocks) with and without effective threshold salinities in comparison with those from its refinement (red 1000x1x20 grid-blocks, blue 2000x1x20 grid-blocks) without effective threshold salinities.

Fig. 4.12b shows the modifications to simulated performance from effective threshold salinities and grid refinement. We observe a delayed water breakthrough and improved recovery in the coarse simulation grid with effective threshold salinities compared to the same grid with initial salinity-thresholds (uncorrected). This is similar to the improvement in performance from the refinement of the coarse grid (100 x 1 x 20 grid-blocks) to reference 1000 x 1 x 20 grid-blocks and 2000 x 1 x 20 grid-blocks with initial salinity-thresholds. Furthermore, simulation time is saved. Besides heterogeneity, we suggest numerical dispersion in the uncorrected coarse grid (i.e. with initial salinity-thresholds) would have contributed to its early water breakthrough and delayed recovery.

4.3.2.2 3D-System

A 3D system is developed from the SPE 10 Model 2 dataset (Christie and Blunt, 2001). It is a combination of layers 83, 84 and 85 in the Upper-Ness formation. All the properties and simulation conditions are maintained as those of previous example. The upscaled permeability map is shown in **Fig. 4.13**a. The 3D-system has a size 365.76 x 670.56 x 1.83 m and discretized into 60 x 220 x 3 grid-blocks for the coarse grid simulation.

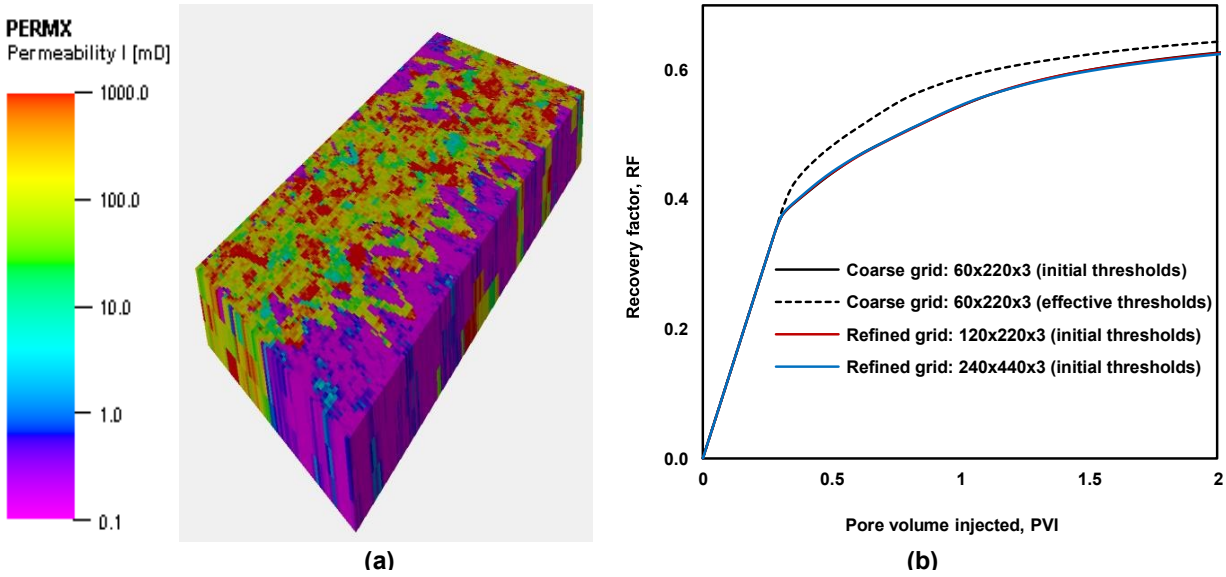


Fig. 4.13. (a) 3D permeability map. (b) Simulated performance from a coarse grid (60x220x3 grid-blocks) with and without effective threshold salinities in comparison with those from its refinement (red 120x220x3 grid-blocks, blue 240x440x3 grid-blocks) without effective threshold salinities.

Fig. 4.13b illustrates the modifications to simulated performance from effective threshold salinities and refinement of the coarse grid (60 x 220 x 3 grid-blocks) to 120 x 220 x 3 grid-blocks and 240 x 440 x 3 grid-blocks with initial salinity-thresholds. Delayed water breakthrough and improved recovery are observed in the coarse simulation with effective threshold salinities compared to the same grid with initial salinity-thresholds. No significant difference is seen in the uncorrected coarse grid (with initial salinity thresholds) following grid refinement. We suggest that the grid refinement is insufficient to make any significant difference to the simulated performance. We cannot draw any further conclusions as there is no definite reference solution to compare with.

4.4 Modelling and Characterization of Effective Longitudinal Dispersion

Earlier in Sections 2.6 and 2.7.1 we discussed the use of numerical dispersion to mimic physical mixing as proposed by Jerauld et al. (2008). Hence, a representative numerical dispersion can be constructed to model physical longitudinal dispersion. We also noted the limitation of this approach for a simulation grid exhibiting larger numerical dispersion effects than the desired physical spread or mixing. In this section, we show how the inherent numerical dispersion effects for a simulation grid are controllably reduced with effective salinity-thresholds.

In **Fig. 4.10**, a change in the spread of the salt front and the size of the mixed zone was observed when the salinity-thresholds were replaced with effective values for advective flow effects. **Fig. 4.14**a shows a further illustration where the initial salinity-thresholds are increased towards the effective threshold salinities, and their range varied for the same simulation grid. The change in the spread of the salt front reflects a changed velocity profile of the concentrations along it. We suggest it results from a varying advection velocity along the front whose distribution is a function of the salinity-thresholds. The impact of this on the production performance is presented in **Fig. 4.14**b. As illustrated in **Fig. 4.14**, widening the range of the effective threshold salinities towards the initial thresholds enlarges the spread of the salt front as well as the size of the mixed zone. This also re-introduces dispersion effects – including the acceleration and retardation of water fronts – back into the corrected simulated performance. It implies the salt front dispersion and its effect on the velocities of the water fronts can be tuned using effective salinity-thresholds.

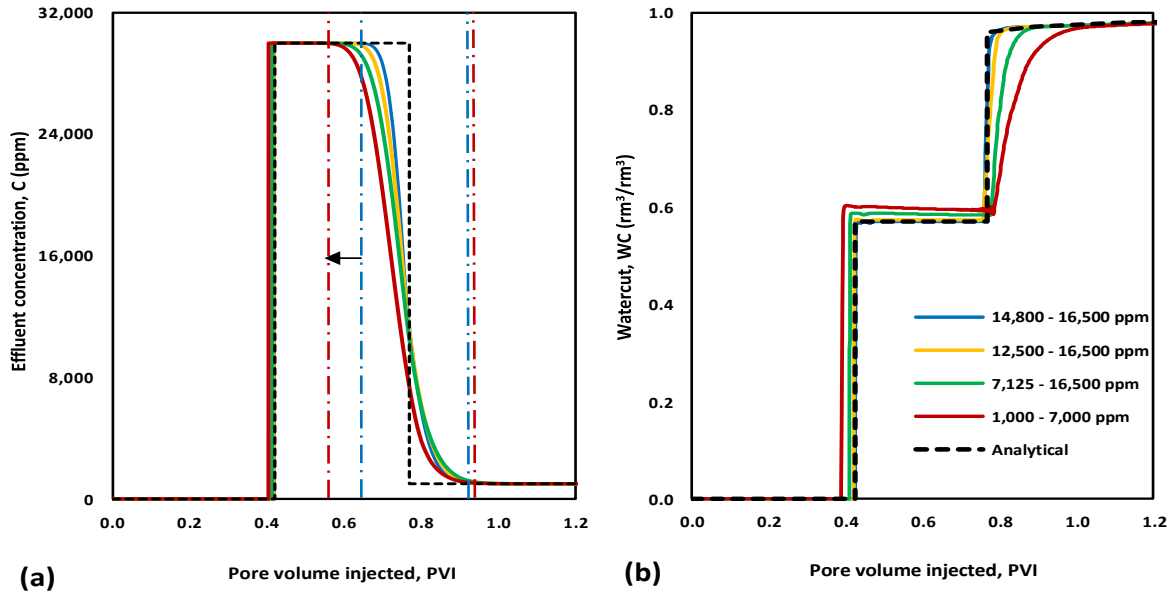


Fig. 4.14. Production profiles of a simulation grid at different salinity-threshold ranges (orange 12,500-16,500 ppm; green 7,125-16,500 ppm) showing effects of widening the effective thresholds (blue 14,800-16,500 ppm) towards the initial salinity-thresholds (red 1,000-7,000 ppm). The analytical solution (black dash) is also presented. (a) Effluent concentration as a function of pore volumes injected. (b) Watercut as a function of pore volumes injected.

For example, dispersion can be modelled by varying the minimum effective salinity-threshold at a constant maximum effective threshold. The equivalent effective dispersivity (α_L) or Peclet number (*Pe*) in the grid arising from each effective threshold range can be fitted with the method of Brigham et al. (1961) – see equations (2.18) – (2.19). This is re-presented in **Appendix A**. A profile of the dispersion-characteristics as a function of the effective thresholds can also be developed for the simulation grid. From such profile, we can simply estimate the effective salinity-thresholds required to model reduced longitudinal dispersion effects. This is useful when history-matching LSWF tests showing the effects of physical mixing without further refining the grid. A range of dispersive prediction studies can also be evaluated with such coarse grid.

4.4.1 1D Demonstration

We demonstrate this method on the 800-grid model of the example system in **Table 4.1**. Its effective salinity-threshold range for advective flow effects was evaluated in **Fig. 4.9**b as 12,800-14,500 ppm. Each new effective threshold range is defined by varying the minimum effective salinity-threshold from 1,000 ppm to 12,800 ppm at a constant maximum effective threshold. **Fig. 4.15**a presents a profile of dispersion-characteristics as a function of the effective thresholds. From the profile, we can simply estimate the effective threshold range required to reduce the inherent numerical dispersion (described by the lowest *Pe*) to a desired longitudinal dispersion effect or spread (described by a higher *Pe*). For example, a reduced effective dispersion (*Pe*=690) is designed from the inherent numerical

dispersion (*Pe*=225). The decrease in longitudinal dispersion or mixing is illustrated in terms of its effect on recovery in **Fig. 4.15**b. This shows that our procedure corrects the large inherent numerical dispersion to match a desired lower effective physical mixing without refining the grid, which can become computationally expensive to run.

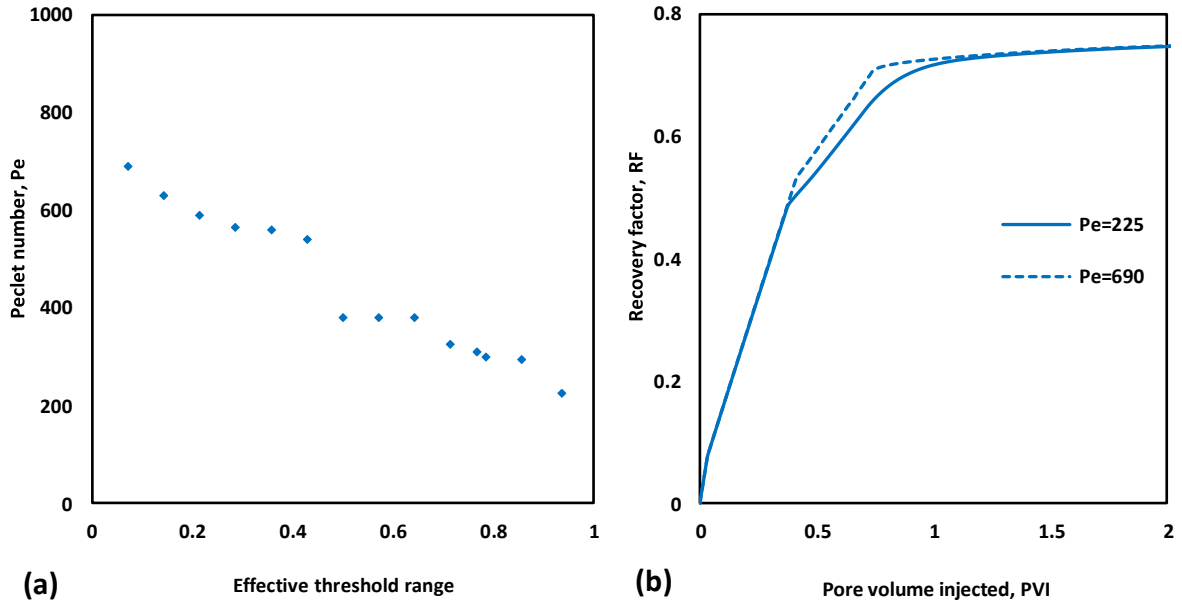


Fig. 4.15. (a) Dispersion-characteristics (Peclet number) as a function of effective salinity-threshold range with constant maximum effective threshold (14,500 ppm). The minimum effective threshold varies from 1,000 ppm to 12,800 ppm. Each effective threshold range, which is the difference between its effective thresholds, is defined as a fraction of the constant maximum threshold on the plot. (b) Recovery factor as a function of pore volumes injected at the inherent numerical dispersion (solid line *Pe*=225) and a reduced effective longitudinal dispersion (dash line *Pe*=690).

4.5 Effective Dispersion in Models: Incorporating the Transverse Component

Numerical errors from misrepresented input dispersivities can be even worse in grids with multidirectional flows. In this section, multidimensional models are used to evaluate the impact on both longitudinal and transverse solute dispersion. We show how to incorporate transverse dispersion in grids combined with numerical longitudinal component that is controlled with effective salinity-thresholds.

CMG's STAR simulator is used in this section because of its ability to explicitly model physical dispersion components in LSWF simulations. It implements a finite-difference approach to discretize the governing equations and fully implicit.

4.5.1 Description of Models

The 1D and 2D models described in **Table 4.2** are used to investigate the influence of numerical dispersion on input longitudinal and transverse dispersion respectively. The relative permeabilities are presented in **Fig. 4.2**a. Simulations were run with initial (uncorrected) salinity-thresholds of 1,000 ppm and 7,000 ppm at different grid-sizes and different input longitudinal and transverse dispersivities. Longitudinal and transverse dispersivities in the simulation results were fitted using the methods of Brigham et al. (1961) and Hiby (1962), described in Chapter 2.7.1, respectively. **Appendix B** provides more detail on how transverse dispersion is evaluated. To minimize the likelihood of numerical instability effect on the solute front, time stepping remains fully implicit despite being very small.

Table 4.2: Descriptions of the 1D and 2D models.

Property (unit)	**Value (1D model)**	**Value (2D model)**
Model dimensions (x, y, z) (m)	30.48 x 0.15 x 0.15	30.48 x 0.30 x 0.15
Porosity	0.2	0.2
Initial water saturation	0.2	0.2
Permeability (x, y, z) (mD)	(500, 500, 500)	(500, 1.0×10^{-4}, 500)
Initial reservoir pressure (Pa)	4.10×10^{7}	4.10×10^{7}
Formation compressibility (1/Pa)	1.93×10^{-8}	1.93×10^{-8}
Water compressibility (1/Pa)	1.89×10^{-8}	1.89×10^{-8}
Oil density (kg/m^3)	786	786
Water density (kg/m^3)	1000	1000
Oil and water viscosity (Pa.s)	4.00×10^{-4}	4.00×10^{-4}
Oil formation volume factor (rm^3/sm^3)	1.98	1.98
Water formation volume factor (rm^3/sm^3)	1.01	1.01

The 200 x 30 x 1 grid of the 2D model in **Table 4.2** is used to examine the simulation response to input transverse dispersion in the presence of effective longitudinal dispersion. Two effective salinity-threshold ranges, evaluated from its equivalent 1D model, are considered for all simulations: 12,000 – 12,600 ppm for zero longitudinal dispersion effect, and 9,000 – 13,000 ppm for the non-zero longitudinal dispersion effect. Three normalized input transverse dispersivities (D_T): 0, 0.00005 and 0.0005 are also considered. These are as defined by Brodie and Jerauld (2014). All dispersivities and grid-sizes are normalized by the corresponding model-length in their respective directions. Details of these dimensionless conversions, earlier presented in Sections 2.6 and 2.7.1, are summarised in Appendices **A** and **B**.

4.5.2 Discussion of Results

The back-calculated (fitted) total longitudinal dispersivities and the corresponding input longitudinal dispersivities as a function of grid-size are presented in **Fig. 4.16**, while those for the transverse dispersivities are presented in **Fig. 4.17**.

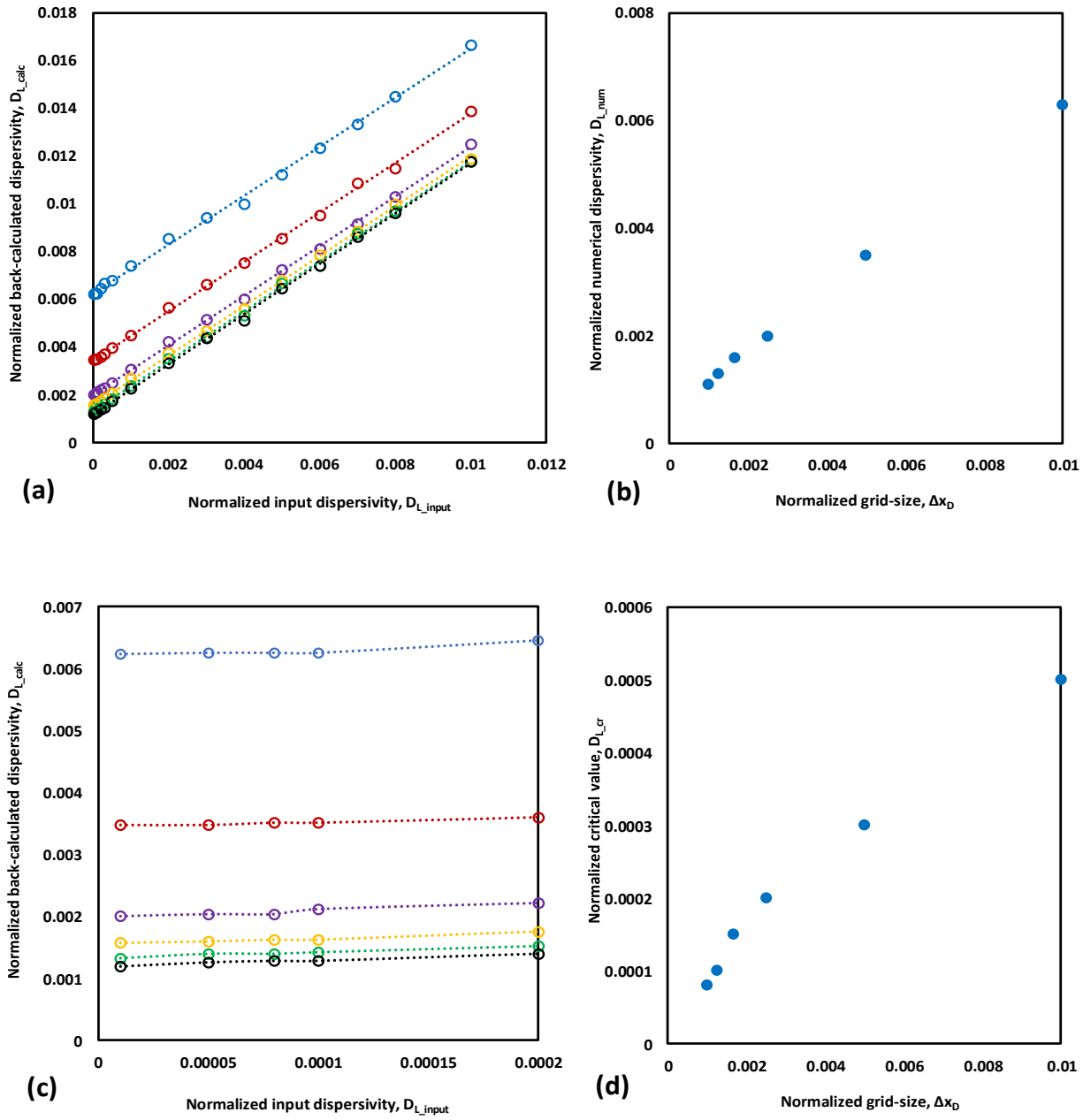


Fig. 4.16. Influence of numerical dispersion on input physical longitudinal dispersion. In all cases, dispersivities and grid-block sizes are normalized by the system length. (a) Back-calculated longitudinal dispersivity as a function of input longitudinal dispersivity with different grid-sizes in the flow direction (blue, 0.01; red, 0.005; purple, 0.0025; yellow, 0.00167; green, 0.00125; and black, 0.001), showing significant exaggeration of each input dispersivity. Each plot converges to a minimum back-calculated dispersivity which represents the inherent numerical dispersion for the grid-size. (b) Inherent numerical dispersivity as a function of grid-size. (c) Expanded section of small input dispersivities in (a) showing a zero-slope region as each plot converges to its minimum back-calculated dispersivity. The zero-slope region terminates around a 'critical input dispersivity' for each grid-size. (d) Critical input dispersivity as a function of grid-size.

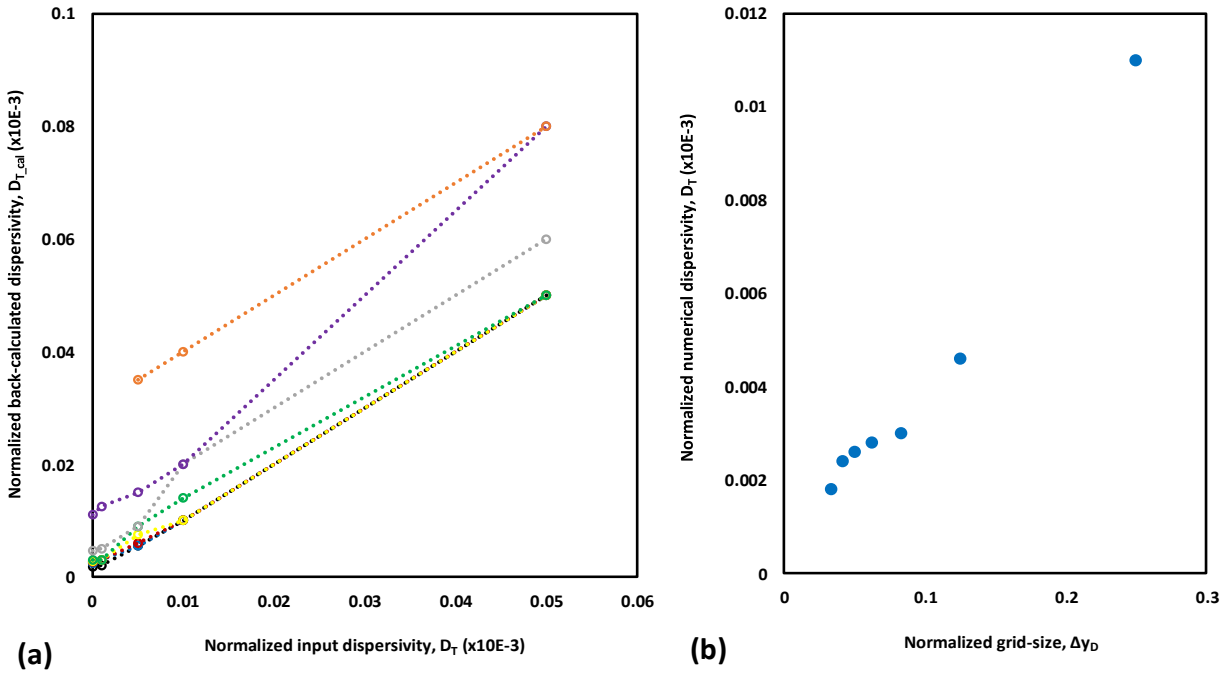


Fig. 4.17. Influence of numerical dispersion on input physical transverse dispersion. The dispersivities and grid-block sizes are normalized by the model size (length) in the transverse direction. (a) Back-calculated transverse dispersivity as a function of input transverse dispersivity with different grid-sizes in the transverse direction (black, 0.033; blue, 0.042; red, 0.05; yellow, 0.0625; green, 0.0833; grey, 0.125; purple, 0.25; and orange, 0.5). Small input dispersivities are exaggerated even with very fine grids. (b) Back-calculated transverse dispersivity as a function of grid-size at zero input transverse dispersivity ($D_T = 0$). This represents the inherent transverse component of numerical dispersion for each grid-size.

Fig. 4.16 shows that numerical dispersion exaggerates every input longitudinal dispersion in the simulations. The back-calculated dispersivities converge to a minimum value at each longitudinal grid-size (**Fig. 4.16**a). This represents the inherent numerical dispersivity for the grid-size (**Fig. 4.16**b). The values appear to vary linearly with grid-size, hence consistent with the analysis based on Taylor series expansion given by Lantz (1971) for a first-order, implicit scheme under a CFL-controlled time-step as discussed in Chapter 2.6.

Furthermore, there exists a minimum input dispersivity threshold at each grid-size below which numerical dispersion completely dominates the total dispersion in the system (**Fig. 4.16**c). This is referred to as the 'critical input longitudinal dispersivity' for the grid-size in this work (**Fig. 4.16**d). Higher input values seem represented in simulations as approximately a sum of their dispersion and the inherent numerical dispersion for the grid-size (**Fig. 4.16**a and b). This suggests that Lantz's analysis (Lantz, 1971) of combined effects of numerical and input dispersion is only reflected at some higher input dispersion for LSWF simulations. In general, the grid-dependent critical input dispersivity is estimated to be between 8% to 13% of the corresponding numerical component across the grid-sizes

(**Fig. 4.16**b and d). This suggests the limits for input dispersion in the presence of a numerical component, thus useful for grid-size selection when considering modelling physical dispersion explicitly.

Fig. 4.17 illustrates that an input transverse dispersivity may be accurately captured (without numerical influence) in simulations with sufficiently fine transverse grids. Such fine grid-size however depends on the value of the input transverse dispersivity and may be unfeasibly small in many cases.

Steady-state salt concentration and residual oil saturation profiles along the selected direction of transverse dispersion in the 200x30x1 grid-model are presented in **Figs. 4.18** and **4.19**. These are used to examine the response of LSWF-simulations to input transverse dispersion in the presence of an effective longitudinal component. At corrected zero effective longitudinal dispersion, the numerical transverse dispersion is also corrected to a zero-effect in the model (**Fig. 4.18**). This is attributed to the effective thresholds being higher with a smaller range which prevents the transversely-mixed injected brine from losing its LSE potential. At the designed non-zero effective longitudinal dispersion, the simulation responds to an increase in the input transverse dispersivity (**Fig. 4.19**).

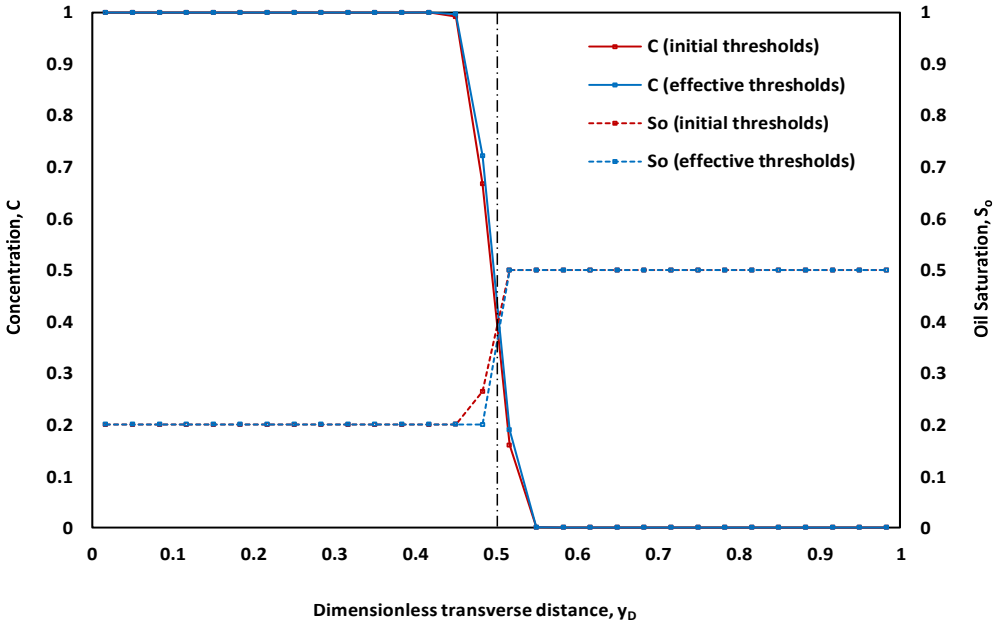


Fig. 4.18. Steady-state salt concentration (solid) and oil saturation (dashed) profiles in the transverse direction $(y_D \; at \; x_D = 1)$ with zero input transverse dispersivity. The concentration and saturation profiles (red) are smeared out by numerical transverse dispersion. However, correcting for zero effective longitudinal dispersion (blue) reduces this spreading.

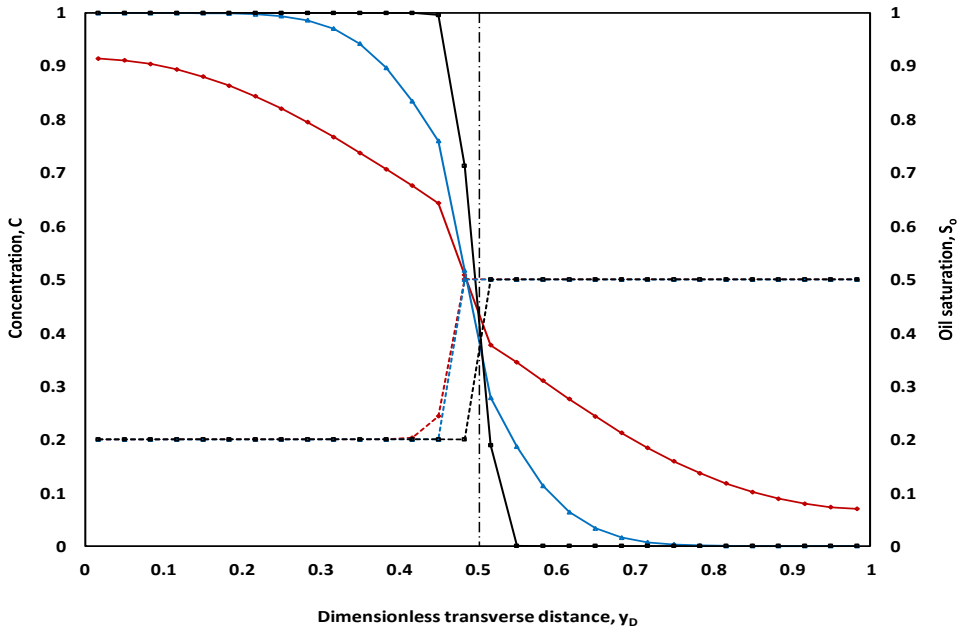


Fig. 4.19. Steady-state salt concentration (solid) and oil saturation (dashed) profiles in the transverse direction $(y_D \; at \; x_D = 1)$ with different input transverse dispersivities (black, 0; blue, 0.00005; and red 0.0005) and equal effective thresholds for a non-zero longitudinal dispersion.

These observations support the application of the proposed correctional procedure when evaluating the LSE in dispersive systems either for history-matching or prediction. In applying the procedure, we suggest that the physical longitudinal dispersion (less than the inherent numerical dispersion at the simulation grid) is designed with effective salinity-thresholds while the transverse component is explicitly defined (inputted).

However, the procedure can be difficult to apply when considering the uncertainty in the initial (or actual) salinity-threshold range as we investigate later in Chapter 5. Therein, evaluating the (possibly) different effective thresholds to constrain numerical dispersion may be difficult to implement practically for all realizations of the initial salinity-threshold range. Furthermore, since dispersivity is defined along grid-coordinates rather than flow axes in most existing codes and considering the presence of 'critical input dispersivity', we use very small time-steps – in addition to selecting smaller transverse grid-sizes as described in **Table 4.2** – to limit the inherent transverse component of numerical dispersion in simulations to ensure the explicitly defined transverse dispersivity, which is relatively small in this case, is reflected. We note that such small time-steps can be typically impractical for field-scale simulations. Nonetheless, this procedure remains effective provided the adopted time-step and transverse grid-size produce an inherent numerical dispersion whose 'critical input dispersivity' at the effective salinity-thresholds is less than the explicitly defined (inputted) transverse dispersivity.

4.6 Modelling Physical Dispersion for Multidirectional Flows

Most available commercial compositional simulators have dispersivity defined for the flow axes along fixed coordinate directions (X, Y, Z). Longitudinal dispersivity is often defined along one assumed principal flow coordinate, while transverse dispersivity is considered along the remaining two other coordinates. The presence of flows transverse to the principal flow direction constantly changes the primary longitudinal and transverse directions to flow. Transverse flow makes the simulator model longitudinal dispersion with the input transverse dispersivity and vice versa. This has been a key limitation in the explicit modelling of dispersion in these simulators. It is therefore necessary to find a way of using only these three input dispersivity values to capture the physical dispersion components reliably along the possible flow directions.

To handle this with the proposed correctional approach, we construct the longitudinal component with effective thresholds while the transverse component is defined explicitly with equal input dispersivity values along all the coordinates. Herein, during transverse flows, the effective thresholds maintain the designed longitudinal dispersion while the input value defines the transverse component along the respective directions of propagation. However, such input dispersivity must be less than the critical input dispersivity for the simulation grid (see **Fig. 4.16**) at the effective thresholds. This is to ensure the longitudinal component is effectively represented by only its numerical equivalent.

The critical input dispersivity is evaluated from an equivalent 1D model. Simulations are run with the effective thresholds at different input longitudinal dispersivities, preferably starting from zero. A plot of the back-calculated longitudinal dispersivity as a function of the input longitudinal dispersivity indicates a zero-slope region. The critical input value is estimated as the minimum input dispersivity where the zero-slope ends. For example, **Fig. 4.20** illustrates the estimation of the critical value for the 2D model of **Fig. 4.19** at its non-zero effective longitudinal dispersion. This is estimated to be 0.01 in this example.

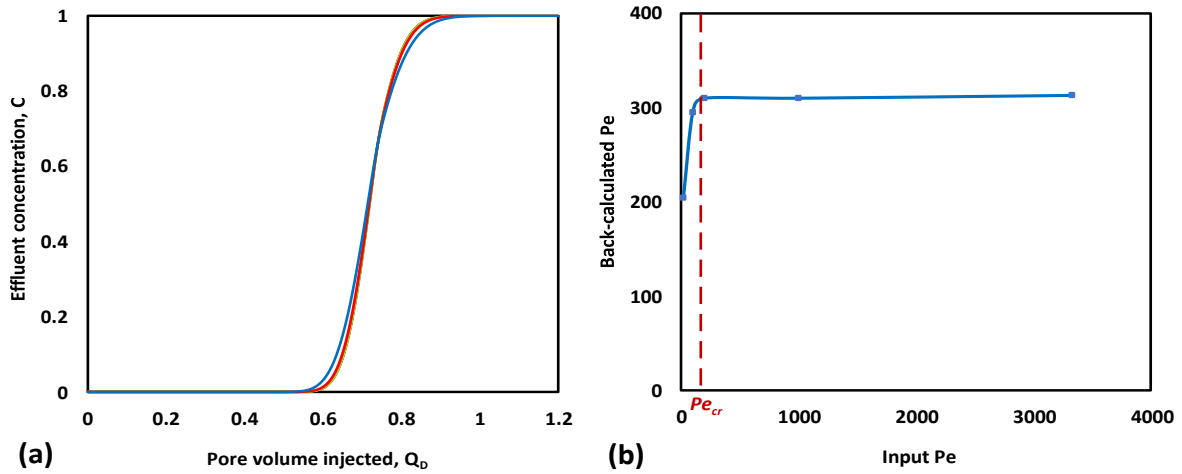


Fig. 4.20. Estimation of the critical input dispersivity for the 2D model of Fig. 4.19 at its non-zero effective longitudinal dispersion. (a) Effluent concentration as a function of pore volumes injected, used to fit the back-calculated longitudinal dispersivities at different input longitudinal dispersivities (black, 0; yellow, 0.001; green, 0.005; red, 0.01; and blue, 0.05). Dispersivities are normalized by the system length. (b) Back-calculated longitudinal dispersivity (*Pe)* as a function of input dispersivity (*Pe*), showing the critical input dispersivity (Pe_{cr}).

4.7 Summary

This chapter has focused on controlling numerical dispersion in LSWF simulations using the active solute-component concentration that defines the LSE. We summarise the chapter with our findings and results in the following:

1. Numerical dispersion was critically evaluated with the standard tracer-component model. In a 1D-homogeneous system, an unphysical mixed zone was observed around the smeared low-salinity water front even at fine grid-sizes. This limited the ability to adequately represent the front with conventional grid refinement. The displacement velocities of the water fronts were altered with incorrect representation of the amounts of HS-resident and LS-injected brines in the system. Large discrepancies occurred in the connate water-oil bank region with incorrect predictions of the watercut.

2. Existing methods to evaluate effective threshold salinities (or active solute-component concentrations) to redefine the LSE to correct these effects of numerical dispersion were examined. It was found that their accuracy is limited for coarse grids. This is because they do not properly account for the change in the speed of the low-salinity front as a function of dispersion.

3. A simple simulation-based approach to evaluate effective threshold salinities to correct numerical errors in coarse-grid simulations was proposed based on conservation of volumes of the resident and injected brines in the reference and upscaled solutions. This method then represented the connate water-oil bank displacement reliably in the upscaled solution. The individual reference

volumes of the distinct brines were used to cut-off the salinity-thresholds in the upscaled or coarse-grid simulation to model advective flow effects. The procedure was validated in 1D, showing improved coarse-grid solutions without adjusting the relative permeabilities. Its effectiveness in multidimensional grids was also demonstrated.

4. The numerical spread of the salt or solute front in a coarse grid was observed to change with salinity-thresholds. A method to control the effects of numerical dispersion in a simulation grid using effective salinity-thresholds was then proposed with no need for grid refinement. This was to characterize lower representative effects of physical longitudinal mixing or dispersion. This is applicable when matching LSWF tests with significant physical mixing without the need for a fine grid simulation. A range of dispersive prediction studies can also be evaluated with this coarse grid. This may replicate situations where active ions are adsorbed, and the injection front is retarded. The method was demonstrated in 1D.

5. Numerical dispersion exaggerated every input longitudinal dispersion and varied linearly with grid-size for the first-order, finite-difference, implicit scheme considered. Input longitudinal dispersivities less than a critical value were completely concealed (negligible) in the total dispersion represented during simulations for every grid-size under controlled time-step. The grid-dependent critical input value was estimated to be between 8% to 13% of the corresponding numerical dispersion for the grid-size. This suggests the limits for input dispersion in the presence of a numerical component, thus useful for selecting appropriate simulation grid-size when modelling physical dispersion explicitly as we will consider in subsequent chapters.

6. Input transverse mixing or dispersion remained active in the presence of effective salinity-thresholds (or effective longitudinal component). Therefore, physical longitudinal dispersion (less than the inherent numerical dispersion at the considered coarse simulation-grid) can be modelled with effective salinity-thresholds while the transverse component is explicitly defined (inputted). This approach was suggested to handle simulations with both longitudinal and transverse components of physical mixing or dispersion. It was potentially extended to model these components accurately in systems with multidirectional flows – a limitation in existing commercial simulators.

Now that we have a model that can accurately capture the movement of fronts during LSWF, in the subsequent chapters we use simulation to study mixing, cross-flow and the design of injection under uncertainty.

5 Impact of Physical Mixing and Heterogeneity Interaction on the Optimal Low Salinity Slug Injection Considering Uncertainty

5.1 Introduction

As discussed in Chapter 2, mixing of brines of different composition is considered as one of the main factors that affect the success of low-salinity waterflooding (LSWF) at the field-scale. This becomes crucial especially for slug injection schemes which are often favoured in field economics with less injected low-salinity (LS) brine and often better displacement and sweep efficiency. The focus here is entirely on the suppression of the low salinity effect (LSE) potential by physical mixing of the brines during inter-well flows. This can now be studied, since we can apply effective salinity thresholds or consider the 'critical input dispersivity' in case of explicit modelling to control numerical effects. Meanwhile, the latter is adopted in this chapter and Chapter 6. The effective salinity-thresholds procedure – introduced in the previous chapter – is not used here, as discussed in Section 4.5.2, because uncertainty in the threshold range itself is considered.

Deterministic studies have previously suggested a minimum LS slug size of 0.4 PV and 0.6 PV for homogeneous (Jerauld et al., 2008) and heterogeneous (Attar and Muggeridge, 2018) reservoirs respectively to contact most of the available residual oil target considering physical mixing. However, uncertainty in the exact magnitude of this physical effect due to reservoir complexity, presented in Chapter 3.1, can impact the flood design performance significantly, potentially discouraging its field-scale application.

For example, distinct LS-displacement stabilities and improved recoveries are shown by the immediate injection of 0.4 PV LS slug followed by a high-salinity (HS) push under different but possible levels of mixing (**Fig. 5.1**). Here, we illustrate with a 2D homogeneous model – 304.8 m x 30.48 m in the X, Y-direction with 200 x 20 isotropic areal grid-blocks – using a line-drive flood pattern. The relative permeabilities and fluid properties are presented in **Fig. 5.2** and **Table 5.1** respectively. Two inter-well physical longitudinal dispersivities from the reported data of Mahadevan et al. (2003) and Jerauld et al. (2008) discussed in Chapter 3.1 are considered – total Peclet number (*Pe*) of 2.5% and 3% (of the length travelled) in Case 1 and Case 2 respectively, to highlight how its uncertainty may impact performance. The slug becomes completely ineffective by mixing with the HS brines in Case 2 with its solute concentrations all above the LSE range for improved recovery before its breakthrough. The

recovery target therefore requires a better and more suitable injection design to sustain the slug integrity for optimal performance and/or reduce the risk from physical mixing during displacement.

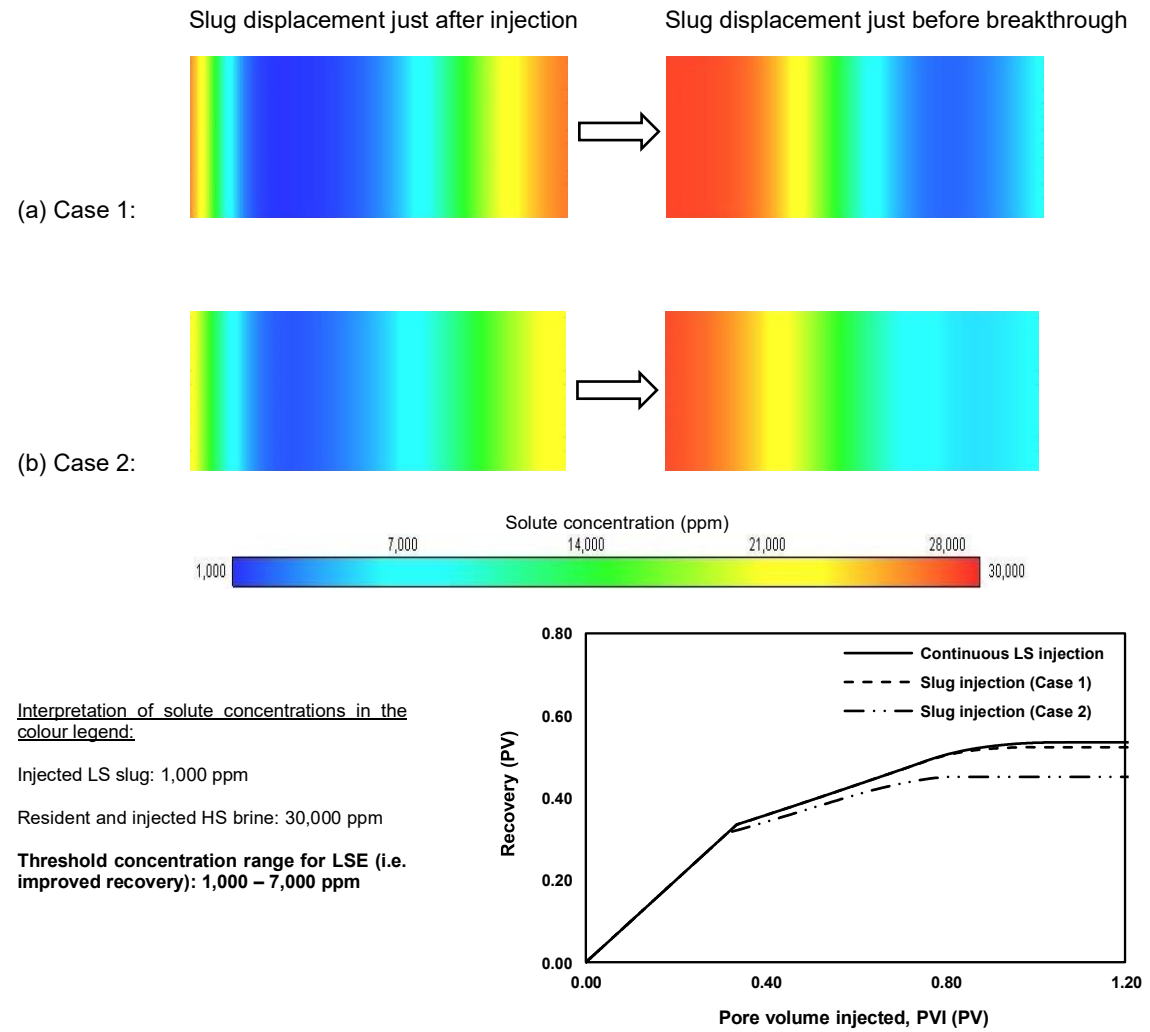


Fig. 5.1: LS displacement stability and performance of an injected slug under flow (mixing) uncertainty at different injection stages.

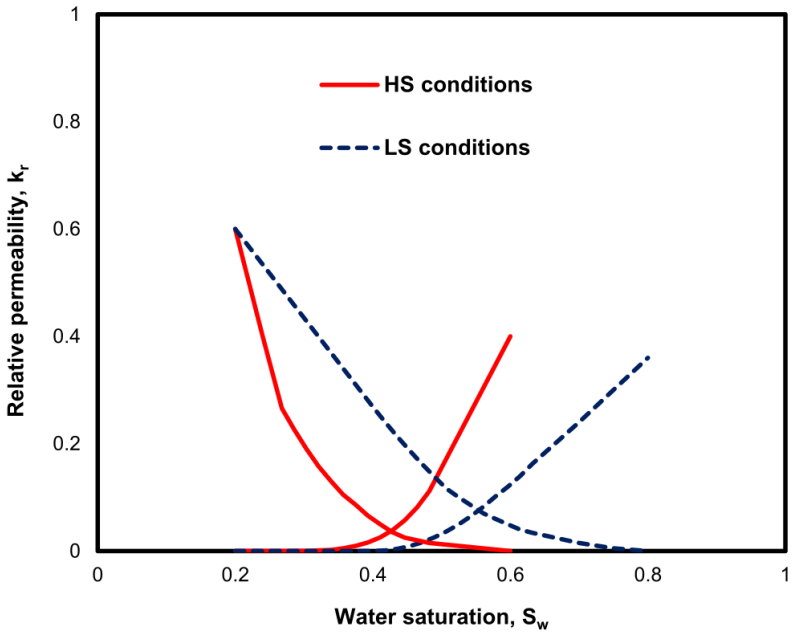


Fig. 5.2: Relative permeabilities: high-salinity (HS) in the *solid lines*, low-salinity (LS) in the *dashed lines*.

Consequently, in this chapter, a detailed simulation study is conducted to investigate the effect of physical mixing of the distinct brines on the optimal slug amount (or size) for the flood considering flow uncertainties. The evaluations exclude the uncertainty in the geological reservoir heterogeneity description – this will be considered in Chapter 6. Nonetheless, a number of numerical models with different levels of well-characterized permeability heterogeneity are used to explore the impact of the flow uncertainties on the LS displacement stability and performance of an injected slug. This is based mainly on reported data on the flow variables from corefloods and field tests. We will focus particularly on finding the inter-well optimal injected slug size to reduce the implementation risk under uncertainty.

After first describing the method adopted, the impact of LS injection start-time on recovery and the effective displacement mode of the flood is investigated in a homogeneous system. We then evaluate its optimal slug size under flow uncertainties and present its sensitivity to injection start-time. The sensitivity of the optimal slug size to heterogeneity is subsequently examined, providing insight into how the interaction between physical mixing and geological heterogeneity influences slug exposure and performance. This will help us to understand the critical effects of uncertainty in physical mixing on the flood performance through heterogeneous reservoirs.

5.2 Method

5.2.1 Description of the Models Used

The low salinity effect (LSE) is modelled with the standard tracer-component approach described in Chapter 2.5.1. Salinity is treated as the single-component tracer that controls wettability alteration and modifies mobilities towards more water-wet conditions. A linear salinity weighting function is adopted for mobilities at intermediate salinities. This is used to model any suppression of the injected slug effectiveness, and its impact on the flood outcome.

In a 2D simulation grid in the horizontal direction (i.e. gravity effects are ignored), two base models are considered in this chapter: i) a model with geological heterogeneity modified from the permeability distribution of the SPE 10 Model 1 dataset (Christie and Blunt, 2001), and ii) a heterogeneous unconditioned geostatistical model with a correlated log-normal permeability distribution. For clarity, the base models are named Heterogeneous A and Heterogeneous B respectively in **Fig. 5.3**. The geostatistical correlation properties are also presented in **Fig. 5.3**. As described in Chapter 2.7.2, the geostatistical permeability field in log space is modelled with the Gaussian Random Function Simulation (GRFS) algorithm in PETREL commercial software (Schlumberger, 2018). The correlation length (or range) is presented as a fraction of the system size (or reservoir dimension) in its direction; and this normalized value is considered equal for the X- and Y-directions. The grid dimensions and fluid properties used throughout this chapter are detailed in **Table 5.1**.

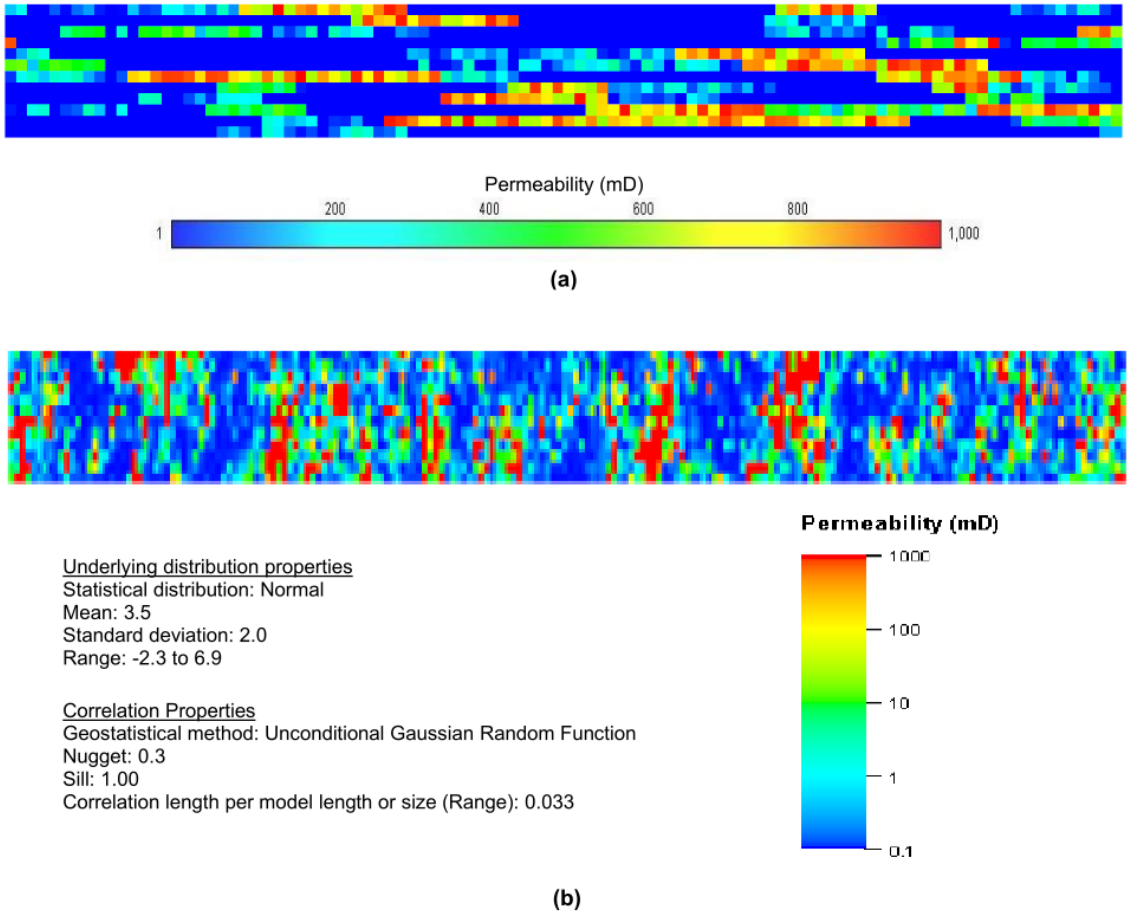


Fig. 5.3: Base models considered. (a) Model with permeability from the SPE 10 Model 1 dataset – Heterogeneous A. (b) Model with a geostatistical-generated permeability field – Heterogeneous B (Inset: statistical properties of the underlying normal distribution and the geostatistical correlation parameters).

Table 5.1: Description of the 2D-System.

Property (unit)	**Value**
Model dimensions (X, Y, Z) (m)	304.8 x 18.28 x 1.52
Grid dimensions (NX, NY, NZ)	200 x 12 x 1
Porosity	0.2
Initial water saturation	0.2
Datum depth (m)	2450
Initial reservoir pressure (Pa)	4.10×10^{7}
Formation compressibility at initial reservoir pressure (1/Pa)	1.93×10^{-8}
Depth of water oil contact (m)	2600
Water compressibility (1/Pa)	1.89×10^{-8}
Oil density (kg/m^3)	786
Water density (kg/m^3)	1000
Oil and water viscosity (Pa.s)	4.00×10^{-4}
Oil formation volume factor (rm^3/sm^3)	1.98
Water formation volume factor (rm^3/sm^3)	1.01

A linear scaling of the permeability distribution range is used to systematically vary the degree of heterogeneity in the base models to generate their correspondingly less heterogeneous realizations.

We use these realizations to expand our evaluation of the sensitivity of the LS displacement stability and performance of injected slug size to heterogeneity considering flow uncertainties.

For the Heterogenous A base model (**Fig. 5.3**a), the range of its permeability distribution or histograms is linearly rescaled while preserving its midpoint value. At each defined lower range, the permeability of each grid block is corrected using

$$k_n = R_n(k - k_{mid}) + k_{mid} \tag{5.1}$$

where k_n is the corrected permeability at the new range, R_n, for a grid block with permeability, k, in the base model. k_{mid} is the mid permeability of the base model which is constant across all the less heterogeneous realizations. R_n is defined as

$$R_n = \frac{k_{n_max} - k_{n_min}}{k_{max} - k_{min}} \tag{5.2}$$

where k_{max} and k_{min} are respectively the maximum and minimum values of the permeability distribution of the reference or base model, and k_{n_max} and k_{n_min} are those at the new distribution range, R_n. This approach ensures similar spatial distributions of the permeability field in the realizations but different variations of permeability values.

For the geostatistical Heterogeneous B base model, the standard deviation of the permeability distribution in log-space is varied while its mean value is fixed with the same geostatistical correlation properties in **Fig. 5.3**b. New models or realizations with different spatial distributions, mean and standard deviation permeabilities are therefore generated for the correlated log-normal distributions. This allows us to explore the influence of the spatial distribution of heterogeneity on the sensitivity of slug performance to heterogeneity under flow uncertainties. In the subsequent analysis, realizations from this approach are represented in terms of the standard deviation of their permeability distribution in log-space which is normalized as

$$\sigma_f = \frac{\sigma_n}{\sigma} \tag{5.3}$$

where σ_f and σ_n are the normalized and actual standard deviation of the permeability distribution (in log-space) respectively at the new realization, and σ is the actual standard deviation of the underlying normal distribution for the reference or base model.

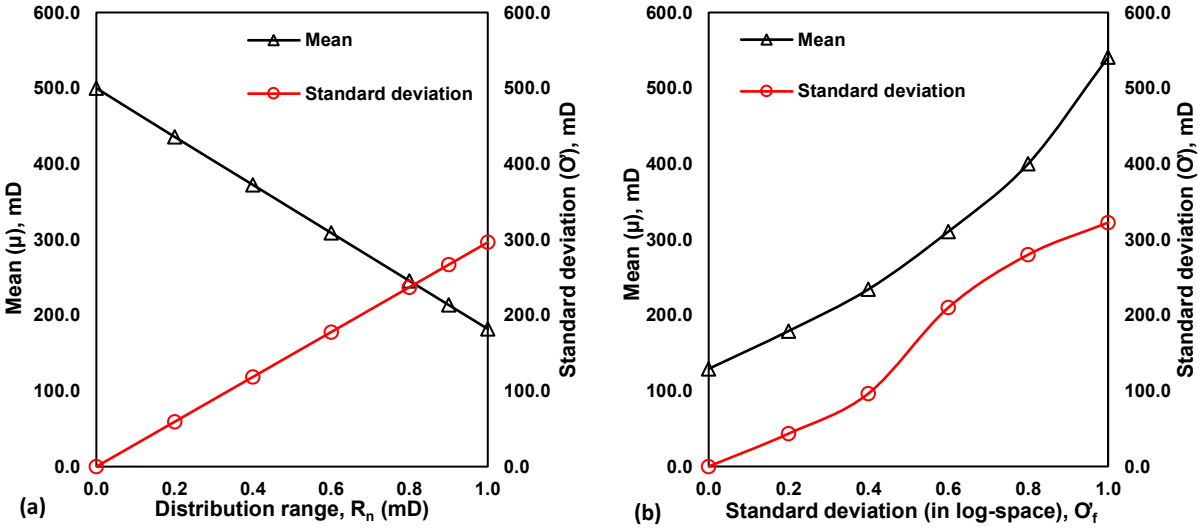


Fig. 5.4: Statistical moments of the permeability distributions in the realizations as a function of the defined degrees of heterogeneity. (a) Realizations from Heterogenous A – Set A models: characterized in terms of a normalized distribution range, R_n, which is the ratio of the actual range of the permeability distribution to that of the base model. (b) Realizations from Heterogeneous B – Set B models: characterized in terms of a normalized standard deviation, σ_f, which is the ratio of the actual standard deviation of the distribution in log-space to that of the base model.

Fig. 5.4 shows the statistical moments of the realizations defining their degree of heterogeneity in terms of their distribution range, R_n (for the Set A case) and standard deviation, σ_f (for the Set B case). The permeability distribution range and standard deviation (in log-space) are normalized by the range and standard deviation of the corresponding base models respectively. For the Set A models (**Fig. 5.4**a), $0 \leq R_n \leq 1$: $R_n = 1$ for the heterogeneous base model, and $R_n = 0$ for its equivalent homogeneous realization. For the Set B models (**Fig. 5.4**b), $0 \leq \sigma_f \leq 1$: $\sigma_f = 1$ for the base model, and $\sigma_f = 0$ for its homogeneous equivalence. The generated realizations or models are presented in **Fig. 5.5**.

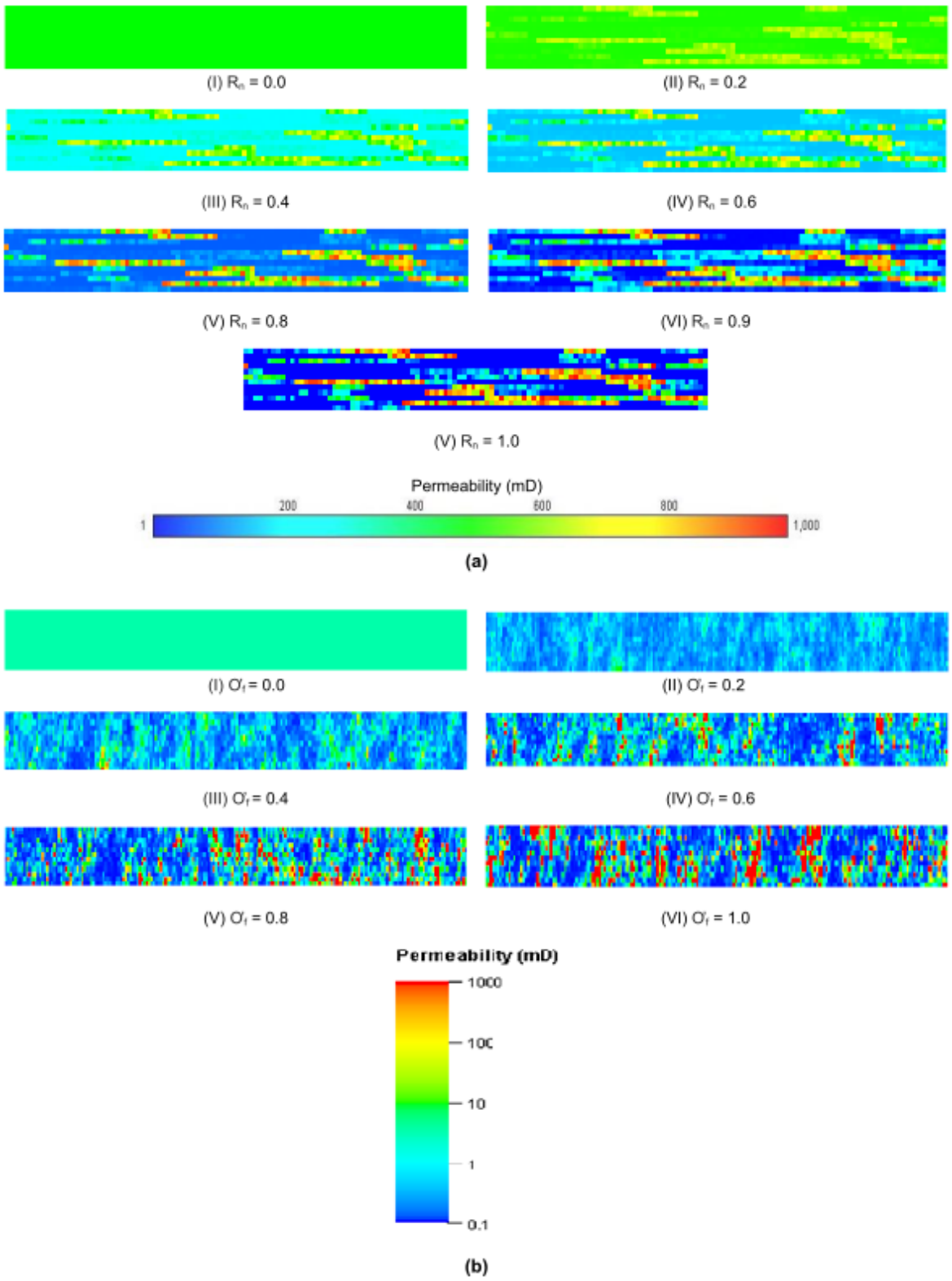


Fig. 5.5: Heterogeneous realizations considered. (a) Set A models with similar spatial distributions of the permeability field. (b) Set B models showing different spatial distributions.

The relative permeabilities for both high- and low-salinity brines are shown in **Fig. 5.2**, as previously used in Chapter 4. They are taken from a template input file of a commercial simulator (Schlumberger, 2015). The low-salinity water and oil relative permeabilities are lower and higher respectively than

those under high-salinity conditions which represents the characteristics of a more water-wet (perhaps less oil-wet) rock. This is typical of the LSE as described in Chapter 2.3 from corefloods matched by Callegaro et al. (2013). The effect of capillary pressure is ignored by setting it to zero. This is generally valid for field-scale simulations where the viscous pressure drop between wells is much higher than the capillary pressure. A line-drive well pattern is considered with the horizontal injector and producer placed and completed along the opposite faces of the models in the X-direction. Injection and production rates are constant and equal at the left and right faces of each model respectively.

All simulations were performed with the CMG STARS commercial simulator because of its ability to model physical dispersion explicitly with input values in LSWF simulations using the standard 'tracer-component' approach. This was introduced in Chapter 2.5.1 and previously adopted to investigate the influence of numerical dispersion on input physical mixing components in Chapter 4.5. The simulator implements a finite-difference approach to discretize the governing equations in space. For all simulations in this chapter, time stepping is fully implicit at a CFL or Courant number of 0.05 – to minimize numerical instability effect on the salt or solute-concentration front. Besides, this ensures that the inherent numerical dispersion is (truly) largely dependent on grid-size as adopted in this thesis to control its effect in simulations. Meanwhile, more practical and typically large timesteps can be used, provided the time-step and grid-size produce an inherent numerical dispersion – presented with equations (2.10) and (2.15) – with a 'critical input dispersivity' less than the explicitly defined (inputted) dispersivity. The grid resolution was described in **Table 5.1**, while the control of dispersion to desired levels of representative mixing evaluated in this chapter is discussed in the next section.

5.2.2 Flow Variables and LS Slug Performance Indicators

As discussed in Chapter 3; physical longitudinal and transverse dispersivities, upper (maximum) salinity threshold, and residual oil saturation to LSE are considered as the flow variables for our multivariate uncertainty assessment of the impact of physical mixing on optimal LS slug injection in this chapter.

Mixing between the injected low-salinity and resident high-salinity brines is evaluated as a combined effect of both the molecular diffusion and physical dispersion of the salt (or active-solute) component – as presented in equations (2.13) and (2.14). For uncertainty considerations, a constant numerical (diffusivity) component is combined with a varying input dispersivity to model the total physical mixing. The presence and grid-dependency of the critical input dispersion – previously described in Chapter 4.5 – is considered to select the suitable simulation grid-size for the range of total dispersion explored. This is to ensure the input physical dispersivity is adequately represented in the total

dispersion, amidst the inherent numerical component, during simulations. At the selected grid resolution ($\Delta X = \Delta Y = \Delta Z = 1.52\ m$), the numerical (diffusivity) component, $D_{L,num}$, gives a numerical Peclet number (*Pe*) of 400 or 0.25% of the model-length L using the formulas: $D_{L,num} = \frac{1}{L}\left(\frac{\Delta X}{2} + v\frac{\Delta t}{2}\right)$ and $Pe = \frac{1}{D_{L,num}}$, equations (2.10) and (2.15) respectively. The constant diffusive term – of equations (2.13) and (2.14) – is limited to this inherent numerical diffusivity at the isotropic grid-size adopted while the advective dispersion (term) is represented and varied through the input physical dispersivity to model the total mixing.

Additional input physical longitudinal dispersivity (α_l) range of $5.40 - 14.50\ m$ is set to model the advective longitudinal component (equation 2.13) to obtain a total Peclet number (*Pe*) range of 2 – 5% of the model-length L (as reported for inter-well distances by Mahadevan et al., 2003 and Jerauld et al., 2008 and discussed in Chapter 3.1). The use of dimensionless *Pe* to characterize physical dispersivity in terms of the measurement- or length-scale of a system was described in Chapter 2.7.1 with equation (2.15). For the selected $D_{L,num}$, this range of α_l ensures that advective dispersion dominates over diffusion in the total component-transport or mixing during flow. In addition, this range of input values is far greater than the critical dispersivity at the designed numerical component to ensure accurate representation in the simulations. The input physical longitudinal dispersivity is set at 0 for the base case simulations where uncertainties are not considered, which implies that mixing in these simulations is influenced by only the residual numerical component. This base level of mixing or dilution is assumed small enough to comparatively describe the field-scale convective flow behaviour of injected slugs in such a typically dispersive EOR process.

As mentioned in Chapter 3.1, transverse dispersivity (α_t) is set at one-thirtieth of the input longitudinal dispersivity (i.e. $\alpha_t \cong \alpha_l/30$) to model the advective transverse component (equation 2.14) at each level of physical mixing. This gives a transverse dispersivity range of $0.18 - 0.48\ m$, and a base input value of 0. This range also exceeds the critical dispersivity at the designed numerical component, thus ensures accurate representation of the transverse component of physical dispersion in the simulations.

The upper salinity threshold represents the cut-off salinity above which an injected brine completely loses its LSE during displacement. This is set to a range of 3,000 – 10,000 ppm as observed in several experiments and field tests presented in Chapter 3.1: 7,000 ppm is used for base case simulations without uncertainty considerations. As seen in earlier studies discussed in Chapters 2.1 and 3.2, the lower threshold is fixed at 1,000 ppm while the injected and connate brine salinities are 1,000 ppm and 30,000 ppm respectively in all simulations. These were also adopted in Chapter 4.

The residual oil saturation to LSE, S_{or_LS}, is used to quantify the overall improved microscopic displacement expected from the wettability alteration tendency of the injected LS slug. This is set at 38 – 60% of the residual oil to high-salinity waterflood (i.e. $0.15 \leq S_{or_LS} \leq 0.24$). $S_{or_LS} = 0.2$ – i.e. 50% of the residual oil saturation to high-salinity waterflood – for base case simulations where uncertainties are not considered.

Table 5.2 summarises these variables, their ranges of values, the assumed distributions, and statistical moments (where applicable). These distributions are selected based on the statistics of the reported data on the variables described in Chapter 3.1. For example, the typical longitudinal dispersivity is largely around the mid-value of its reported range as seen in data from Mahadevan et al. (2003), and interpreted tests at the Endicott field by Seccombe et al. (2008). A normal distribution fits such a spread of likely values better. A similar trend is also observed largely in the reported data on the upper salinity threshold – normalized as a fraction of the salinity range between the distinct brines, as summarised by Al-Ibadi et al. (2019). No significant skewness is seen in existing data on the possible drop in the residual oil saturation units from LSE relative to a high-salinity waterflood, as summarised by Bartels et al. (2019). We therefore assume a uniform distribution of its values spanning the range considered to investigate its effect on slug performance. Such a continuous, equiprobable distribution has been adopted for the residual oil saturation to other EOR processes (Alkhatib and King, 2014).

Table 5.2: Summary of the variables used in the simulations in this chapter.

Variable (unit)	**Base value**	**Reported range**	**Input population distribution**	
			Statistical moments	*Distribution*
Upper salinity threshold (ppm)	7,000	3,000 – 10,000	Mean: 6,575 Standard deviation: 1,480	Normal
Longitudinal dispersivity: $\boldsymbol{\alpha_l}$ ($\boldsymbol{m}$) ($\boldsymbol{Pe}$, % of the system length)	0	5.40 – 14.50 (2 – 5%)	Mean: 9.20 m (3.25 %) Standard deviation: 1.97 m (0.645 %)	Normal
Transverse dispersivity, $\boldsymbol{\alpha_t}$ ($\boldsymbol{m}$)	0	$\alpha_l/30$		
Residual oil saturation to LSE	0.2		Range: 0.15 – 0.24	Uniform

Two objective functions – total and marginal slug efficiencies – are defined to assess the performance of injected slugs and present how LS displacement stability affects recovery as a function of slug sizes under physical dispersion and geological heterogeneity. These are evaluated as the average and differential improved or incremental recovery as a function of slug sizes respectively. Total and marginal efficiencies at each injected slug size are defined as:

$$E_1(X) = \frac{URF_{LS}^{X} - URF_{HS}}{X} \tag{5.4}$$

$$E_2(X) = \frac{d(URF_{LS}^{X} - URF_{HS})}{dX} \tag{5.5}$$

where $E_1(X)$ and $E_2(X)$ are respectively the total and marginal efficiency at slug size X, relative to an injection time. $(URF_{LS}^{X} - URF_{HS})$ is the incremental recovery at slug size X. URF_{HS} is the total recovery from a continuous injection of resident high-salinity water while URF_{LS}^{X} is the total recovery obtained from combining a LS slug of size X with the waterflood. The recovery performance and slug size are in pore-volumes (PV) of the oil-zone.

Fig. 5.6 shows typical profiles of total and marginal efficiencies for LS slug injection under the influence of physical mixing in a homogeneous system – with only the principal inter-well flow path. The maximum impact of mixing from dispersion on recovery seems to be repressed around the point of maximum total efficiency; we refer to its corresponding slug as the 'stability-threshold size' for slug injection. Conceptually, this appears to represent the slug size limit to maintain slug integrity in the model. The LS displacement from smaller slug sizes is rather unstable and completely lost after a short travel time. Larger sizes show substantially improved recovery as their LS displacement stability is further sustained along the flow path. Completely stable LS displacement is achieved at zero marginal efficiencies with the minimum slug defined as the 'optimal size'. We adopt the two slug sizes – stability-threshold and optimal, to distinguish economic from technical optimal injected amounts in terms of recovery per unit slug volume.

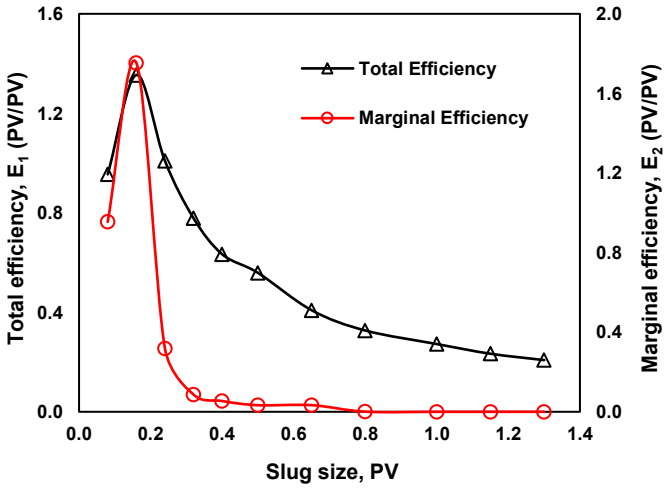


Fig. 5.6: Typical profiles of total and marginal efficiencies for LS slug injection under physical dispersion.

Because of the permeability heterogeneity between wells, (longer) secondary flow paths are often created thereby reducing the size of the principal path. Besides physical mixing, the bypassing of flow through these paths further impairs the LS displacement stability and slug performance. Meanwhile, most of the injected slug preferentially flows along the principal path, usually with the greatest improved recovery; hence it shows greater influence on the slug with maximum total efficiency. The threshold slug size therefore characterizes the principal flow path and defines an early-time performance such as the water breakthrough. Its total efficiency incorporates displacements along other (secondary) paths and reflects the late-time performance – total recovery. The higher this efficiency, the higher the total recovery. However, it is noted that whilst the maximum total efficiency is proportional to performance-defined heterogeneity, the threshold slug size may not, and this is shown later in this chapter.

5.2.3 Slug Performance Uncertainty Assessment and Injection Design Optimization

The influence of LS injection start-time on the displacement stability and slug performance is first evaluated using the base values of the flow variables (**Table 5.2**). The injected slug is then optimized for total efficiency to estimate the stability-threshold size. Optimization techniques such as the iterative Designed Exploration and Controlled Evolution genetic algorithm procedure (DECE) and Latin Hypercube (LH) Plus Proxy introduced in Chapter 3.3.2 are both considered to ensure the results are reliable. These are implemented with the CMG CMOST commercial optimizer.

The sensitivity of recovery to the variables is subsequently examined at the threshold slug size as a function of each variable. This involves varying each variable within its defined range of values while keeping the other variables constant at their base values (see **Table 5.2**). The effect of each variable in terms of changes in the base recovery is classified into gross and net. The gross effect is the sum of the maximum upside and the maximum downside percentage changes in the base performance. The maximum upside less the maximum downside value is the net effect. The gross effect ranks the relative significance of each variable to slug performance while the net effect shows if the variable has some favourable influence on performance.

For performance uncertainty quantification, experimental design and response surface generation procedures described in Chapter 3.3.1 (with equations 3.1 – 3.4) are adopted to effectively explore the uncertainty space and efficiently minimize the required simulation runs respectively. The near-orthogonal Latin hypercube is used to sample the parameter uncertainty space and design experiments. This ensures independence amongst the coefficient estimates for regression modelling

with better space-filling compared to absolute orthogonal designs with zero orthogonality value (equation 3.1). Nevertheless, a good design for sensitivity analysis and uncertainty assessment should have an orthogonality value < 0.2 (CMG, 2019). In this thesis, a more stringent orthogonality value of less than 0.1 is adopted as good for response surface generation or proxy modelling to assess performance uncertainty. Proxy models are trained from qualitative experimental designs using Artificial Neural Network (ANN) which is non-intrusive (Haykin, 1999; Christie et al., 2006). The Radial Basis Function (RBF) is adopted to train the proxy with ANN; Euclidean and non-Euclidean metrics are considered depending on the size (number of realizations) of the design. Blind tests are carried out with the proxy model for each case study to verify its accuracy outside its local sample space and validate its prediction reliability in lieu of real simulations. These involve a few randomly selected realizations outside those used to train the proxy. Upon this verification, many random realizations are generated with Monte Carlo simulation (MCS) to provide a wider representative sample of the experiment-region or parameter-space, with the performance uncertainty evaluated using the proxy model. The CMG CMOST optimizer is selected to perform this.

5.3 Results

5.3.1 Inter-well Homogeneity

5.3.1.1 Nominal Slug Performance

We investigate how slug performance and the effective displacement mode of the flood are influenced by the LS injection start-time. For the homogeneous model (**Fig. 5.5**ai), we consider the incremental recovery (relative to an equivalence high-salinity resident brine injection) at different injected slug sizes and injection start-times after a cumulative water injection (LS slug + high-salinity resident brine) of 2.0 PV. These are evaluated at the base values of the flow variables on **Table 5.2**. For example, the water cut profiles of a 0.35 PV injected slug size at different injection times is shown in **Fig. 5.7**. It is observed that the secondary-mode displacement (i.e. formation of connate water bank) extends beyond an immediate LS injection. **Fig. 5.8** presents the flood fronts – with stable inter-well displacement of the slug, highlighting the effective displacement mode at different LS injection start-times.

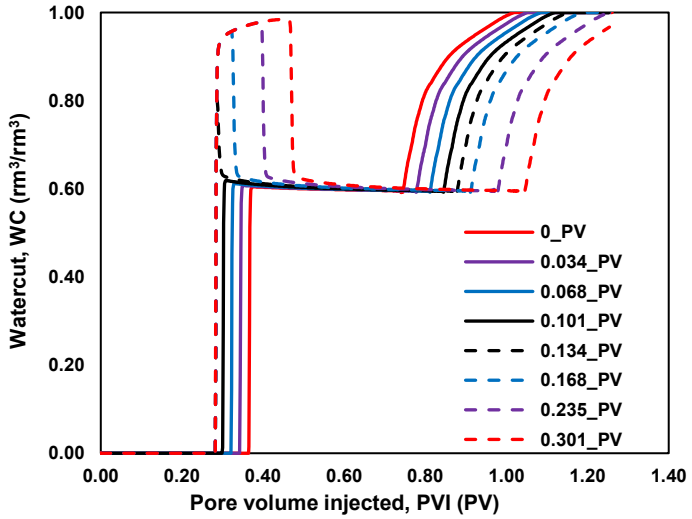


Fig. 5.7: Watercut (WC) as a function of cumulative pore volumes injected (PVI) in a LSWF of 0.35 PV slug size injected after pre-injecting different volumes (PV) of HS formation water. No oil banking (i.e. tertiary-mode displacement) commences till after pre-injecting 0.101 PV HS water.

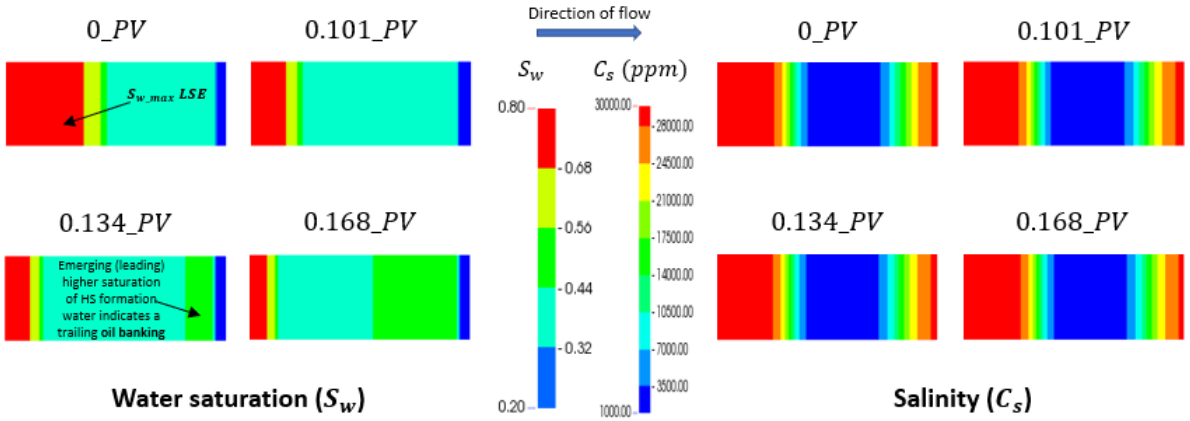


Fig. 5.8: Water saturation and salinity distribution just before breakthrough of a 0.35 PV LS-slug size injected after pre-injecting different volumes (PV) of HS formation water showing the effective displacement mode. No oil bank is observed till after pre-injecting 0.101 PV HS water. The water salinity distribution indicates a stable inter-well LS displacement of the slug at all the injection start-times for the level of dispersion considered.

The incremental recovery as a function of the initialization time for LS water injection at different injected slug sizes is presented in **Fig. 5.9**. Performance is classified into early (where displacement mimics secondary-mode: formation/connate water banking), middle (where displacement mimics tertiary-mode: oil banking), and late (where LS slug is injected post-breakthrough of the earlier injected formation brine) injection periods. Early or immediate LS injection favours recovery as seen in **Fig. 5.9**.

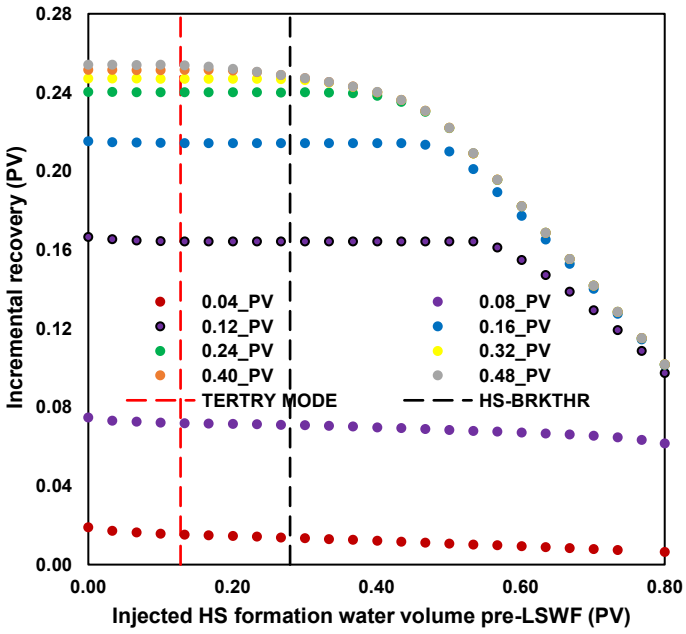


Fig. 5.9: Incremental recovery as a function of initialization times of LS water injection at different injected slug sizes (PV) in the homogeneous model. The commencement of tertiary-mode displacement (*red dashed line*) and the breakthrough of earlier injected HS brine (*black dashed line*) are also shown.

For the model and dispersion considered, a slug size of 0.4 PV is sufficient to contact most of the available residual oil target, as suggested by Jerauld et al. (2008). Furthermore, at the cumulative water injection considered, the incremental recovery and the optimal slug size are largely insensitive to LS injection start-time until tertiary-mode displacement becomes established. This is key to LSWF design as LS injection needs not commence immediately for the favourable secondary-mode displacement to be established. Meanwhile the uncertainties associated with the effect of mixing are not considered in this case.

5.3.1.2 Slug Performance Considering Uncertainty

The stability-threshold slug is evaluated to examine the sensitivity of performance to mixing from physical dispersion under inter-well homogeneity. The nominal optimization techniques – DECE and LH Plus Proxy discussed in Chapter 3.3.2 are considered for a robust estimation of the threshold injection from different injection start-times and slug sizes. This is highlighted in **Fig. 5.10** and the summary is shown in **Table 5.3**. Both techniques show the same optimal start-time of an immediate LS injection. The Latin Hypercube Plus Proxy technique is noted to be more efficient in terms of computational resources – it converges faster to a solution (i.e. requires fewer realizations).

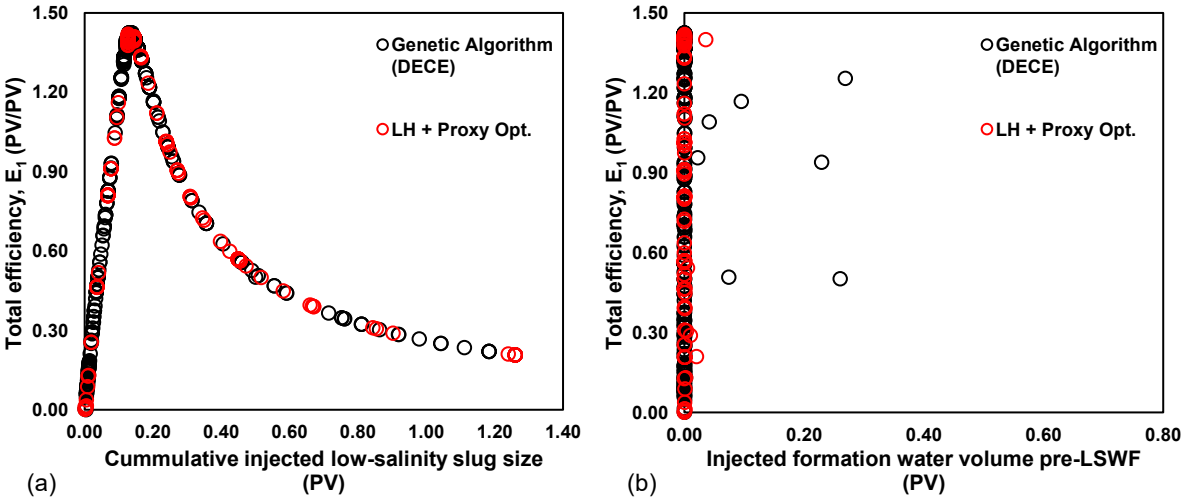


Fig. 5.10: Estimation of the stability-threshold injection from different optimization techniques (*black* DECE, *red* LH + Proxy). (a) Total efficiency as a function of slug sizes. (b) Total efficiency as a function of injection times.

Table 5.3: Summary of the nominal optimization results for the threshold strategy.

Performance indicators (units)	**Optimization techniques**	
	DECE	*LH + Proxy*
Threshold slug size (PV)	0.13	0.127
~ Threshold start time (PV)	0	0
Maximum total efficiency, $\mathbf{E_1}$ (PV/PV)	1.4250	1.4194
Incremental recovery (PV)	0.185	0.180
Total recovery (PV)	0.484	0.479
Experiment size (realizations)	500	190

An immediate injection of 0.13 PV slug size is selected as the stability-threshold. The sensitivity, in this case, of the base recovery and total efficiency (presented in **Table 5.3**) to longitudinal dispersivity, transverse dispersivity, maximum (upper) salinity threshold and residual oil saturation to LSE is shown in **Fig. 5.11**. The performance indicators at this threshold injection are observed to be highly sensitive to the longitudinal dispersion and the upper salinity threshold. This is because, as previously discussed in Chapter 4, these parameters control the velocities of the displacement fronts in a LSWF which influence the impact of physical dispersion on the LS displacement stability of injected brine. Their uncertainties therefore need to be appropriately considered in any optimal slug size design. Conversely, performance shows no significant sensitivity to the residual oil saturation to LSE within the range considered as shown in **Fig. 5.11**. We suggest this is because the overall flood performance is largely influenced by the change in the water saturation at the cross-over of the oil and water relative permeabilities (**Fig. 5.2**) rather than just the end points. Such rightward shift of the cross-over saturation towards more water-wetness during LSWF appears here to be more sensitive to physical dispersion than the residual oil saturation to LSE. However, a combination of both variables may substantially affect slug performance especially under inter-well heterogeneity as we show in subsequent sections. No impact of transverse dispersion is seen on recovery since the case is a homogeneous line-drive model.

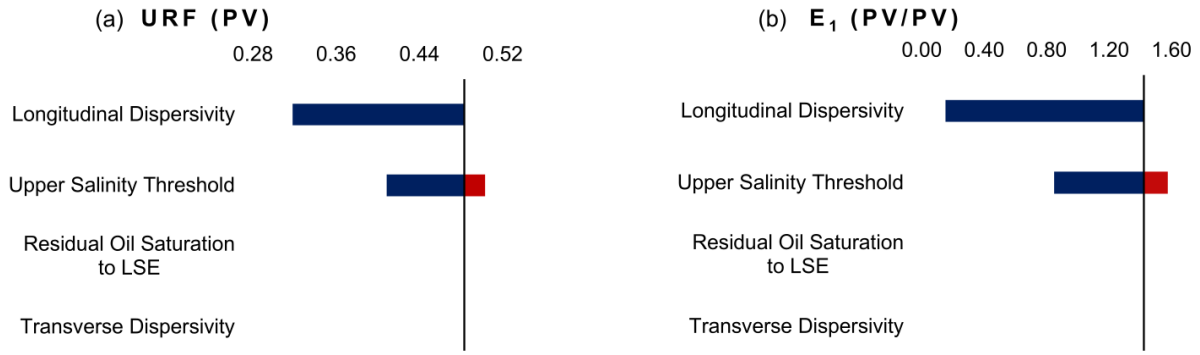


Fig. 5.11: Tornado plots showing the sensitivity of the base performance of the stability-threshold injection to the flow variables. (a) Total recovery (URF). (b) Total efficiency (E_1).

We now assess the uncertainty in the LSWF performance under inter-well homogeneity at different slug sizes and injection start-times in detail. The selected injection strategies are guided by the nominal performance of **Fig. 5.7** and **Fig. 5.9** to ensure a widespread evaluation. The variables are as defined in **Table 5.2**.

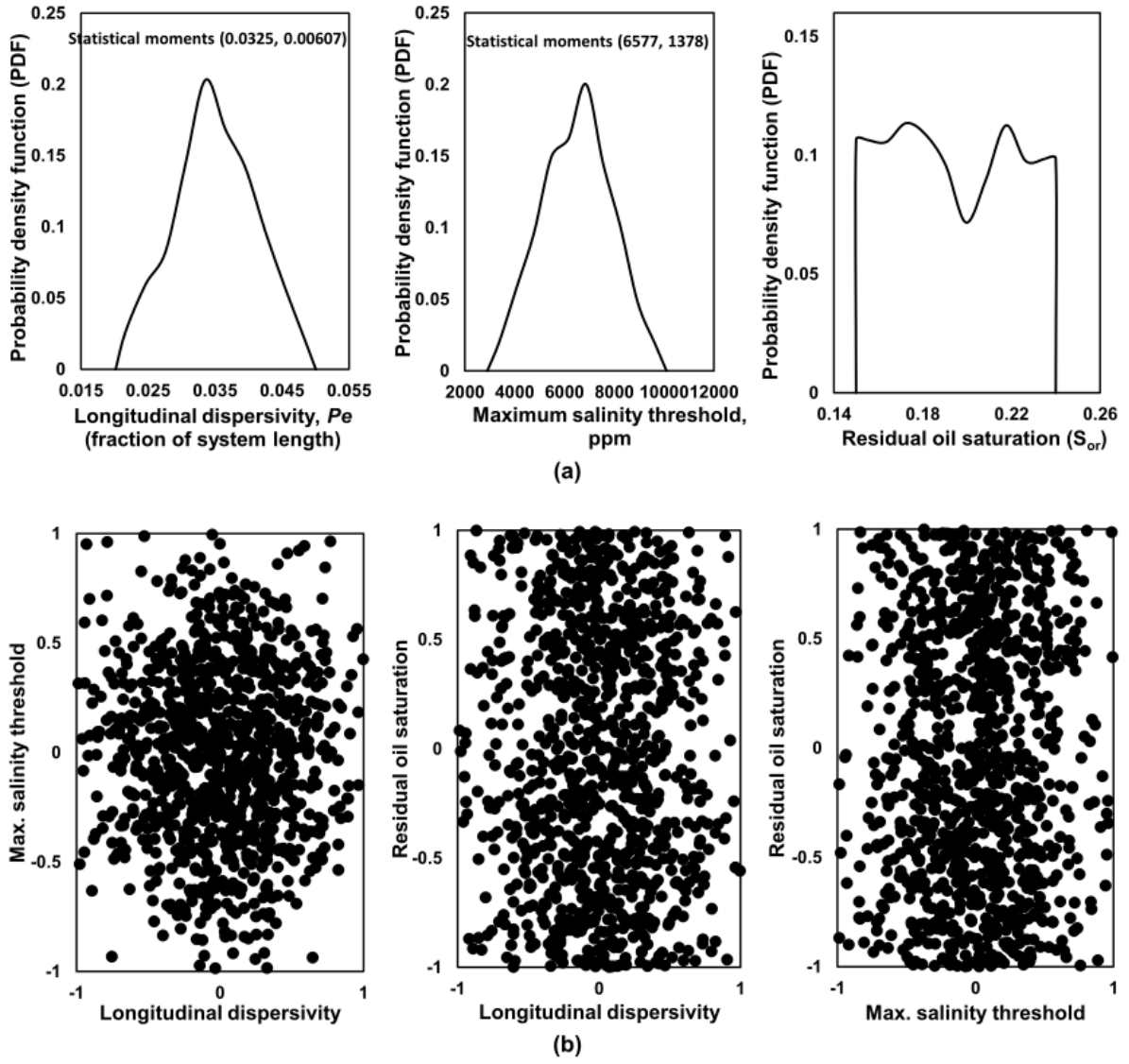


Fig. 5.12: Sampling quality of 5,000 realizations of input variables. (a) Probability density functions (PDFs) of the sampled variables. (b) Two-dimensional projections of the sampled variable-pairs over discretized parameter uncertainty space. This shows a pairwise scattering (space-filling) over the uncertainty space that is uniformly representative of defined prior distributions.

The uncertainty space for the flow variables is sampled first with the Latin hypercube method at multiple iterations of additional 80 realizations per iteration. About 5,000 realizations would be needed to establish a representative space-filling sample size for the defined parameter uncertainty space. The sampling quality at this size is presented in **Fig. 5.12** in terms of the probability density functions (PDFs) of the sampled input variables, as well as the two-dimensional projections of the

sampled variable-pairs over the discretized uncertainty space. The statistical moments and distributions of its sampled parameter space (**Fig. 5.12**a) are approximately equal to those of the defined population uncertainty space (i.e. input population statistics in **Table 5.2)**. The 2D projections (**Fig. 5.12**b) visually shows a good space-filling based on the defined prior distributions of the variables (**Table 5.2**) within the interval [-1, 1].

It is often computationally not feasible to run simulations for the large number of realizations required for each injection strategy considered to quantify the performance uncertainty. Proxy models are therefore trained for each strategy from near-orthogonal Latin Hypercube (LH) designs for the first five progressive iterations – 80, 160, 240, 320 and 400 realizations, using the RBF Artificial Neural Network (Haykin, 1999; Christie et al., 2006). All these experimental designs show an orthogonality less than 0.1 (equation 3.1), which meet our suggested criterion for a good design, but different in their space-fillings. We use performance uncertainty at a few injection strategies to verify and validate the proxy models. For example, the recovery predictions of the proxy-models from the first five progressive iterations for the stability-threshold slug at different LS injection start-times are shown in **Fig. 5.13** in comparison with reservoir simulation results from the 5,000 realizations. A perfect match of the reference solution (i.e. original reservoir model simulation) is achieved especially at the third-, fourth- and fifth-iteration proxies (240, 320 and 400 realizations respectively). Besides, blind tests are carried out with a few injection scenarios to compare the proxy prediction accuracies of polynomial regression and neural network (ANN). The proxy-model from ANN shows a consistently better and exact approximation of the reservoir model within 0.2% error across all scenarios (**Fig. 5.14**). The third-iteration proxies are adopted in this chapter for our uncertainty quantifications with 65,000 Monte-Carlo realizations.

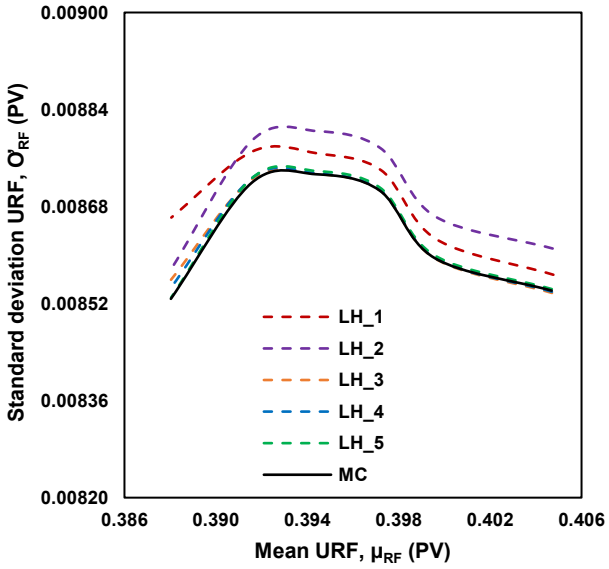


Fig. 5.13: Statistical moments of predicted stability-threshold slug performance distributions at different injection times using proxy-models trained from near-orthogonal LH designs for different numbers of LH-iterations (or sampled realizations) in comparison with real reservoir simulation results (MC) for 5,000 realizations. A perfect match of the reference solution – reservoir simulation results (MC) – is achieved from the third-iteration proxies onwards (i.e. ≥LH_3 – 240 realizations).

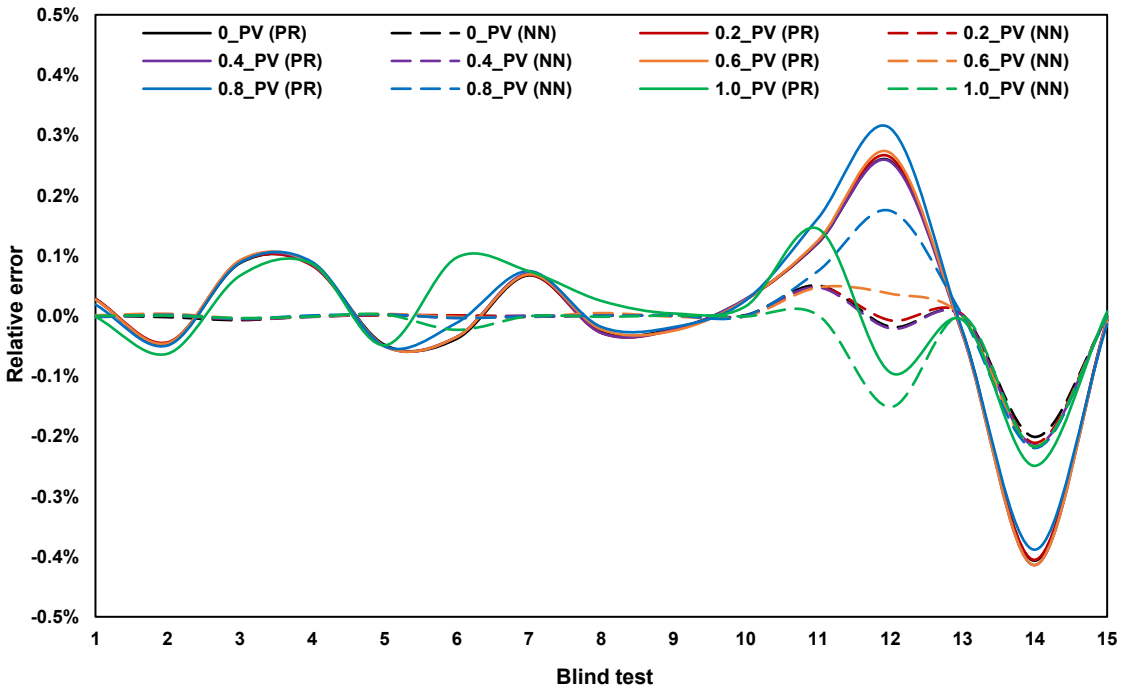


Fig. 5.14: Blind tests with some injection strategies or scenarios – at different injected formation HS water volumes (PV) pre-LSWF – showing the prediction accuracy of representative proxy-models from polynomial regression (PR) and artificial neural network (NN) relative to results from reservoir model simulations.

The stochastic moments of the performance distributions are presented as a function of injected slug sizes in **Fig. 5.15**. Considering the defined uncertainty in physical mixing, a 0.8 PV slug size would be

needed to contact most of the available residual oil target (**Fig. 5.15**a). This is twice the amount evaluated without the flow uncertainties – 0.4 PV (**Fig. 5.9**) and represents the minimum slug size to maximize the expected recovery with reduced associated risks. About 0.44 PV is estimated for the stability-threshold slug size under uncertainty (**Fig. 5.15**b). This represents the injection design limit to optimize slug size for both stable LS displacement and economics to reduce the risks from mixing in the model. Besides, this value shows a larger and less-efficient stability-threshold slug under the flow uncertainties.

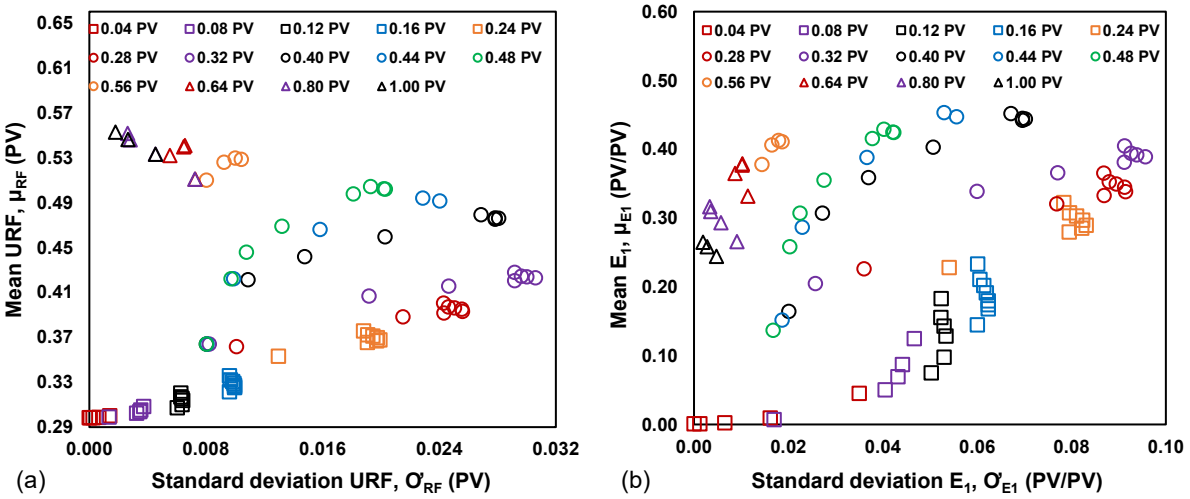


Fig. 5.15: Statistical moments of performance distributions at different injected slug sizes (PV). (a) Mean of total recovery as a function of standard deviation. (b) Mean of total efficiency as a function of standard deviation.

Fig. 5.15 is replotted in **Fig. 5.16** and **Fig. 5.17** in terms of LS injection start-times – after pre-injecting different volumes of HS formation water, and relative to the breakthrough of pre-injected HS formation water respectively. Early or immediate slug injection favours recovery and the associated risk under uncertainty as highlighted in **Fig. 5.16**. In addition, mean performance and the optimal slug size remain less sensitive to LS injection start-time until around the breakthrough of the pre-injected HS formation brine (**Fig. 5.17**). Nonetheless, delays of LS injection need to consider the associated slug performance risks.

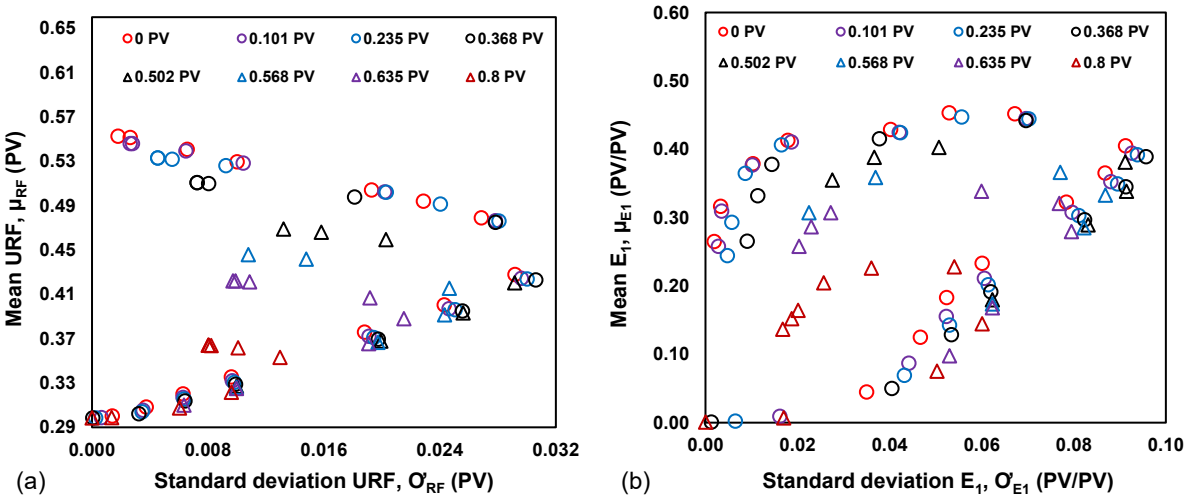


Fig. 5.16: Statistical moments of performance distributions at different LS injection times after pre-injecting different volumes (PV) of high-salinity formation water. (a) Mean of total recovery as a function of standard deviation. (b) Mean of total efficiency as a function of standard deviation.

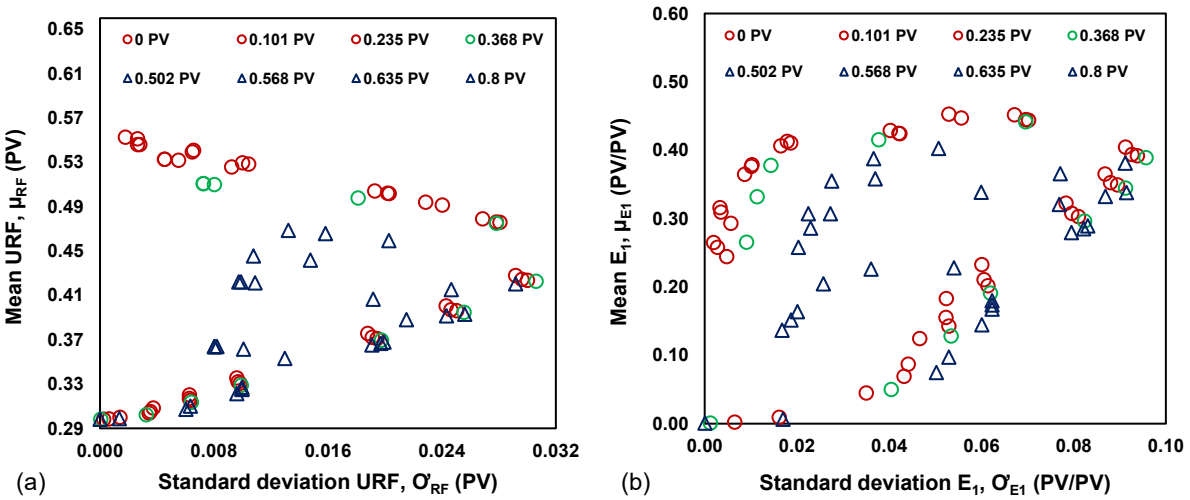


Fig. 5.17: Statistical moments of performance distributions at different LS injection times relative to the breakthrough of any pre-injected high-salinity formation water (*red* pre-breakthrough, *green* around breakthrough, *blue* post-breakthrough). (a) Mean of total recovery as a function of standard deviation. (b) Mean of total efficiency as a function of standard deviation.

The stability of the LS displacement under uncertainty is characterized by the slug performance risks (standard deviation) for total efficiency (σ'_{E1}) and total recovery (σ'_{RF}). As a function of slug sizes (**Fig. 5.16** and **Fig. 5.17**): σ'_{E1} or σ'_{RF} initially increases then decreases for each LS injection start-time which is similar to the trend in **Fig. 5.6**. This indicates that the LS displacement stability at the injection start-time increases with slug size and at a decreasing impact of uncertainty in physical mixing from around the stability-threshold size. As a function of LS injection start-times (**Fig. 5.15**): decreasing σ'_{E1} or σ'_{RF} indicates unstable LS displacement; increasing σ'_{E1} or σ'_{RF} shows a stable LS displacement; increasing then decreasing σ'_{E1} or σ'_{RF} signifies an initially stable then unstable LS displacement if injection of the slug size is delayed.

5.3.2 Sensitivity of Slug Performance and its Optimal Injection Design to Inter-well Heterogeneity

5.3.2.1 Set A Models Modified from SPE 10 Model 1

The LS displacement stability and the performance of the injected slug is investigated in the presence of geological heterogeneity considering uncertainty in mixing from physical dispersion. This is to examine the sensitivity of the optimal slug size to heterogeneity. Here, we evaluate with immediate slug injection at a cumulative water injection of 2.0 PV. The influence of heterogeneity is examined first with the Set A realizations of **Fig. 5.5**a relative to a homogeneous condition (**Fig. 5.5**ai).

Fig. 5.18 shows the nominal or base performance (i.e. without flow uncertainties) at different slug sizes for the range of heterogeneities studied. The base performance shows more sensitivity to heterogeneity and slug size between 0.1 to 1.0 PV slug injections across the models, with sensitivity to slug size increasing with heterogeneity (**Fig. 5.18**a). The slug size to contact most of the oil target also increases with heterogeneity – 0.4 PV (for $R_n = 0.00$) to 1.1 PV (for $R_n = 1.00$), at a decreasing recovery performance (**Fig. 5.18**a and c). The maximum total efficiency (E_1) indicates a decreasing trend with heterogeneity at an increasing corresponding slug size – i.e. stability-threshold (**Fig. 5.18**b). This shows that the LS displacement of the injected slug consistently becomes less stable with heterogeneity at the base conditions. It results in the substantial marginal efficiencies (E_2) observed at large slug sizes as heterogeneity increases, which reflects late-time improved recovery (**Fig. 5.18**c).

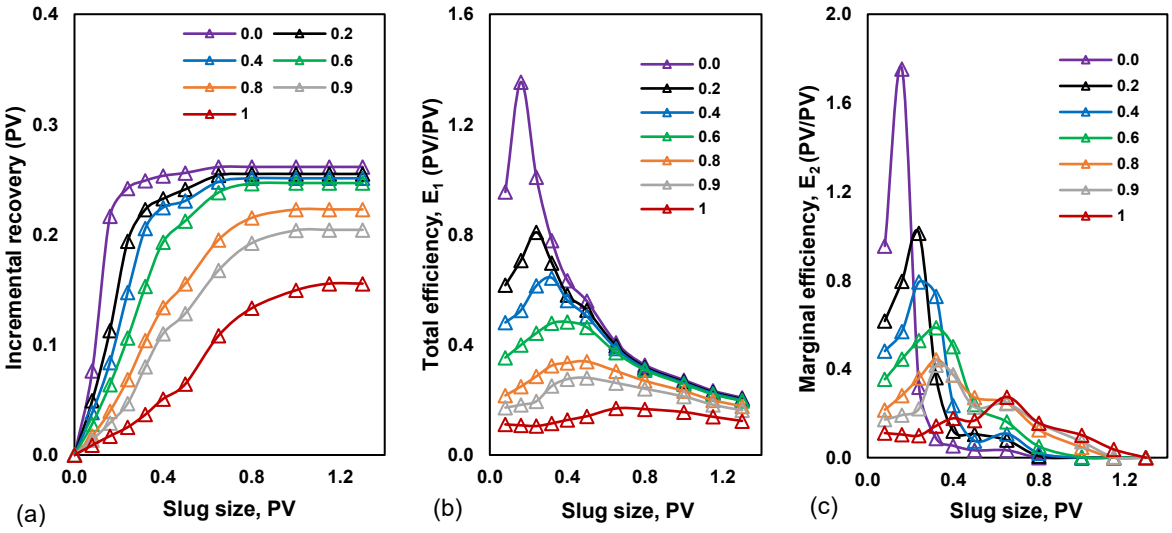


Fig. 5.18: Base performance as a function of injected slug size at different degrees of heterogeneity ($0.0 \leq R_n \leq 1$: *purple* $R_n = 0.0$, *black* $R_n = 0.2$, *blue* $R_n = 0.4$, *green* $R_n = 0.6$, *orange* $R_n = 0.8$, *grey* $R_n = 0.9$, *red* $R_n = 1.0$). (a) Incremental recovery. (b) Total efficiency. (c) Marginal efficiency.

Furthermore, the stability-threshold slug size and its total efficiency are estimated accurately with the nominal optimization techniques – DECE and LH Plus Proxy (Yang et al., 2009; 2011). As observed in

Fig. 5.19, the threshold slug size increases with heterogeneity at a decreasing maximum total efficiency supporting the previous deductions from **Fig. 5.18**. The linearity of the maximum total efficiency with heterogeneity shows its suitability to characterize total recovery under performance-defined levels of heterogeneity as earlier introduced in Section 5.2.2. The stability-threshold slug size is also linear with heterogeneity in this case. This is because the size of the principal flow path is reduced uniformly by heterogeneity that is of similar spatial distributions in these models.

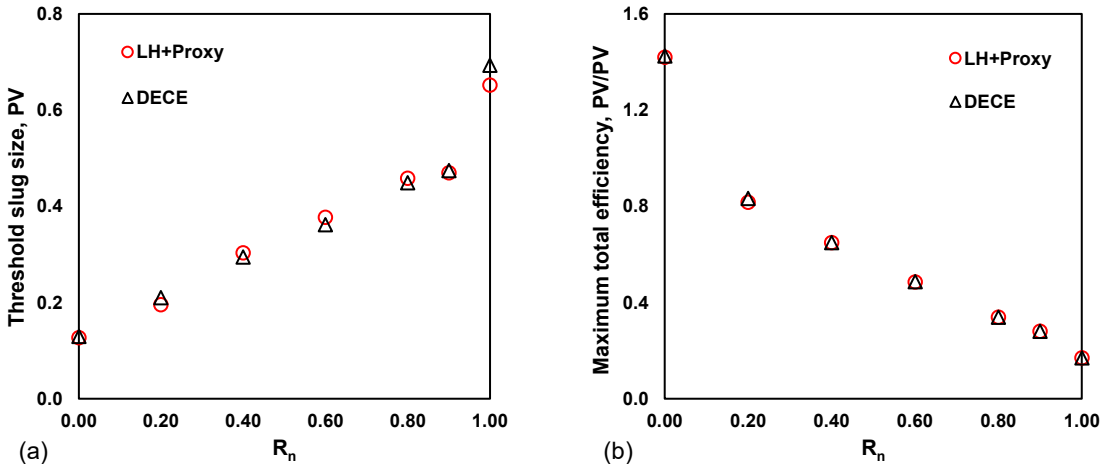


Fig. 5.19: Threshold slug size and maximum total efficiency from the nominal optimization techniques (circle LH + Proxy, triangle DECE) as a function of heterogeneity (R_n).

The sensitivity of slug performance to the flow variables considering mixing is evaluated as a function of inter-well heterogeneity at their respective stability-threshold slugs of **Fig. 5.19**. **Fig. 5.20**a shows the gross effect of variations in each parameter on recovery (i.e. gross sensitivity of recovery to each parameter). High sensitivity of slug performance and recovery to physical dispersivity is seen to decrease with heterogeneity. This is because heterogeneity reduces the overall sweep with additional distorted displacement fronts and often longer flow paths to suppress the slug *ab initio*. Therefore, unlike a homogeneous model where dispersion substantially influences recovery along the large flow path, its impact on recovery is reduced in heterogeneous models. However, recovery in heterogeneous models shows more sensitivity to the upper or maximum salinity threshold. This is because the stability of the heterogeneity-enhanced dispersed and distorted displacement fronts becomes highly dependent on the salinity-threshold range.

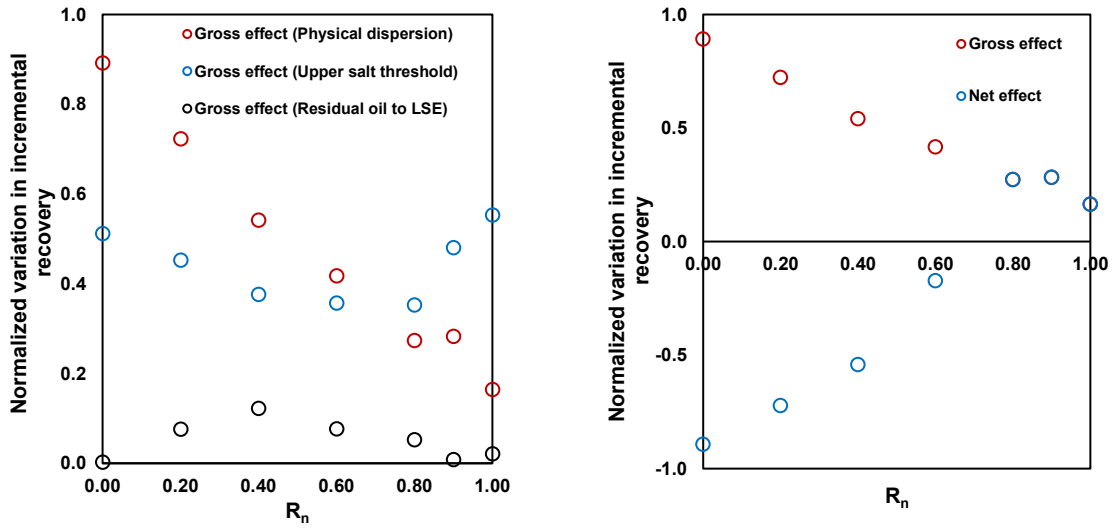


Fig. 5.20: Sensitivity of slug performance and recovery to flow variables as a function of heterogeneities. (a) Gross sensitivity to each parameter. (b) Gross and net sensitivities to physical dispersion. All variations are normalized with the base performance.

From the net effect in **Fig. 5.20**b, some favourable sensitivity of recovery to physical dispersivity is observed in heterogenous models ($0.60 \leq R_n \leq 1.00$). This indicates active transverse dispersion in areal heterogeneity with the positive effect due to the LS displacement of fluids in the less permeable regions. Contrary to the suggestion of Attar and Muggeridge (2018), transverse dispersion in LSWF is seen here to be important when heterogeneity modifies the areal sweep efficiency. The favourable influence of transverse dispersion is illustrated in **Fig. 5.21** which shows the performance sensitivity of the stability-threshold slug injection to only physical dispersion in the heterogeneous models. A potential improvement in the LS displacement front (i.e. the salinity-thresholds spread: $1{,}000 - 7{,}000\ ppm$) and recovery is seen from (transverse) dispersion in $R_n \geq 0.6$ if compared to $R_n = 0.4$ where mixing impairs performance across the range of physical dispersivity (*Pe*) considered.

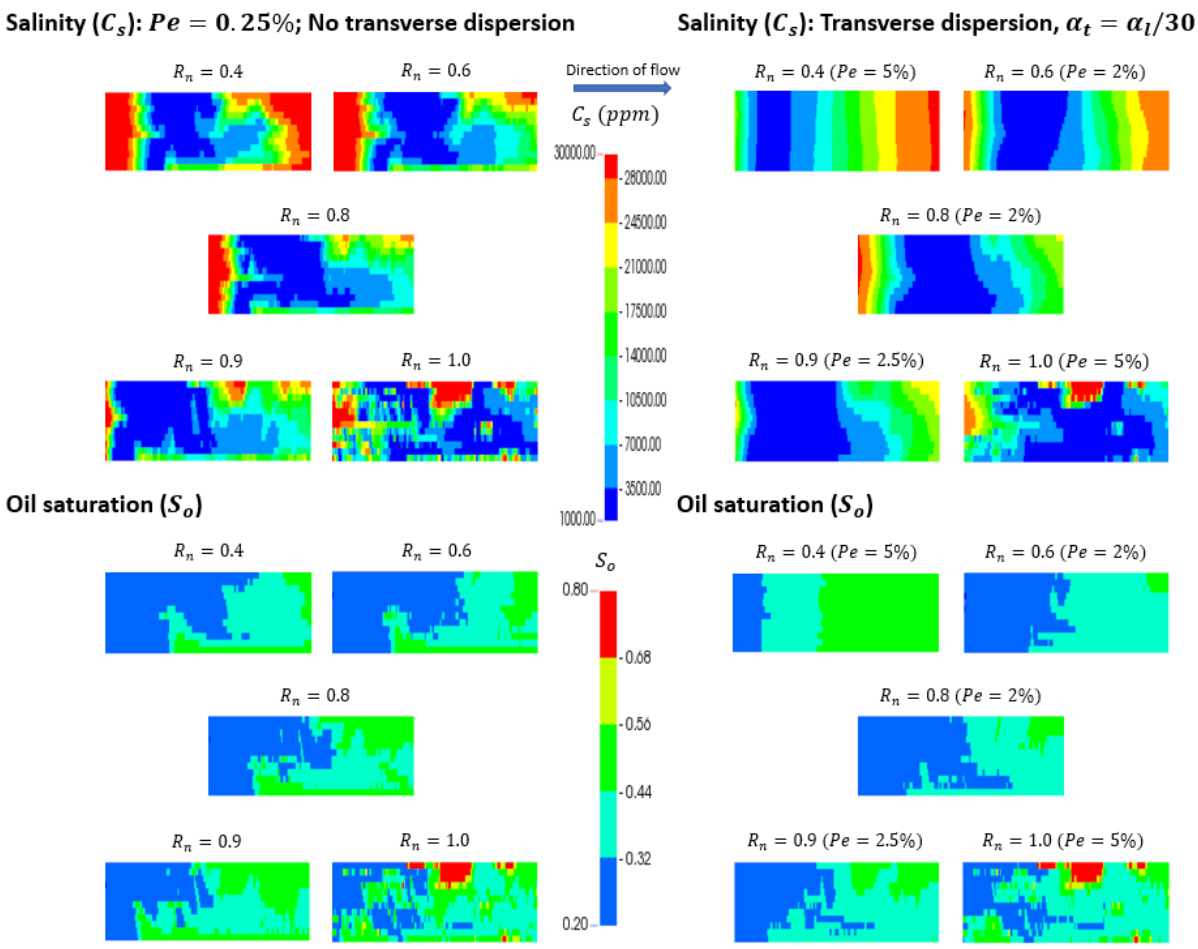


Fig. 5.21: Salinity and oil saturation distributions illustrating the favourable influence of transverse dispersion in areal heterogeneity on recovery. The water salinity profile shows the salinity-thresholds spread and the LS displacement stability of the injected slug just at its breakthrough and/or the commencement of the HS push. The oil saturation distribution indicates the recovery at the end of the flood – i.e. pre-injected LS slug + HS push.

The mean slug performance considering flow uncertainties is presented in **Fig. 5.22**. In comparison to the base case, the mean performance is substantially influenced by flow uncertainties with less sensitivity to slug size and heterogeneity (**Fig. 5.22**a). Slug performance is impaired by the risk of physical mixing in less heterogeneous models ($R_n \leq 0.40$) with reduced E_2 at small slug sizes indicating late-time (delayed) improved recovery (**Fig. 5.22**c). In contrast, the more heterogeneous models ($R_n \geq 0.60$) show increased E_2 at small slug sizes indicating early-time improved recovery because of the favourable effects of transverse dispersion (**Fig. 5.22**c). This improves the total efficiency (E_1) of injected slugs in these models but with no significant changes in their stability-threshold sizes (**Fig. 5.22**b). The optimal slug size increases with heterogeneity from 0.8 PV for $R_n = 0.00$ to about 1.1 PV for $R_n = 1.00$ (**Fig. 5.22**c). The stability-threshold size for slug injection also increases with heterogeneity from about 0.4 PV for $R_n = 0.00$ to over 0.65 PV for $R_n = 1.00$ (**Fig.**

5.22b). This implies that the sensitivity of the optimal slug design – in terms of these slug sizes – to heterogeneity is also reduced under mixing when the flow uncertainties are considered.

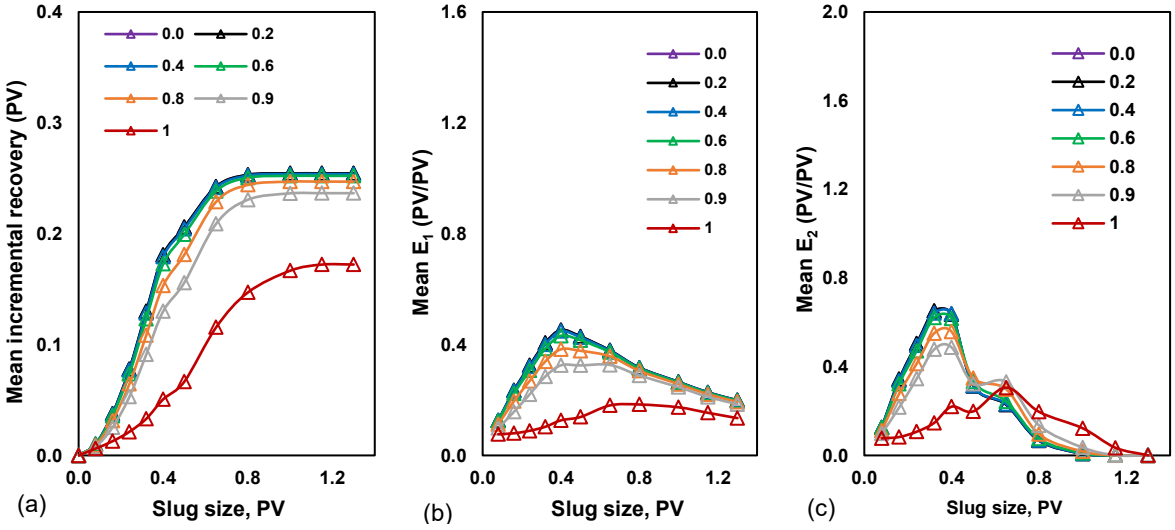


Fig. 5.22: Mean performance under flow uncertainties as a function of injected slug size at different degrees of heterogeneity ($0.0 \leq R_n \leq 1$: *purple* $R_n = 0.0$, *black* $R_n = 0.2$, *blue* $R_n = 0.4$, *green* $R_n = 0.6$, *orange* $R_n = 0.8$, *grey* $R_n = 0.9$, *red* $R_n = 1.0$). (a) Incremental recovery. (b) Total efficiency. (c) Marginal efficiency.

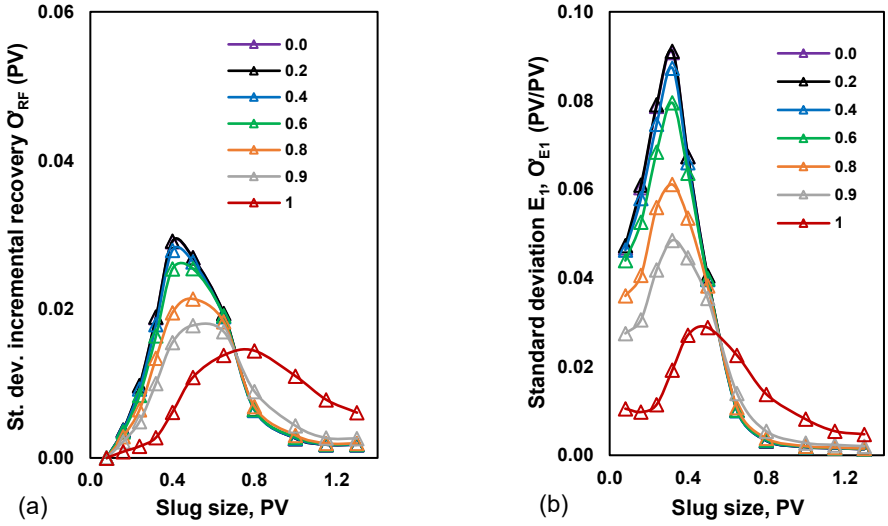


Fig. 5.23: Performance risks under flow uncertainties as a function of injected slug sizes at different degrees of heterogeneity ($0.0 \leq R_n \leq 1$: *purple* $R_n = 0.0$, *black* $R_n = 0.2$, *blue* $R_n = 0.4$, *green* $R_n = 0.6$, *orange* $R_n = 0.8$, *grey* $R_n = 0.9$, *red* $R_n = 1.0$). (a) Standard deviation of incremental recovery. (b) Standard deviation of total efficiency.

The sensitivity of the LS displacement stability of an injected slug size to heterogeneity is reflected in the performance risks for total efficiency (σ'_{E1}) and recovery (σ'_{RF}) in **Fig. 5.23**a and b. Decreasing σ'_{E1} or σ'_{RF} with heterogeneity for small slugs below the stability-threshold size indicates that the LS displacement stability decreases with heterogeneity, which is similar to an unstable slug under delayed LS injection start-times (**Fig. 5.15**). Increasing σ'_{E1} or σ'_{RF} with heterogeneity for large slugs

above the stability-threshold size also signifies a decreasing LS displacement stability with heterogeneity, similar to a stable slug under delayed LS injection start-times (**Fig. 5.15**). The active transverse dispersion enhances the LS displacement stability in the more heterogeneous models, especially $R_n = 0.60$ and $R_n = 0.80$, as seen in their homogeneous-like fast-descending $\mathcal{O}_{E1}$ or $\mathcal{O}_{RF}$ profiles post their stability-threshold sizes. This is achieved by modifying the dispersed and distorted slug fronts along the flow paths.

5.3.2.2 Set B Models from Geostatistical Property Modelling

The Set B models (**Fig. 5.5**b) are now considered. The nominal (base) slug performance for the models is presented in **Fig. 5.24** as a function of injected sizes. The performance shows more sensitivity to heterogeneity and slug size between 0.1 to 0.65 PV slug injections across the models, with sensitivity to slug size increasing with heterogeneity (**Fig. 5.24**a). The slug size to contact most of the oil target increases with heterogeneity – 0.4 PV (for $\sigma_f = 0.00$) to 0.8 PV (for $\sigma_f = 1.00$), at a decreasing recovery performance (**Fig. 5.24**a and c). The maximum total efficiency shows a decreasing trend with heterogeneity which also reflects the decreasing slug performance with heterogeneity (**Fig. 5.24**b).

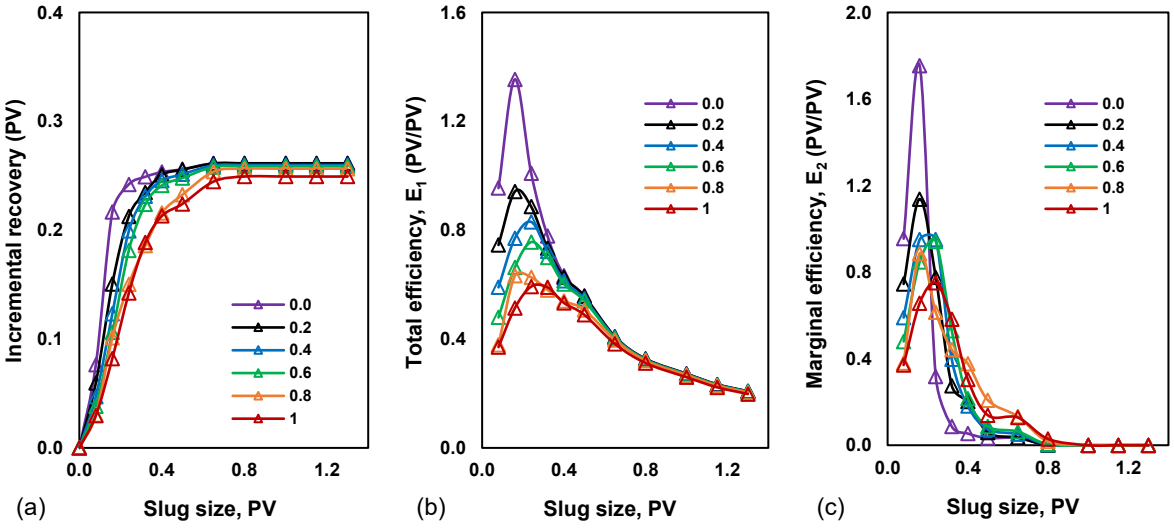


Fig. 5.24: Base performance as a function of injected slug size at different degrees of heterogeneity ($0.0 \leq \sigma_f \leq 1$: *purple* $\sigma_f = 0.0$, *black* $\sigma_f = 0.2$, *blue* $\sigma_f = 0.4$, *green* $\sigma_f = 0.6$, *orange* $\sigma_f = 0.8$, *red* $\sigma_f = 1.0$). (a) Incremental recovery. (b) Total efficiency. (c) Marginal efficiency.

The stability-threshold slug size and its total efficiency are estimated accurately using the DECE and LH Plus Proxy optimization techniques (Yang et al., 2009; 2011). The linearity of the maximum total efficiency with heterogeneity is still honoured (**Fig. 5.25**b). For this case, the stability-threshold slug size shows non-linearity with heterogeneity at $\sigma_f = 0.8$ because of the non-uniform spatial distributions of heterogeneity in the models (**Fig. 5.25**a). As it was stated in Section 5.2.2, the threshold size characterizes the principal flow path not the total displacement and may not be linearly

proportional to heterogeneity. However, this shows that the spatial distribution of heterogeneity influences the characteristics of the principal path which may impact the overall slug performance significantly regardless of the defined heterogeneity geostatistics.

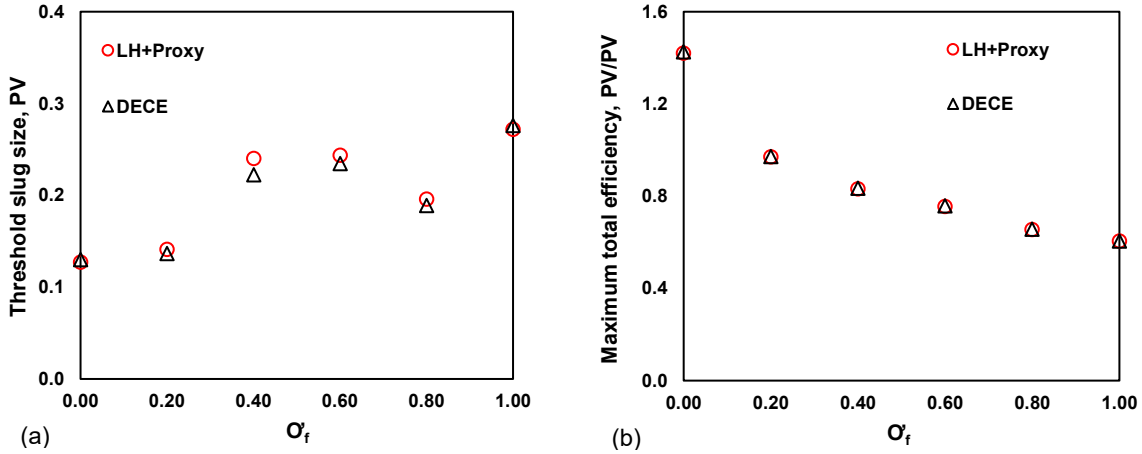


Fig. 5.25: Threshold slug size and maximum total efficiency from the nominal optimization techniques (circle LH + Proxy, triangle DECE) as a function of heterogeneities (σ_f).

The performance sensitivity to the flow variables is evaluated as a function of heterogeneity at the estimated stability-threshold slugs of **Fig. 5.25**. The slug performance is more sensitive to physical dispersivity and the sensitivity grossly decreases with heterogeneity (**Fig. 5.26**a). This trend is similar to that observed in the results from the Set A models discussed in the previous section. In contrast, no favourable impact of physical dispersion is seen across the models as its net and gross effects on recovery are equal (**Fig. 5.26**b). This implies that transverse dispersion further degrades the slug at these injected sizes. It is suggested that the spatial distribution of heterogeneity in the models either prevents fluid displacement in less permeable grids which is conditional for favourable transverse dispersion or delays the favourable impact. **Fig. 5.27** shows the performance sensitivity of the stability-threshold slug injection to only physical dispersion in the heterogeneous models. For the range of dispersivity (*Pe*) considered, the LS flood front and recovery are impaired further with mixing in this set of models: the LSE (i.e. its salinity-thresholds spread of $1{,}000 - 7{,}000\ ppm$) from the injected slug becomes lost earlier during the inter-well displacement.

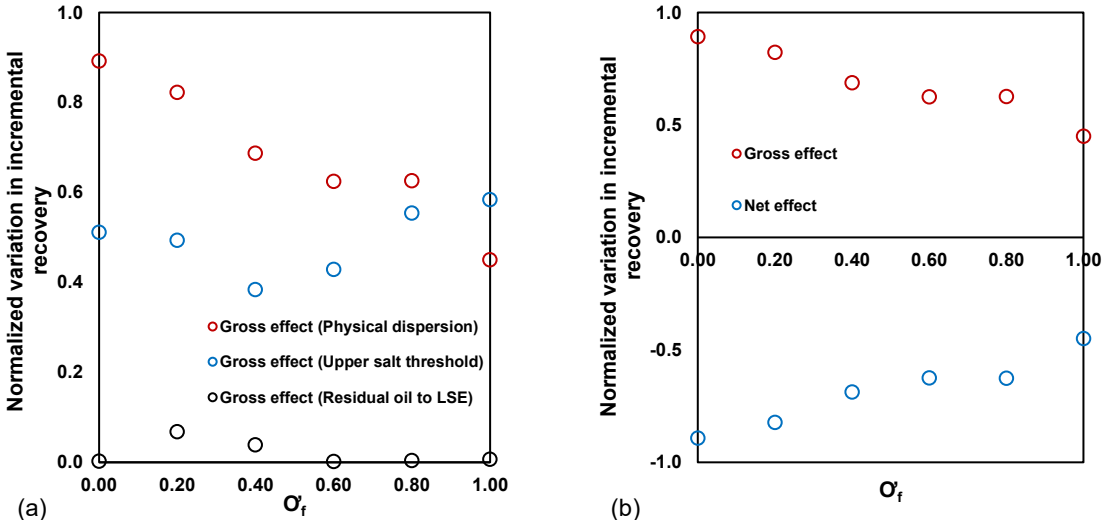


Fig. 5.26: Sensitivity of slug performance and recovery to flow variables as a function of heterogeneities. (a) Gross sensitivity to each parameter. (b) Gross and net sensitivities to physical dispersion. All variations are normalized with the base performance.

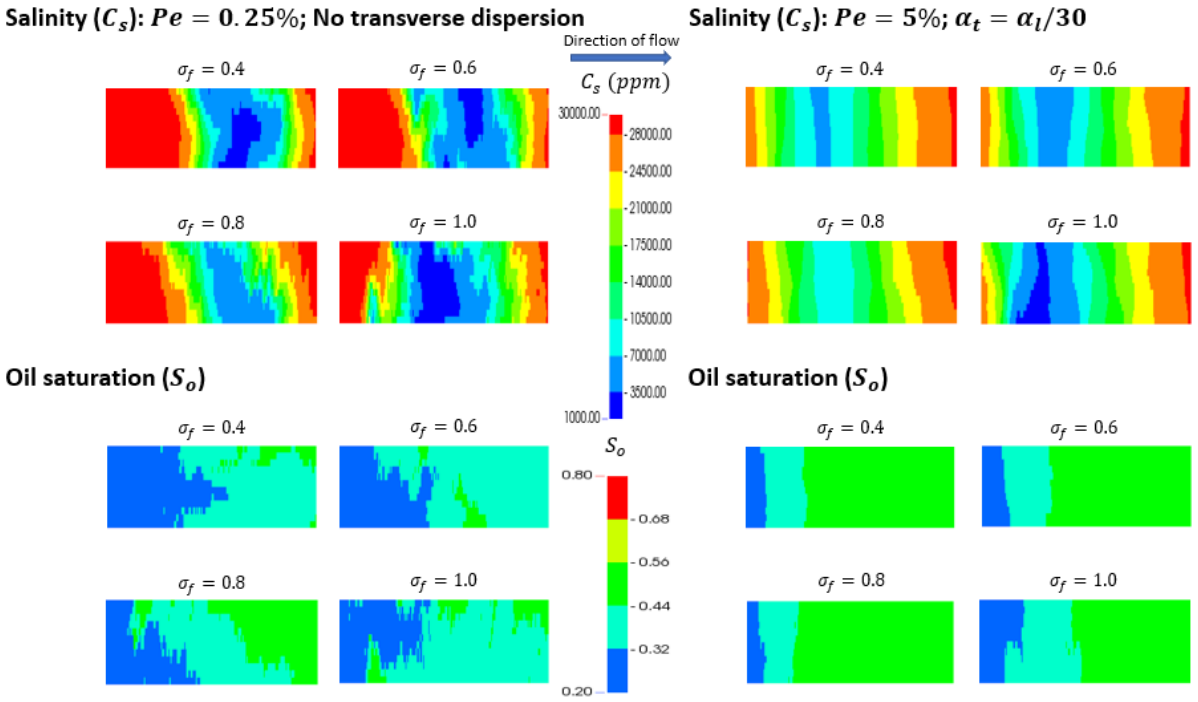


Fig. 5.27: Salinity and oil saturation distributions with areal heterogeneity. The water salinity profile shows the spreading of the salinity-thresholds and LS displacement stability of the injected slug just at its breakthrough and/or the commencement of the HS push. The oil saturation distribution indicates the recovery at the end of the flood – i.e. pre-injected LS slug + HS push. No favourable impact of physical dispersion is observed in the models at their stability-threshold slug injections.

The mean slug performance considering flow uncertainties is shown in **Fig. 5.28** for the Set B models. In comparison to the base case, the mean performance is rendered relatively insensitive to heterogeneity by flow uncertainties thereby showing similar sensitivity to slug size across the models (**Fig. 5.28**a). The reduced performance of the injected slug from the risk of physical mixing, where high

efficiencies shift from small to moderate slug sizes indicating delayed improved recovery, decreases with heterogeneity (**Fig. 5.28**b and c). This shows unfavourable dispersion at small slug sizes under the flow uncertainties. About 0.4 PV and 0.8 PV are estimated for the stability-threshold and optimal sizes for slug injection respectively with little or no sensitivity to heterogeneity (**Fig. 5.28**b and c).

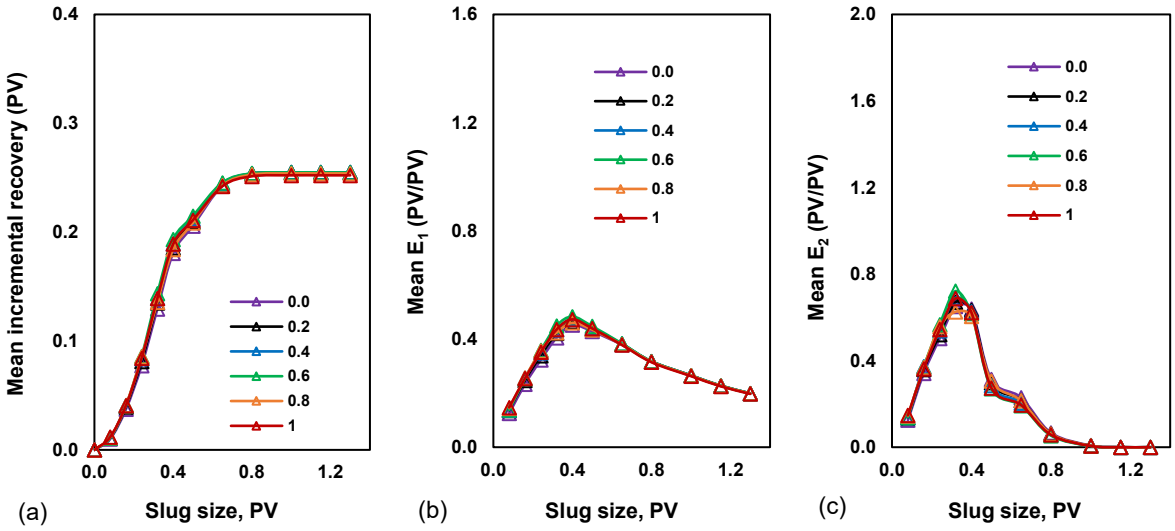


Fig. 5.28: Mean performance under flow uncertainties as a function of injected slug size at different degrees of heterogeneity ($0.0 \leq \sigma_f \leq 1$: *purple* $\sigma_f = 0.0$, *black* $\sigma_f = 0.2$, *blue* $\sigma_f = 0.4$, *green* $\sigma_f = 0.6$, *orange* $\sigma_f = 0.8$, *red* $\sigma_f = 1.0$). (a) Incremental recovery. (b) Total efficiency. (c) Marginal efficiency.

Fig. 5.29a and b present the sensitivity of the LS displacement stability of the injected slug sizes to heterogeneity. σ'_{E1} or σ'_{RF} decreases with heterogeneity for small slug sizes lower than the stability-threshold indicating a decreasing LS displacement stability with heterogeneity. Whereas a decreasing σ'_{E1} or σ'_{RF} with heterogeneity is also observed for moderate slug sizes post the stability-threshold (especially 0.4 – 0.65 PV) which signifies improved LS displacement stability with heterogeneity. This must have resulted in the high mean slug efficiencies at those sizes as earlier observed in **Fig. 5.28**c. It is suggested that this is due to a delayed favourable impact of transverse dispersion with heterogeneity which is controlled by its spatial distribution in the models. The flood displacement fronts herein appear to be effectively separated further at those slug sizes under inter-well heterogeneity compared to the corresponding homogeneous realization.

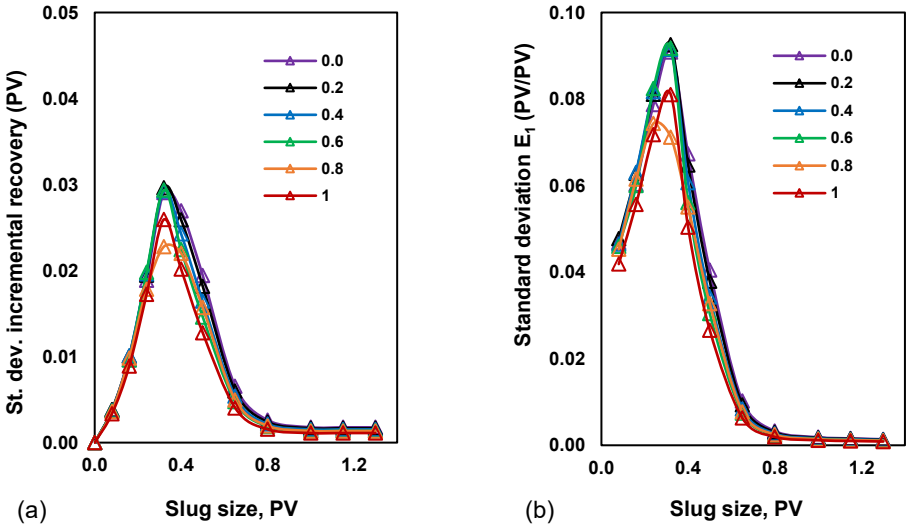


Fig. 5.29: Performance risks under flow uncertainties as a function of injected slug sizes at different degrees of heterogeneity ($0.0 \leq \sigma_f \leq 1$: *purple* $\sigma_f = 0.0$, *black* $\sigma_f = 0.2$, *blue* $\sigma_f = 0.4$, *green* $\sigma_f = 0.6$, *orange* $\sigma_f = 0.8$, *red* $\sigma_f = 1.0$). (a) Standard deviation of incremental recovery. (b) Standard deviation of total efficiency.

5.4 Summary

This chapter investigated the effect of physical mixing in LSWF on optimal slug injection considering some associated flow uncertainties – physical longitudinal and transverse dispersivities, upper (maximum) salinity threshold, and residual oil saturation to the LSE. This was evaluated with two-dimensional areal reservoir simulation that accurately captured physical dispersion complemented by proxy modelling. We explored the displacement stability and performance of a LS slug while optimizing its injected size considering risks associated with the field-scale mixing of the distinct brines.

In the first part, the workflow examined the impact of LS injection start-time on the slug performance and its effective displacement mode while finding the optimal injected amounts under inter-well homogeneity. The second part scaled-up the optimal slug injection for heterogeneous descriptions and presented further insights on the interaction between physical dispersion and heterogeneity, and its impact on the LS displacement stability, performance, and optimal amounts of the injected slug. The specific findings and conclusions from this chapter are summarised as follows:

1. Secondary-mode displacement (i.e. formation of connate water bank) can extend beyond an immediate injection of low-salinity (LS) brine. For the (line-drive) flood pattern considered, LS slug performance is relatively insensitive to its injection start-time until the tertiary-mode displacement becomes established in a system.
2. The LS displacement stability and performance of the injected slug can potentially be influenced favourably by heterogeneity depending on its spatial distribution. This is linked to transverse

dispersion which, contrary to earlier reports, is found to be active when heterogeneity modifies the areal sweep. Transverse dispersion tends to improve the areal sweep efficiency.

3. As much as twice the optimal slug size under nominal conditions may be needed to reduce the performance risks if flow uncertainties are considered. This ratio reduces with heterogeneity, hence the sensitivity of the optimal slug injection to uncertainty in physical mixing during LSWF decreases with heterogeneity. However, the extent of geological heterogeneity impact on this is significantly influenced by its spatial distribution relative to the flood displacement paths.
4. Slug injection schemes require a design of at least 0.8 PV optimal size and 0.4 PV minimum stability-threshold size to reduce risk under uncertainty. This is found to be generally favoured by an early injection – specifically before the breakthrough of any pre-injected HS formation brine if flow is predominantly along homogeneous inter-well paths. Injection optimization can prioritize the slug range between the stability-threshold and optimal sizes to balance the technical and financial performance of the flood. This essentially minimizes the computational requirements for such evaluation.
5. The spatial distribution of geological heterogeneity remarkably controls the favourability or otherwise of the effect of physical mixing on the displacement stability and performance of injected LS slug. Besides, its representation remains a major source of uncertainty in petroleum recovery plans and this was excluded in this chapter.

Our results here are limited to evaluations considering only line-drive flood pattern to optimize the injected slug size. In the next chapter, we will investigate how flood patterns and the geological uncertainty influence the optimal injected amounts through the study of multi-dimensional realizations characterised with more heterogeneous formations.

6 Influence of Flood Pattern and Geological Uncertainty on the Impact of Mixing on Optimal Low Salinity Slug Injection

6.1 Introduction

This chapter extends our investigation, to explore the influence of geological uncertainty and flood pattern (or well arrangement) on the optimal injected slug amounts using multi-dimensional realizations characterised with more heterogeneous reservoir connectivity. In Chapter 5, we investigated the effect of physical mixing in low-salinity waterflooding (LSWF) on the optimal slug injection. The analysis in Chapter 5 was limited to evaluations considering uncertainties in the field-scale level of physical dispersion, as well as the upper (maximum) salinity threshold and the residual oil saturation to the low salinity effect (LSE), under a line-drive flood pattern. Geological heterogeneity was found to have a significant influence on how the mixing of the distinct brines impacts the displacement stability and performance of injected LS slug. Geological heterogeneity in this context refers to the spatial permeability distribution. However, its representation is a major source of uncertainty in reservoir descriptions to predict recovery performance accurately, and this was excluded in Chapter 5.

In this chapter, we first examine how the flood pattern influences the impact of LS injection start-time on the slug performance, its effective displacement mode, and the optimal injected amounts under inter-well homogeneity – in two-dimensional simulation grids. This is then extended to the sensitivity of the optimal slug size when heterogeneity is accounted for. Later, uncertainty in geological heterogeneity is introduced to evaluate its impact on the optimal slug injection. Last, we examine the susceptibility of the optimal injection design to more representative reservoir heterogeneities characterized by different geostatistical models – in two- and three-dimensions. This is of broad significance in the design of LS flooding, and scaling up its optimal slug injection considering uncertainty in the effects of both inter-well physical mixing and geological heterogeneity.

6.2 Method

6.2.1 Description of the Models Used

The low salinity effect (LSE) is modelled with the standard tracer-component approach described in Chapter 2.5.1. It is adopted here in this chapter as described for the prior investigation in Chapter 5.2.1.

For each of the two flood patterns or well arrangements considered in this chapter – line-drive (LD) and quarter five-spot (Q5S), a heterogeneous unconditioned geostatistical base model with a correlated log-normal permeability distribution is used with a 2D simulation grid in the horizontal direction (i.e. gravity effects are ignored). The heterogeneous base models and the geostatistical correlation properties are shown in **Fig. 6.1**. The 2D line-drive (LD) heterogeneous base model was described previously in Chapter 5.2.1. In addition, a heterogeneous unconditioned geostatistical base model with a correlated log-normal permeability distribution is otherwise considered in 3D for a Q5S flood pattern to examine our findings in three dimensions including the effects of better reservoir connectivity and gravity. This is presented in **Fig. 6.2** with the geostatistical correlation properties. For all these models, the geostatistical permeability field in log space – as described in Chapter 2.7.2 – is modelled with the Gaussian Random Function Simulation (GRFS) algorithm in PETREL commercial software (Schlumberger, 2018). The grid dimensions and fluid properties are detailed in **Table 6.1**.

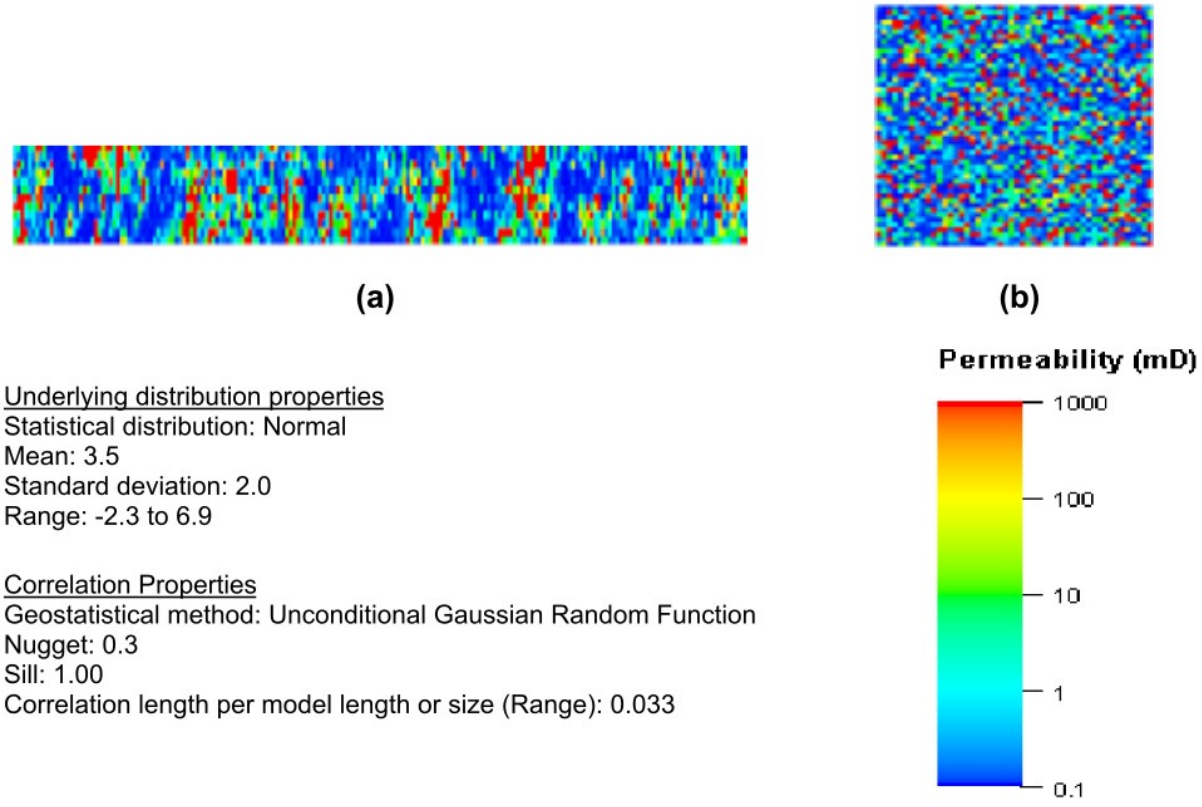


Fig. 6.1: 2D base models considered. (a) Line-drive, as presented previously in Chapter 5. (b) Quarter five-spot. (Inset: statistical properties of the underlying normal distribution and the geostatistical correlation parameters).

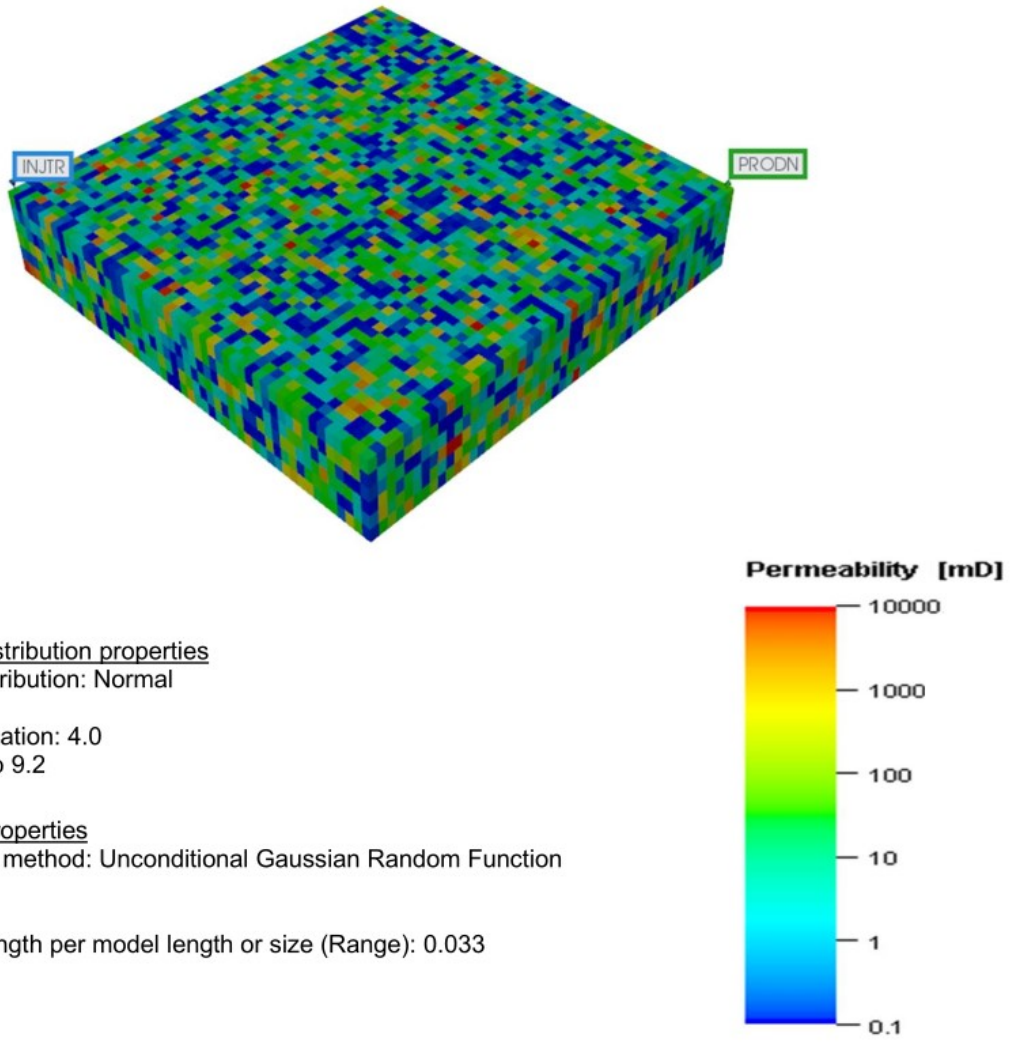


Fig. 6.2: 3D base model considered under a quarter five-spot flood pattern. (Inset: statistical properties of the underlying normal distribution and the geostatistical correlation parameters).

Table 6.1: Description of the 2D and 3D models.

Property (unit)	**Value**
Model dimensions (X, Y, Z) (m) – 2D LD	304.8 x 18.28 x 1.52
Grid dimensions (NX, NY, NZ) – 2D LD	200 x 12 x 1
Model dimensions (X, Y, Z) (m) – 2D Q5S	304.8 x 304.8 x 1.52
Grid dimensions (NX, NY, NZ) – 2D Q5S	100 x 100 x 1
Model dimensions (X, Y, Z) (m) – 3D Q5S	304.8 x 304.8 x 18.3
Grid dimensions (NX, NY, NZ) – 3D Q5S	100 x 100 x 6
Porosity	0.2
Initial water saturation	0.2
Datum depth (m)	2450
Initial reservoir pressure (Pa)	4.10×10^{7}
Formation compressibility at initial reservoir pressure (1/Pa)	1.93×10^{-8}
Depth of water oil contact (m)	2600
Water compressibility (1/Pa)	1.89×10^{-8}
Oil density (kg/m^3)	786
Water density (kg/m^3)	1000
Oil and water viscosity (Pa.s)	4.00×10^{-4}
Oil formation volume factor (rm^3/sm^3)	1.98
Water formation volume factor (rm^3/sm^3)	1.01

The standard deviation of the permeability distribution or histograms for each heterogeneous base model in log-space is varied while its mean value is fixed with the same geostatistical correlation properties in **Fig. 6.1** and **6.2** accordingly. As described in Chapter 5.2.1 (equation 5.3), this is used to linearly scale the distribution range and systematically vary its degree of heterogeneity to generate its corresponding less heterogeneous realizations. The generated realizations or models for 2D and 3D are presented in **Fig. 6.3** and **6.4** respectively in terms of the standard deviation of their permeability distribution in log-space, σ_f. These are normalized by the standard deviation of the underlying normal distribution for the reference or base (heterogeneous) model – equation (5.3). $0 \leq \sigma_f \leq 1$: $\sigma_f = 1$ for the base model, and $\sigma_f = 0$ for its homogeneous equivalence.

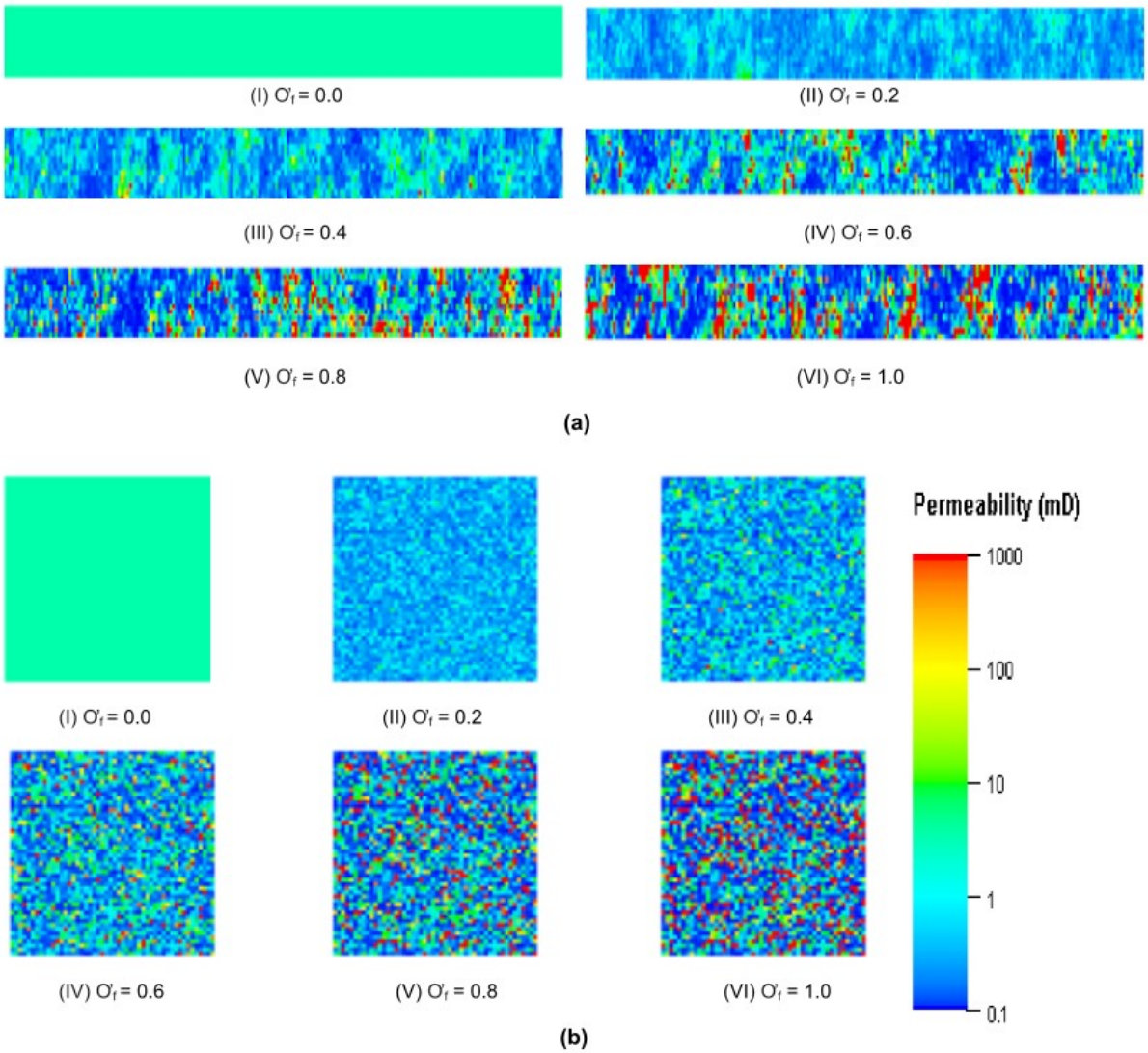


Fig. 6.3: 2D heterogeneous realizations considered for each well pattern: characterized in terms of a normalized standard deviation, σ_f, which is the ratio of the actual standard deviation of the distribution in log-space to that of the base model. (a) Line-drive (LD). (b) Quarter five-spot (Q5S).

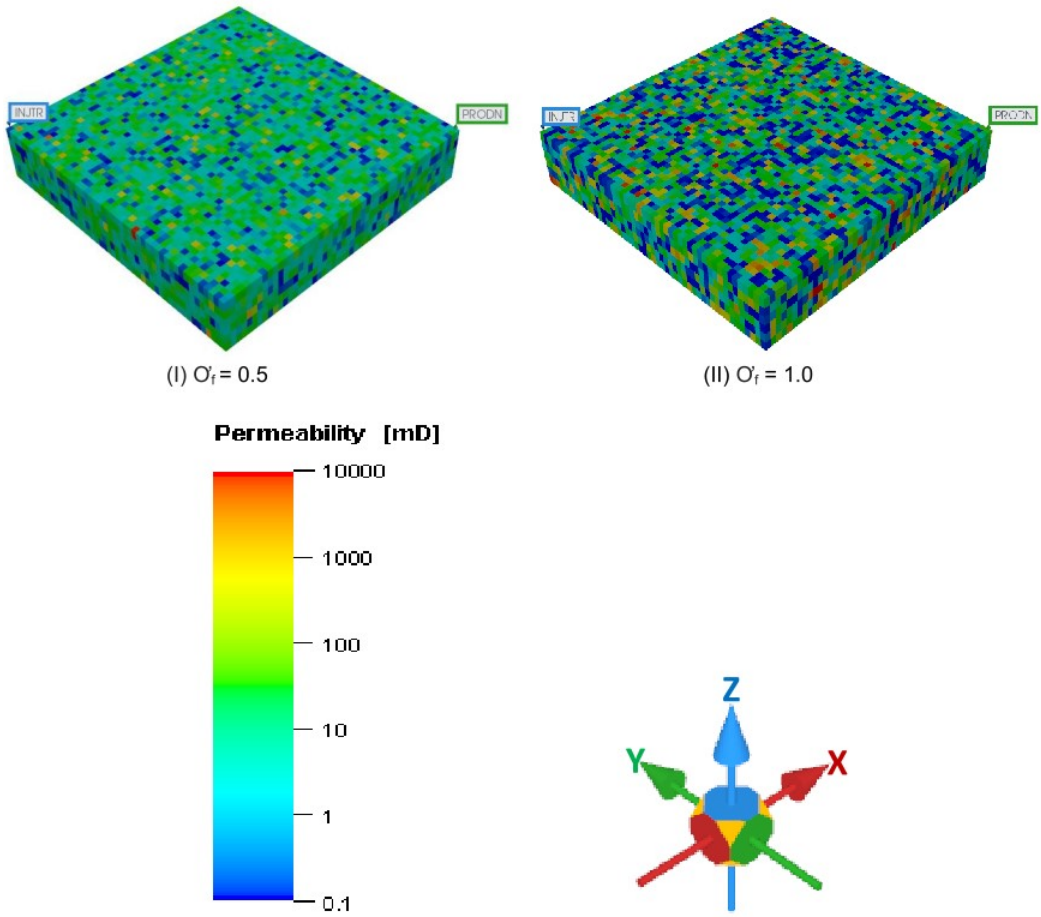


Fig. 6.4: 3D heterogeneous realizations considered under quarter five-spot (Q5S) well pattern: characterized in terms of a normalized standard deviation, σ_f, which is the ratio of the actual standard deviation of the distribution in log-space to that of the heterogeneous base model.

The correlation length (or range) is presented as a fraction of the system size (reservoir dimension) in its direction; and this normalized value (R) is considered equal for the coordinate directions. For the base geostatistical correlation of $R = 0.033$ (**Fig. 6.1** and **6.2**), this represents a correlation length or range of approximately 2-3 grid-blocks – hence, shows little (or no) correlation with indifferent spatial property distribution across variogram models. To capture the uncertainty in a geological model, we construct one hundred and one permeability realizations – honouring the geological constraints – with the same geostatistical correlation. The correlation length is varied within the range $0.033 \leq R \leq 0.4$ under conditions of exponential and Gaussian variogram models separately to characterize more heterogeneities. As discussed in Chapter 2.7.2, the correlation length (or variogram range) is a good geostatistical parameter to characterize reservoir continuity or connectivity in a specified direction under heterogeneous property considerations. Furthermore, both the Gaussian and exponential variograms are utilized as they represent the boundary (or extreme) levels of heterogeneity or spatial property variation within a correlation distance.

On the other hand, the mobility functions including relative permeabilities for both high- and low-salinity brines as well as capillary pressure effect remain as defined previously in Chapter 5.2.1 (**Fig. 5.2**). For the 3D models, the water density is kept constant for both LS and HS brines as density differences resulting from practical salinity variations have negligible effects on the vertical water-oil displacement (Attar and Muggeridge, 2018). We also confirmed this through simulations in vertical models with and without density difference for the brines which are not reported here.

The LD well pattern is considered with the horizontal injector and producer placed and completed along the opposite faces of the 2D models in the X-direction. The Q5S well pattern for the 2D and 3D models has the injector and producer placed at the upper-left and lower-right edges (i.e. grids) respectively and completed along all the layers. Injection and production rates are constant and equal for each combination of model and flood pattern. All simulations were performed with the CMG STARS commercial simulator: the numerical method and time-stepping are as adopted previously for the preceding investigation in Chapter 5. The grid resolutions were described in **Table 6.1**. The control of dispersion to desired levels of representative mixing was discussed earlier in Section 5.2.2 for the 2D LD models. For the Q5S grid resolutions introduced in this chapter, modifications to control dispersion in their simulations are presented below.

The flow variables in this chapter – physical longitudinal and transverse dispersivities, upper (maximum) salinity threshold, and residual oil saturation to LSE – are as defined earlier in Chapter 5.2.2 (**Table 5.2**). As adopted in Chapter 5, the lower salinity threshold is fixed at 1,000 ppm in all simulations. The injected and connate brine salinities are also set at 1,000 ppm and 30,000 ppm respectively. However, for the new 2D-areal and 3D Q5S models, the constant numerical (diffusivity) component at the these grid resolutions ($\Delta X = \Delta Y = 3.04\,m$ and $\Delta X = \Delta Y = \Delta Z = 3.04\,m$ respectively), $D_{L,num}$, gives a numerical Peclet number (*Pe*) of 200 or 0.5% of the model-length L using the formulas: $D_{L,num} = \frac{1}{L}\left(\frac{\Delta X}{2} + v\frac{\Delta t}{2}\right)$ and $Pe = \frac{1}{D_{L,num}}$, equations (2.10) and (2.15) respectively. Therefore, additional input physical longitudinal dispersivity (α_l) range of $4.60 - 13.70\,m$ is set to model the advective longitudinal component (equation 2.13) to obtain a total Peclet number (*Pe*) range of 2 – 5% of the model-length L as considered for the 2D LD models in Chapter 5. This gives a transverse dispersivity (α_t) range of $0.15 - 0.45\,m$ (i.e. $\alpha_t \cong \alpha_l/30$) to model the advective transverse component (equation 2.14) – with a base input value of 0. These values are summarized in **Table 6.2**. The LS slug performance is assessed with the total and marginal slug efficiencies discussed in Chapter 5.2.2, in addition to the total and/or incremental recovery from low-salinity water injection.

Table 6.2: Summary of the variables used in the simulations in this chapter.

Variable (unit)	**Base value**	**Reported range**	**Input population distribution**	
			Statistical moments	*Distribution*
Upper salinity threshold (ppm)	7,000	3,000 – 10,000	Mean: 6,575 Standard deviation: 1,480	Normal
Longitudinal dispersivity: LD: $\boldsymbol{\alpha_l}$ $(\boldsymbol{m})$ ($\boldsymbol{Pe}$, % of the system length)	0	5.40 – 14.50 (2 – 5%)	Mean: 9.20 m (3.25 %) Standard deviation: 1.97 m (0.645 %)	Normal
Q5S: $\boldsymbol{\alpha_l}$ $(\boldsymbol{m})$ ($\boldsymbol{Pe}$, % of the system length)	0	4.60 – 13.70 (2 – 5%)	Mean: 8.40 m (3.25 %) Standard deviation: 1.97 m (0.645 %)	Normal
Transverse dispersivity, $\boldsymbol{\alpha_t}$ $(\boldsymbol{m})$	0	$\alpha_l/30$		
Residual oil saturation to LSE	0.2		Range: 0.15 – 0.24	Uniform

The same procedure to quantify LS slug performance uncertainty and optimize its injection design described in Chapter 5.2.3 is adopted in this chapter. In summary, this involves: (i) Optimization of the injected slug for total efficiency with the Designed Exploration and Controlled Evolution (DECE) and Latin Hypercube Plus Proxy techniques to estimate the stability-threshold size at the base realization; (ii) Sensitivity evaluation of recovery to the flow variables at the threshold slug size to examine the gross and net effects of each variable; and (iii) Performance uncertainty quantification with experimental design and response surface generation (or proxy modelling) methods.

Due to the high computational cost of LSWF simulations, it is impractical to use all the permeability realizations at a characterized (geostatistical) degree of heterogeneity to quantify the uncertainty in slug performance. We therefore present a robust optimization process similar to that of Yang et al. (2011) introduced in Chapter 3.3.2. It is a practical approach that can reduce computational cost significantly and still account for the overall geological uncertainty of the model. This is achieved by first ranking the entire set of geological realizations using their recovery performance at the stability-threshold slug injection for the (corresponding) base model. A small set of eleven representative realizations that span the entire ranked performance distribution is then selected to use for the performance uncertainty quantification.

6.3 Results

6.3.1 2D Models

6.3.1.1 Nominal Slug Performance Under Inter-well Homogeneity

The influence of LS injection start-time on slug performance and the effective displacement mode is examined in a Q5S flood pattern relative to the LD pattern described in Chapter 5.3.1. The incremental recovery (relative to an equivalence high-salinity resident brine injection) from the homogeneous models of **Fig. 6.3** at different injected slug sizes and injection start-times is considered after a cumulative water injection (LS slug + high-salinity resident brine) of 2.0 PV. These are evaluated at the base values of the flow variables on **Table 6.2**. The water cut profiles of a 0.35 PV injected slug size, for example, at different injection times is compared between the LD and Q5S well patterns in **Fig. 6.5**.

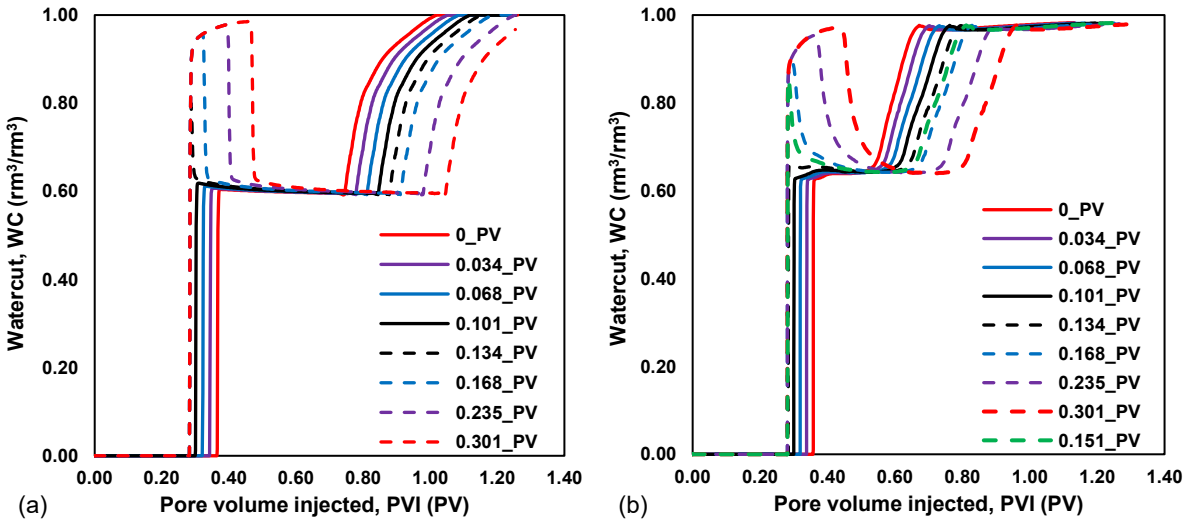


Fig. 6.5: Watercut (WC) as a function of cumulative pore volumes injected (PVI) in a LSWF of 0.35 PV slug size injected after pre-injecting different volumes (PV) of HS formation water with different flood patterns. (a) Line-drive. (b) Quarter five-spot. No oil banking (tertiary-mode displacement) commences till after pre-injecting at least 0.101 PV HS water for both well arrangements.

We observe that the secondary-mode displacement (i.e. formation of a connate water bank) extends beyond an immediate LS injection regardless of the flood pattern (or well arrangement). Despite its higher base dispersion, Q5S shows further extension of the secondary-mode displacement with delayed LS injection – until about 0.151 PV pre-injected HS brine, compared to LD – of about 0.134 PV pre-injected HS brine. It is suggested that the reduced flow area around the injector in Q5S limits the early exposure of injected slug to physical mixing thereby sustaining its LS displacement stability further. However, this does not always translate into better slug performance as we show later in this chapter. The flood fronts – with stable inter-well displacement of the slug – are presented in **Fig. 6.6**,

highlighting the effective displacement mode at different LS injection start-times in a Q5S pattern. A similar trend of the secondary-mode displacement extending beyond an immediate LS injection was shown earlier in **Fig. 5.8** for a LD flood pattern.

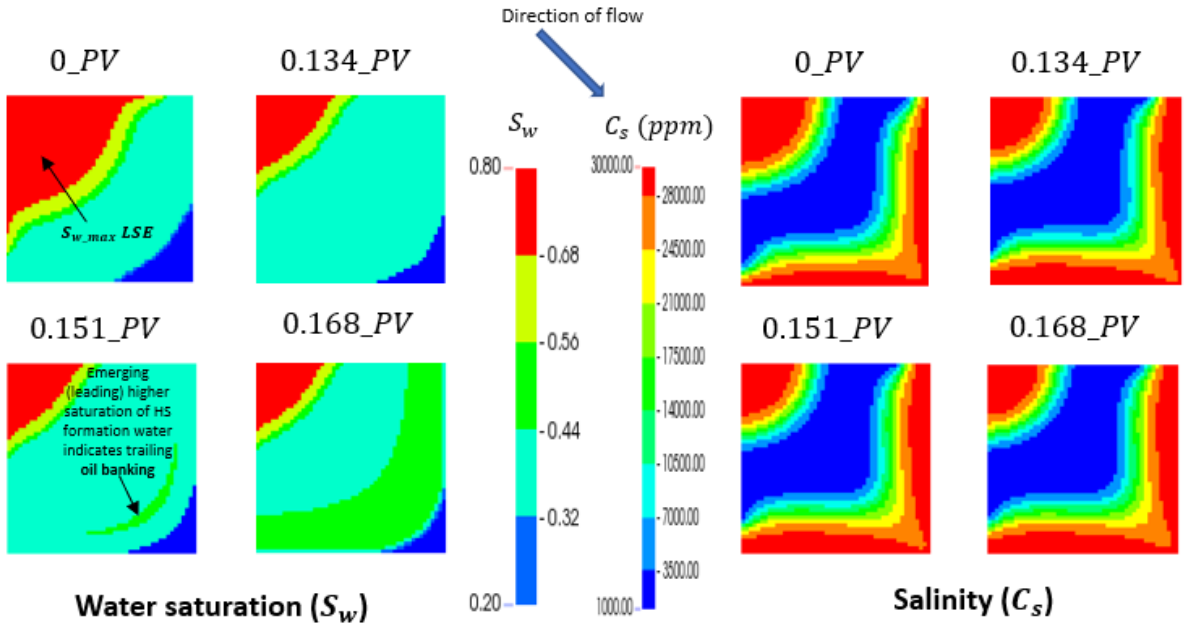


Fig. 6.6: Water saturation and salinity distributions just before breakthrough of a 0.35 PV LS-slug size injected after pre-injecting different volumes (PV) of HS formation water showing the effective displacement mode in a Q5S flood pattern. No oil banking appears till about 0.151 PV HS water has been pre-injected. The salinity distribution indicates a stable inter-well LS displacement of the injected slug at all the injection start-times for the level of dispersion considered.

Fig. 6.7 presents the incremental recovery as a function of the start-time of LS water injection for different injected slug sizes. Early or immediate LS injection generally favours recovery irrespective of the flood pattern. The Q5S case requires a larger optimal slug size because of the higher (inherent) dispersion considered. Regardless of this, the incremental recovery is sensitive to LS injection start-time at the cumulative water injection considered even for secondary-mode displacement. This contrasts with the LD pattern where the incremental recovery and the optimal slug size are insensitive to LS injection start-time until tertiary-mode displacement becomes established, as discussed in Chapter 5. It indicates that flood or well pattern influences performance sensitivity to LS injection start-time. However, the uncertainty in the effect of physical mixing from the flow variables has not been considered yet.

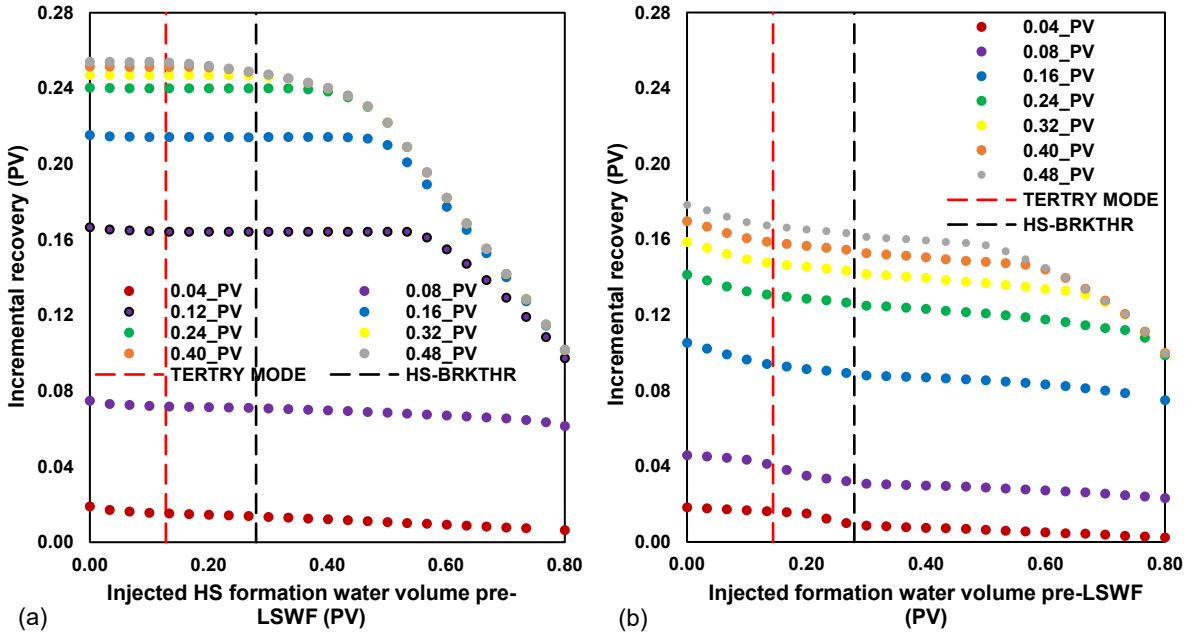


Fig. 6.7: Incremental recovery as a function of initialization times of LS water injection at different injected slug sizes (PV) for the homogeneous case under different flood patterns. (a) Line-drive. (b) Quarter five-spot. The commencements of tertiary-mode displacement (*red dashed line*) and the breakthrough of earlier injected HS brine (*black dashed line*) are also shown.

6.3.1.2 Slug Performance Under Inter-well Homogeneity Considering Uncertainty

The uncertainty in LS slug performance for the homogeneous case is now assessed with the Q5S flood pattern at different slug sizes and injection start-times. This is evaluated relative to that for the LD pattern described in Chapter 5.3.1. The variables are as defined in **Table 6.2**.

The stochastic moments of the performance distributions are presented as a function of injected slug sizes for both well patterns in **Fig. 6.8**. Injected LS slug shows better efficiency at small sizes in Q5S (**Fig. 6.8**d) compared to LD (**Fig. 6.8**b). This is because, at those sizes, its effective exposure to physical mixing is limited by the reduced flow area around the injector in Q5S which sustains its LS displacement further. However, this delayed impact of mixing renders large slug sizes less efficient in Q5S. Optimal and stability-threshold sizes of at least 1.0 PV and 0.2 PV respectively are estimated for LS slug injection under Q5S considering the flow uncertainties (**Fig. 6.8**c and d). For the LD case, these were evaluated earlier in Chapter 5.3.1 as 0.8 PV and about 0.44 PV respectively (re-presented here as **Fig. 6.8**a and b).

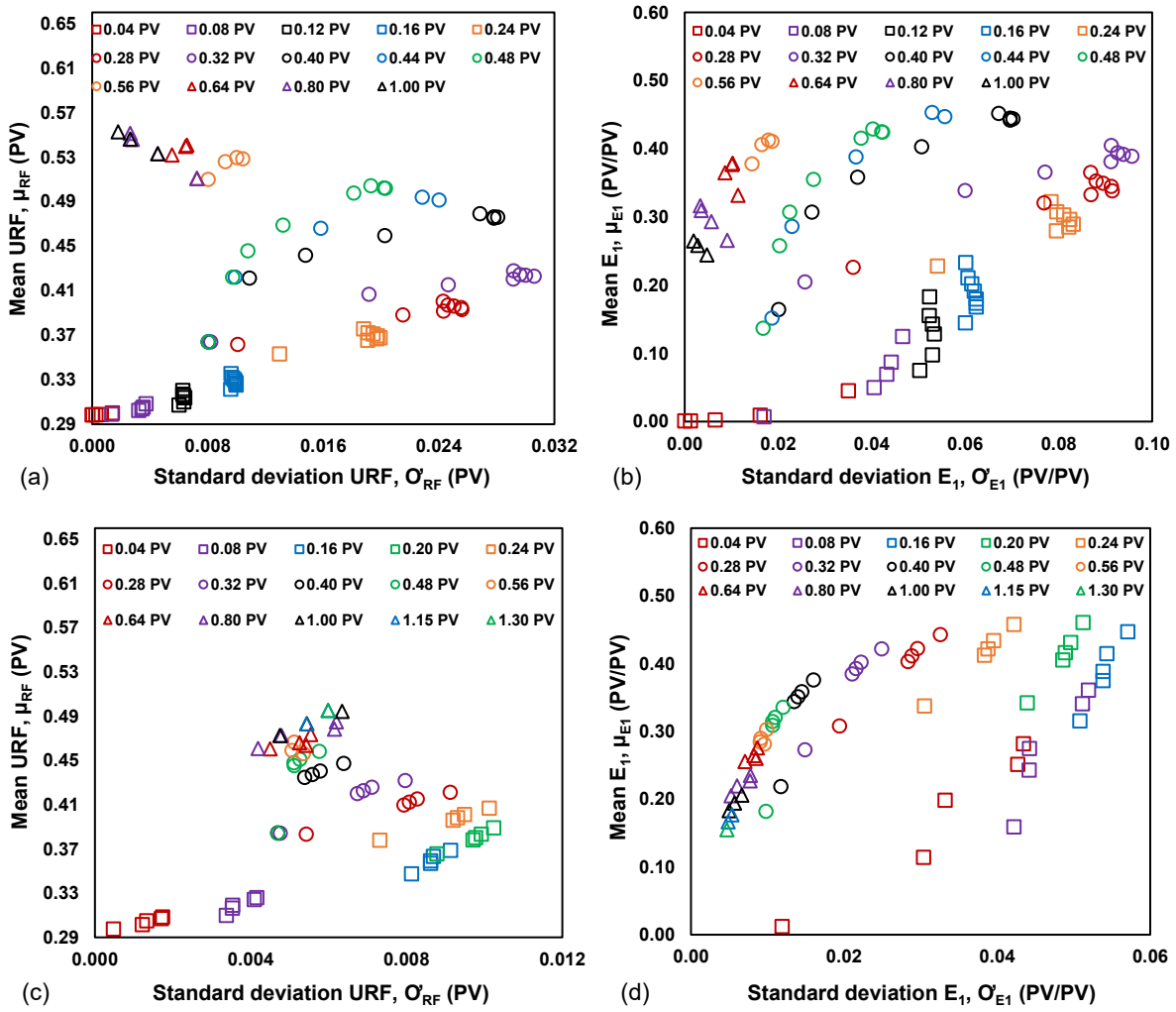


Fig. 6.8: Statistical moments of performance distributions at different injected slug sizes (PV). For LD: (a) Mean of total recovery as a function of standard deviation. (b) Mean of total efficiency as a function of standard deviation. For Q5S: (c) Mean of total recovery as a function of standard deviation. (d) Mean of total efficiency as a function of standard deviation.

Fig. 6.8 is replotted in **Fig. 6.9** and **Fig. 6.10** in terms of LS injection start-times – after pre-injecting different volumes of HS formation water, and relative to the breakthrough of pre-injected HS formation water respectively. Early or immediate slug injection favours recovery and the associated risk under uncertainty for both well arrangements as illustrated in **Fig. 6.9**. The sensitivities of mean performance and the optimal slug size to LS injection start-time are observed to be pronounced in Q5S regardless of the displacement mode (**Fig. 6.10**c and d). Whereas for the LD case (**Fig. 6.10**a and b), they are less sensitive to the LS injection start-time until around the breakthrough of the pre-injected HS formation brine.

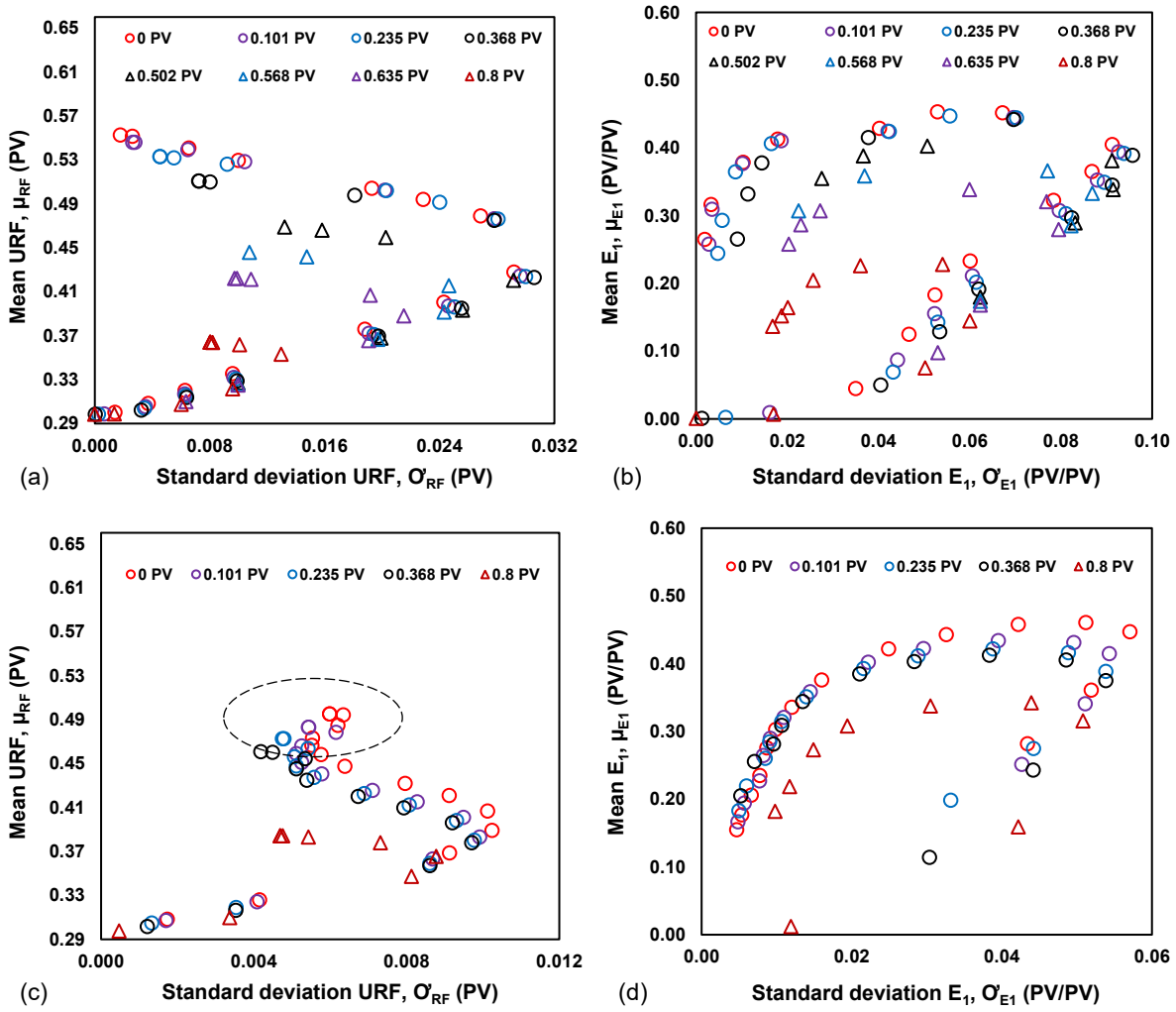


Fig. 6.9: Statistical moments of performance distributions at different LS injection times after pre-injecting different volumes (PV) of high-salinity formation water. For LD: (a) Mean of total recovery as a function of standard deviation. (b) Mean of total efficiency as a function of standard deviation. For Q5S: (c) Mean of total recovery as a function of standard deviation showing an increase in σ'_{RF} at large slug sizes (inset *black dashed region*). (d) Mean of total efficiency as a function of standard deviation.

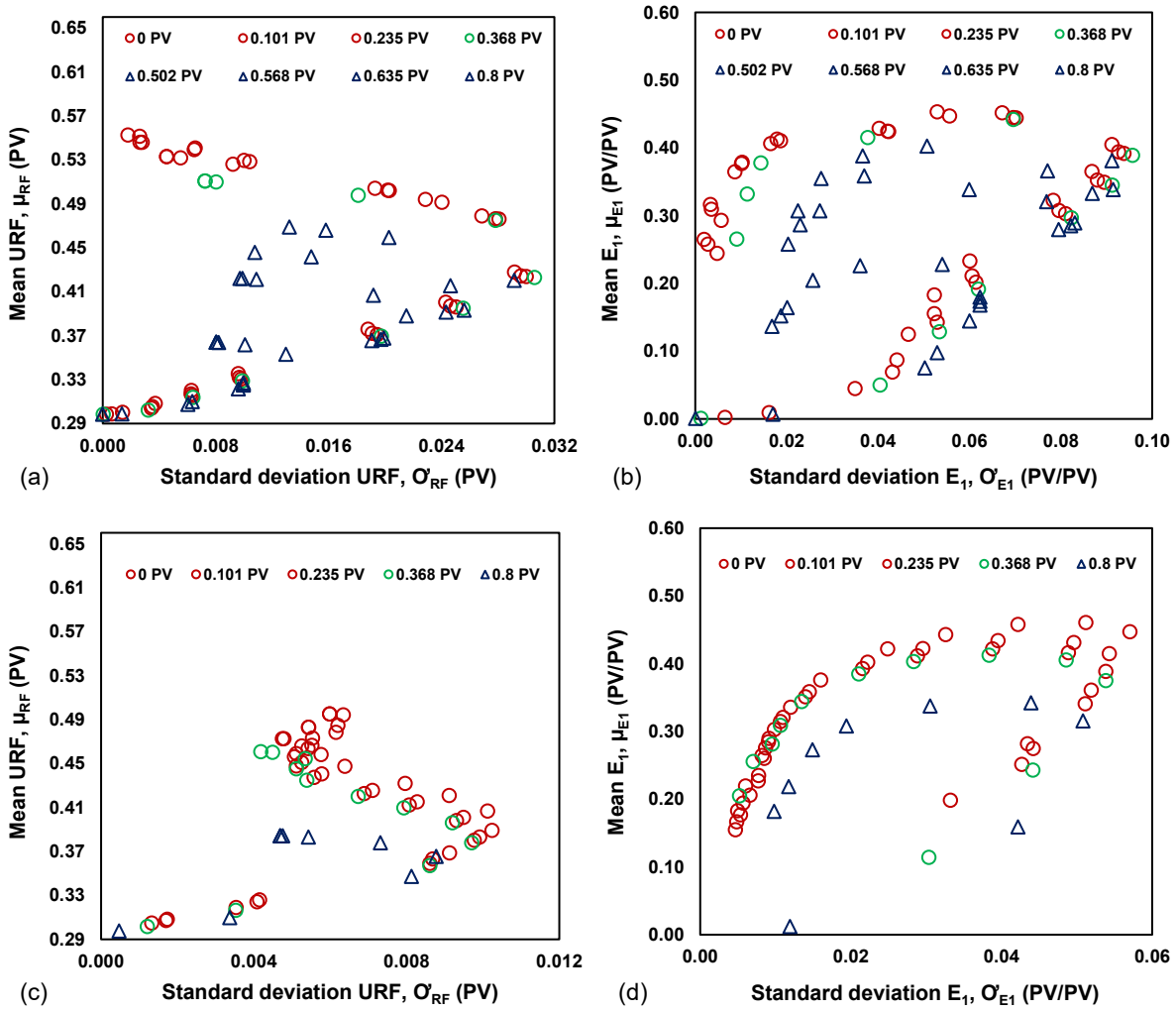


Fig. 6.10: Statistical moments of performance distributions at different LS injection times relative to the breakthrough of any pre-injected high-salinity formation water (*red* pre-breakthrough, *green* around breakthrough, *blue* post-breakthrough). For LD: (a) Mean of total recovery as a function of standard deviation. (b) Mean of total efficiency as a function of standard deviation. For Q5S: (c) Mean of total recovery as a function of standard deviation. (d) Mean of total efficiency as a function of standard deviation.

In contrast to the initial increase then decrease in σ'_{E1} or σ'_{RF} for each LS injection start-time as a function of slug sizes associated with LD, an increase in σ'_{RF} at large slug sizes is observed for Q5S (**Fig. 6.9** and **Fig. 6.10**). This behaviour indicates a delayed localized influence of transverse dispersion around the 'unswept' regions at these sizes in a Q5S pattern. This is because the slugs are stable enough to reach those regions during displacement thereby getting exposed to possible late-time transverse mixing. For the Q5S case in **Fig. 6.8**, σ'_{E1} or σ'_{RF} largely decreases if injection of the LS slug is delayed even at sizes post the stability-threshold relative to LD. Therefore, as discussed previously in Chapter 5.3.1, this trend basically shows that LS displacement is generally unstable with delayed injections in Q5S compared to LD.

6.3.1.3 Sensitivity of Optimal Slug Injection to Inter-well Heterogeneity

The nominal (base) slug performance for the 2D models in **Fig. 6.3** is presented in **Fig. 6.11** as a function of injected sizes. This is evaluated with immediate slug injection at a cumulative water injection of 2.0 PV. The performance is seen to be sensitive to heterogeneity for both well patterns (**Fig. 6.11**a and d). The optimal slug size increases with heterogeneity for LD – 0.4 PV (for $\sigma_f = 0.0$) to 0.8 PV (for $\sigma_f = 1.0$) – at a decreasing recovery performance (**Fig. 6.11**a and c). It remains insensitive to heterogeneity for Q5S – about 1.0 PV – also at a decreasing performance (**Fig. 6.11**d and f). Nevertheless, the maximum total efficiency generally decreases with heterogeneity for an increasing threshold slug size for both well patterns (**Fig. 6.11**b and e). This also reflects a decreasing LS displacement stability and slug performance with heterogeneity under both flood patterns.

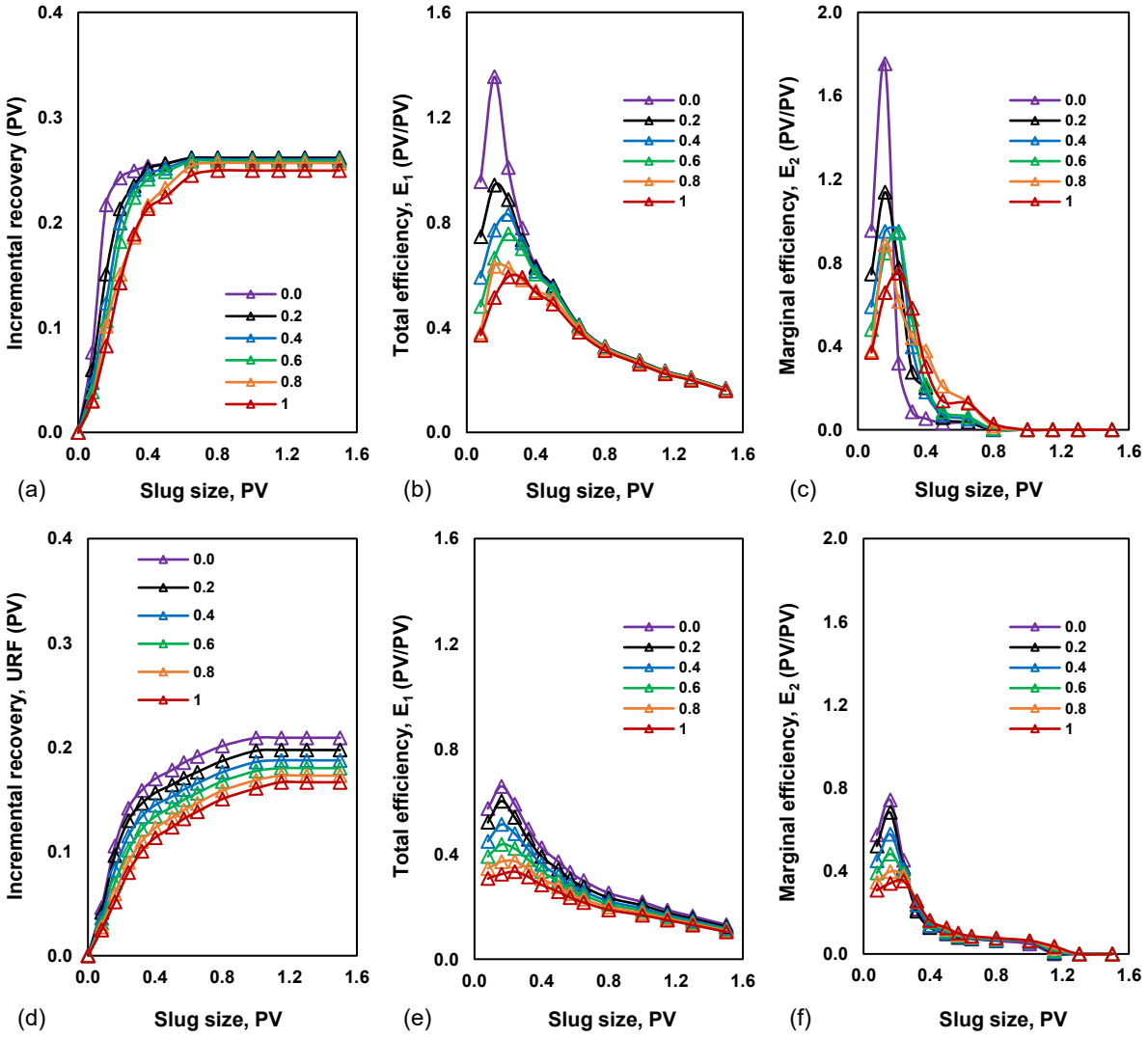


Fig. 6.11: Base performance as a function of injected slug size at different degrees of heterogeneity ($0.0 \leq \sigma_f \leq 1$: *purple* $\sigma_f = 0.0$, *black* $\sigma_f = 0.2$, *blue* $\sigma_f = 0.4$, *green* $\sigma_f = 0.6$, *orange* $\sigma_f = 0.8$, *red* $\sigma_f = 1.0$). For LD: (a) Incremental recovery. (b) Total efficiency. (c) Marginal efficiency. For Q5S: (d) Incremental recovery. (e) Total efficiency. (f) Marginal efficiency.

The DECE and LH Plus Proxy optimization techniques discussed in Chapter 3.3.2 are used to estimate the stability-threshold slugs for the Q5S models to evaluate their performance sensitivities to the flow variables. As shown in Chapter 5.3.2 for LD pattern (**Fig. 6.12**a and b), the decreasing sensitivity of slug performance to physical dispersivity with heterogeneity persists under Q5S (**Fig. 6.12**c and d). A similar trend of high sensitivity of recovery to upper or maximum salinity threshold in heterogeneous models is seen for both well patterns. In addition, some favourable sensitivity of recovery to physical dispersivity is observed in some heterogenous models for Q5S ($0.80 \leq \sigma_f \leq 1.00$) indicating active transverse dispersion in areal heterogeneity (**Fig. 6.12**d).

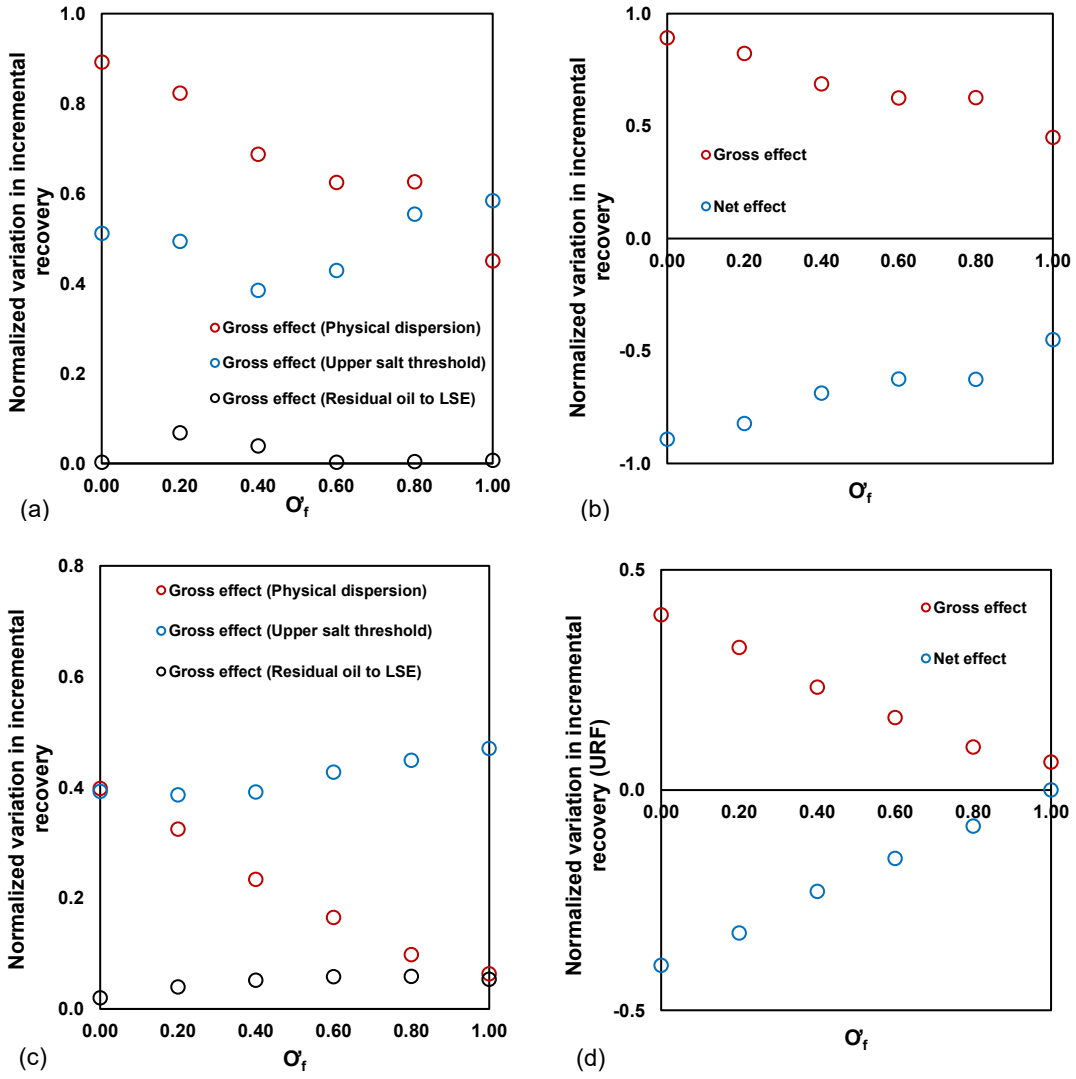


Fig. 6.12: Sensitivity of slug performance and recovery to flow variables as a function of heterogeneities. For LD: (a) Gross sensitivity to each parameter. (b) Gross and net sensitivities to physical dispersion. For Q5S: (c) Gross sensitivity to each parameter. (d) Gross and net sensitivities to physical dispersion. All variations are normalized with the base performance.

The favourable influence of transverse dispersion is illustrated in **Fig. 6.13** which shows the performance sensitivity of the stability-threshold slug injection to only physical dispersion for the Q5S

pattern. A potential improvement in the LSE and recovery by (transverse) dispersion is observed in $\sigma_f \geq 0.8$ if compared to $0.4 \leq \sigma_f \leq 0.6$ where the LS displacement stability (i.e. spread of the threshold salinities: 1,000 – 7,000 ppm) and recovery (i.e. residual oil saturation) from the slug injection are impaired further with mixing for the range of dispersivity (*Pe*) considered. A similar (favourable) effect of transverse dispersion was presented earlier in **Fig. 5.21** for a LD flood pattern.

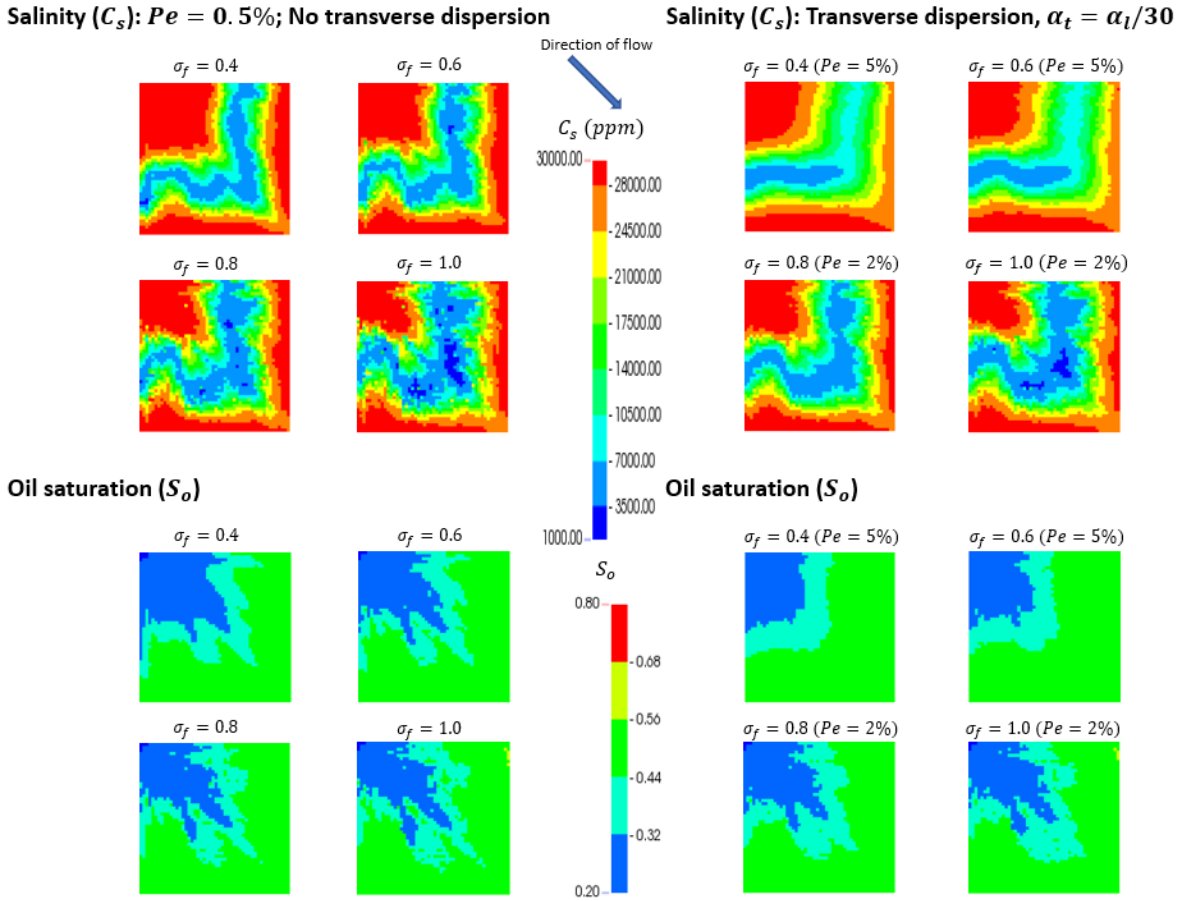


Fig. 6.13: Salinity and oil saturation distributions illustrating the favourable influence of transverse dispersion in areal heterogeneity on recovery in a Q5S flood pattern. The water salinity profile indicates the salinity-thresholds spread and LS displacement stability of the injected slug just at its breakthrough with the commencement of the HS push. The oil saturation distribution shows the recovery at the end of the flood – i.e. pre-injected LS slug + HS push.

The mean slug performance considering flow uncertainties is shown in **Fig. 6.14** for both flood patterns. In comparison to the base case, the mean performance remains sensitive to heterogeneity for Q5S (**Fig. 6.14**d) while it is rendered insensitive by flow uncertainties for LD (**Fig. 6.14**a). Meanwhile, the optimal and stability-threshold sizes for slug injection are insensitive to heterogeneity for both well patterns (**Fig. 6.14**b, c, e, and f). The optimal size is larger for Q5S – around 1.15 PV (**Fig. 6.14**f), with a smaller stability-threshold size – about 0.24 PV (**Fig. 6.14**e), compared to LD with 0.8 PV and 0.4 PV respectively (**Fig. 6.14**b and c). This indicates an extended range of target slug sizes to balance technical and financial performance for Q5S which may be a commercial and computational

disadvantage. The more- and less-efficient slugs at small and large (pre and post stability-threshold) sizes respectively, seen earlier under homogeneous condition for Q5S compared to LD, persist under inter-well heterogeneity (**Fig. 6.14**b and e). The reduced performance of the injected slug from the risk of physical mixing, where high efficiencies shift from small to moderate slug sizes indicating delayed improved recovery, decreases with heterogeneity in both well patterns (**Fig. 6.14**b, c, e, and f). This shows unfavourable dispersion at small slug sizes under the flow uncertainties irrespective of the flood pattern.

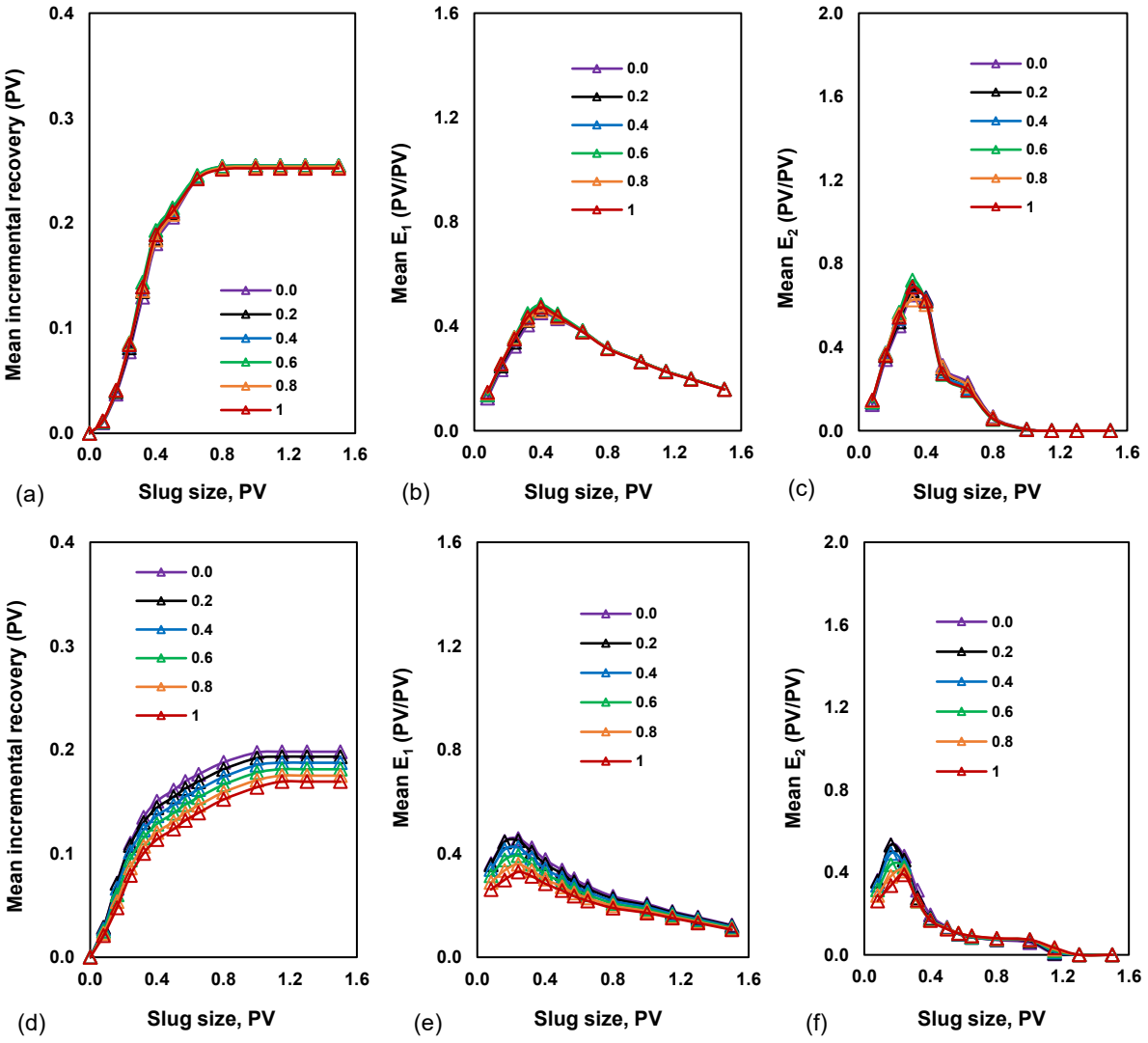


Fig. 6.14: Mean performance under flow uncertainties as a function of injected slug size at different degrees of heterogeneity ($0.0 \leq \sigma_f \leq 1$: *purple* $\sigma_f = 0.0$, *black* $\sigma_f = 0.2$, *blue* $\sigma_f = 0.4$, *green* $\sigma_f = 0.6$, *orange* $\sigma_f = 0.8$, *red* $\sigma_f = 1.0$). For LD: (a) Incremental recovery. (b) Total efficiency. (c) Marginal efficiency. For Q5S: (d) Incremental recovery. (e) Total efficiency. (f) Marginal efficiency.

The sensitivity of the LS displacement stability of the injected slug sizes to heterogeneity is presented in **Fig. 6.15**. Based on the trend of $\mathcal{O}'_{E1}$ or $\mathcal{O}'_{RF}$ with slug size and heterogeneity discussed in Chapter 5, LS displacement stability is seen to be generally sensitive to heterogeneity for both well patterns.

However, LS displacement is generally more stable in LD than Q5S as the former shows lower $\mathcal{O}_{E1}$ or $\mathcal{O}_{RF}$ especially at target slugs post the stability-thresholds and around the optimal sizes. The delayed localized influence of transverse dispersion at large slug sizes for Q5S persists under inter-well heterogeneity (**Fig. 6.15**c).

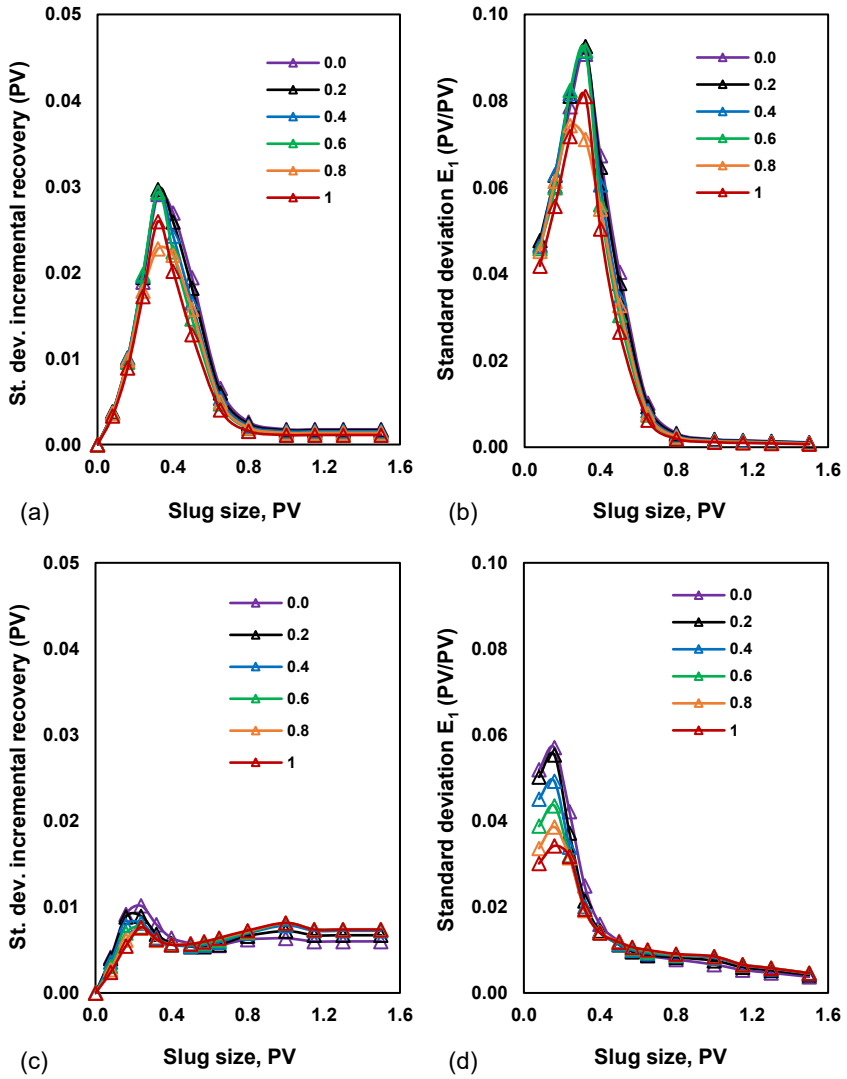


Fig. 6.15: Performance risks under flow uncertainties as a function of injected slug size at different degrees of heterogeneity ($0.0 \leq \sigma_f \leq 1$: *purple* $\sigma_f = 0.0$, *black* $\sigma_f = 0.2$, *blue* $\sigma_f = 0.4$, *green* $\sigma_f = 0.6$, *orange* $\sigma_f = 0.8$, *red* $\sigma_f = 1.0$). For LD: (a) Standard deviation of incremental recovery. (b) Standard deviation of total efficiency. For Q5S: (c) Standard deviation of incremental recovery. (d) Standard deviation of total efficiency.

6.3.1.4 Optimal Slug Injection Design Considering Geological Uncertainty

The impact of uncertainty in geological heterogeneity on the optimal injected amounts evaluated in the previous section is examined here. We evaluate the sensitivity of the slug performance, its optimal injection design, and the LS displacement stability to inter-well heterogeneity under geological uncertainty (GU). The geostatistical correlation properties of the 2D (heterogeneous) base models in **Fig. 6.3** (i.e. $R = 0.033$) are considered here and subsequently scaled up to more realistic descriptions in the next section.

In this thesis, the ranking method used is direct (numerical) reservoir simulation of the LSWF process in each of the (geostatistical) geological realizations. This method works by applying the nominal stability-threshold LS slug injection (i.e. using the base variable values in **Table 6.2**) at each base model and well pattern to its 101 realizations and running 101 simulations. The realizations are then ranked by the total recovery (ultimate recovery factor, URF) value from low to high. This is to ensure the ranking results are accurate, and the geological uncertainties are adequately represented by a small set of realizations whose simulation runs, compared to multiples of hundreds, are now insignificant. The 11 realizations with the 0^{th}, 10^{th}, 20^{th}, 30^{th}, 40^{th}, 50^{th}, 60^{th}, 70^{th}, 80^{th}, 90^{th}, and 100^{th} percentiles of the URF are selected as the representative realizations to quantify the slug performance uncertainty.

Table 6.3 compares the statistics of the computed URF from both case-simulations – 101 realizations and 11 realizations, for the base heterogeneous model, $R = 0.033$, of each well pattern. The comparison shows that the mean is almost identical while the standard deviation is close to each other. This indicates that the 11 representative realizations selected in this thesis are sufficient to estimate reliable statistics of the entire 101 realizations ranked for this method. As discussed in Chapter 3.3.2, larger sample sizes could also be adopted to rank and/or select (representative) realizations to assess geological uncertainty depending on available computational limitations. Some of the random geological realizations considered for the base heterogeneous models of the well arrangements are presented in **Fig. 6.16**.

Table 6.3: Mean and standard deviation of the computed ultimate recovery factor, URF.

Flood pattern ($R = 0.033$)	**No. of realizations**	**URF statistics (PV)**	
		Mean	*Standard deviation*
Line-drive (LD)	101	0.4848	0.0148
	11	0.4834	0.0198
Quarter five-spot (Q5S)	101	0.3742	0.0049
	11	0.3741	0.0061

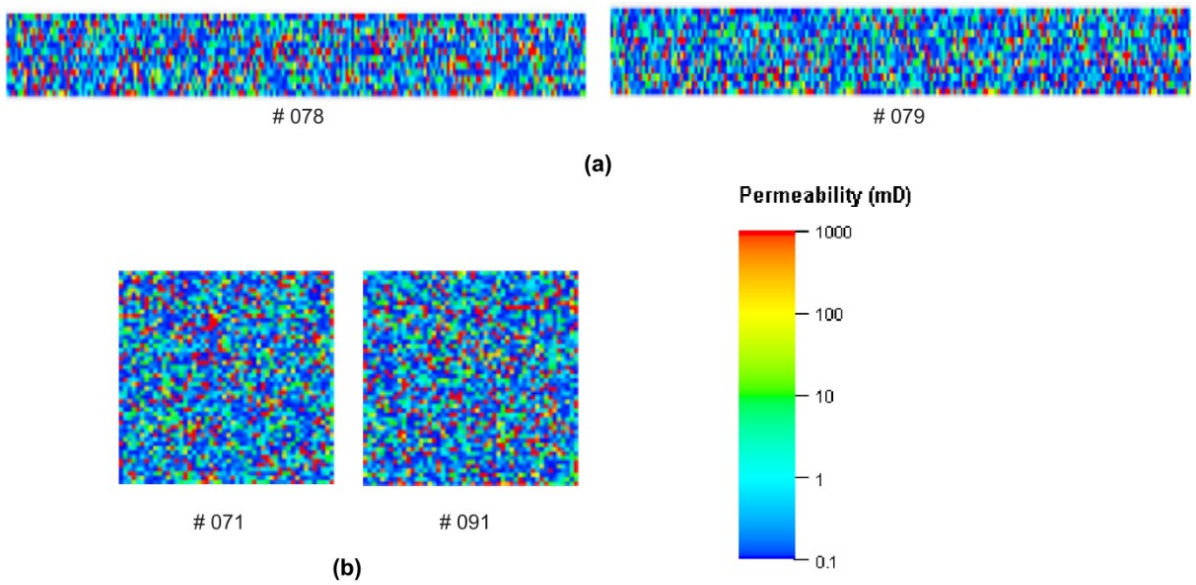


Fig. 6.16: Random geostatistical realizations (#) of spatial permeability distribution for inter-well heterogeneity at a normalized correlation length or range of $R = 0.033$ in both coordinate directions. (a) Line-drive. (b) Quarter five-spot.

The slug performance considering uncertainty in both physical mixing and geological heterogeneity is shown in **Fig. 6.17** for both flood patterns. For the LD case, the mean slug performance remains insensitive to heterogeneity (**Fig. 6.17**a). Its possible enhanced performance with heterogeneity observed at moderate slugs (especially 0.3 – 0.5 PV) under only flow uncertainties (PM) is impaired by geological uncertainty (GU). Meanwhile, despite the enhanced slug performance for Q5S under GU compared to without GU (PM), the mean performance decreases with heterogeneity (**Fig. 6.17**a). No substantial impact of geological uncertainty is seen on the optimal slug injection design – optimal and stability-threshold sizes – for both well patterns (**Fig. 6.17**b and c). The trend of more- and less-efficient slug at small and large sizes respectively for Q5S compared to LD remains under GU (**Fig. 6.17**b).

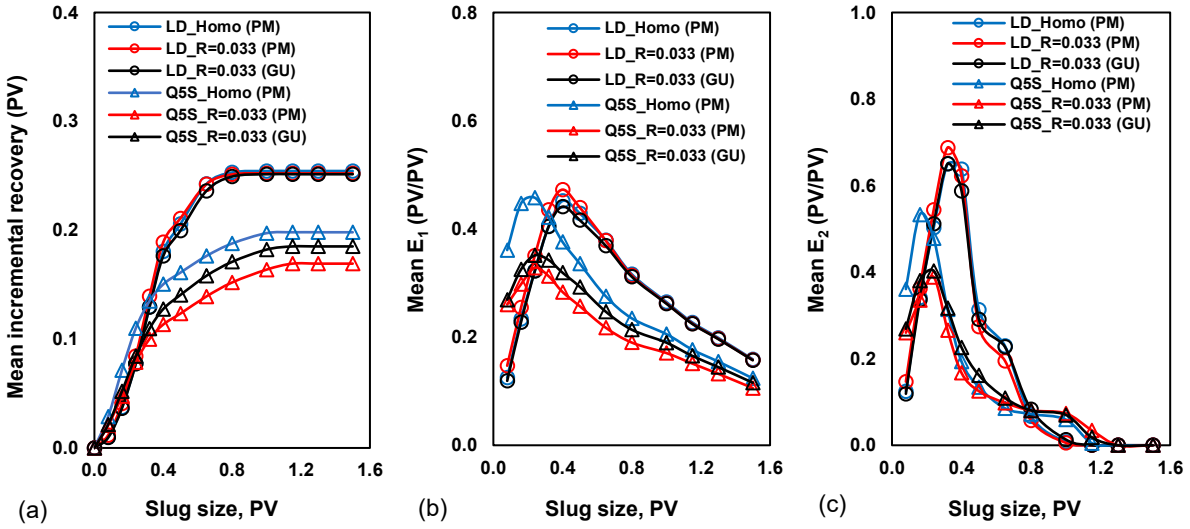


Fig. 6.17: Mean performance under only flow uncertainties (red PM) and in combination with geological uncertainty (black GU) as a function of injected slug size for the base heterogeneous case ($R = 0.033$) in comparison to the homogeneous equivalence (blue Homo) for both well patterns (*circle* LD, *triangle* Q5S). (a) Incremental recovery. (b) Total efficiency. (c) Marginal efficiency.

LS displacement stability remains sensitive to heterogeneity under GU for both well patterns – $\mathcal{O}'_{E1}$ or $\mathcal{O}'_{RF}$ generally either increases or decreases with heterogeneity (**Fig. 6.18**). Furthermore, unlike in Q5S, the sensitivity of the LS displacement stability to heterogeneity is evident only for slugs below and around the stability-threshold size in LD. Possible improved LS displacement stability with heterogeneity observed for LD at moderate slugs post the stability-threshold size without GU (PM) is stunted after considering GU. For Q5S, the LS displacement stability is improved for small slugs pre stability-threshold size under GU compared to without GU (PM). Whereas, the LS displacement stability is further impaired by GU in slugs post the stability-threshold size while delayed localized influence of transverse dispersion persists. LS displacement remains generally more stable in LD even under GU.

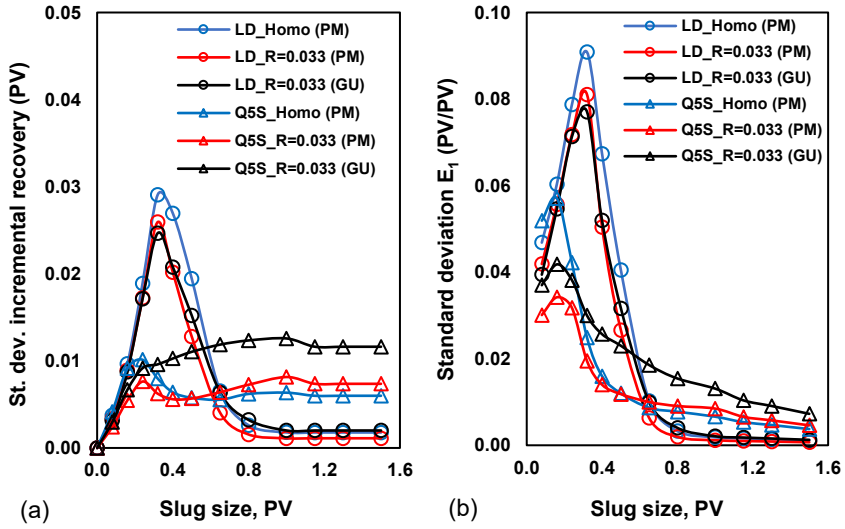


Fig. 6.18: Performance risks under only flow uncertainties (red PM) and in combination with geological uncertainty (black GU) as a function of injected slug size for the base heterogeneous case ($R = 0.033$) in comparison to the homogeneous equivalence (blue Homo) for both well patterns (*circle* LD, *triangle* Q5S). (a) Standard deviation of incremental recovery. (b) Standard deviation of total efficiency.

6.3.1.5 Optimal Slug Injection Design for More Representative Inter-well Heterogeneities

So far in this chapter, the optimal slug injection has been evaluated considering uncertainty in both the effect of inter-well physical mixing and geological heterogeneity. In this section, we examine the sensitivity of the optimal slug injection to more heterogeneous descriptions often seen in petroleum reservoirs. These are characterized with modified sets of the base geostatistical correlation properties in **Fig. 6.3** using larger correlation lengths – $0.033 < R \leq 0.4$, and different variogram models – exponential and Gaussian. The normalized correlation length is limited to $R < 0.5$ because higher values rather model the spatial continuity of a property back towards homogeneity in each realization (Isaaks and Srivastava, 1989; Deutsch and Journel, 1998; Lantuéjoul, 2002). Nonetheless, different realizations will vary significantly from each other. Again, both variogram models are chosen in this thesis because they present the extreme cases of variability in a property within a spatial correlation distance.

Fig. 6.19 shows the mean and standard deviation of the URF resulting from the base stability-threshold LS slug injection applied to the entire 101 realizations in comparison to the selected 11 representative realizations for each combination of well pattern and correlation length with the exponential variogram model. Similar statistics are achieved for both case-simulations. On the other hand, the statistics of the computed URF with the Gaussian variogram model are highlighted in **Fig. 6.20**. Similar statistics are also achieved for both cases. **Fig. 6.21** shows some of these heterogeneous realizations considered with their characteristic geostatistical correlation properties – normalized correlation length, R and variogram models – for both well patterns.

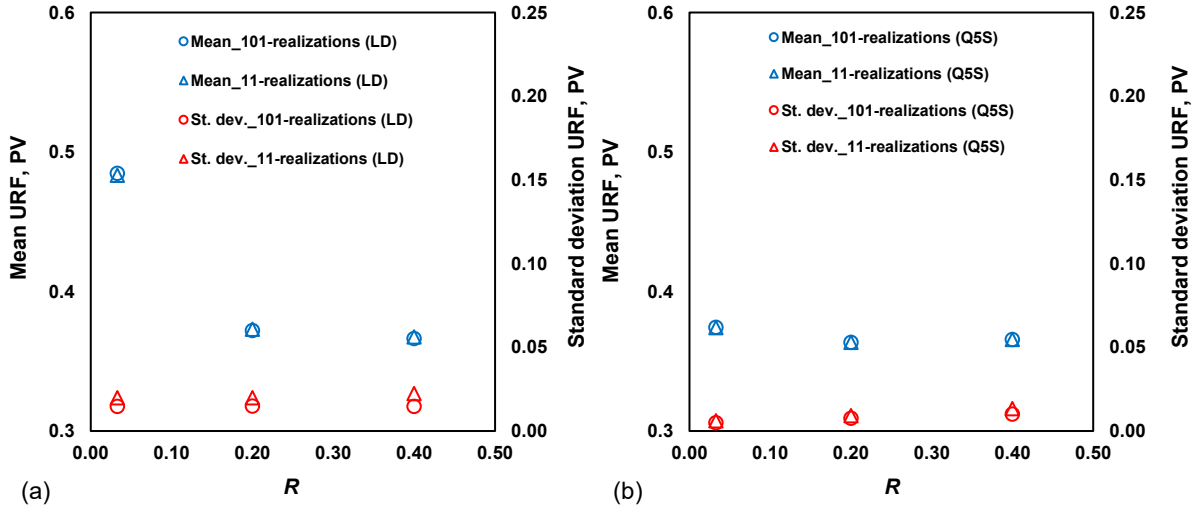


Fig. 6.19: Statistical moments of the computed ultimate recovery factor, URF, from both case-simulations as a function of normalized correlation length, R, for inter-well heterogeneity with an exponential variogram model. (a) Line-drive. (b) Quarter five-spot.

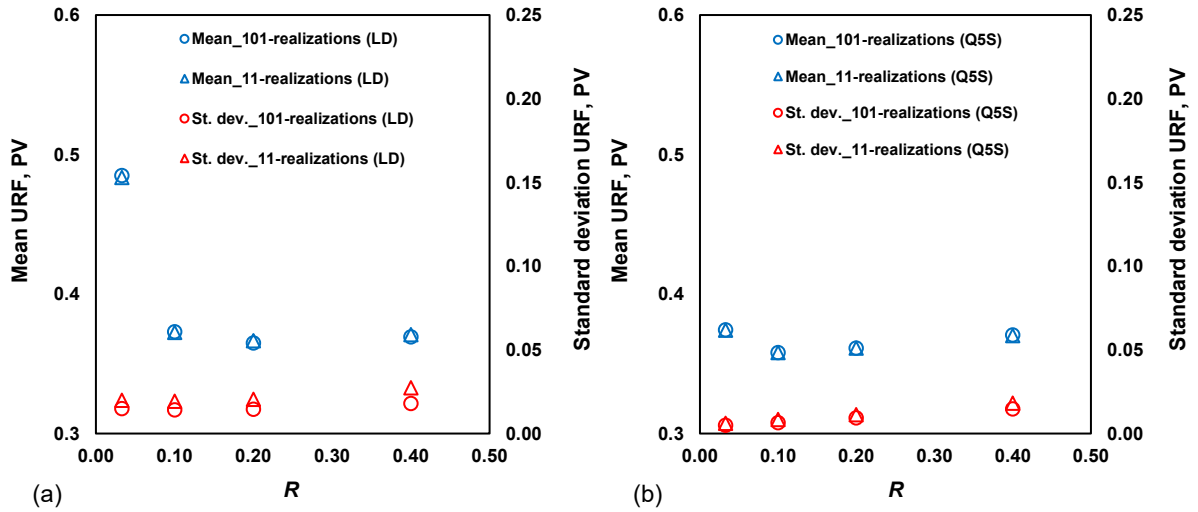
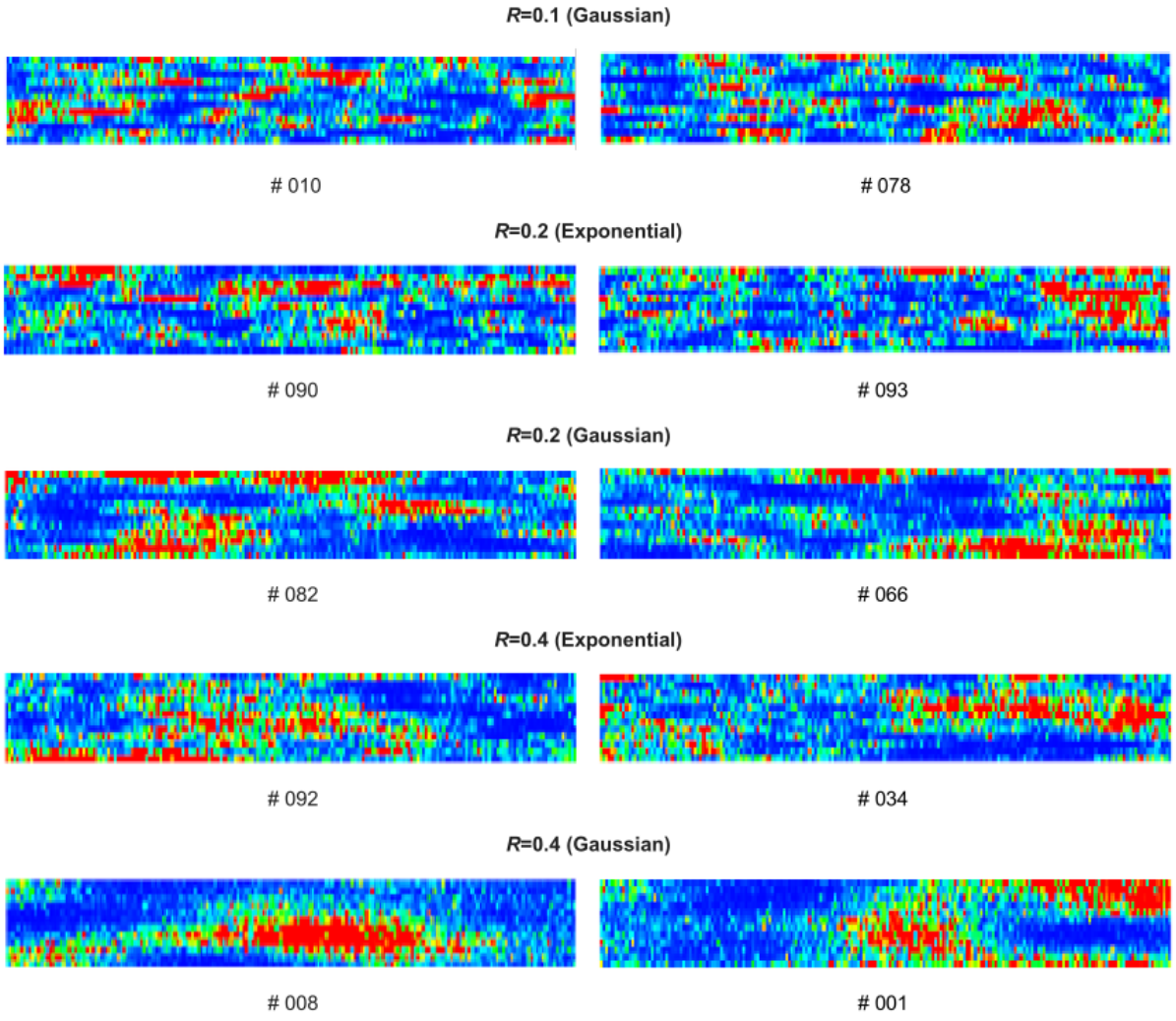


Fig. 6.20: Statistical moments of the computed ultimate recovery factor, URF, from both case-simulations as a function of normalized correlation length, R, for inter-well heterogeneity with a Gaussian variogram model. (a) Line-drive. (b) Quarter five-spot.


R=0.1 (Gaussian)
# 010
# 078
R=0.2 (Exponential)
# 090
# 093
R=0.2 (Gaussian)
# 082
# 066
R=0.4 (Exponential)
# 092
# 034
R=0.4 (Gaussian)
# 008
# 001

(a)

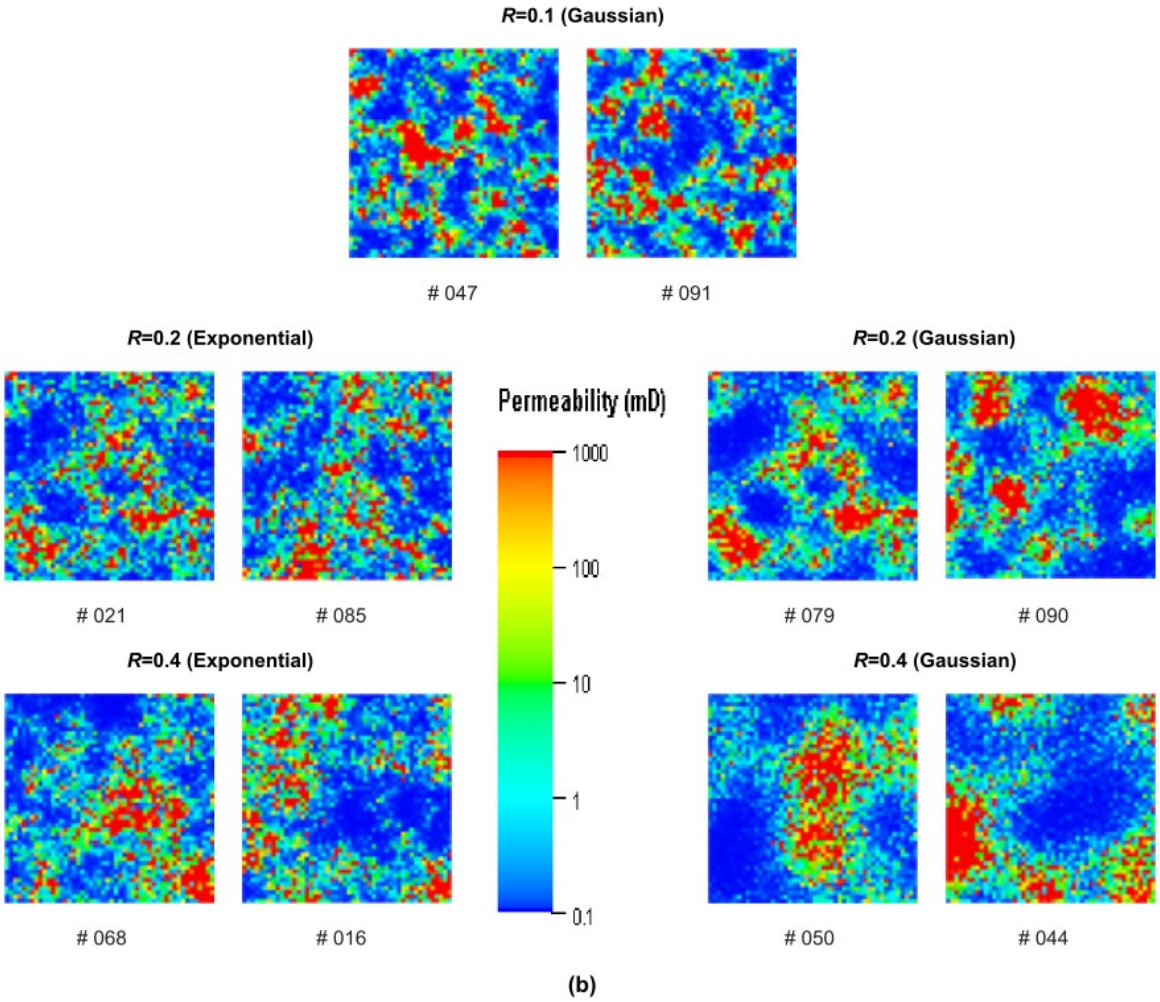


Fig. 6.21: Random geostatistical realizations (#) of spatial permeability distribution for inter-well heterogeneity at different normalized correlation lengths, R, and variogram models – exponential and Gaussian. (a) Line-drive. (b) Quarter five-spot.

The slug performance considering uncertainty in both physical mixing and geological heterogeneity is shown in **Fig. 6.22** for the exponential variogram model. Mean slug performance generally decreases with heterogeneity and R for both flood patterns (**Fig. 6.22**a and d). The optimal slug design for LD now shows sensitivity to heterogeneity but insensitive to R – stability-threshold and optimal sizes increase to about 0.65 PV and 1.15 PV respectively, which are the same for $R = 0.2$ and $R = 0.4$ (**Fig. 6.22**b and c). For Q5S (**Fig. 6.22**e and f), the optimal slug design remains insensitive to heterogeneity and R – stability-threshold and optimal sizes of approximately 0.24 PV and 1.15 PV respectively. An enhanced slug efficiency pre stability-threshold size is observed at $R = 0.4$ relative to $R = 0.2$ for Q5S (**Fig. 6.22**e). We link this to improved displacement from possible greater spatial continuity in permeability at large Rs in addition to the reduced flow area of those slugs around the injector. The trend of more- and less-efficient slug at small and large sizes respectively for Q5S compared to LD remains for all the Rs.

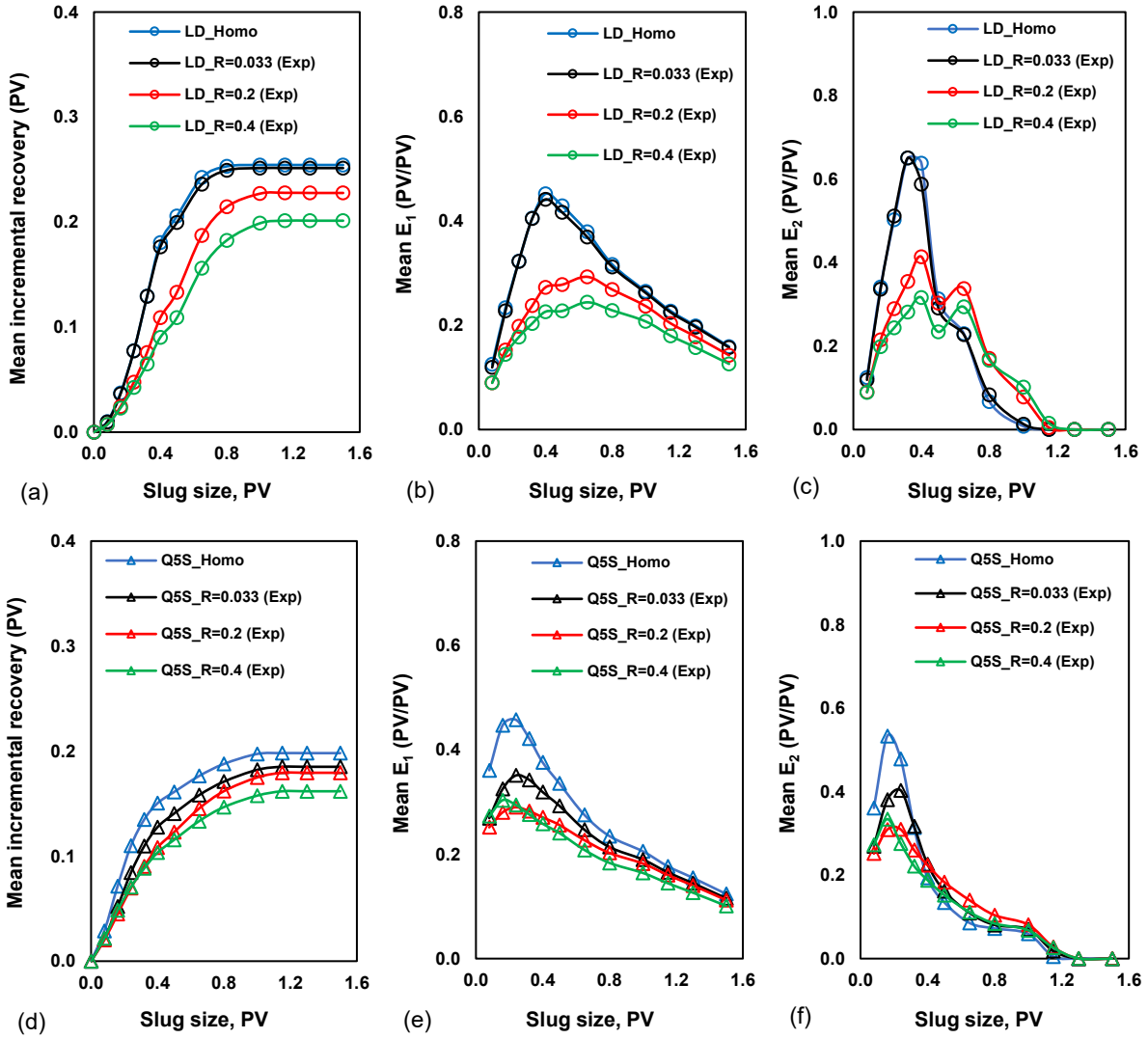


Fig. 6.22: Mean performance as a function of injected slug size for inter-well heterogeneity with an exponential variogram model at different correlation lengths (*black* $R = 0.033$, *red* $R = 0.2$, *green* $R = 0.4$) in comparison to the homogeneous equivalence (*blue* Homo). For LD: (a) Incremental recovery. (b) Total efficiency. (c) Marginal efficiency. For Q5S: (d) Incremental recovery. (e) Total efficiency. (f) Marginal efficiency.

The sensitivity of the LS displacement stability of the injected slug sizes to heterogeneity and R for the exponential variogram model is presented in **Fig. 6.23**. LS displacement stability decreases with heterogeneity and R post stability-threshold slug for both well patterns – increasing $\mathcal{O}_{E1}$ or $\mathcal{O}_{RF}$ with R. In addition, the LS displacement in slug injections post the stability-threshold size is less stable for Q5S compared to LD for the correlation lengths considered.

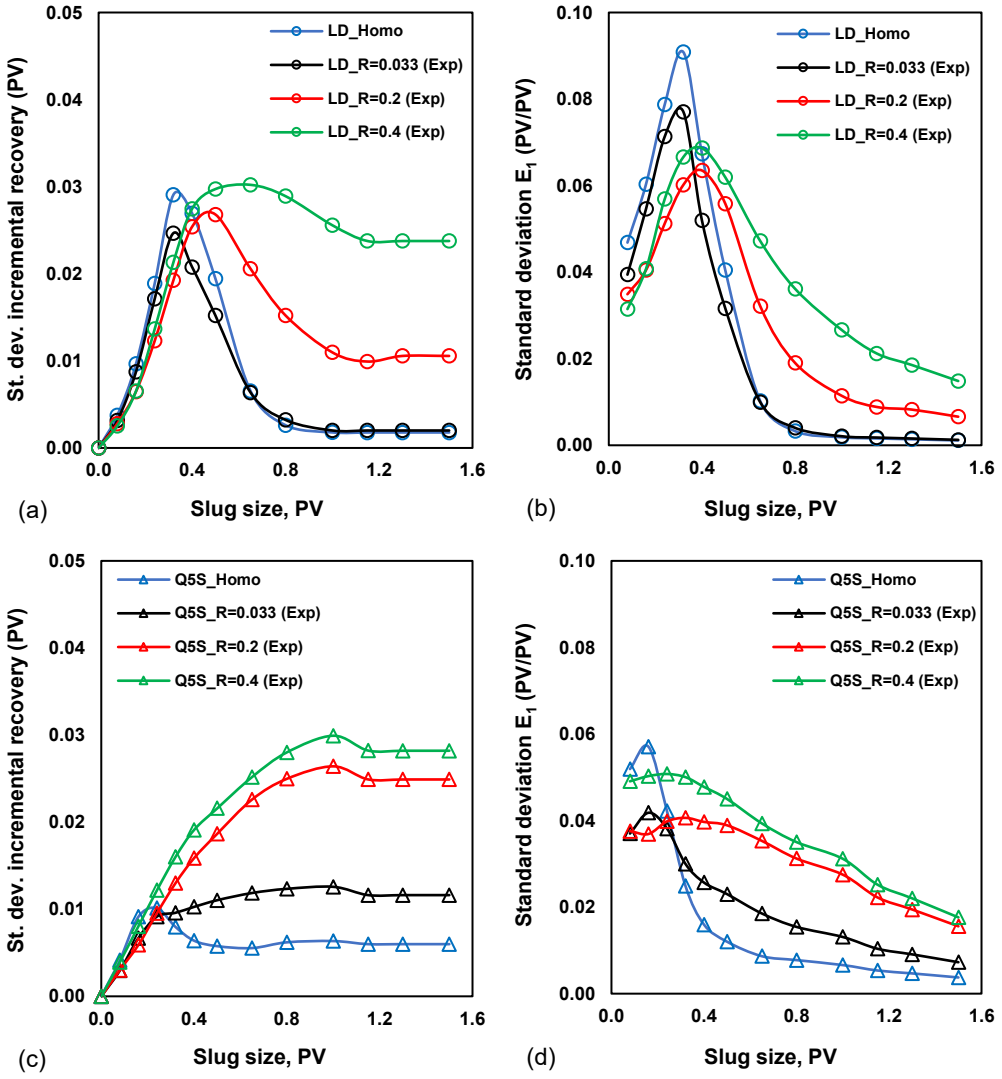
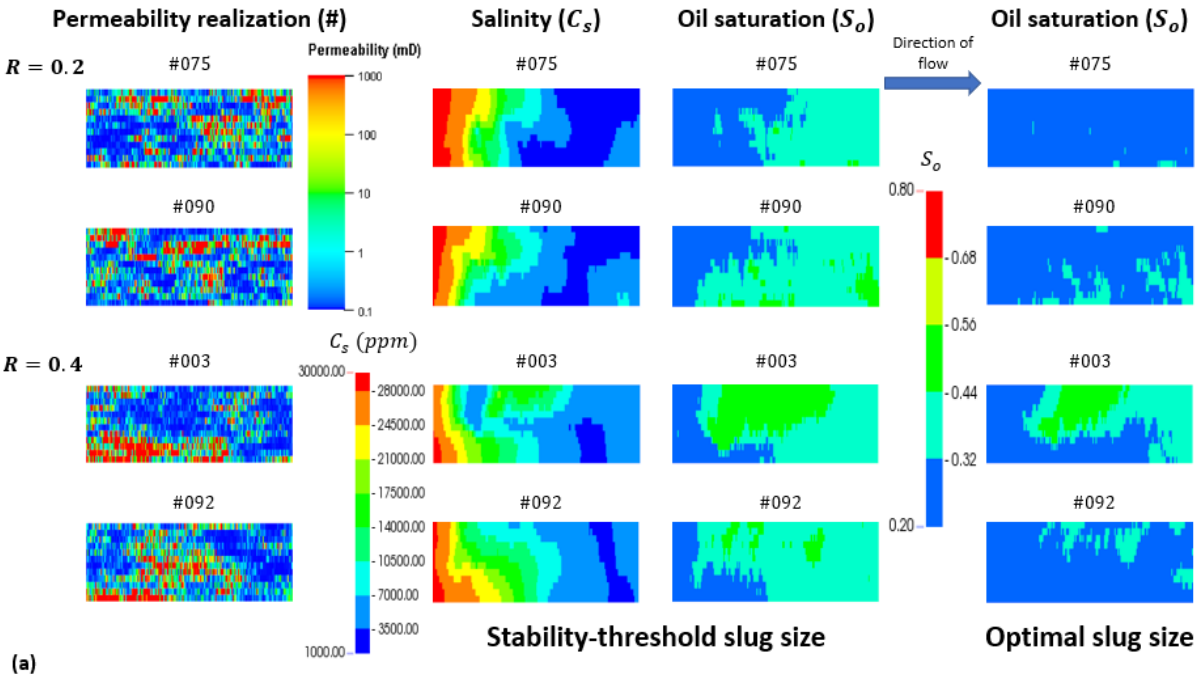


Fig. 6.23: Performance risks as a function of injected slug size for inter-well heterogeneity with an exponential variogram model at different correlation lengths (*black* $R = 0.033$, *red* $R = 0.2$, *green* $R = 0.4$) in comparison to the homogeneous equivalence (*blue* Homo). For LD: (a) Standard deviation of incremental recovery. (b) Standard deviation of total efficiency. For Q5S: (c) Standard deviation of incremental recovery. (d) Standard deviation of total efficiency.

The flood fronts and recovery from the evaluated optimal slug injection design – i.e. stability-threshold and optimal sizes – are illustrated in **Fig. 6.24** for different realizations with the exponential variogram model. The mean physical dispersivity adopted in this chapter ($Pe \cong 3.5\%$) is used here with the base values of the flow variables defined in **Table 6.2**. As described in Chapter 5.2.2, the stability-threshold size appears enough for a stable inter-well displacement at the threshold salinities (i.e. $\leq 7{,}000\ ppm$), but is insufficient to maximize recovery in these cases. However, a more efficient displacement of the oil towards its residual saturation to the LSE is observed with the optimal slug size especially within the flooded flow paths or regions.



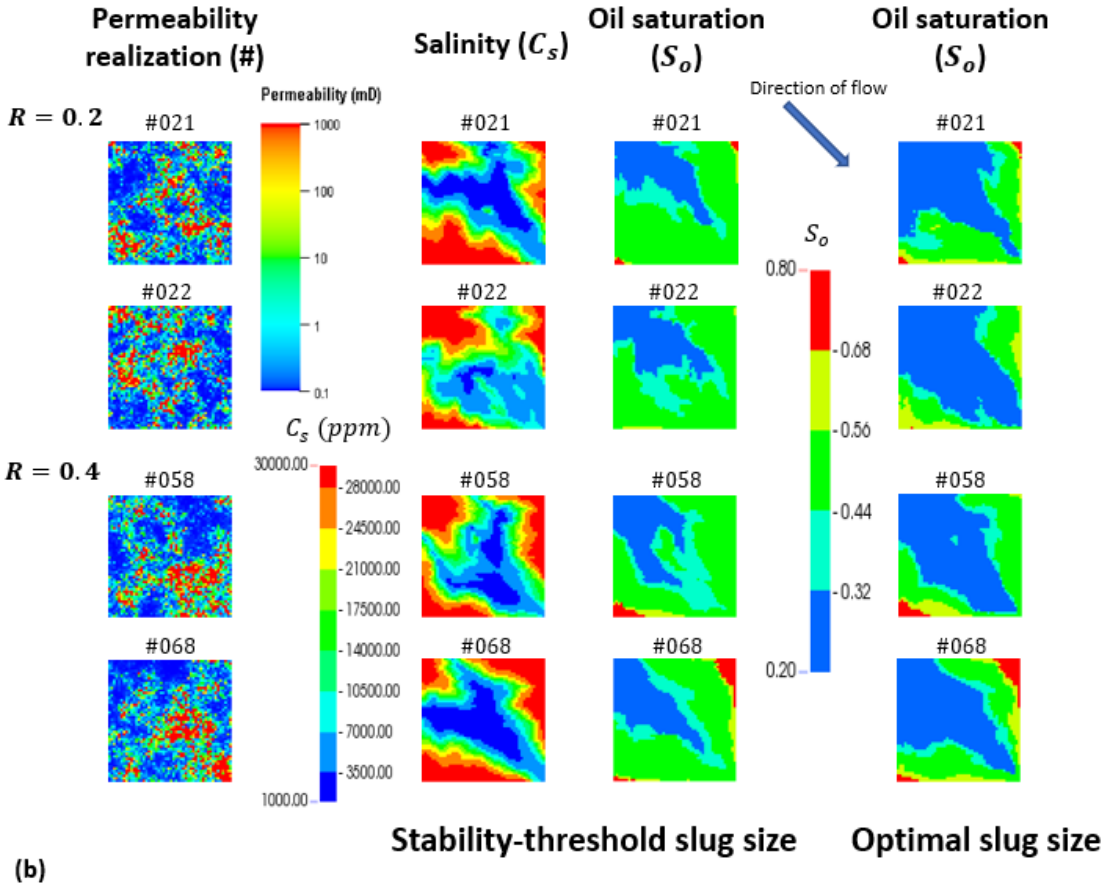


Fig. 6.24: Flood fronts and recovery from the optimal slug injection for inter-well heterogeneity with an exponential variogram model at different correlation lengths (R). (a) Line-drive. (b) Quarter five-spot. The water salinity profile shows the salinity-thresholds spread and LS displacement stability of the injected slug or flood front just at its breakthrough while being trailed by the HS push. The oil saturation distribution indicates the recovery at the end of the flood – i.e. pre-injected LS slug + HS push.

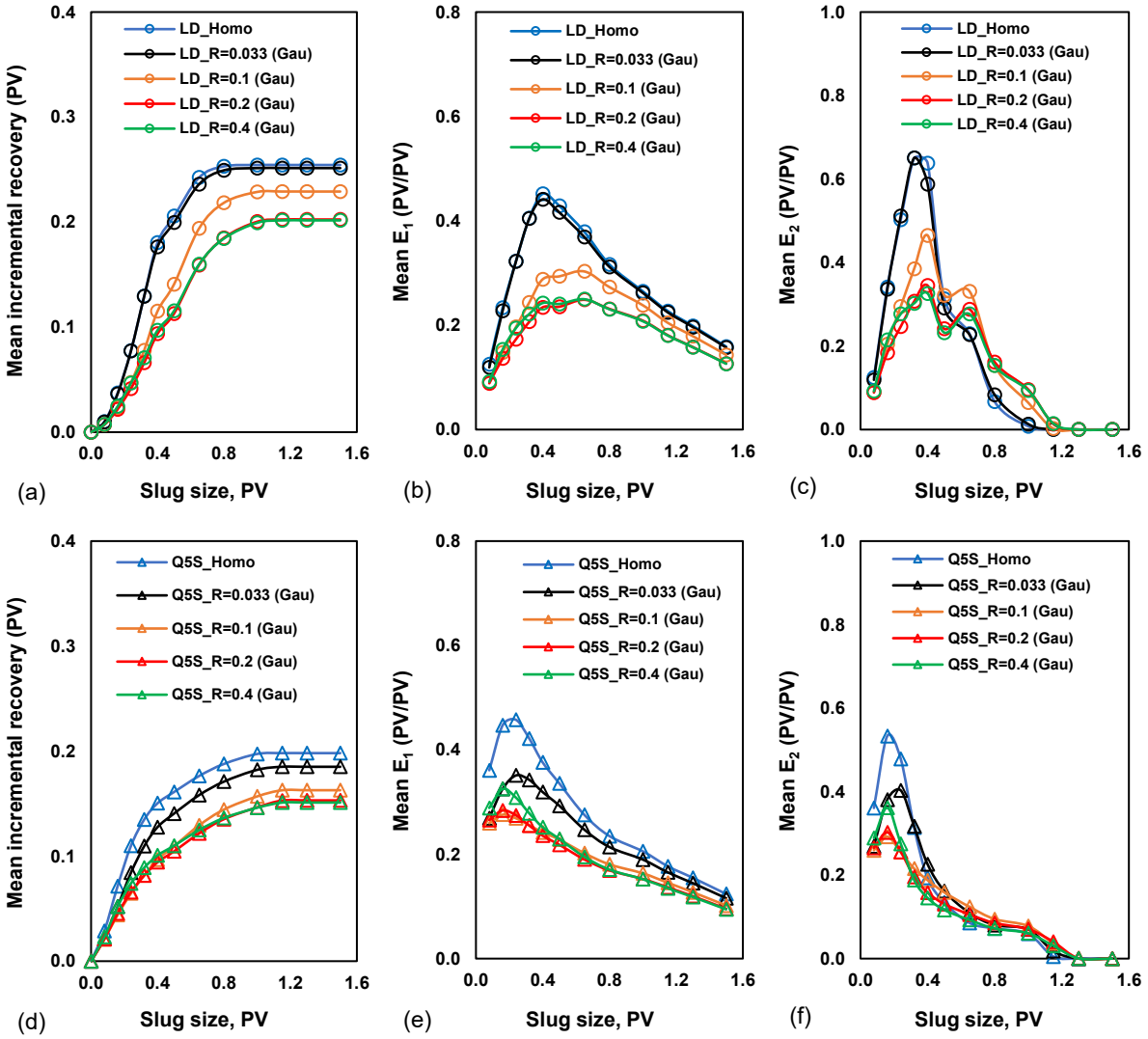


Fig. 6.25. Mean performance as a function of injected slug size for inter-well heterogeneity with a Gaussian variogram model at different correlation lengths (*black* $R = 0.033$, *orange* $R = 0.1$, *red* $R = 0.2$, *green* $R = 0.4$) in comparison to the homogeneous equivalence (*blue* Homo). For LD: (a) Incremental recovery. (b) Total efficiency. (c) Marginal efficiency. For Q5S: (d) Incremental recovery. (e) Total efficiency. (f) Marginal efficiency.

Fig. 6.25 shows the slug performance considering uncertainty in both physical mixing and geological heterogeneity for the Gaussian variogram model. Mean slug performance is sensitive to heterogeneity and R; it decreases with heterogeneity for both flood patterns (**Fig. 6.25**a and d). Similar to the exponential model, optimal slug design for LD shows sensitivity to heterogeneity but it is insensitive to R – stability-threshold and optimal sizes increase to around 0.65 PV and 1.15 PV respectively, which are the same for $R > 0.033$ (**Fig. 6.25**b and c). The optimal slug design for Q5S is independent of variogram model – it is the same for both exponential and Gaussian variograms. Enhanced efficiency of small to moderate slug sizes at $R = 0.4$ for both well patterns (**Fig. 6.25**b and e) also reflects the greater spatial continuity of permeability (or smaller heterogeneity) at large R values. This is more pronounced here for the Gaussian variogram model because of its slower variation of a heterogeneous

property within a correlation distance. The trend of more- and less-efficient slug at small and large sizes respectively for Q5S compared to LD remains for all values of R.

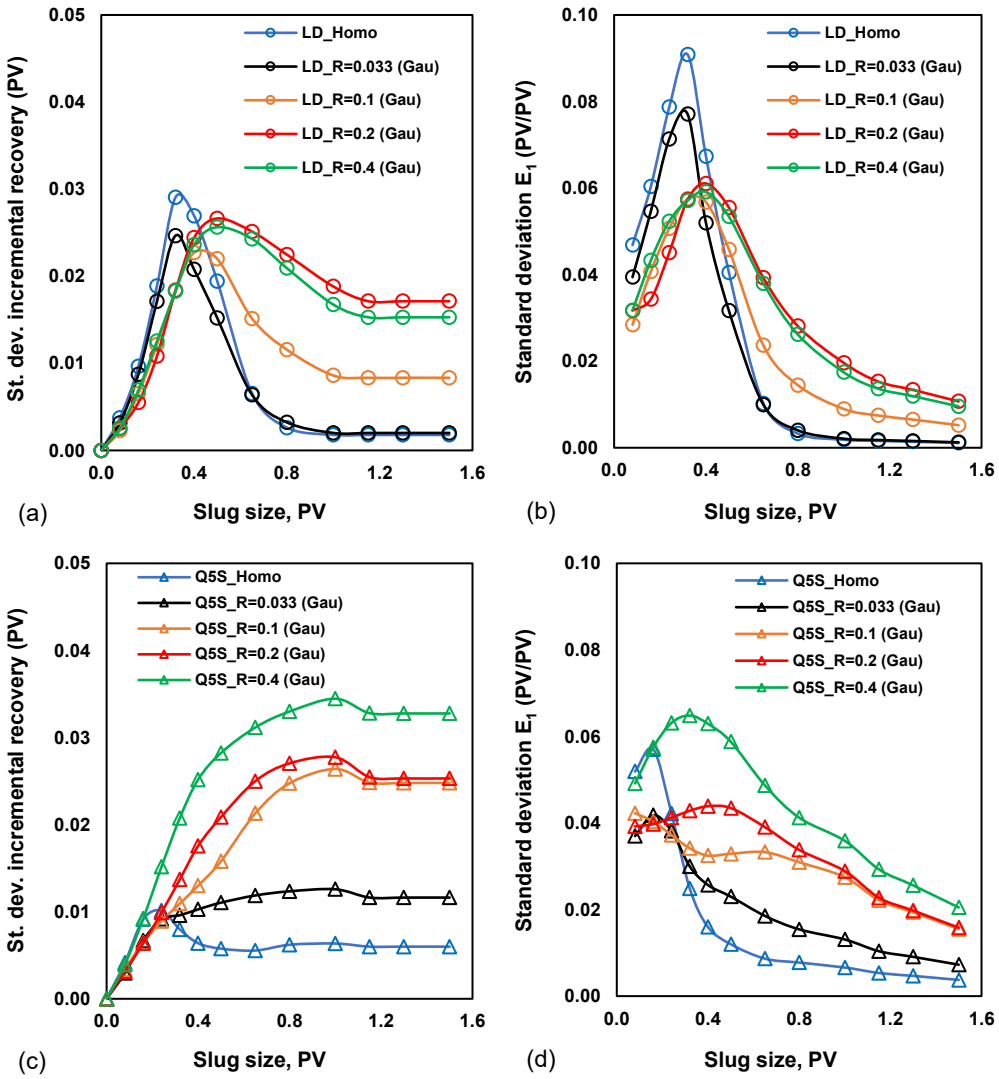
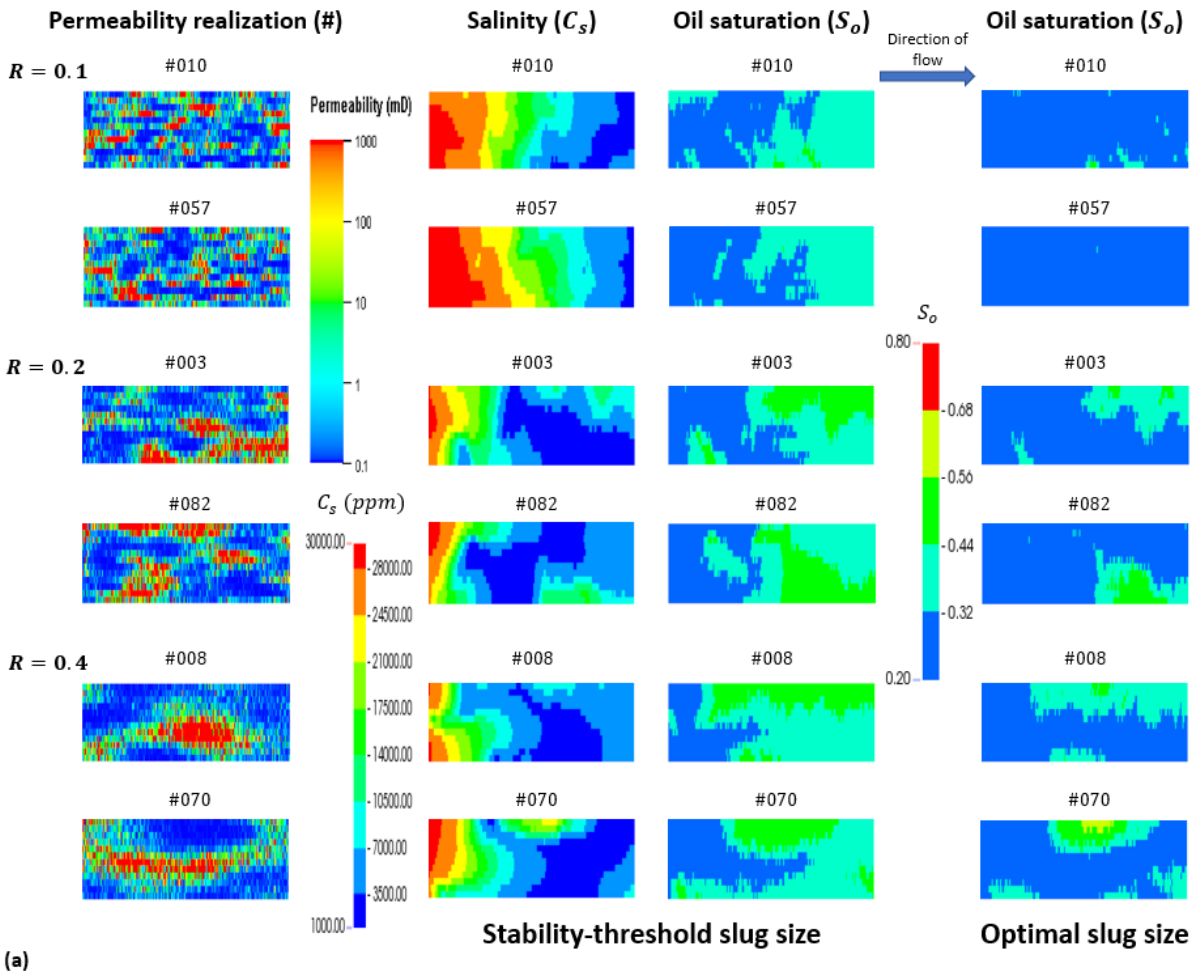


Fig. 6.26. Performance risks as a function of injected slug size for inter-well heterogeneity with a Gaussian variogram model at different correlation lengths (*black* $R = 0.033$, *orange* $R = 0.1$, *red* $R = 0.2$, *green* $R = 0.4$) in comparison to the homogeneous equivalence (*blue* Homo). For LD: (a) Standard deviation of incremental recovery. (b) Standard deviation of total efficiency. For Q5S: (c) Standard deviation of incremental recovery. (d) Standard deviation of total efficiency.

The sensitivity of the LS displacement stability of the injected slug sizes to heterogeneity and R for the Gaussian variogram model is presented in **Fig. 6.26**. For both well patterns, LS displacement stability decreases with heterogeneity – increasing σ'_{E1} or σ'_{RF}, post stability-threshold slug. Enhanced LS displacement stability post stability-threshold slug for LD at $R = 0.4$ relative to $R = 0.2$ indicates its less heterogeneity from greater spatial permeability continuity which is more favourable for LD at those slug sizes than Q5S. LS displacement appears less stable for Q5S with a Gaussian variogram compared to exponential variogram. For all the Rs and both variogram models considered, the LS

displacement in slugs post the stability-threshold and around the optimal size is more stable in LD than Q5S.

Fig. 6.27 highlights the flood fronts and recovery from the optimal slug injection – i.e. stability-threshold and optimal sizes – for different realizations with the Gaussian variogram model. The mean physical dispersivity ($Pe \cong 3.5\%$) is also used with the base values of the flow variables defined in **Table 6.2**. While the stability-threshold size seems enough for a stable inter-well displacement at the threshold salinities (i.e. $\leq 7{,}000\ ppm$), it remains insufficient to maximize recovery as seen earlier with the exponential variogram model. Injecting the optimal slug size displaces the target oil in the flooded flow paths or regions more efficiently towards its residual saturation to the LSE in all the cases.



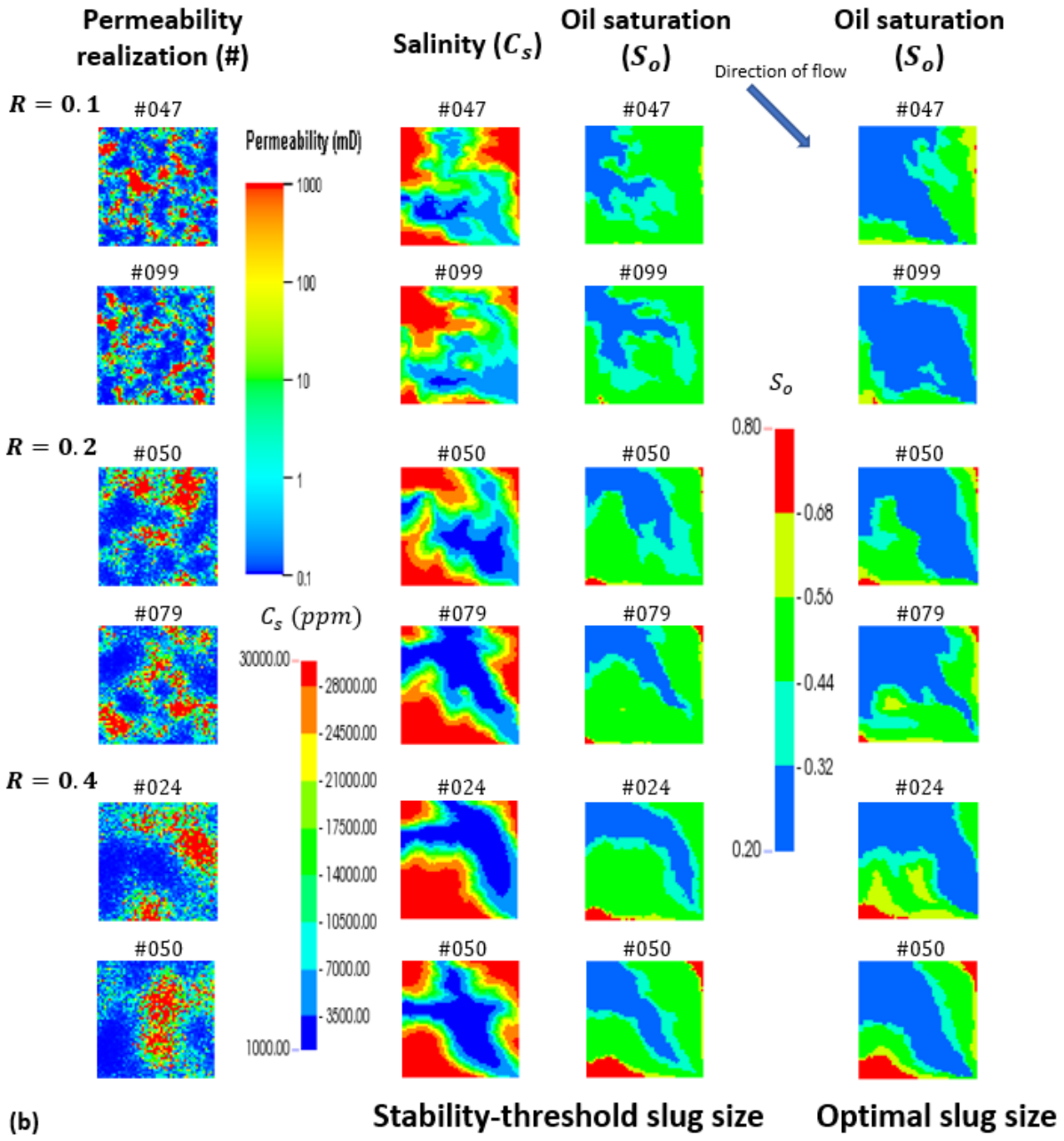


Fig. 6.27: Flood fronts and recovery from the optimal slug injection for inter-well heterogeneity with a Gaussian variogram model at different correlation lengths (R). (a) Line-drive. (b) Quarter five-spot. The water salinity profile shows the salinity-thresholds spread and LS displacement stability of the injected slug or flood front just at its breakthrough while being trailed by the HS push. The oil saturation distribution indicates the recovery at the end of the flood – i.e. pre-injected LS slug + HS push.

6.3.2 3D Models

Previously, the influence of flood or well pattern and geological uncertainty was examined on how inter-well mixing affects LS slug performance in 2D areal models. While the injected slug performance and its LS displacement stability remained sensitive to heterogeneity for both flood patterns – with potential favourable transverse dispersion, the optimal amounts to inject showed insensitivity to

heterogeneity for the Q5S pattern. We now explore the impact of the interaction between geological heterogeneity and physical mixing on the slug performance and its displacement stability in 3D models. This is to test the generality of the optimal slug injection in more representative heterogeneous reservoir connectivity considering uncertainty. Essentially, this section investigates with three-dimensional flows, the insensitivity of the optimal injected slug amounts to heterogeneity for Q5S flood pattern observed in 2D. The LS flood performance is evaluated with immediate slug injection at a cumulative water injection of 2.5 PV.

6.3.2.1 Optimal Slug Injection Sensitivity to Heterogeneity

The mean slug performance considering only flow uncertainties (defined in **Table 6.2**) is presented in **Fig. 6.28** for the 3D models of **Fig. 6.4** and the equivalent homogenous model ($\sigma_f = 0.0$) for a Q5S well pattern. Similar to the 2D case, the performance is sensitive to heterogeneity – recovery decreases with heterogeneity (**Fig. 6.28**a). In addition, for the cumulative water injection considered, the optimal slug size of about 1.75 PV remains insensitive to heterogeneity (**Fig. 6.28**c). However, the stability-threshold size increases with heterogeneity (**Fig. 6.28**b) – about 0.24 PV (for $\sigma_f = 0.0$) to 0.5 PV (for $\sigma_f = 1.0$), unlike for 2D. This also shows a range of target slug sizes – to balance technical and financial performance – that narrows with heterogeneity in 3D.

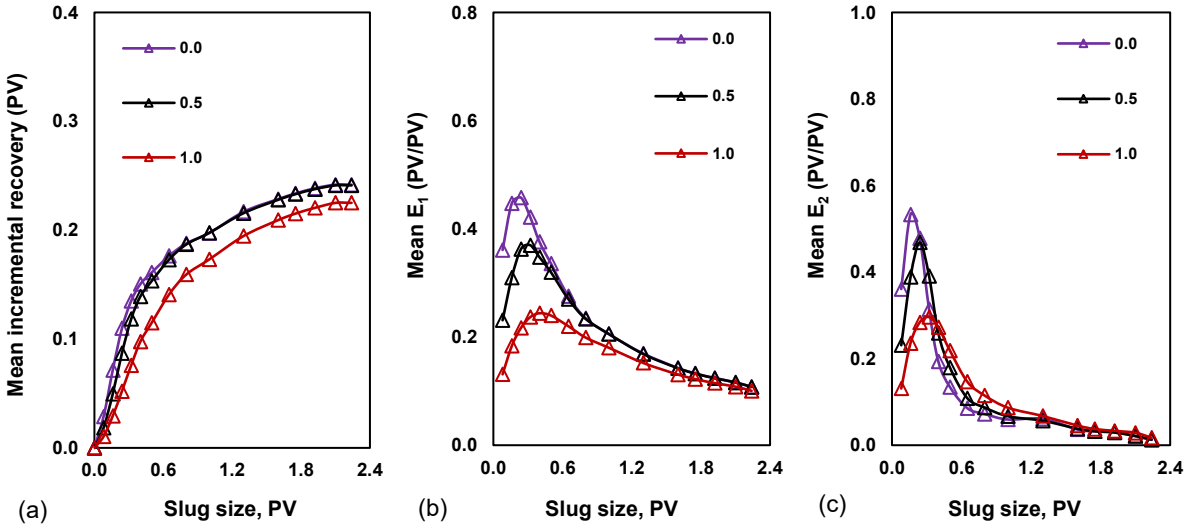


Fig. 6.28: Mean performance under flow uncertainties as a function of injected slug size at different degrees of heterogeneity ($0.0 \leq \sigma_f \leq 1$: *purple* $\sigma_f = 0.0$, *black* $\sigma_f = 0.5$, *red* $\sigma_f = 1.0$). (a) Incremental recovery. (b) Total efficiency. (c) Marginal efficiency.

Fig. 6.29 highlights the sensitivity of the LS displacement stability of the injected slug sizes to heterogeneity. Improved LS displacement stability with heterogeneity is seen at large slugs around the optimal size – $\mathcal{O}'_{E1}$ or $\mathcal{O}'_{RF}$ decreases with heterogeneity (especially at $\sigma_f = 1.0$). This results from delayed favourable transverse dispersion discussed previously, and now indicates that heterogeneity-

enhanced stability of the LS displacement fronts in the presence of physical mixing is independent of dimension. Furthermore, the delayed localized influence of transverse dispersion (often associated with Q5S as observed in 2D) decreases with heterogeneity (**Fig. 6.29**a) which reflects the improved LS displacement stability at those slug sizes.

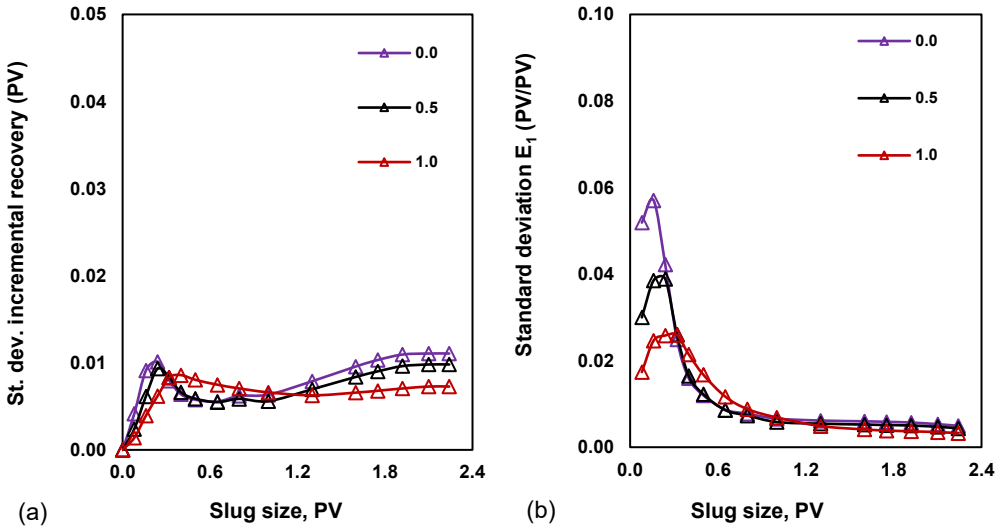
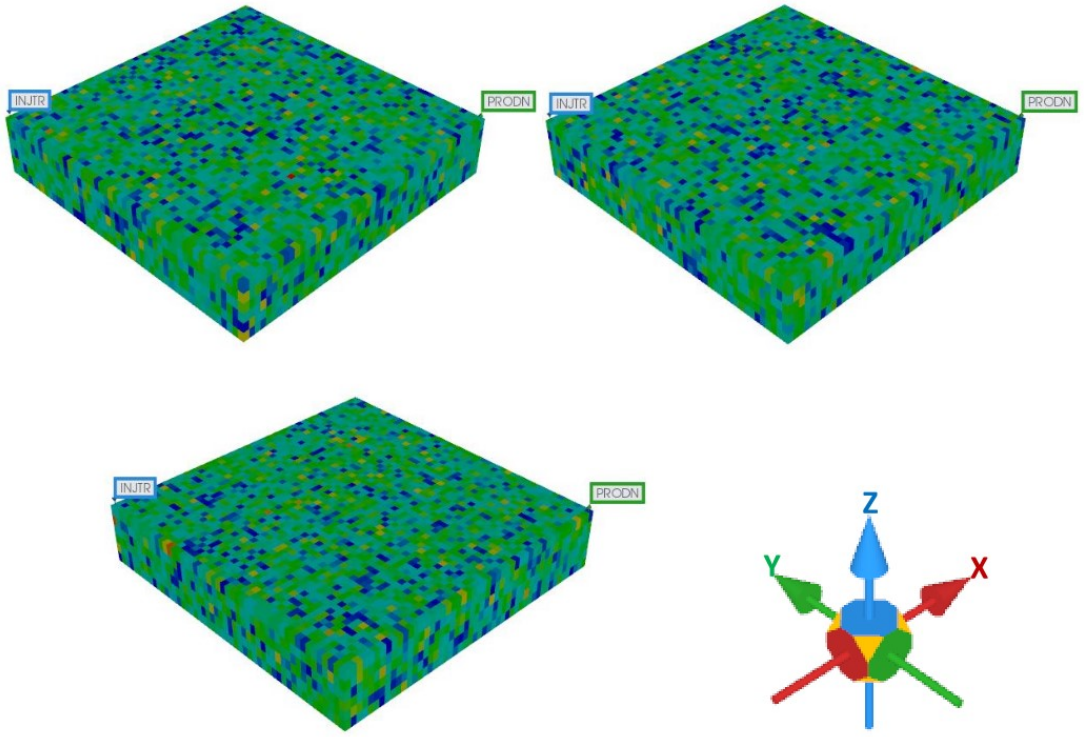
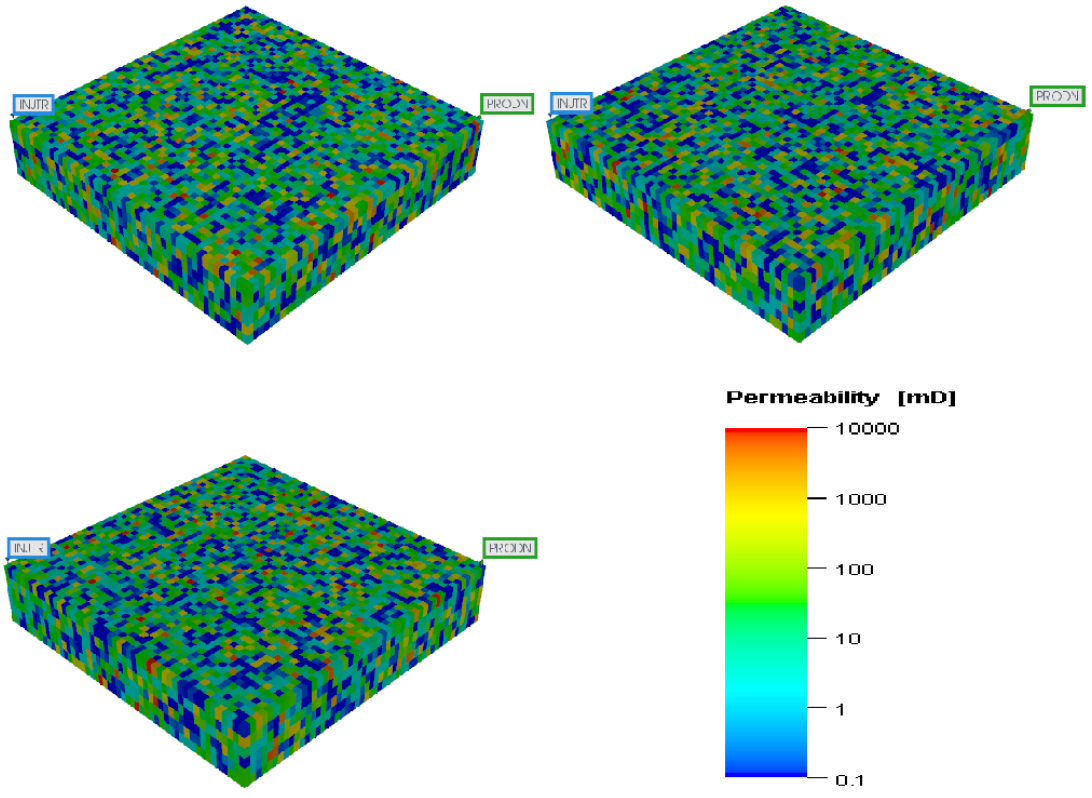


Fig. 6.29: Performance risks under flow uncertainties as a function of injected slug size at different degrees of heterogeneity ($0.0 \leq \sigma_f \leq 1$: *purple* $\sigma_f = 0.0$, *black* $\sigma_f = 0.5$, *red* $\sigma_f = 1.0$). (a) Standard deviation of incremental recovery. (b) Standard deviation of total efficiency.

To evaluate the impact of uncertainty in the geological representation (GU) of the 3D models of **Fig. 6.4** on the slug performance, 11 out of the ranked 101 realizations are selected as discussed earlier. The corresponding realizations for each of the (base) models in **Fig. 6.4** are generated with its geostatistical correlation properties respectively. Some of these random geological realizations considered are presented in **Fig. 6.30** for each 3D base heterogeneous model (or level of heterogeneity).



(a)



(b)

Fig. 6.30: Random geostatistical realizations of spatial permeability distribution for inter-well heterogeneity at a normalized correlation length or range of $R = 0.033$ in all coordinate directions. (a) $\sigma_f = 0.5$. (b) $\sigma_f = 1.0$.

The slug performance considering uncertainty in both physical mixing and geological heterogeneity is shown in **Fig. 6.31**. Decreasing mean slug performance with heterogeneity remains under geological uncertainty (GU) – **Fig. 6.31**a. Increasing stability-threshold slug size with heterogeneity – about 0.24 PV (for $\sigma_f = 0.0$) to 0.5 PV (for $\sigma_f = 1.0$) – also remains under GU (**Fig. 6.31**b). No substantial impact of geological uncertainty is seen on the optimal slug injection design – optimal and stability-threshold sizes – at both levels of heterogeneity (**Fig. 6.31**b and c), which is similar to the results in 2D. Meanwhile, the sensitivity of the mean slug performance to geological uncertainty is observed to decrease slightly with heterogeneity in 3D.

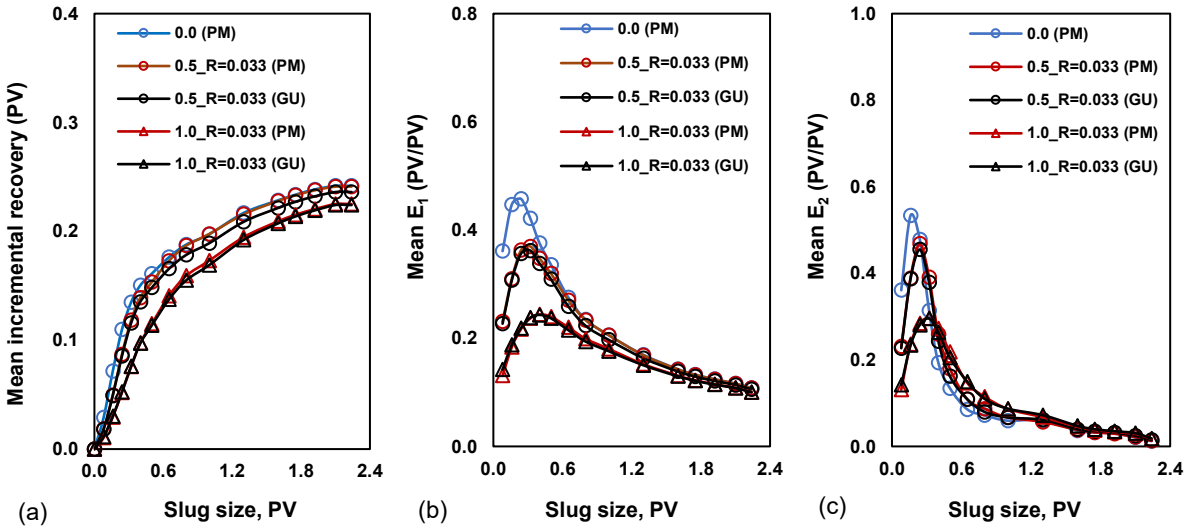


Fig. 6.31: Mean performance under only flow uncertainties (red PM) and in combination with geological uncertainty (black GU) as a function of injected slug size for the base heterogeneous models at $R = 0.033$ (*circle* $\sigma_f = 0.5$, *triangle* $\sigma_f = 1.0$) in comparison to the homogeneous equivalence (*blue* $\sigma_f = 0.0$). (a) Incremental recovery. (b) Total efficiency. (c) Marginal efficiency.

LS displacement stability remains sensitive to heterogeneity under GU in 3D – $\mathcal{O}'_{E1}$ or $\mathcal{O}'_{RF}$ generally changes with heterogeneity (**Fig. 6.32**). As seen in 2D, the LS displacement stability is impaired under GU compared to without GU (PM) in slugs post the stability-threshold size. Furthermore, there is a possible improvement in the LS displacement stability for small slugs pre-stability-threshold size after considering GU especially at high degree of heterogeneity ($\sigma_f = 1.0$). Whereas, the improved stability of the LS displacement with heterogeneity at large slugs around the optimal size observed earlier without GU (PM) is now impaired by GU. This is indicated by the reverse (or increasing) trend of the delayed localized influence of transverse dispersion with heterogeneity at those slugs under GU.

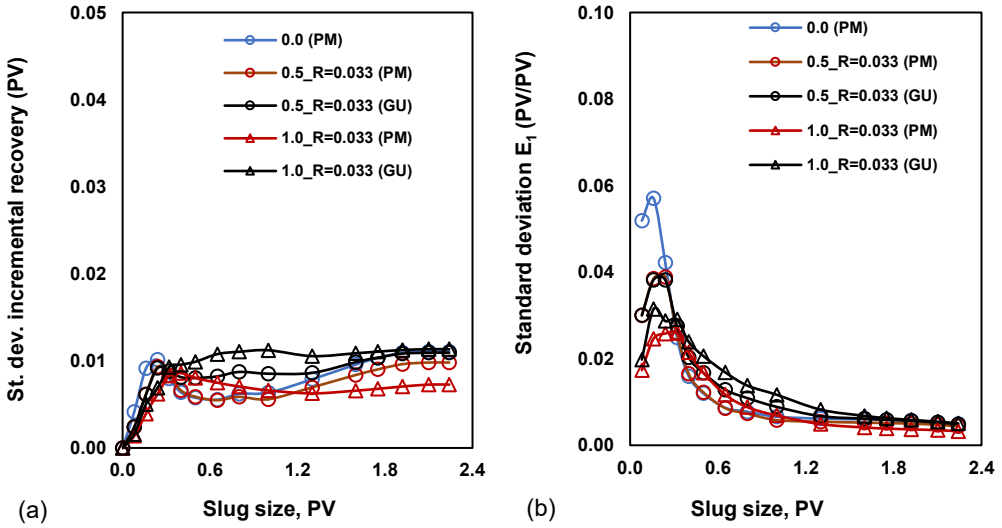
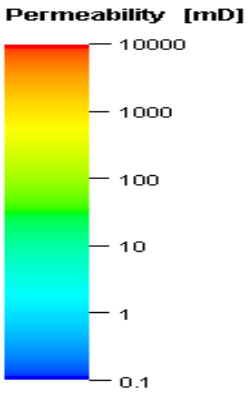
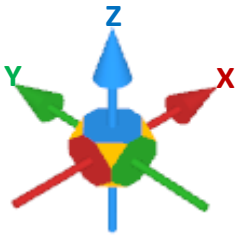


Fig. 6.32: Performance risks under only flow uncertainties (red PM) and in combination with geological uncertainty (black GU) as a function of injected slug size for the base heterogeneous models at $R = 0.033$ (*circle* $\sigma_f = 0.5$, *triangle* $\sigma_f = 1.0$) in comparison to the homogeneous equivalence (*blue* $\sigma_f = 0.0$). (a) Standard deviation of incremental recovery. (b) Standard deviation of total efficiency.

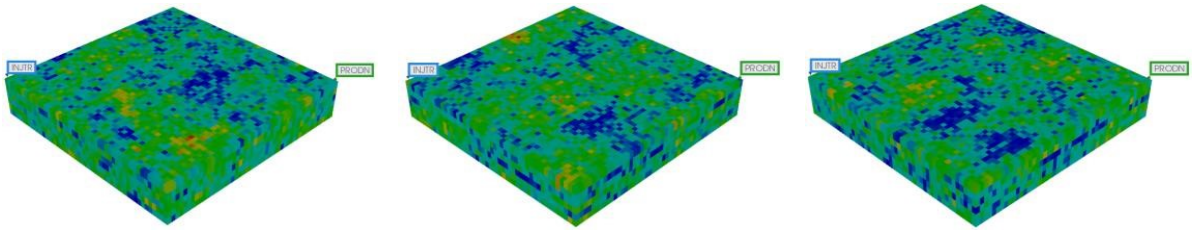
6.3.2.2 Optimal Slug Injection for More Heterogeneous Reservoir Connectivity

The sensitivity of the optimal injected slug amounts is examined here in more heterogeneous descriptions. As adopted earlier for 2D, these realizations are characterized with modified sets of the geostatistical correlation properties of the 3D (base) models in **Fig. 6.4** using larger correlation lengths – $0.033 < R \leq 0.4$, and different variogram models – exponential and Gaussian. 11 out of the ranked 101 realizations are selected to evaluate the impact of geological uncertainty for each combination of correlation length, variogram model, and normalized standard deviation (σ_f), as described previously. **Fig. 6.33** shows some of these heterogeneous realizations considered with their characteristic geostatistical correlation properties – normalized correlation length, R and variogram models – for both base normalized standard deviation (σ_f).

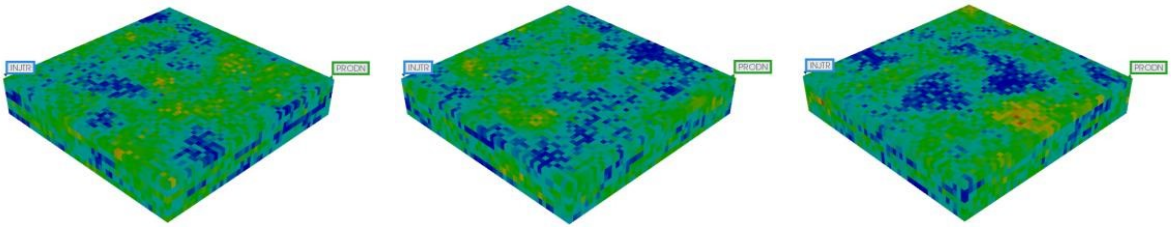




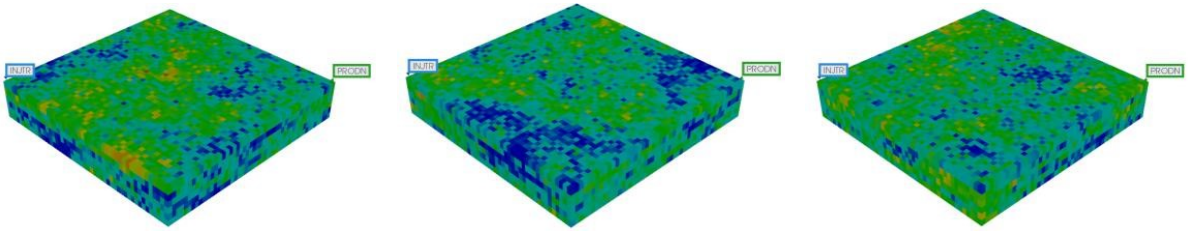
***R*=0.2 (Exponential)**



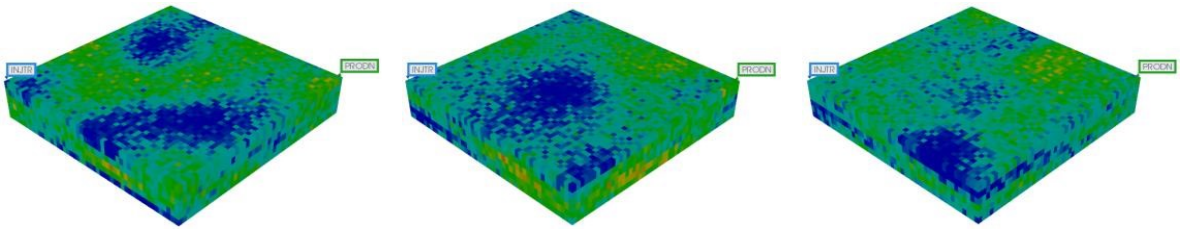
***R*=0.2 (Gaussian)**



***R*=0.4 (Exponential)**



***R*=0.4 (Gaussian)**



(a)

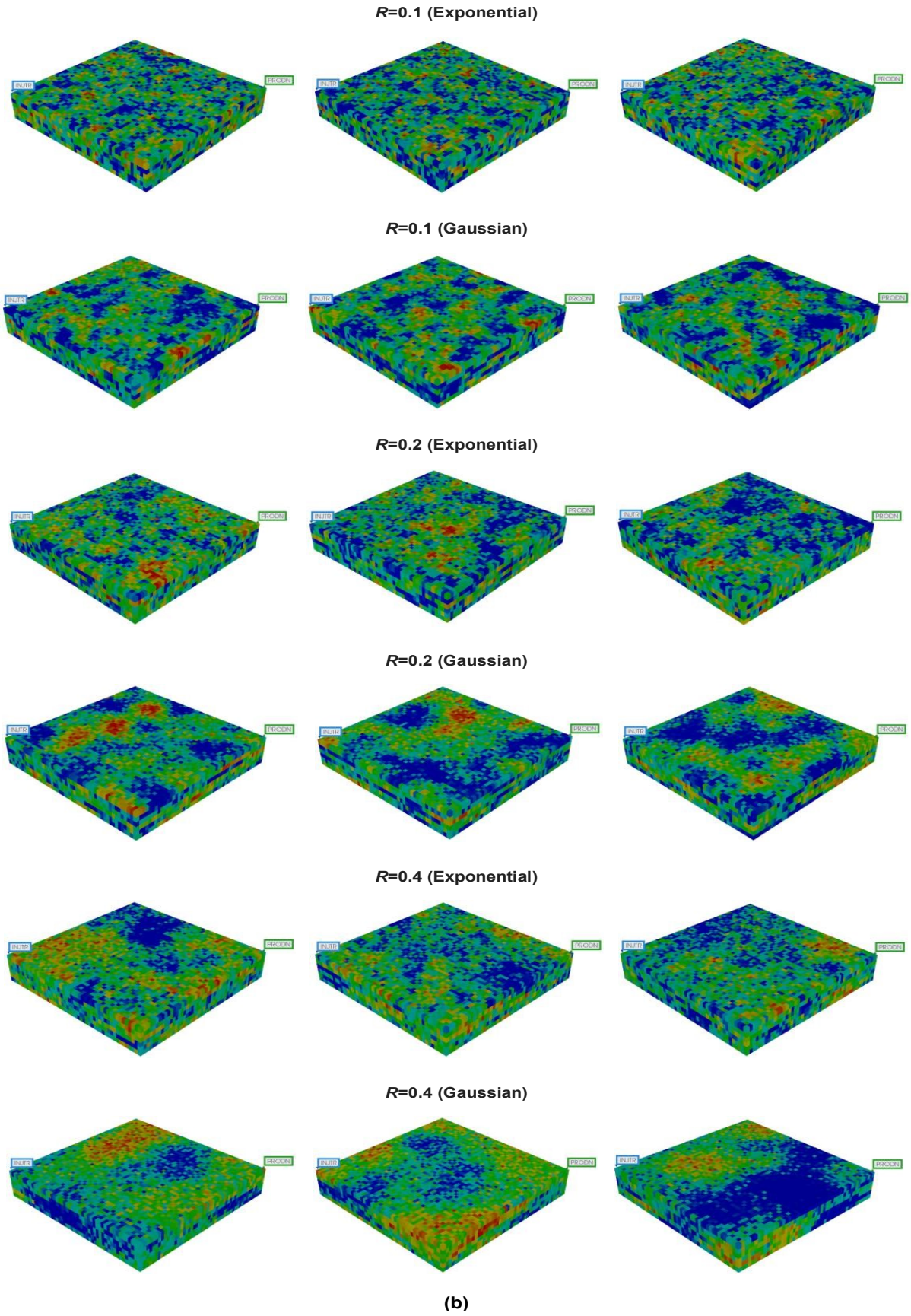


Fig. 6.33: Random geostatistical realizations of spatial permeability distribution for inter-well heterogeneity at different normalized correlation lengths, R, and variogram models – exponential and Gaussian. (a) $\sigma_f = 0.5$. (b) $\sigma_f = 1.0$.

The slug performance considering uncertainty in both physical mixing and geological heterogeneity is shown in **Fig. 6.34** for the exponential variogram model. Decreasing mean slug performance with heterogeneity and R persists in 3D (**Fig. 6.34**a and d). The optimal slug size of about 1.75 PV remains insensitive to heterogeneity and R (**Fig. 6.34**c and f). While the stability-threshold slug size is sensitive to heterogeneity – increases from about 0.24 PV (for $\sigma_f = 0.0$) to 0.5 PV (for $\sigma_f = 1.0$) – as also observed previously, it is insensitive to R at each base σ_f (**Fig. 6.34**b and e).

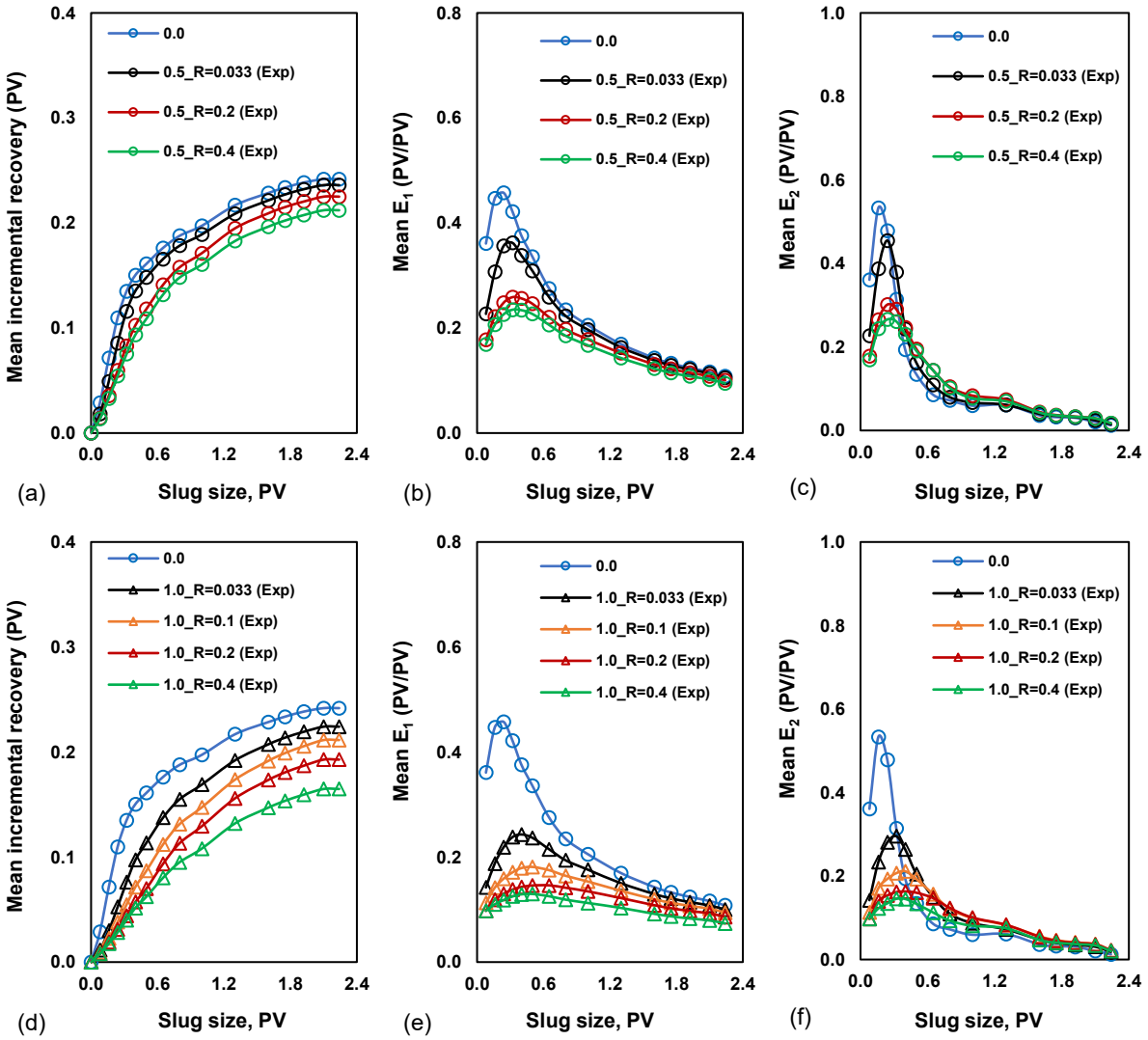


Fig. 6.34: Mean performance as a function of injected slug size for inter-well heterogeneity with an exponential variogram model at different correlation lengths (*black* $R = 0.033$, *orange* $R = 0.1$, *red* $R = 0.2$, *green* $R = 0.4$) in comparison to the homogeneous equivalence (*blue* $\sigma_f = 0.0$). For $\sigma_f = 0.5$: (a) Incremental recovery. (b) Total efficiency. (c) Marginal efficiency. For $\sigma_f = 1.0$: (d) Incremental recovery. (e) Total efficiency. (f) Marginal efficiency.

The sensitivity of the LS displacement stability of the injected slug sizes to heterogeneity and R for the exponential variogram model is presented in **Fig. 6.35**. LS displacement stability largely decreases with heterogeneity and R post stability-threshold slug – increasing $\mathcal{O}_{E1}$ or $\mathcal{O}_{RF}$ with R, as seen in 2D.

However, LS displacement in 3D (at $\sigma_f = 1.0$) appears more stable with slugs around the optimal size for $R = 0.4$ relative to $R = 0.2$ despite the former showing lower mean performance. It is suggested that this is due to the more restraining inter-well flow path(s) from better reservoir continuity or connectivity at larger R in 3D. This reduces the (delayed) localized influence of transverse dispersion around the 'unswept' regions on the slug displacement which persists at those injected sizes and correlation lengths.

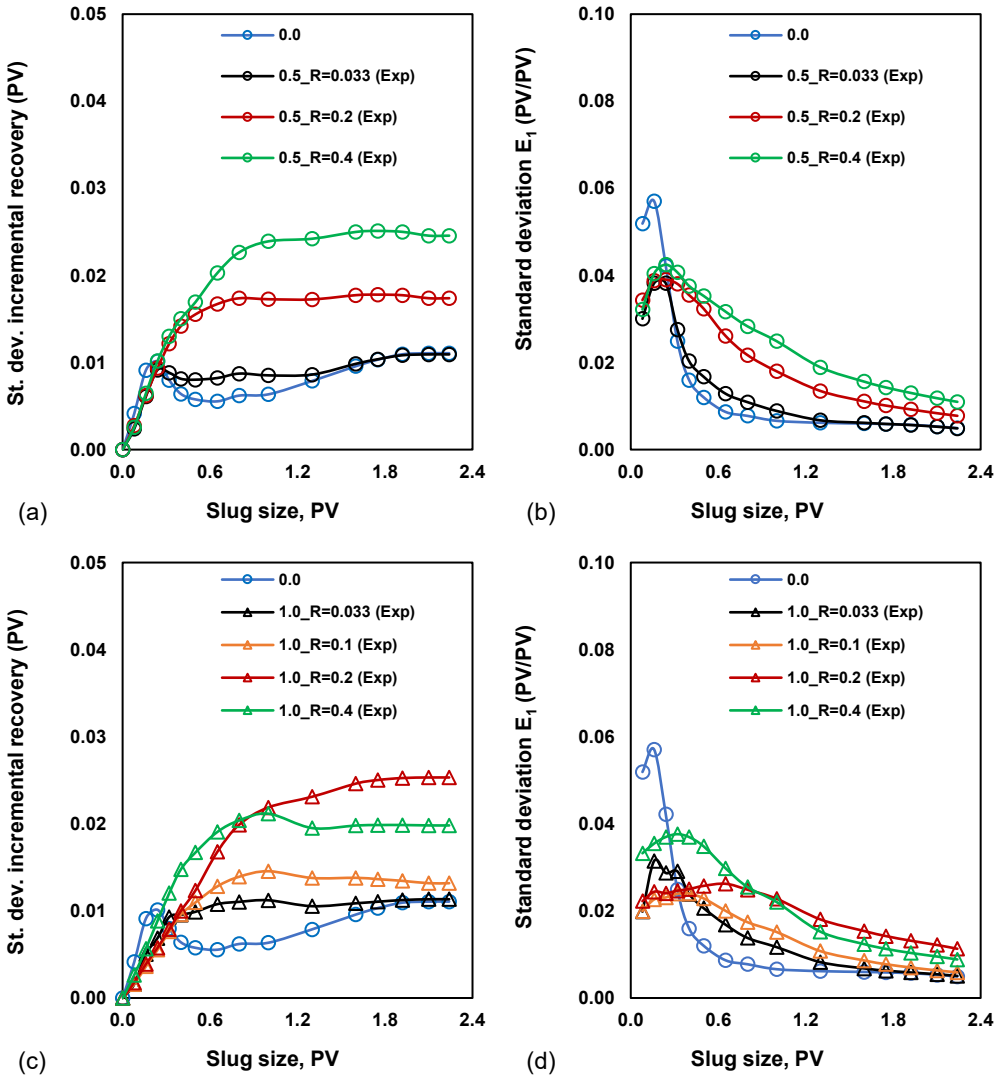


Fig. 6.35: Performance risks as a function of injected slug size for inter-well heterogeneity with an exponential variogram model at different correlation lengths (*black* $R = 0.033$, *orange* $R = 0.1$, *red* $R = 0.2$, *green* $R = 0.4$) in comparison to the homogeneous equivalence (*blue* $\sigma_f = 0.0$). For $\sigma_f = 0.5$: (a) Standard deviation of incremental recovery. (b) Standard deviation of total efficiency. For $\sigma_f = 1.0$: (c) Standard deviation of incremental recovery. (d) Standard deviation of total efficiency.

Fig. 6.36 shows the slug performance considering uncertainty in both physical mixing and geological heterogeneity for the Gaussian variogram model. Mean slug performance remains sensitive to heterogeneity and R; it decreases with heterogeneity and R (**Fig. 6.36**a and d). The optimal slug size

is independent of variogram model – it is the same for both exponential and Gaussian variograms (**Fig. 6.36**c and f). The stability-threshold size which increases with heterogeneity from about 0.24 PV (for $\sigma_f = 0.0$) to 0.5 PV (for $R = 0.033$ at $\sigma_f = 1.0$) is insensitive to R at each base σ_f – it is the same for $R \geq 0.033$ (**Fig. 6.36**b and e).

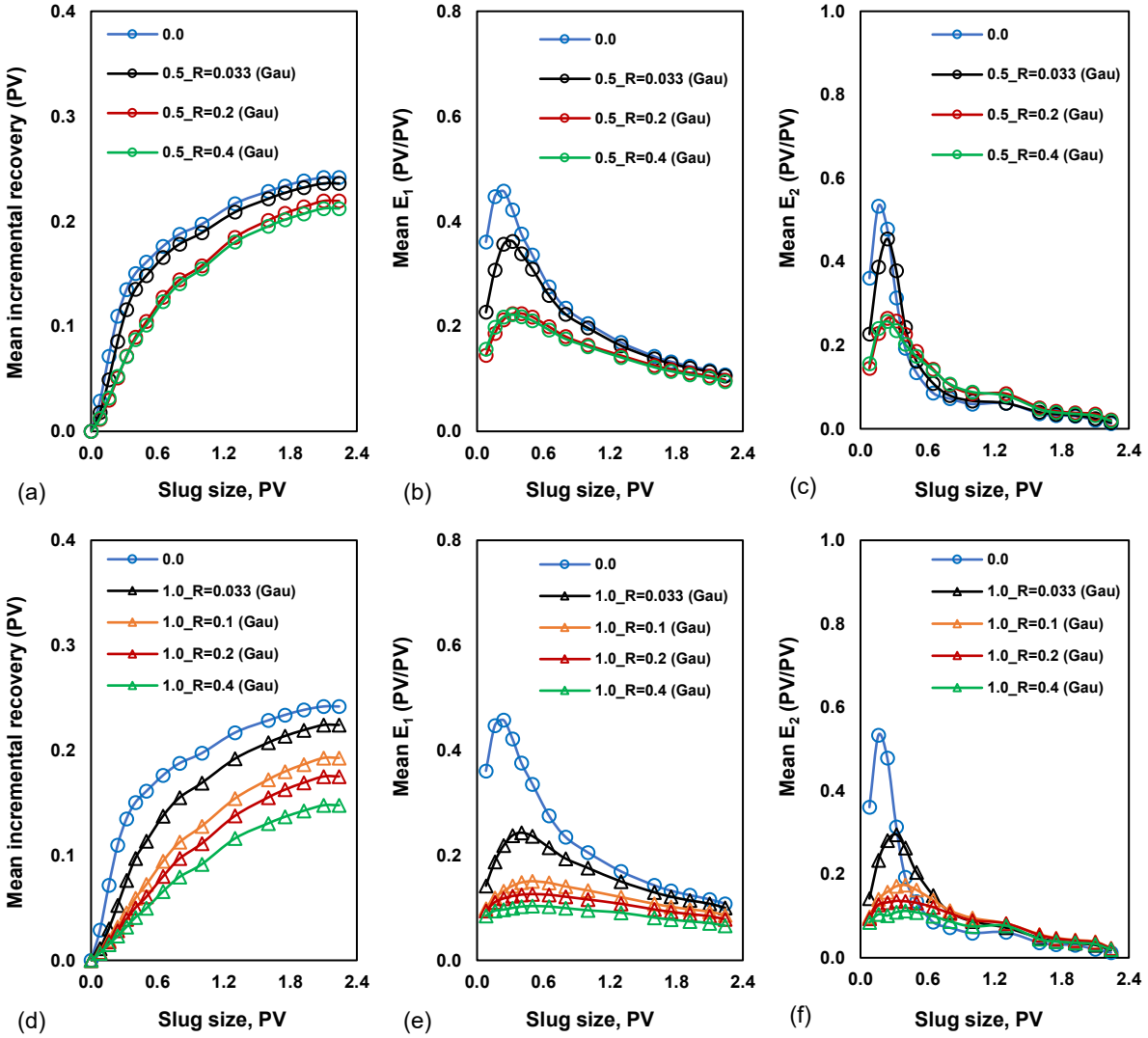


Fig. 6.36: Mean performance as a function of injected slug size for inter-well heterogeneity with a Gaussian variogram model at different correlation lengths (*black* $R = 0.033$, *orange* $R = 0.1$, *red* $R = 0.2$, *green* $R = 0.4$) in comparison to the homogeneous equivalence (*blue* $\sigma_f = 0.0$). For $\sigma_f = 0.5$: (a) Incremental recovery. (b) Total efficiency. (c) Marginal efficiency. For $\sigma_f = 1.0$: (d) Incremental recovery. (e) Total efficiency. (f) Marginal efficiency.

The sensitivity of the LS displacement stability of the injected slug sizes to heterogeneity and R for the Gaussian variogram model is presented in **Fig. 6.37**. As highlighted in the 2D results, the decrease in the LS displacement stability with heterogeneity and R post stability-threshold slug also remains in 3D – increasing $\mathcal{O}_{E1}$ or $\mathcal{O}_{RF}$ with R. In addition, the localized influence of transverse dispersion persists with R, similar to the exponential variogram model. Meanwhile, enhanced stability of the LS

displacement with slugs around the optimal size for $R = 0.4$ relative to $R = 0.2$ observed with an exponential variogram is not seen here under a Gaussian variogram. This is because of its slower or less short-range variation of heterogeneity than the exponential model (within a correlation distance). Thus, the more restrained inter-well flow path(s) from a larger R value is rendered less-distinctive.

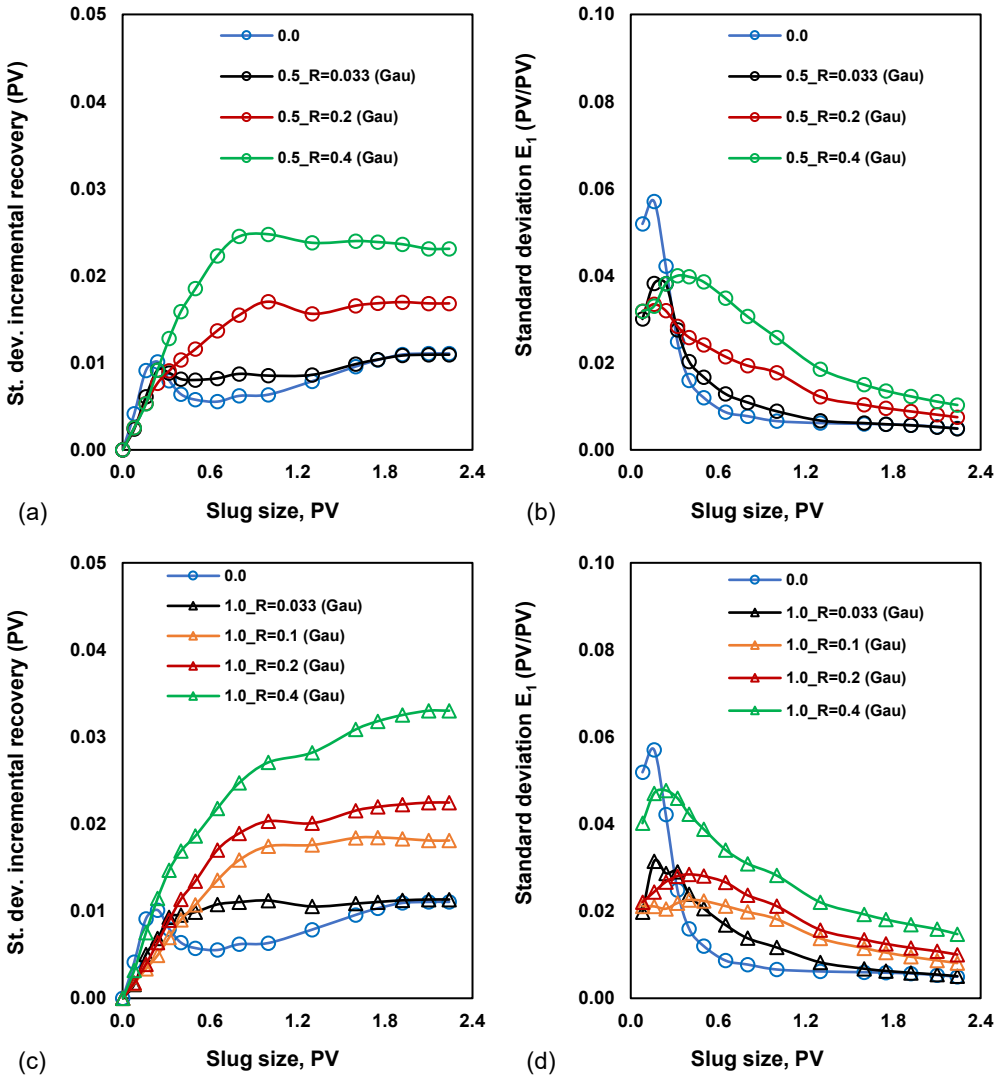


Fig. 6.37: Performance risks as a function of injected slug size for inter-well heterogeneity with a Gaussian variogram model at different correlation lengths (*black* $R = 0.033$, *orange* $R = 0.1$, *red* $R = 0.2$, *green* $R = 0.4$) in comparison to the homogeneous equivalence (*blue* $\sigma_f = 0.0$). For $\sigma_f = 0.5$: (a) Standard deviation of incremental recovery. (b) Standard deviation of total efficiency. For $\sigma_f = 1.0$: (c) Standard deviation of incremental recovery. (d) Standard deviation of total efficiency.

6.4 Summary

The impact of physical mixing in LSWF on optimal slug injection was investigated further in this chapter introducing geological uncertainty in two- and three-dimensional reservoir models. The displacement stability and performance of a LS slug was explored while optimizing its injected size under both physical mixing and geological uncertainty for line-drive and quarter five-spot well patterns. In 2D, the

first section examined the influence of flood pattern on how the interaction between physical dispersion and heterogeneity affects LS slug performance, its displacement stability, and the optimal amounts to inject. In the second section, the generality of the sensitivity of the optimal injected amounts to heterogeneity for quarter five-spot flood pattern is tested in 3D with more representative heterogeneous reservoir connectivity. Our results from this chapter are summarized in the following:

1. Flood pattern influences the sensitivity of LS slug performance to its injection delay (or start-time) regardless of the effective displacement mode of the flood. While the slug performance remains insensitive to injection start-time until the tertiary-mode displacement becomes established for a line-drive well pattern, performance is sensitive to injection start-time irrespective of the flood displacement mode for a quarter five-spot well arrangement.
2. The interaction between physical mixing and areal geological heterogeneity can potentially modify favourably the LS displacement stability and performance of the injected slug in a quarter five-spot flood pattern. Thus, transverse dispersion tends to improve the areal sweep efficiency for both well patterns.
3. For a cumulative water injection of 2 PV, LS slug design considering uncertainty requires at least 0.8 PV optimal size and 0.24 PV minimum stability-threshold size across well patterns. This can vary with the cumulative water injected and flood pattern but remains generally favoured by an early injection.
4. The LS displacement stability and performance of the injected slug are very sensitive to heterogeneity while the sensitivity of its optimal design is dependent on the well pattern. Specifically, the optimal slug size is found to be insensitive to heterogeneity for the quarter five-spot flood pattern both in two- and three-dimensional flows. The line-drive flood pattern shows a narrower slug range between the target stability-threshold and optimal sizes, which is of essential computational advantage when optimizing its injection in such EOR process.
5. Slug injection is more- and less-efficient at small and large sizes respectively for quarter five-spot flood pattern. LS displacement in large slugs are more stable for line-drive well pattern. This indicates a slug size dependence of performance – under physical mixing in multi-dimensional models – that is a function of well arrangement.

Meanwhile, it is noted that the relative permeability is considered reversible in the modelling approach adopted here, and this lacks realism relating to wettability alteration of pore surfaces: altered wettability does not change back instantaneously following high-salinity displacement. This can potentially over-predict the optimal slug size especially under heterogeneity since subsequent displacement of a LS flooded area by HS push may under-recover the residual oil to the LSE. Furthermore, the optimal amounts to inject were only investigated for a unit oil-water viscosity ratio,

and the oil viscosity, in this case, is anomalously low. For a higher oil viscosity (and viscosity ratio), a larger slug size may be required to maximize the LS sweep and recovery if the resulting displacement front is unfavourable.

In the next chapter, we will investigate crossflow during LSWF in more detail in stratified reservoirs.

7 Crossflow Effects on Low Salinity Displacement in Stratified Heterogeneity

7.1 Introduction

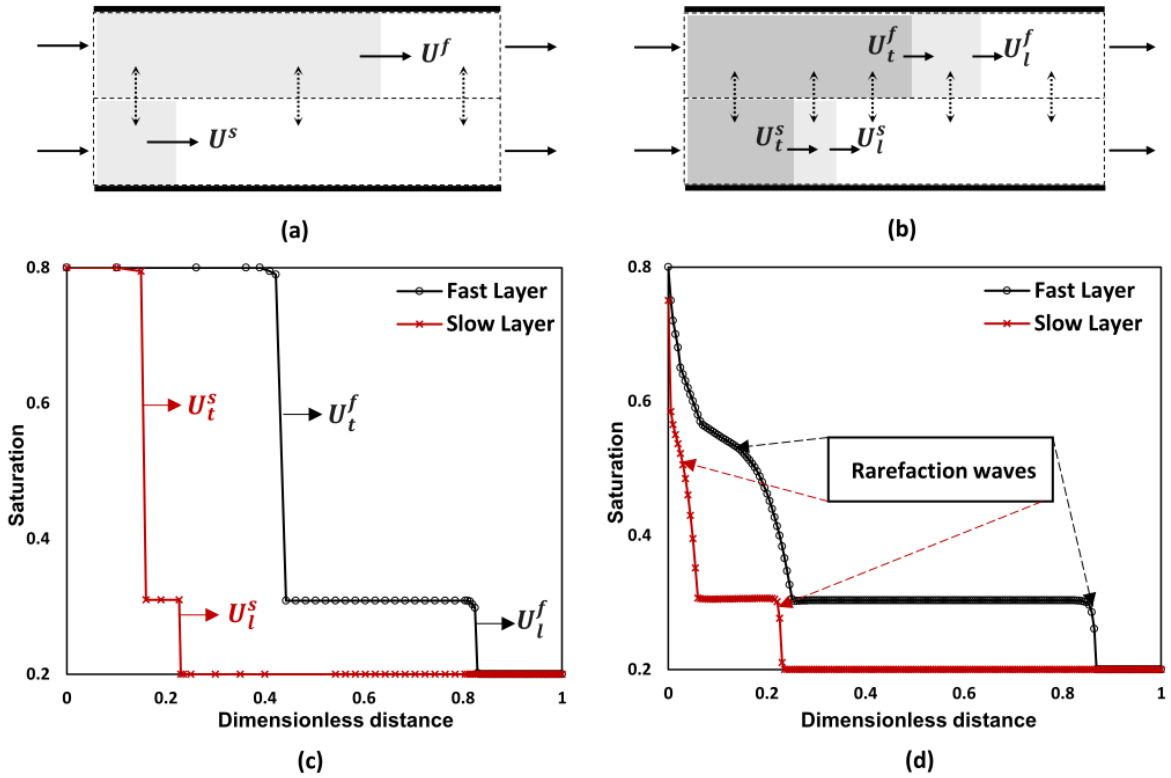


Fig. 7.1: Schematics of the displacing-phase distribution and regions contacted along a two-layered porous medium neglecting capillarity and gravity during (a) a typical waterflood and (b) an EOR-engineered water injection; both showing contrasting frontal advance velocity in both layers ($U^f \neq U^s$) due to property contrasts, and possible viscous crossflow between the layers (indicated with transverse arrows between the layers). Typical injected- or displacing-phase saturation profiles along each layer (in the absence of crossflow) during an EOR-engineered water injection are reported for (c) piston-like displacements, in which entire saturation change occurs at the shock-fronts, and (d) non-piston-like displacements, in which some of the saturation change occurs over the shock-fronts, and some occurs over a rarefaction wave following the shock-front.

A common type of geological heterogeneity consists of alternating layers or strata of different lithologies and physical properties at many different length scales (Campbell, 1967; Jones et al., 1994; Koltermann and Gorelick, 1996; Jackson et al., 2003; Deveugle et al., 2011). It is therefore important to understand how flow in such media affects fluid displacement for accurate prediction and better design of many subsurface hydrocarbon recovery processes. Among the factors influencing fluid flow in heterogeneous permeable media is crossflow – flow across the strata in directions other than that of the bulk flow. This is illustrated for a simple two-layer system in **Fig. 7.1**. Crossflow effects on the

displacement efficiency of recovery processes – volumetric and microscopic – is controlled by the property contrasts of the layers (Zhou et al., 2019), and the driving forces present – viscous, capillarity, gravity, and dispersion or dilution (Kereluk and Crawford, 1968; Lake and Hirasaki, 1981). Property contrasts influence the differences in the displacement-front velocity in the layers, distinguishing high-velocity (fast) from low-velocity (slow) layers, with significant impact on the displacement efficiency with or without crossflow (**Fig. 7.1**).

In this chapter, we use numerical experiments to investigate the effects of crossflow caused by viscous forces, commonly termed viscous crossflow (VC), on displacements along stratified media of contrasting properties during an EOR process – Low-salinity Waterflooding (LSWF) (see **Fig. 7.1**b). In addition, VC effects are examined in the presence of other interacting driving forces, here limited to dispersion and gravity, that are typical of field-scale oil recovery processes. This work does not attempt to predict the exact behaviour of a given geologic reservoir or flow system, but to predict where and how VC affects fluid displacements as a function of some key dimensionless numbers, in order to support mechanistic interpretations of predictions from more complex numerical models of the process regardless of length-scale (King and Mansfield, 1999).

We consider the effects of cross-flow for engineered or low-salinity (LS) waterflood that includes (i) non-piston-like displacements, (ii) different cases of mobility ratios across both leading and trailing shock-fronts, and (iii) different plausible scenarios of the relative velocity of the displacing-phase or chemical-front in both layers, which may influence the impact of VC on the chemical sweep as suggested by Zapata and Lake (1981).

After first describing the model adopted for the EOR process, the dimensionless numbers used to characterize two-phase flow along layered porous media are presented. The influence of property contrasts on VC in stratified heterogeneous systems is then examined. VC behaviours for non-piston-like displacements are rationalized and explored with numerical solutions for no-crossflow, using a pair of mobility-ratios each evaluated across each of the two shock-fronts in a layer. These potential behaviours are thereafter confirmed under viscous crossflow. The sensitivity of VC recovery and chemical-sweep efficiency to mobility-ratios across shock-fronts with non-piston-like displacements is evaluated at different performance times relative to NC displacement. We identify a mobility-ratio case, which has not been reported previously, that is generally unfavourable to VC in engineered or low-salinity waterfloods. The control of unfavourable displacements with VC for this mobility-ratio case is later presented and discussed to aid better flood design.

7.2 Model and Method: Scaling Analysis with Dimensionless Numbers

The Low Salinity Effect (LSE) is modelled with the standard tracer-model approach described in Chapter 2.5.1, where salinity is treated as the 'proxy' single-component tracer that controls wettability alteration towards more water-wetness. The salinity thresholds for LSE are $1{,}000 - 7{,}000$ ppm while the injected low-salinity water and connate (high-salinity) brine salinities are $1{,}000$ ppm and $30{,}000$ ppm respectively.

Two-phase displacement is investigated through a two-layered medium in which the layers have contrasting properties (**Fig. 7.2**). The injection and production rates are the same along the left-hand and right-hand faces respectively. The top and bottom edges of the medium are no-flow boundaries. The numerical model is a two-dimensional X, Z-symmetry element of an n-layered system, finely discretized into 200 grid-blocks along the X-direction, in which alternating layers have the same contrasting properties. Layers are discretized into equal number of grid-blocks in the Z-direction – ranging from 2 to 50 across simulations to model different shape factors. However, each grid-block is isotropic (i.e. $\Delta X = \Delta Y = \Delta Z$) to control numerical dispersion effects accurately. Solutions are obtained using CMG STARS, which implements a finite-difference approach to discretize the governing equations in space. Flow is also simulated with higher resolutions of up to 500 grid-blocks along the X-direction to demonstrate that the solutions converge. For all simulations in this chapter, time stepping is small at a CFL or Courant number of 0.05 and fully implicit as adopted in previous chapters. This ensures that the inherent numerical dispersion is (truly) largely dependent on grid-size – as presented in equations (2.10) and (2.15).

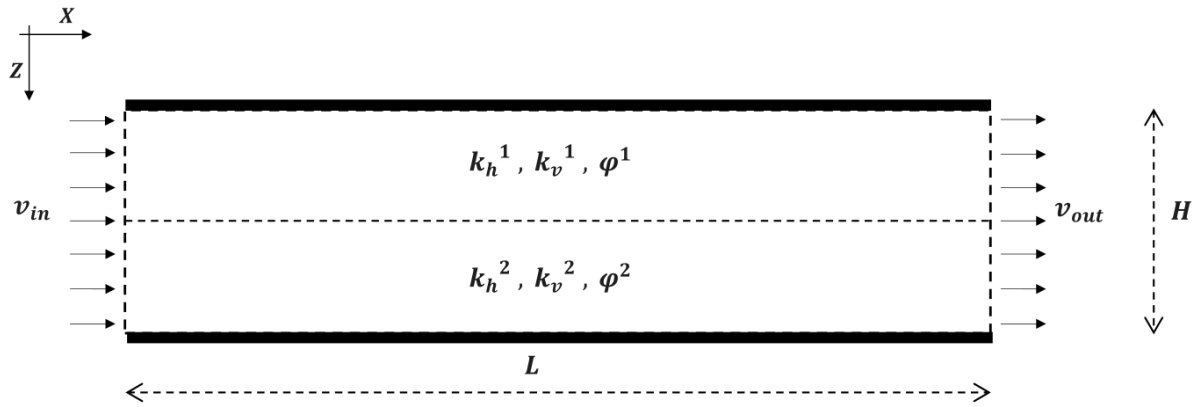


Fig. 7.2: Schematic diagram of the two-layer model used.

Each layer is internally homogeneous with identical length L and thickness $H/2$, but differ in longitudinal absolute permeability k_h and porosity φ. The layers are assumed to have identical local

absolute permeability anisotropy k_v/k_h, typical of field-scale numerical experiments, where k_v is the transverse absolute permeability.

The layer property contrast ratio or the permeability-storage contrast ratio C is defined as

$$C = \frac{R_k}{R_s} \tag{7.1}$$

where R_k and R_s; the longitudinal permeability ratio and porosity (storage) ratio between the layers respectively, are given by

$$R_k = \frac{{k_h}^1}{{k_h}^2} \tag{7.2}$$

$$R_s = \frac{\varphi^1}{\varphi^2} \tag{7.3}$$

where the superscripts 1 and 2 denote the two layers. R_k scales the ratio of influxes into each layer, R_s scales the ratio of fluid volumes in each layer, and C scales the displacing-phase or its shock-front relative velocity in both layers – U^f and U^s for the fast and slow layers respectively (**Fig. 7.1**a). As C approaches unity, U^f and U^s become the same with their displacement shock-fronts getting closer towards a single-front displacement across both layers where recovery efficiency is maximum at breakthrough.

R_k and R_s values can vary over several orders of magnitude (Nelson, 1994), but measured data often show a poor correlation between them (e.g. Thompson et al., 1987). Such an investigation is outside the scope of this study. The focus here is to explore how R_k influences the existence of crossflow in layered porous media, as well as evaluate the impact of the plausible scenarios of the displacing-phase relative velocity in both layers on VC behaviour and efficiency during engineered waterflooding as suggested by Zapata and Lake (1981). For the sake of generality, R_k is varied over the range $1 - 10^6$ with $R_s = 1$, from which representative values of C are selected for the plausible combinations of U_t^f and U_l^s that are of importance to this study (**Fig. 7.1**b).

Neglecting gravity and capillary forces, total relative mobility of fluids λ_T is defined as

$$\lambda_T = \frac{k_{r,i}}{\mu_i} + \frac{k_{r,d}}{\mu_d} \tag{7.4}$$

where $k_{r,i}(s)$ and $k_{r,d}(s)$ are the relative permeabilities of the injected (displacing) and displaced phases respectively at a normalized injected phase saturation s, μ_i and μ_d are the viscosities of the

injected (displacing) and displaced phases respectively. The normalized injected phase saturation s is given by

$$s = \frac{S_i - S_{i,r}}{1 - S_{i,r} - S_{d,r}} \tag{7.5}$$

where s varies between 0 and 1, S_i is the injected (displacing) phase saturation, $S_{i,r}$ and $S_{d,r}$ are the injected and displaced phase residual saturations.

Since different mobility-ratio cases are considered in this chapter, the relative permeabilities as functions of the normalized injected phase saturation s are defined as

$$k_{r,i}(s) = k_{r,i}^{e} s^{n_i} \tag{7.6}$$

$$k_{r,d}(s) = k_{r,d}^{e} (1 - s)^{n_d} \tag{7.7}$$

where $k_{r,i}^{e}$ and $k_{r,d}^{e}$ are the end-point relative permeabilities, n_i and n_d are the Corey exponents of the injected and displaced phases respectively, and are defined for each state of wettability considered. n controls the sharpening or otherwise of a displacement front: sharpening or piston-like fronts are associated with large n values and vice versa for non-piston-like displacements. Accordingly, the values of these parameters are selectively varied to generate the different relative permeabilities used to characterize the different mobility-ratio cases of non-piston-like shock-fronts for high- and low-salinity conditions. These are presented in the next section for the respective scenarios.

The mobility ratio across a shock-front M_F describes the ratio of the total relative mobility across the shock-front. This is evaluated at saturation values that bound the discontinuity that defines the shock, and is given by

$$M_F = \frac{\lambda_T(s_F)}{\lambda_T(s_i)} \tag{7.8}$$

where s_F and s_i are the upper and lower bounds of the displacing-phase saturation across the shock-front and are evaluated using the Buckley-Leverett fractional flow curve described in Chapters 2.3 and 4.2. Displacements are favourable when $M_F < 1$ and unfavourable for $M_F > 1$, with VC feasible. For the special case of $M_F = 1$, there can be no crossflow (NC). Therefore, values that span this threshold, $M_{F,fav} = 0.5$ and $M_{F,unfav} = 1.5$, are investigated in this chapter.

M_F has been shown to control the viscous crossflow behaviour in layered porous media (Zapata and Lake, 1981; Debbabi et al., 2017). It should be noted that the shock-front mobility ratio, as evaluated in this thesis, and the end-point mobility ratio, adopted in previous studies for piston-like displacements, may not be identical. This is because the relative permeabilities of the two phases vary

behind the shock-front when displacements are not piston-like. However, as shown later, this assumption is sufficient to approximate the viscous crossflow behaviour for two-phase non-piston-like displacements under layered heterogeneity, hence, suitable for the purpose of this research.

For an immediate injection of low salinity water in a water-oil system, mobility ratio across the leading chemical-free (or high-salinity, HS) water-oil bank shock-front $M_{F,HS}$ is therefore given by

$$M_{F,HS} = \frac{\frac{k_{ro,HS}(s_{w,HS})}{\mu_o} + \frac{k_{rw,HS}(s_{w,HS})}{\mu_{w,HS}}}{\frac{k_{ro,HS}(s_{wi})}{\mu_o}} \tag{7.9}$$

The mobility ratio across the trailing injected chemical (or low-salinity, LS water) shock-front $M_{F,LS}$ is

$$M_{F,LS} = \frac{\frac{k_{ro,LS}(s_{w,LS})}{\mu_o} + \frac{k_{rw,LS}(s_{w,LS})}{\mu_{w,LS}}}{\frac{k_{ro,HS}(s_{w,HS})}{\mu_o} + \frac{k_{rw,HS}(s_{w,HS})}{\mu_{w,HS}}} \tag{7.10}$$

where $k_{ro,HS}(s_{w,HS})$ and $k_{rw,HS}(s_{w,HS})$ are the relative permeabilities of the oil and water respectively at the upper bound water saturation across the leading displaced chemical-free shock-front $s_{w,HS}$ under oil-wet conditions, $k_{ro,LS}(s_{w,LS})$ and $k_{rw,LS}(s_{w,LS})$ are the relative permeabilities of the oil and water respectively at the upper bound water saturation across the trailing injected chemical shock-front $s_{w,LS}$ under water-wet conditions, $k_{ro,HS}(s_{wi})$ is the oil relative permeability at initial water saturation or lower bound water saturation across the leading displaced chemical-free shock-front s_{wi} evaluated under oil-wetness, μ_o, $\mu_{w,HS}$ and $\mu_{w,LS}$ are the oil, resident HS-water, and injected LS-water viscosities respectively. For a LSWF, it is a practical assumption that $\mu_{w,HS} \approx \mu_{w,LS}$.

The amount of crossflow between layers is quantified with the effective shape factor R_l and the transverse gravity number N_{gv} for viscous and gravity-assisted crossflow respectively as defined by Zhou et al. (1994). These are scaling groups that have been reported consistent with experimental and numerical observations for displacement of oil by water in systems that contain some simple heterogeneity such as layers (Cinar et al., 2006). They are also adopted here to further check their consistency when describing crossflow between layers in typical EOR water-oil displacements such as engineered waterfloods.

The effective shape factor R_l is the permeability anisotropy-weighted shape factor. R_l^2 represents the time ratio for a fluid to flow a distance L in the horizontal direction to the distance H in the vertical direction with the same potential difference across the distance. The viscous flow capacities of the medium in vertical and horizontal directions is given by

$$R_l^2 = \left(\frac{L}{H}\right)^2 \frac{\bar{k}_v}{\bar{k}_h} \tag{7.11}$$

where $\frac{L}{H} = R$ and is the shape factor which scales the dimensions of the layered system, and $\frac{\bar{k}_v}{\bar{k}_h}$ is the global (or average) absolute permeability anisotropy across the layers. The average of the absolute longitudinal permeability to the injected or displacing phase $\bar{k}_h$ is taken to be the arithmetic mean, while it is the harmonic mean in the transverse direction $\bar{k}_v$. When $R_l^2 < 0.01$, for example if the layers are separated by an impermeable barrier, then the layers are non-communicating and, of course, there is no crossflow (NC). In the limit of large R_l^2 ($R_l^2 > 22$), the layers are perfectly communicating and crossflow occurs instantaneously such that transverse pressure gradients are negligible compared with longitudinal pressure gradients (Zhou et al., 1994). This limit is referred to as viscous crossflow equilibrium (VCE) or maximum crossflow, when flow may be treated as a single front (Zapata and Lake, 1981; Lake, 1989; Yortsos, 1995; Zhou et al., 1994). However, R_l typically varies between $0.1 - 100$ in layered sedimentary systems, with R often large, of order $10 - 100$, while k_v/k_h is typically small, of order $10^{-4} - 1$ (Zapata and Lake, 1981; Debbabi et al., 2017).

The transverse gravity number N_{gv} is the characteristic time ratio for fluid to flow in the transverse direction due to gravity forces to that in horizontal direction due to viscous forces. It is given as

$$N_{gv} = \frac{\Delta\rho g \bar{k}_h}{v\mu} \frac{L}{H} \frac{\bar{k}_v}{\bar{k}_h} \tag{7.12}$$

where $\Delta\rho$ is the density difference between the two immiscible fluids or phases, $v = \frac{q_t}{\varphi}$ and q_t is the total Darcy velocity, μ is the displaced phase viscosity, and g is the gravitational constant. In the absence of capillary effects, flow is viscous-dominated when $N_{gv}M_F(1 + M_F) < 0.2$ and gravity-dominated for $N_{gv}M_F(1 + M_F) > 5.0$, with transitioning behaviour between both dominated regions for $0.2 < N_{gv}M_F(1 + M_F) < 5.0$ (Zhou et al., 1994; Cinar et al., 2006). Gravity influence on crossflow effects is evaluated both when the fast layer is atop and when the slow layer is atop, to examine the significance of layer-ordering on gravity-assisted crossflow.

The impact of the dimensionless numbers on flow is characterized in terms of the oil recovery efficiency, defined as

$$URF = \frac{Oil\ recovered}{Oil\ Initially\ In\ Place} \tag{7.13}$$

where URF is the oil recovery efficiency in pore-volumes (PV) of the oil-zone, and $0 < URF < 1$.

Crossflow effects on recovery efficiency relative to no-crossflow (NC) displacement is presented as change in recovery efficiency, given by

$$\Delta URF = URF_C - URF_{NC} \tag{7.14}$$

where ΔURF is the change in recovery efficiency, URF_C and URF_{NC} are respectively the crossflow and no-crossflow recovery efficiency. Crossflow is favourable with improvement in oil recovery efficiency when compared to no-crossflow if ΔURF is positive, and it is unfavourable for negative ΔURF. Crossflow becomes unimportant to recovery efficiency at $\Delta URF = 0$.

Recovery efficiency is evaluated three times: after injection of 0.5, 1.0 and $2.0\ PV$ EOR-chemical or LS-slug sizes at a cumulative water injection (LS + HS brine) of $2.5\ PV$. These are adopted as representative early-, mid-, and late-time performance of injected engineered water or LS-slug respectively. The different performance-times are used to primarily explore the displacement stability of injected LS-slug and the extent of crossflow importance, both as functions of VC behaviours during LSWF.

Crossflow effects on recovery efficiency is considered under two flow regimes – convective and dispersive flow, to comparatively evaluate the significance of physical mixing during displacement. The combined effects of molecular diffusion and physical dispersion (Perkins and Johnston, 1963) discussed in Chapter 2.7.1 – and presented in equations (2.13) and (2.14) – are also adopted here to model mixing or dilution between the injected low-salinity (or engineered water) and resident high-salinity brines.

For convective flow, only the numerical diffusivity $D_{L,num}$ at the isotropic grid-block size adopted ($\Delta X = \Delta Y = \Delta Z = 1.5\ m$) is considered with no input longitudinal or transverse dispersivity. This gives a numerical Peclet number (*Pe*) of 400 or 0.25% of the model-length L using the formulas: $D_{L,num} = \frac{1}{L}\left(\frac{\Delta X}{2} + v\frac{\Delta t}{2}\right)$ and $Pe = \frac{1}{D_{L,num}}$, equations 2.10 and 2.15 respectively. This level of mixing or dilution is assumed small enough for the injected slug sizes to describe the field-scale convective flow behaviour of such a typically dispersive EOR process.

Under dispersion, an additional input longitudinal physical dispersivity (α_l) range of $2.25 - 14.25\ m$ is considered, equating to a total Peclet number (*Pe*) range of $20 - 100$ or $1 - 5\%$ of the model-length L. This is similar to how the total dispersion in simulations was modelled and controlled in Chapters 5 and 6. As discussed in Chapter 3.1 and adopted in previous chapters, this range adequately captures and agrees with reported levels of physical mixing associated with larger-scale heterogeneities present in field-scale porous media. Besides, for the selected $D_{L,num}$, such range of α_l ensures that the component-transport is advection-controlled or convection-dominated during

flow as reported for practical displacements. The range also exceeds the 'critical input dispersivity' at the grid resolutions thereby enabling its accurate representation in simulations considering the (constant) numerical component present. Furthermore, transverse physical dispersivity $\alpha_t \cong \alpha_l/30$ at each level of physical mixing in all the evaluations considered – which gives a transverse dispersivity range of $0.08 - 0.48\ m$ for the case studied here.

7.3 Results

7.3.1 Effect of Property Contrasts on Viscous-dominated Crossflow (VC)

The existence of crossflow between layers is defined by the flow transmissibility across their interface, and this is principally controlled by the lower transverse permeability of the two layers. While the interlayer storage (porosity) contrast R_s modifies the influence of the permeability contrast R_k on the displacing-phase relative velocity in the layers through the resulting property-contrast ratio C (Debbabi et al., 2017), R_k exclusively defines the existence of crossflow, see equations (7.1) – (7.3). This section evaluates the impact of R_k on VC, and explores for representative C, with adequate VC, to characterize the plausible scenarios of the displacing-phase relative velocity in both layers in subsequent analysis.

For this analysis we assume $R_s = 1$, therefore $C = R_k$, and R_k is varied over the range $1 - 10^6$ which makes ${k_h}^1 > {k_h}^2$. The local absolute permeability anisotropy in each layer is set at 1 (i.e. $\frac{k_v}{k_h} = 1$), thus, ${k_h}^1 > \bar{k}_v > {k_h}^2$ for each C. This ensures maximum flow transmissibility (absolute open crossflow) across the interface for each C. To control the amount of crossflow for each C, R_l^2 is varied with the shape factor R (over a range $10 \leq R \leq 100$) since the global permeability anisotropy $\frac{\bar{k}_v}{\bar{k}_h}$ is constant and already at maximum (i.e. $\frac{k_v}{k_h} = 1$). For the (single) mobility-ratios case considered here, the selected Corey exponents are $n_w = 2.3$, $n_o = 3.7$ for high-salinity (oil-wet) conditions and $n_w = 2.5$, $n_o = 2.3$ for low-salinity (water-wet) conditions – which are typical for geologic porous media and yield non-piston-like displacements (e.g. **Fig. 7.1**d). $k_{r,w}^e$, $k_{r,o}^e$, μ_o, and μ_w are all set for both wettability states such that $M_{F,HS} = 0.5$ (favourable displacement) and $M_{F,LS} = 1.5$ (unfavourable displacement). The relative permeabilities – used to characterize the high- and low-salinity mobilities – that result from the set values of these parameters which are likely for this case in real systems are presented in **Appendix C**. Recovery efficiency is evaluated at different performance times (or injected LS-slug sizes) and flow regimes – convective and dispersive flows, to distinguish EOR-LS crossflow from chemical-free HS cross-streams.

Fig. 7.3 highlights the regions in which viscous crossflow is important in water-oil displacements in stratified systems with a permeability contrast. No VC exists for $C > 10^3$ regardless of the shape factor (R) as recovery converges to a single-layer homogeneous performance. While the crossflow of displaced or injected chemical-free HS-brine is feasible for $C \leq 10^3$, a significant cross-stream of injected EOR-chemical or LS-water requires $C \leq 50$ between the layers. This is because the equal late-time performance ($2.0\ PV$) for $C > 50$ under convection and dispersion indicates no dispersion effects in the slow layer as the fast layer is completely swept with the LSE at such LS-slug injection (if compared to $0.5\ PV$) hence, no LS crossflow. This also implies that the injected LS-brine is of almost zero front-velocity in the slow layer ($U_t^s = 0$; see **Fig. 7.1**b) for $C > 50$ since ${k_h}^1 >> \bar{k}_v >> {k_h}^2$.

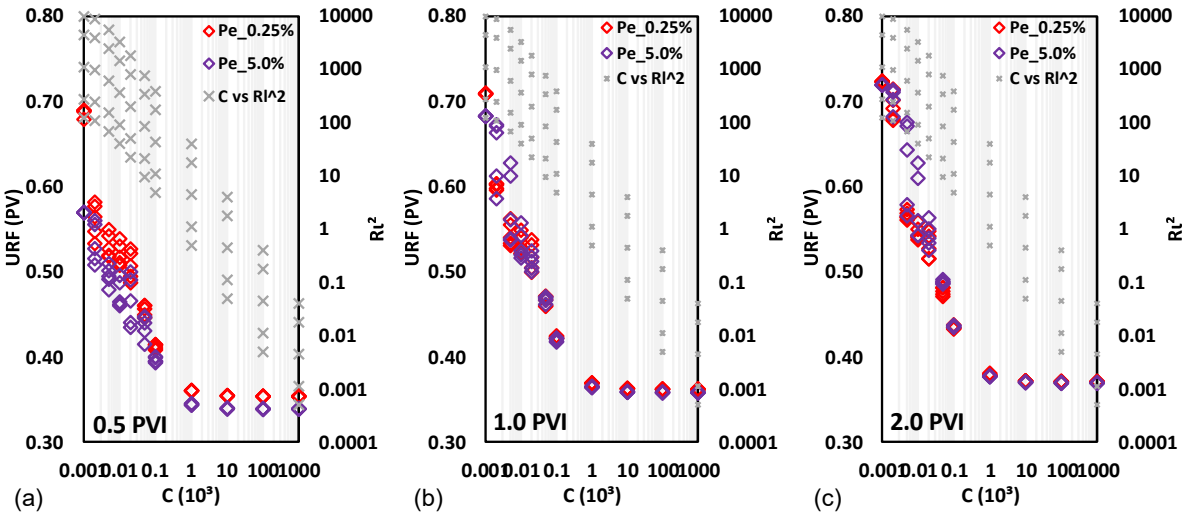


Fig. 7.3: Recovery efficiency (URF) as a function of property-contrast ratios (C) for convective ($Pe_0.25\%$) and dispersive ($Pe_5.0\%$) LSWF at different performance times (injected LS-slug sizes) (a) $0.5\ PV$. (b) $1.0\ PV$. (c) $2.0\ PV$. Also included is the range of R_l^2 considered for each property-contrast ratio (C).

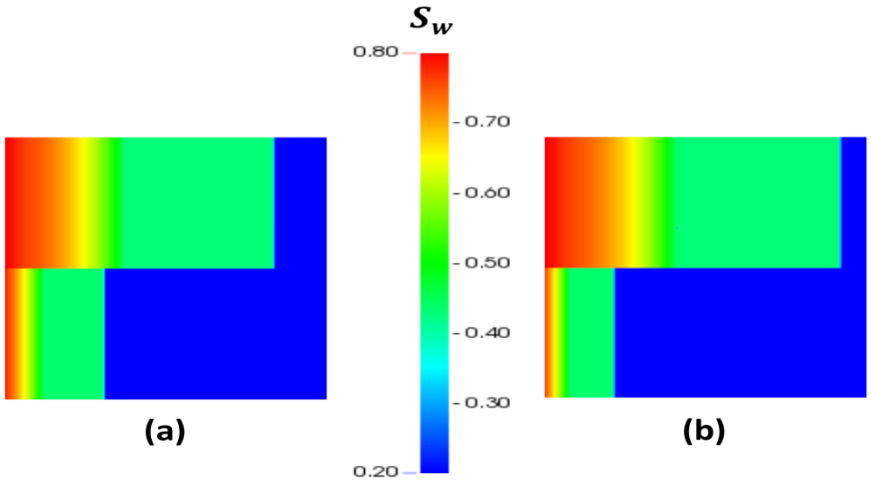


Fig. 7.4: Displacing-phase (water) saturation profile showing its relative velocity or mobility in the layers just before breakthrough at different property-contrast ratio (a) $C = 5$ ($U_t^f < U_l^s$). (b) $C = 10$ ($U_t^f > U_l^s$).

For subsequent analysis of VC behaviour during LSWF, $C = 5$ and $C = 10$ are selected as representative to characterize the two plausible scenarios of the displacing-phase relative velocity in both layers (i.e. $U_t^f < U_l^s$ and $U_t^f > U_l^s$; shown in **Fig. 7.4**) which are of interest in this study. Both permeability-storage contrast ratios maintain wider dispersion effects across performance times, with adequate range of possible R_l^2 across shape factors (**Fig. 7.3**). Their range of C has also been explored in previous work to investigate the impact of VC on displacement efficiency in layered porous media (Zapata and Lake, 1981; Debbabi et al., 2017).

7.3.2 Prediction of Viscous Crossflow (VC) Regimes in LSWF

The impact of property contrasts on the presence of VC in layered systems was discussed in the previous section, and representative property-contrast ratios were identified to characterize the crossflow behaviour. The crossflow regimes in a LSWF are now considered under the two plausible scenarios of the displacing-phase relative velocity in the layers (**Fig. 7.4**).

Mobility ratio-induced VC regimes are predicted by comparing the pressure profiles obtained in each layer when there is no crossflow ($R_l^2 \ll 1$). This is because VC results from transverse contrasts in total fluid mobility across a stratified or layered section which create horizontal flow potentials that are different vertically across some positions. Uniform pressure boundary conditions at the inlet and outlet allow direct comparison of the pressure profiles obtained in the two layers. Displacing-phase crossflow is predicted to occur from high to low pressure regions, while the displacing-phase can only crossflow out of the invaded part of a layer behind the shock-front. Since non-piston-like displacements are considered and pressure gradients may vary behind the shock-front due to spatial

changes in total fluid mobility, the pressure profiles are constructed by assuming that the total mobility behind the shock-front may be approximated by the total mobility at the shock-front (Debbabi et al. 2017). Thus, pressure decreases linearly behind the shock-front and its profile can therefore be described as linear by parts. While the effect of property contrasts on the displacing-phase velocities in the layers is considered, mobility ratio is assumed equal across identical shock-fronts in both layers.

For all the mobility-ratio cases considered here, the Corey exponents are interchanged between $n_w = 2$ and 3.7, $n_o = 2.3$ and 3 for high-salinity (oil-wet) conditions; and $n_w = 2.5$ and 4, $n_o = 2.3$ and 2.5 for the low-salinity (water-wet) effect to yield non-piston-like displacements. $k^e_{r,w}$, $k^e_{r,o}$, μ_o, and μ_w are all set such that each shock-front mobility ratio is either 0.5 or 1.5. The relative permeabilities – used to characterize the high- and low-salinity wetting conditions – that result from the values of these parameters which are likely for the cases in real systems are presented in **Appendix C**. Numerical solutions are obtained for a convective flow regime (i.e. *Pe* of 400 or 0.25% of the model-length L). Pressure profiles are expressed in terms of the mobility ratios across the identical pairs of shock-fronts along both layers and are summarised in **Fig. 7.5** and **Fig. 7.6** for a typical waterflood and a LSWF respectively. These can be interpreted to predict crossflow by comparing the pressure and the location of each shock-front in each layer, since VC is centred around the shock-fronts. For the fully-favourable and fully-unfavourable mobility-ratio cases in LSWF (the lower-left and the upper-right quadrants in **Fig. 7.6**), we recover the two crossflow regimes in **Fig. 7.5** respectively if only the HS-brine is injected.

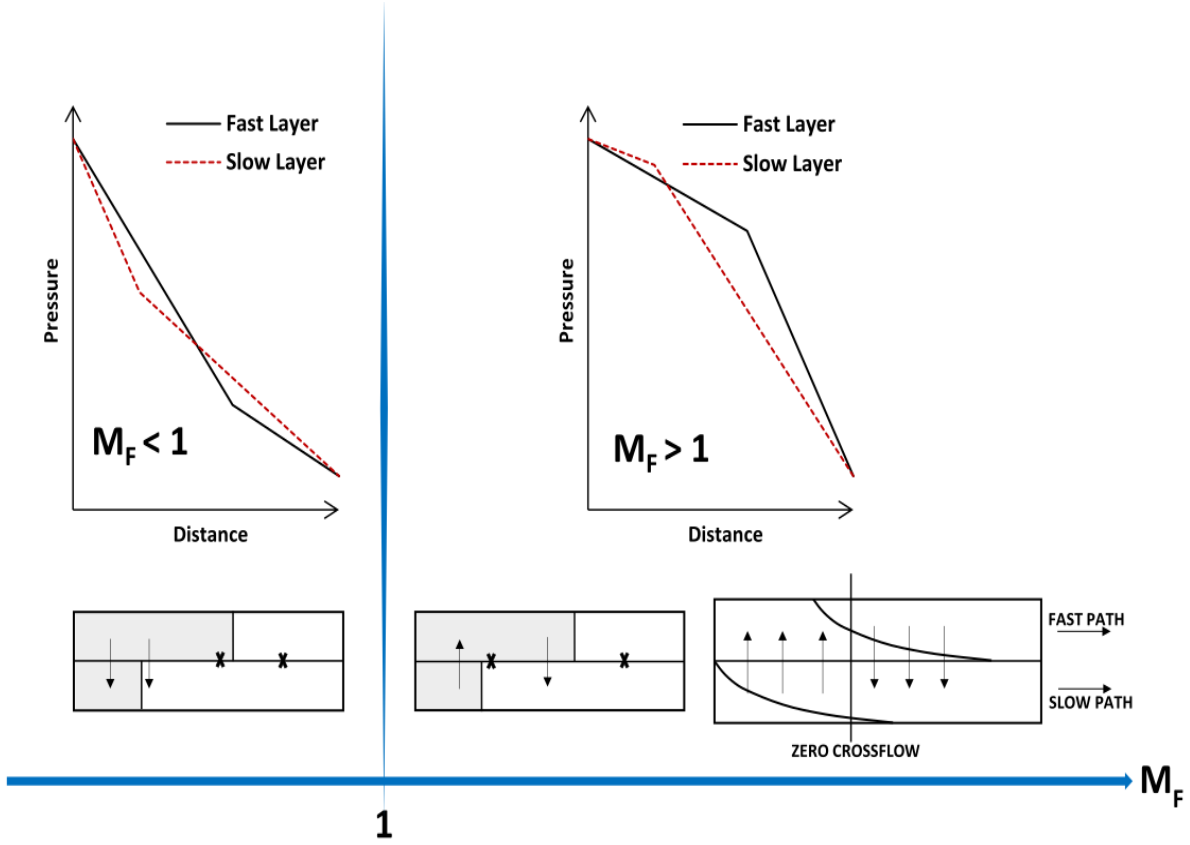


Fig. 7.5: Schematic of pressure profiles obtained in the fast and slow layers for a typical waterflood without crossflow ($R_l^2 \ll 1$) for favourable (left half) and unfavourable (right half) shock-front mobility ratios. Displacing-phase crossflow shown in the adjacent schematics are predicted from the pressure profiles. Arrows indicate the displacing-phase crossflow direction across the interface separating the two layers. Crosses indicate no-crossflow of the displacing-phase. The zero-crossflow point is indicated between opposing crossflow directions for unfavourable mobility-ratio displacement (right half).

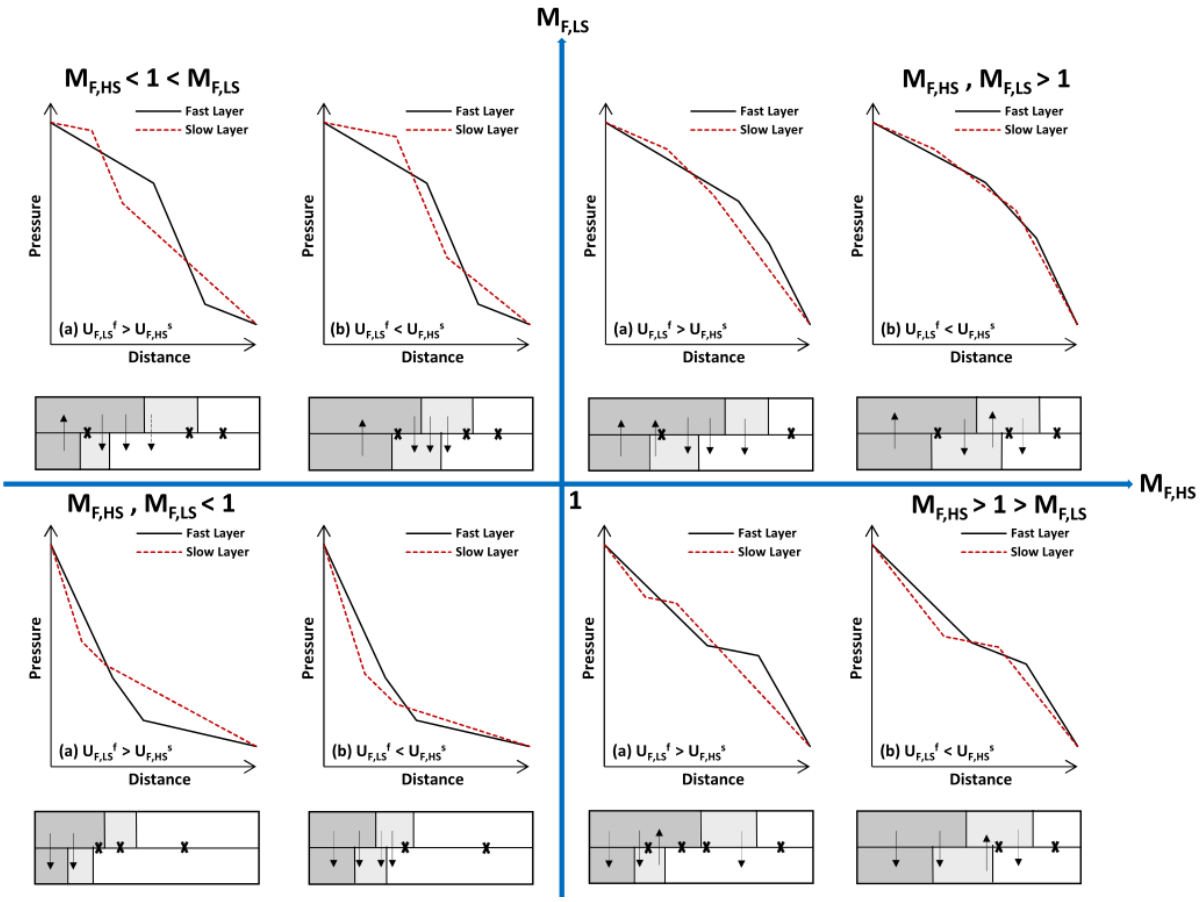


Fig. 7.6: Schematic of pressure profiles obtained in the fast and slow layers for a LSWF without crossflow ($R_l^2 \ll 1$) for four shock-front mobility-ratio cases considering the two plausible scenarios of the displacing-phase relative velocity in both layers. Crossflow behaviour shown in the adjacent schematics are predicted from the pressure profiles. Arrows indicate crossflow direction across the interface separating the two layers. Crosses indicate no-crossflow. The zero-crossflow point is indicated between opposing crossflow directions which signifies the presence of an unfavourable mobility-ratio displacement.

For a typical water-oil displacement with a single shock-front along each layer during flow, two crossflow regimes or directions are identifiable if the mobility ratio across the shock-front is assumed equal in both layers (**Fig. 7.5**). These are also observed in previous studies (Zapata and Lake, 1981; Debbabi et al., 2017). They include: (1) a unidirectional crossflow regime across the interface between the layers for $M_F < 1$, in which the displacing-phase crossflow is only from the fast layer to the slow layer behind and around its shock-front (the left half in **Fig. 7.5**), with reduced distance between the two shock-fronts which leads to delayed breakthrough and better recovery efficiency if compared to the no crossflow (NC) displacement; and (2) significant crossflow in both directions behind and ahead of the slow shock-front for $M_F > 1$ (the right half in **Fig. 7.5**), with elongated distance between the two shock-fronts (whose impact on recovery efficiency compared to NC displacement is a function of performance times), and a stable point of zero-crossflow, between the opposing crossflow directions,

with complex saturation changes along the interface as observed in other studies (Zapata and Lake, 1981; Debbabi et al., 2017).

Conversely, for an engineered waterflood or LSWF with two shock-fronts along each layer during flow, VC is centred around four shock-fronts and four possible mobility-ratio cases (**Fig. 7.6**). Two distinct crossflow regimes or directions are observed considering the two plausible scenarios of the displacing-phase relative velocity in both layers (i.e. $U^f_{F,LS} > U^s_{F,HS}$ and $U^f_{F,LS} < U^s_{F,HS}$, presented in **Fig. 7.4**) for each mobility-ratio case. They include: (1) a unidirectional crossflow from the fast to the slow layer for only $M_{F,HS},\ M_{F,LS} < 1$ (the lower left quadrant in **Fig. 7.6**); and (2) crossflow in both directions for other mobility-ratio cases (i.e. $M_{F,HS} < 1 < M_{F,LS}$; $M_{F,HS},\ M_{F,LS} > 1$; and $M_{F,HS} > 1 > M_{F,LS}$).

7.3.3 Viscous Crossflow During Non-piston-like Displacements in LSWF

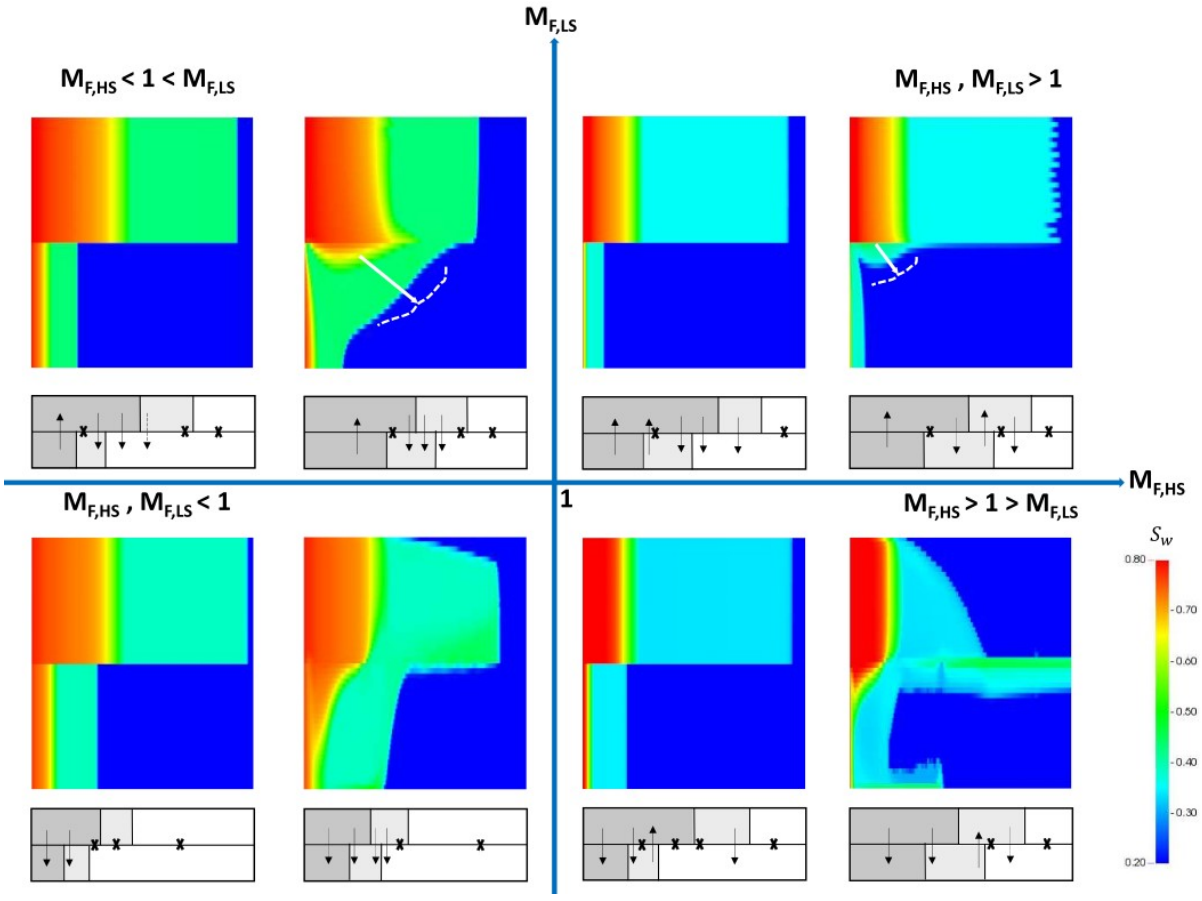


Fig. 7.7: Displacing-phase viscous crossflow behaviours (right of each quadrant), relative to a no crossflow (NC) displacement (left of each quadrant), as a function of the characterized shock-front mobility-ratio cases. White arrow with dashed curve in top quadrants indicates emerging secondary chemical-free or HS-front from the LS crossflow in the slow layer.

Viscous crossflow is now examined with $R^2_l > 1$ under the convective flow regime to confirm predictions from the previous section. **Fig. 7.7** shows the displacing-phase saturation obtained with

crossflow relative to a no-crossflow displacement (NC) for one of the two plausible scenarios considering the displacing-phase relative velocity in both layers. This is presented for the four mobility-ratio cases with their characterized possible crossflow directions also highlighted as shown earlier in **Fig. 7.6**. These profiles confirm the crossflow directions predicted in the previous section.

An emerging secondary chemical-free or HS-front that results from the LS crossflow is observed in the slow layer (see arrows with dashed curves in top quadrants of **Fig. 7.7**). This propagates rapidly with displacement; and facilitates the connectivity of the (two) primary leading HS-fronts across both layers, thereby converting a potentially $U_{F,LS}^{f} > U_{F,HS}^{s}$ scenario under NC to a $U_{F,LS}^{f} < U_{F,HS}^{s}$ scenario of the mobility-ratio case under VC. The secondary chemical-free shock-front is also found to be distinctly pronounced when its initiating chemical crossflow is of a shock-front with unfavourable mobility-ratio displacement (i.e. $M_{F,LS} > 1$ – a forward-acting crossflow).

The formation of viscous fingers, which is expected when $M_F > 1$, is also observed in both the fast and the slow layers (Riaz and Tchelepi, 2006) – **Fig. 7.7** (right-top and -bottom quadrants). The displacing-phase volumes in each layer, relative to the NC displacement, is influenced by crossflow considering the positions of identical shock-fronts in both layers with and without VC. It is found that crossflow reduces the distance between connected identical shock-fronts in adjacent layers when $M_F < 1$ and vice versa for $M_F > 1$. Crossflow occurs in both directions for other mobility-ratio cases except for $M_{F,HS}$, $M_{F,LS} < 1$. However, their point of zero-crossflow between opposing crossflow directions remains stable along the interface of the layers only when the chemical-free or HS-front is of a favourable mobility-ratio displacement ($M_{F,HS} < 1 < M_{F,LS}$). This is further confirmed at higher grid resolutions to eliminate the possibility of being influenced by numerical errors. It is suggested here that its instability between opposing crossflow directions of the displacing-phase when $M_{F,HS} > 1$ results from the opposing dilution effect from the HS crossflow from adjacent layer, even under limited mixing.

7.3.4 Viscous Crossflow Recovery Efficiency as Function of Shock-front Mobility Ratios

Our analysis now explores the sensitivity of VC recovery and chemical-sweep efficiency to the mobility-ratios across shock-fronts with non-piston-like displacements during engineered waterflooding or LSWF. This is evaluated in terms of the change in recovery efficiency due to crossflow (ΔURF) at different performance times (i.e. injected LS-slug sizes) within the limits of no-crossflow (NC) and maximum crossflow (VCE). The two plausible scenarios of the displacing-phase relative velocity in both layers (characterized earlier by $C = 5$ and $C = 10$ and presented in **Fig. 7.4**) are considered, to assess

its influence on the effect of crossflow on recovery efficiency. The flood performance is considered under separate flow regimes as before – convective and dispersive flow – to evaluate the impact of physical mixing on crossflow recovery efficiency relative to NC displacement.

For convective LSWF (**Fig. 7.8**), the improved recovery efficiency with crossflow ($+\Delta URF$) is found to decrease from moderate to maximum crossflow limit ($R_l^2 \geq 1$) for the $M_{F,HS} < 1 < M_{F,LS}$ mobility-ratio case. Moreover, its crossflow recovery efficiency becomes generally worse than NC, regardless of R_l^2, as the displacing-phase relative velocity or mobility in the slow layer increases (i.e. from $C = 10$ to $C = 5$). This trend, which is independent of performance times (or injected EOR chemical-slug sizes), has not been reported previously and will be discussed later in this section.

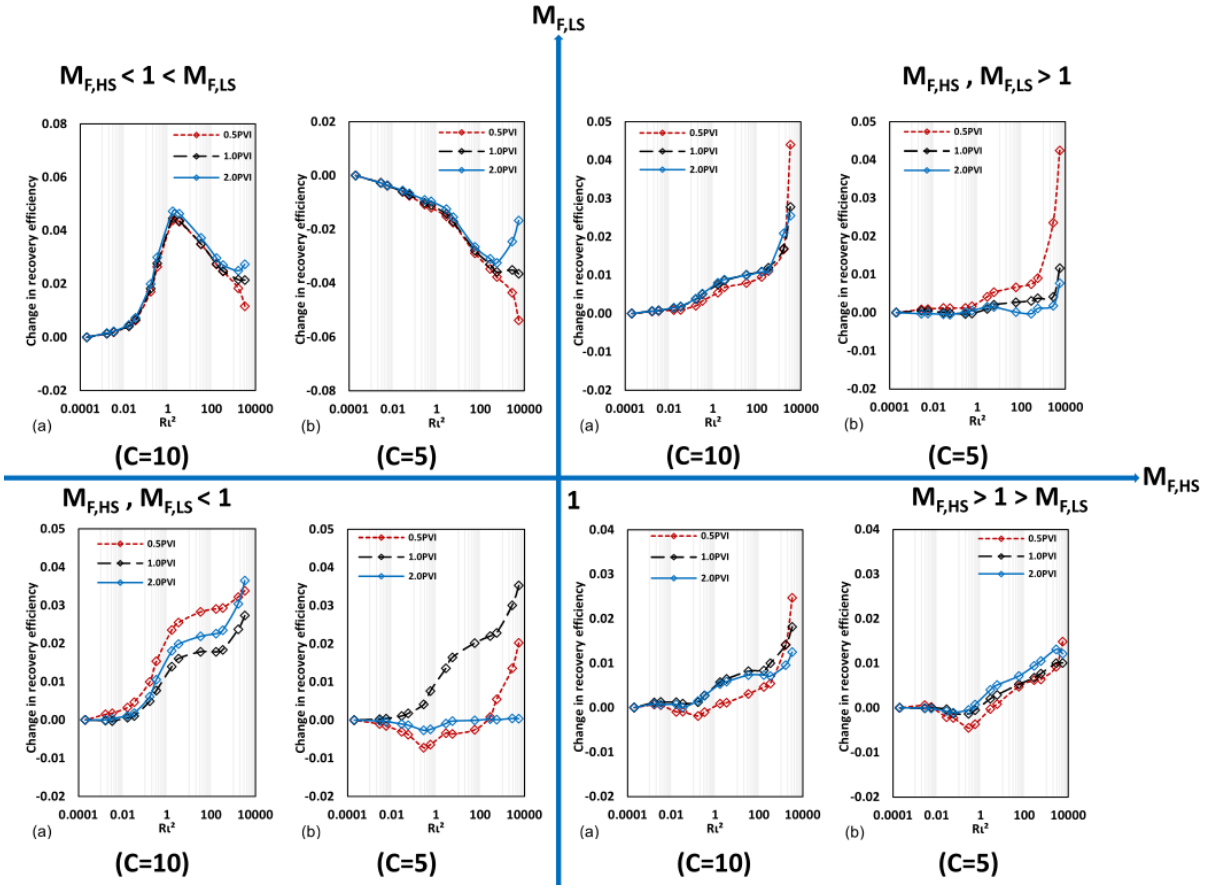


Fig. 7.8: Change in recovery efficiency due to crossflow (ΔURF) as a function of crossflow amount (R_l^2) for various shock-front mobility-ratio cases in a convective secondary LSWF (*Pe* of 0.25% of the model-length L). Results are shown for $C = 5$ and $C = 10$ at different performance times (or injected LS-slug sizes: *red* $0.5\ PVI$, *black* $1.0\ PVI$, *blue* $2.0\ PVI$) in a cumulative injection (LS + HS) of $2.5\ PVI$.

Conversely, crossflow recovery efficiency is better than NC displacement at other mobility-ratio cases considered if a sufficiently large slug is injected ($\geq 1\ PVI$). For these favourable mobility-ratio cases, crossflow recovery efficiency at early times (i.e. small injected slug sizes, $0.5\ PVI$) gets worse and may be unfavourable at increased displacing-phase velocity in the slow layer (U^S) if the crossflow is limited

($R_l^2 < 1$). This is because, at limited R_l^2, the crossflow chemical-sweep in the slow layer becomes less stable with lower C (i.e. increased U^s reduces the crossflow chemical volume in the slow layer) especially in the absence of any (transverse) dispersion support. At late-times under moderate property-contrast ratios, recovery efficiency has been reported to be weakly-dependent or independent of R_l^2 in a typical waterflood due to improved NC displacement (Zapata and Lake, 1981; Debbabi et al., 2017). This is found here to be true for engineered waterflood or LSWF (at $2.0\ PVI$ for $C = 5$) only when the shock-fronts are of similar mobility-ratio displacements (i.e. both are either favourable or unfavourable). This appears consistent with earlier findings in a typical waterflood where displacement is also convective because it is under only such mobility-ratios combination that the shock-fronts remain single-acting either forwardly (unfavourable displacement) or backwardly (favourable displacement).

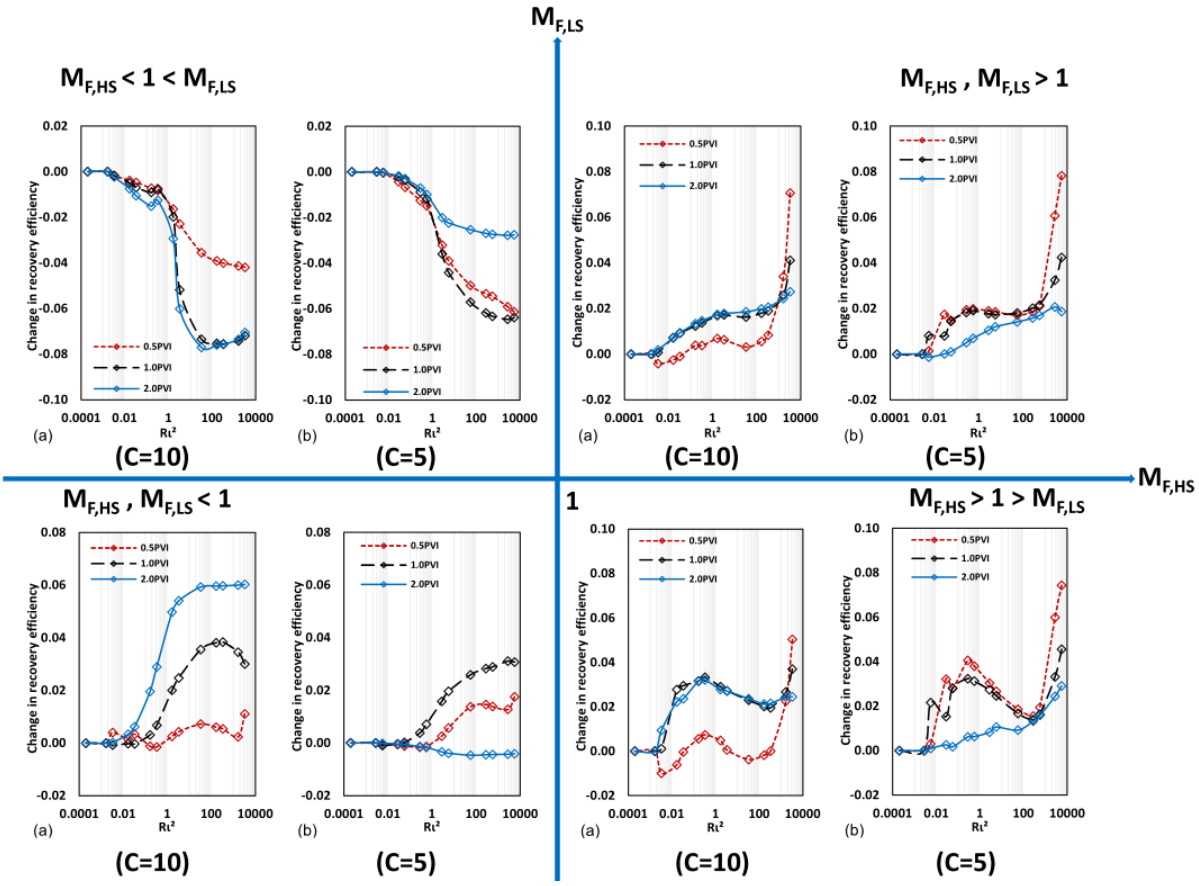


Fig. 7.9: Change in recovery efficiency due to crossflow (ΔURF) as a function of crossflow amount (R_l^2) for various shock-front mobility-ratio cases in a secondary LSWF with significant dispersion (*Pe* of 2.0% of the model-length L). Results are shown for $C = 5$ and $C = 10$ at different performance times (or injected LS-slug sizes: *red* $0.5\ PVI$, *black* $1.0\ PVI$, *blue* $2.0\ PVI$). Similar results for other levels of dispersion (*Pe*) are presented in **Appendix D**.

With significant dispersion (**Fig. 7.9**), viscous crossflow is unfavourable to recovery efficiency across performance times (or injected slug sizes) for the $M_{F,HS} < 1 < M_{F,LS}$ mobility-ratio case. For other

mobility-ratio cases, crossflow recovery efficiency remains better than NC displacement with sufficient slug sizes ($\geq 1\ PVI$). However, their early-time performance ($0.5\ PVI$) under limited crossflow ($R_l^2 < 1$) is seen to be favourable here at high or increased displacing-phase velocity in the slow layer (U^s). This shows improved crossflow chemical-sweep stability in the slow layer at limited R_l^2 and slug injection, which results from the (transverse) dispersion of chemical flow in the fast layer.

As suggested by Zapata and Lake (1981), we confirm that increasing the displacing-phase relative mobility or velocity in the slow layer such that $U_{F,LS}^f < U_{F,HS}^s$ (e.g. from $C = 10$ to $C = 5$) renders the chemical sweep efficiency generally favourable with R_l^2 under dispersion, especially when the injected EOR-slug size is limited ($0.5\ PVI$). However, this is found to be ineffective for the $M_{F,HS} < 1 < M_{F,LS}$ case and would also be discussed later in this section. Besides, unfavourable crossflow at early-times ($0.5\ PVI$) due to unfavourable mobility-ratio displacement across the chemical-free shock-front ($M_{F,HS} > 1$) and reduced or low displacing-phase velocity in the slow layer ($U_{F,LS}^f > U_{F,HS}^s$, e.g. $C = 10$), is observed to be largely favourable if the EOR-chemical crossflow is forward-acting (i.e. $M_{F,LS} > 1$). Therefore, a favourable VC effect on recovery efficiency can be harnessed through the shock-front mobility-ratios combination and the displacing-phase relative mobility or velocity in the layers when designing such mixing-sensitive EOR-displacements with limited slug injections. The weak-dependence or independence of recovery efficiency on R_l^2 at late-times ($2.0\ PVI$ and $C = 5$) persists under dispersion but only for the $M_{F,HS},\ M_{F,LS} < 1$ mobility-ratio case. VC remains important to recovery efficiency at late-times for $M_{F,HS},\ M_{F,LS} > 1$ because of the favourable dispersion induced by its forward-acting crossflow over NC displacement.

For $C = 10$ where VC is important irrespective of performance times, mobility-ratio cases, and dispersion levels (**Fig. 7.8** and **Fig. 7.9**), the optimal slug or chemical amount to inject to stabilize its EOR sweep or displacement appears largest (e.g. $> 1.0\ PVI$) when $M_{F,HS},\ M_{F,LS} < 1$. This is reflected in the increasing change in recovery efficiency (ΔURF) with injected slug size (i.e. no convergence in its improved performance as at $2.0\ PVI$). We suggest it results from the preferential flow of the chemical-free bank with low-mobility through the slow layer. This further delays the already low mobility of the crossflow-chemical and its sweep stability which is responsible for the improved recovery efficiency in the layer.

We investigate the generally unfavourable viscous crossflow effect on recovery efficiency earlier identified with the $M_{F,HS} < 1 < M_{F,LS}$ mobility-ratio case (the upper left quadrants in **Fig. 7.8** and **Fig. 7.9**). This is explored with the EOR-chemical (or LS-slug) sweep efficiency or effectiveness within the limits of no-crossflow (NC) and maximum crossflow (VCE), using its concentration (salinity) and water saturation profiles during displacement.

For convective flow (**Fig. 7.10**), the crossflow chemical sweep efficiency or effectiveness in the slow layer decreases with R_l^2 (for $R_l^2 \geq 1$) despite $M_{F,HS} < 1$ (i.e. no crossflow of chemical-free water-bank into the fast layer irrespective of U^s). The profiles show viscous crossflow to be unfavourable because of enhanced dilution in the slow layer with R_l^2. This results from the forward-acting chemical or LS crossflow in the slow layer now in closer contact with the enlarged chemical-free water-bank – a combination of the connecting (crossflow-induced) secondary HS-front and the (two) primary leading HS-fronts in both layers. In addition, the connected enlarged chemical-free water-bank preferentially flows through the slow layer since $M_{F,HS} < 1$ (backward-acting crossflow). We observe the same enhanced dilution effects from the enlarged chemical-free water-bank preferentially flowing through the slow layer under dispersion (**Fig. 7.11**a).

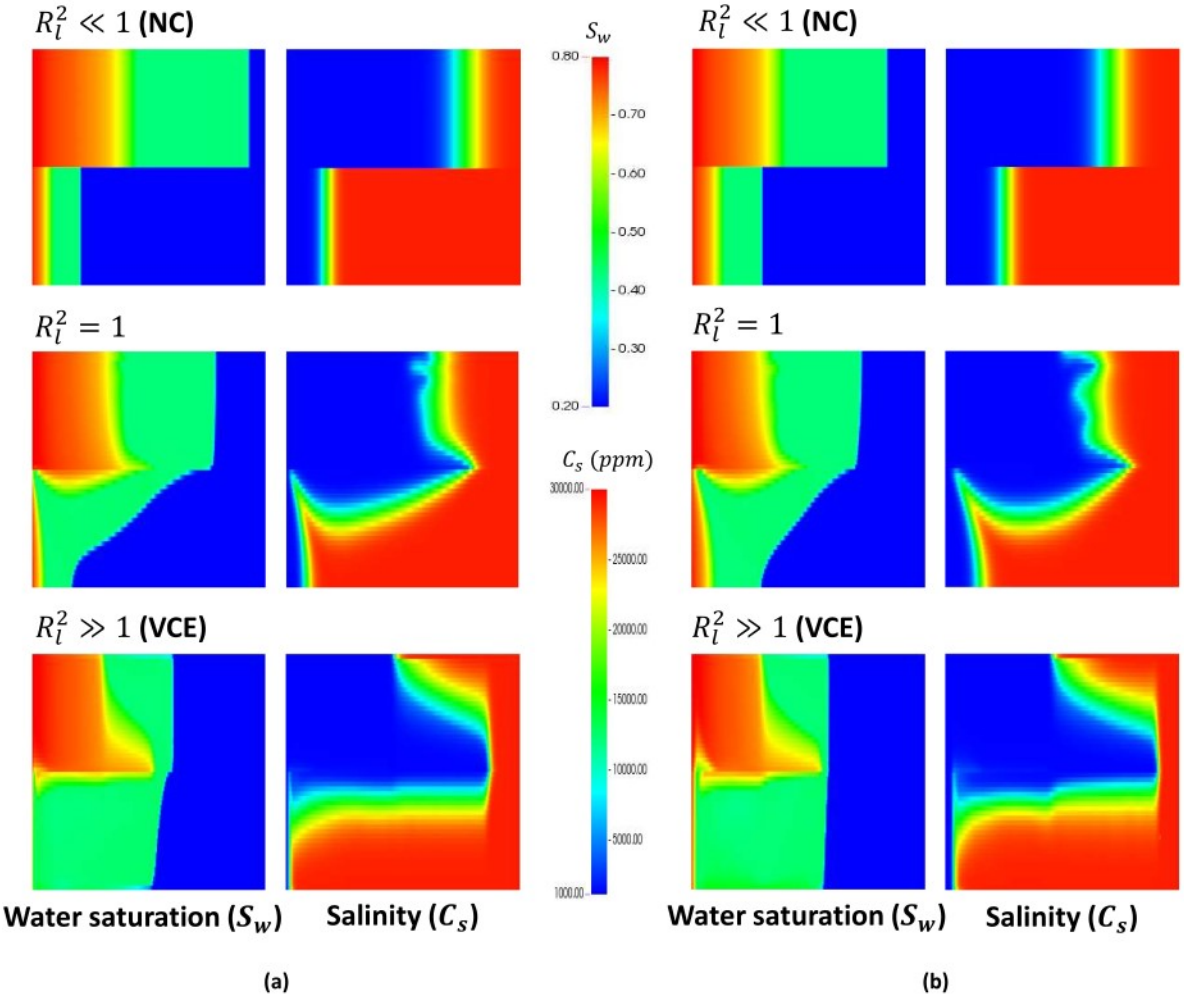


Fig. 7.10: Water saturation and salinity profiles within the limits of no viscous crossflow (NC) and viscous crossflow equilibrium (VCE) for the $M_{F,HS} < 1 < M_{F,LS}$ mobility-ratio case for a convective secondary LSWF (*Pe* of 0.25% of the model-length L) at different permeability-storage contrast ratios. (a) $C = 10$. (b) $C = 5$.

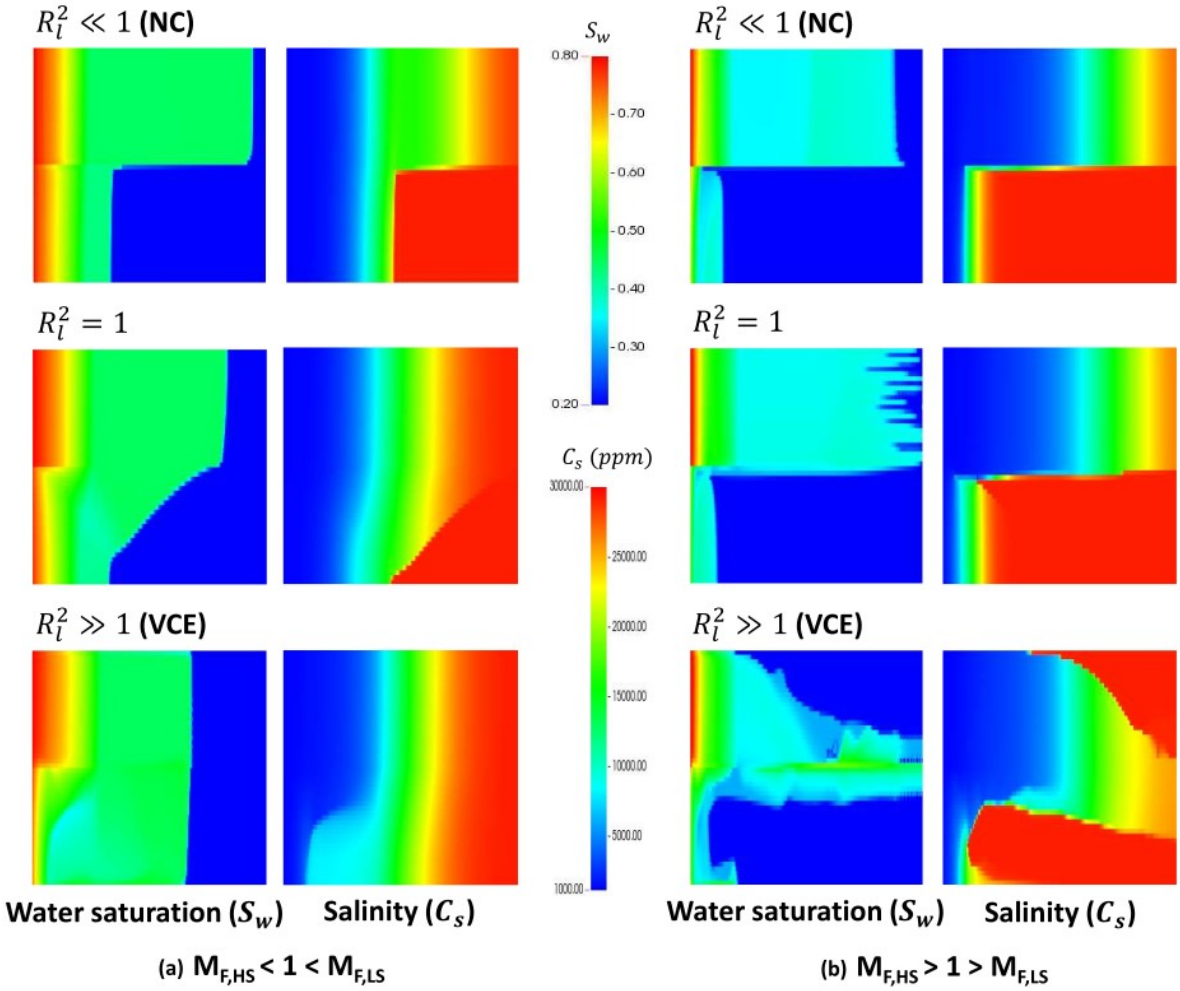


Fig. 7.11: Water saturation and salinity profiles within the limits of no viscous crossflow (NC) and viscous crossflow equilibrium (VCE) for a secondary LSWF with significant dispersion (*Pe* of 2.0% of the model-length L) at $C = 5$ for different mobility-ratio cases. (a) $M_{F,HS} < 1 < M_{F,LS}$. (b) $M_{F,HS} > 1 > M_{F,LS}$.

Therefore, it can be concluded that unfavourable VC occurs when the connected chemical-free water-banks preferentially flows through the slow layer, and not necessarily due to chemical-free crossflow into the fast layer suggested by Zapata and Lake (1981). This explains why their proposed increase in displacing-phase relative mobility in the slow layer for favourable VC chemical sweep efficiency under dispersion, especially with limited slug injections, appears ineffective for $M_{F,HS} < 1 < M_{F,LS}$. It is effective, for example, for $M_{F,HS} > 1 > M_{F,LS}$ because the displacing chemical crossflow is behind and around its shock-front in the slow layer with reduced distance between its adjacent identical shock-fronts relative to NC displacement (**Fig. 7.11**b). This lessens the dilution interference from the connected enlarged leading chemical-free bank which, besides, now preferentially flows through the fast layer ($M_{F,HS} > 1$), faster and ahead of the displacing crossflow chemical. Either of these displacement mechanisms similarly plays out at other mobility-ratio cases. However, the exact reverse

is the case with $M_{F,HS} < 1 < M_{F,LS}$ – forward-acting chemical crossflow and backward-acting chemical-free water-bank crossflow (**Fig. 7.11**a).

7.3.5 Designing Favourable Crossflow Effects with $M_{F,HS} < 1 < M_{F,LS}$

The unfavourable shock-front mobility-ratios combination for VC recovery efficiency was identified and discussed previously for an engineered waterflood or LSWF. This section focuses on how favourable crossflow recovery efficiency can be designed under such conditions. We first examine the impact of gravity and shape-factor on the crossflow effect and recovery efficiency, and then suggest approaches to a favourable viscous crossflow displacement for the $M_{F,HS} < 1 < M_{F,LS}$ mobility-ratio case.

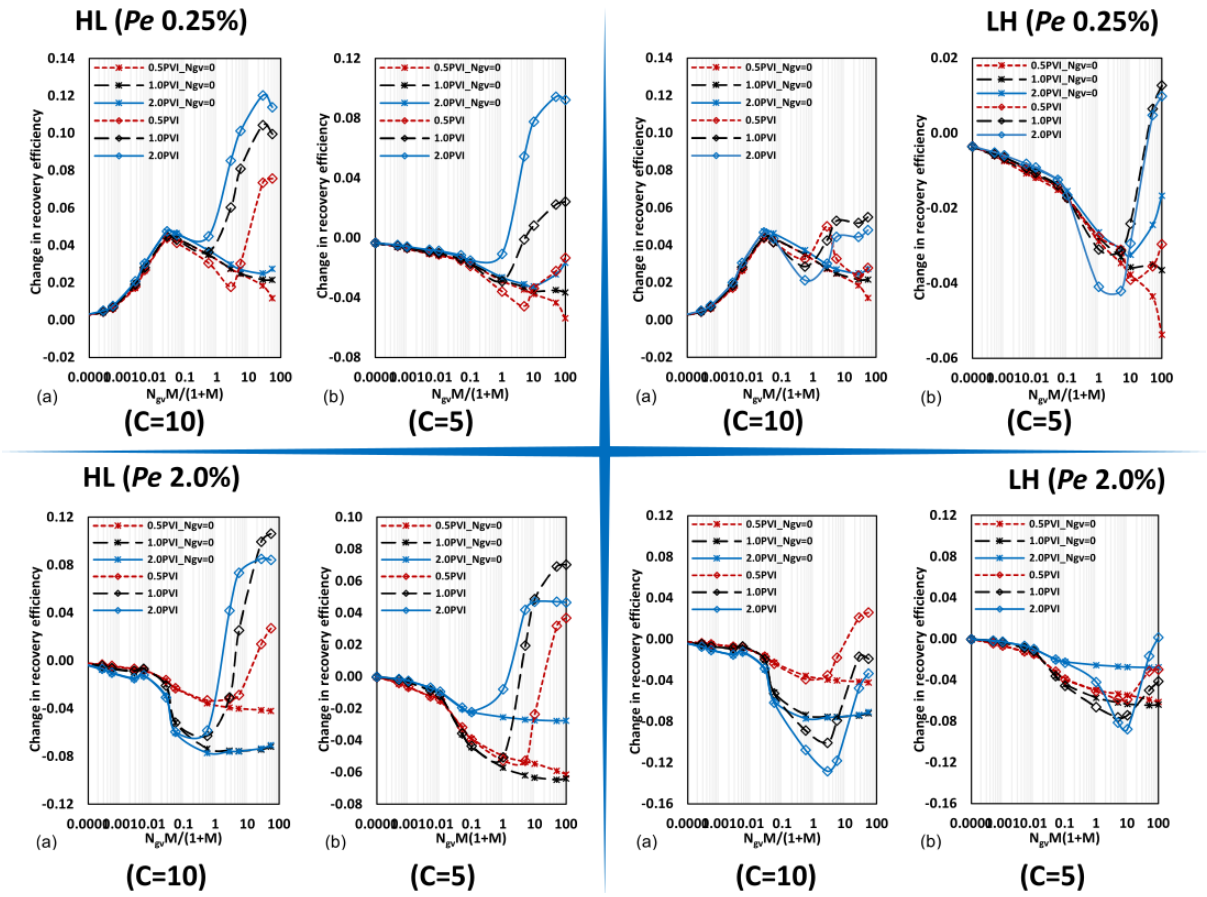


Fig. 7.12: Change in recovery efficiency due to gravity-assisted crossflow (ΔURF) as a function of crossflow amount ($N_{gv}M_F(1+M_F)$) in comparison to that without gravity (i.e. viscous-dominated, $N_{gv}=0$) in a secondary LSWF for a convective flow regime (*Pe* of 0.25% of the model-length) and dispersion (*Pe* of 2.0% of the model-length). Results are shown for two layer-orderings (HL – fast-layer ordered above; LH – slow-layer ordered above), each at $C=5$ and $C=10$, for different performance times (or injected LS-slug sizes: *red* $0.5\ PVI$, *black* $1.0\ PVI$, *blue* $2.0\ PVI$). Similar results for other levels of dispersion (*Pe*) are presented in **Appendix E**.

The influence of gravity-induced crossflow on recovery efficiency is explored for plausible scenarios of both the displacing-phase relative velocity in the slow layer (U^s) and layer-ordering – fast-layer ordered above, and slow-layer ordered above (**Fig. 7.12**). Change in recovery efficiency (ΔURF) due to gravity-assisted crossflow is evaluated at different performance times and compared to that from viscous-dominated crossflow for both convective and dispersive flow regimes.

Recovery efficiency remains viscous-dominated for $N_{gv}M_F(1+M_F) < 0.2$ across layer-orderings and dispersion levels (i.e. equal viscous-dominated and gravity-assisted performance), as suggested by Zhou et al. (1994). Crossflow improves recovery under gravity-dominance, $N_{gv}M_F(1+M_F) > 5$, at sufficient chemical or slug injections ($\geq 1.0\ PVI$), irrespective of U^s and *Pe*, if the fast layer is ordered above. However, in the transition zone where both the viscous and gravity forces are important for displacement, $0.2 < N_{gv}M_F(1+M_F) < 5$, crossflow effect on recovery efficiency depends on U^s and *Pe*. It can be concluded that the unfavourable effect of the $M_{F,HS} < 1 < M_{F,LS}$ mobility-ratio case on crossflow recovery efficiency is of less importance to the flood design when displacement is gravity-dominated. In addition, we found the boundaries of flow regions proposed by Zhou et al. (1994) to be consistent here for an engineered waterflood or LSWF. A largely unfavourable influence of gravity is expectedly observed when both forces (gravity and viscous) act in opposite directions (i.e. slow-layer ordered above).

We explore the influence of shape factor (R) for the unfavourable $M_{F,HS} < 1 < M_{F,LS}$ mobility-ratio case (**Fig. 7.13**). This is evaluated at different levels of dispersion (*Pe*) considering the plausible scenarios of the displacing-phase relative velocity in the slow layer (U^s). **Fig. 7.13**a shows that the recovery efficiency for NC limit ($R_l^2 \ll 1$) is dependent on R in the presence of transverse dispersion irrespective of the displacing-phase relative mobility in both layers. This is corroborated under VC, where ΔURF without transverse dispersion (**Fig. 7.13**b) is independent of R compared to R-dependent ΔURF seen under transverse dispersion (**Fig. 7.13**c and d). Furthermore, transverse dispersion dominance on recovery efficiency is observed to increase with R regardless of U^s (**Fig. 7.13**a). This implies that displacement efficiency is dominated by transverse dispersion in thin layers.

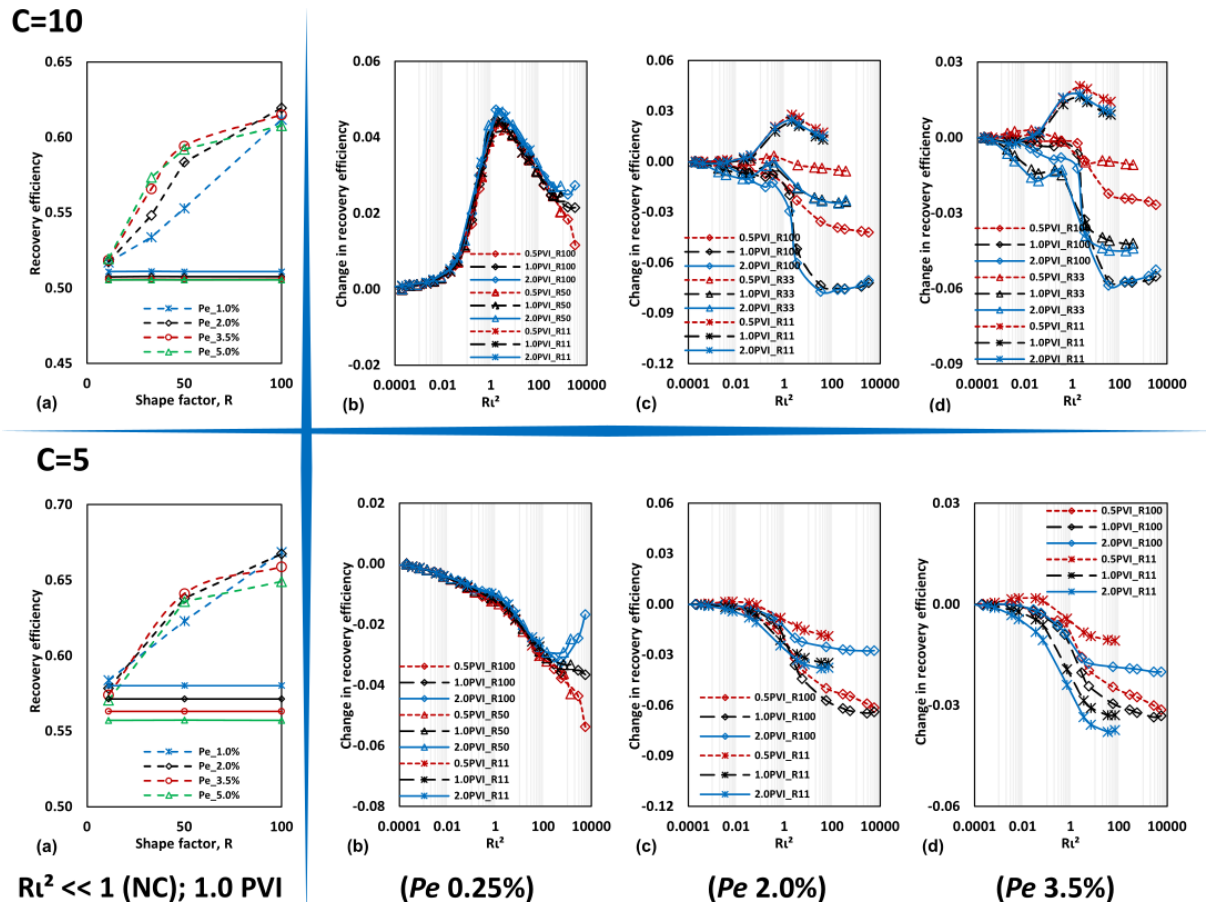


Fig. 7.13: (a) Mid-time (1.0 PVI) recovery efficiency as a function of shape factor (R) at different levels of physical mixing (*Pe*) with (dashed lines) and without (solid lines) transverse dispersion for the NC limit ($R_l^2 \ll 1$). Change in recovery efficiency due to VC (ΔURF) as a function of crossflow amount (R_l^2) at different shape factor (R) and performance times (or injected LS-slug sizes: *red* 0.5 PVI, *black* 1.0 PVI, *blue* 2.0 PVI) under different levels of dispersion (in terms of percentage of model-length L). (b) $Pe = 0.25\%$. (c) $Pe = 2.0\%$. (d) $Pe = 3.5\%$. Results are shown for $C = 10$ (upper half) and $C = 5$ (lower half) in all cases.

For convective flow (**Fig. 7.13**b), the VC recovery efficiency for $M_{F,HS} < 1 < M_{F,LS}$ becomes favourable (across performance times) with reduced U^s (i.e. from $C = 5$ to $C = 10$) independent of R. This is contrary to earlier suggestions by Zapata and Lake (1981) for such EOR-displacements. It rather highlights the need to reduce interaction of the (two) primary leading chemical-free or HS shock-fronts in the adjacent layers for a favourable crossflow effect at $M_{F,HS} < 1 < M_{F,LS}$. Whereas under dispersion (**Fig. 7.13**c and d), VC recovery or sweep efficiency is found to be better than NC displacement with reduced U^s only at small shape factors ($R < 33$). This results from increasing dominance of displacement by transverse dispersion with R which unfavourably enhances interactions amongst the leading chemical-free or HS shock-fronts regardless of U^s.

Since the chemical-free water-bank is inevitable and C cannot be altered, we suggest that, for favourable crossflow effects on viscous-dominated displacements with $M_{F,HS} < 1 < M_{F,LS}$ shock-front mobility-ratios, the flood design should consider:

1. Modifying or reducing the chemical or LS shock-front mobility ratio ($M_{F,LS}$) to a favourable regime or case – $M_{F,HS},\ M_{F,LS} < 1$ or $M_{F,HS} > 1 > M_{F,LS}$ – using weighting additives such as polymers, if there is significant dispersion.
2. Conversely, increasing the displacing-phase mobility or velocity in the fast layer to further separate or reduce the interaction amongst the chemical-free water-banks (primary and secondary) if flow is convective. This can be achieved through increasing $M_{F,LS}$ relative to C: the displacing-phase or chemical shock-fronts in adjacent layers travel as a single-front (i.e. equal relative mobility or velocity) if $M_{F,LS} \leq \frac{1}{C}$ (Zapata and Lake, 1981). Therefore, the higher the $M_{F,LS}$ relative to $\frac{1}{C}$, the larger the $U^f_{F,LS}$ relative to $U^s_{F,HS}$. However, this may require more EOR-chemical or slug amount to inject to stabilize the crossflow chemical-sweep.
3. Where the displacing-phase mobility or velocity in the fast layer is increased towards favourable conditions $U^f_{F,LS} > U^s_{F,HS}$, the flood design may become limited to candidate-systems with small shape factor ($R < 33$), depending on *Pe*, for a favourable VC effect if under dispersion. Moreover, such shape factors will unlikely reach maximum crossflow (VCE).

7.4 Summary

In this chapter, we investigated the effects of viscous crossflow on recovery or displacement efficiency along stratified media of contrasting properties during an engineered waterflooding or LSWF. The two-phase displacement was characterized using dimensionless numbers, so results are directly applicable regardless of scale. Our results are summarised as follows:

1. The permeability contrast between layers determines if viscous crossflow (VC) occurs in stratified heterogeneous reservoirs irrespective of the shape factor or aspect ratio. The extent of existing VC in such systems is however influenced by the shape factor. VC is only a factor in water-oil displacements where the permeability contrast is $\leq 10^3$, hence, VC is inevitable unless a continuous geological barrier to flow is present between layers. However, permeability contrast becomes less important for EOR-chemical or LS crossflow once it is > 50.

2. Two distinct VC regimes or directions are identified from four basic shock-front mobility-ratio cases assuming the mobility ratio is equal across identical fronts in adjacent layers – crossflow from fast to slow layer for $M_{F,HS},\ M_{F,LS} < 1$ and in both directions for other cases, considering

the two plausible scenarios of displacing-phase relative velocity in both layers. A secondary chemical-free shock-front in slow layer from crossflow from fast layer further facilitates the connectivity of the primary leading shock-fronts thereby enlarging them across both layers during displacement. This significantly impacts VC effects on recovery and chemical-sweep efficiency.

3. The improvement in oil recovery and chemical-sweep efficiency due to VC for non-piston-like displacements, when compared to no crossflow, NC, is related to the shock-front mobility-ratios. VC recovery efficiency is generally better than if the displacement had no crossflow for most mobility-ratio cases if sufficient EOR-chemical or slug is injected, except when the mobility ratios across the HS and LS fronts obey $M_{F,HS} < 1 < M_{F,LS}$. This is because of its enhanced dilution effect from the now closer contact between the chemical crossflow and the enlarged chemical-free water-oil bank which preferentially flows through slow layer. This has not been reported previously.

4. For the favourable mobility-ratio cases, the weak dependency of late-time recovery efficiency on VC in LSWF is a function of the mobility-ratio case and dispersion, unlike a typical water-oil displacement. Under limited slug injections, favourable VC effect on recovery efficiency can still be designed through the shock-front mobility-ratios combination and the displacing-phase relative mobility or velocity in the layers. Where VC remains important across performance times, the optimal EOR-chemical amount required to stabilize the crossflow chemical-sweep is largest when both shock-fronts are favourable mobility-ratio displacements.

5. For the identified unfavourable mobility-ratio case ($M_{F,HS} < 1 < M_{F,LS}$), recovery efficiency is worse with viscous-dominated crossflow (VC) under dispersion regardless of the displacing-phase relative velocity or mobility in both layers. The unfavourable effect of $M_{F,HS} < 1 < M_{F,LS}$ on crossflow recovery efficiency is of less importance to the flood design when displacement is gravity-dominated. The boundaries of flow regions proposed by Zhou et al. (1994) are found to be consistent with the numerical experiments reported here for an engineered waterflood or LSWF. Shape factor influences crossflow effects on recovery efficiency under dispersion. Transverse dispersion dominates recovery efficiency when layers are thin.

6. Possible ways suggested to improve flood design for favourable viscous-dominated crossflow given $M_{F,HS} < 1 < M_{F,LS}$ include: (1) increasing the mobility-ratio across the displacing-phase or chemical shock-front relative to the permeability-storage contrast ratio, to separate or reduce interactions amongst the leading chemical-free water-banks further if flow is convective; (2) in addition to (1), limiting the candidate-system to a small shape factor if displacement is dispersive; or (3) conversely, modifying or reducing $M_{F,LS}$ using weighting additives such as polymers, to

favourable mobility-ratio cases – $M_{F,HS}$, $M_{F,LS} < 1$ or $M_{F,HS} > 1 > M_{F,LS}$, if we have a dispersion-dominated flow regime.

8 Summary and Recommendations

This thesis addressed four key areas on field-scale physical mixing and its impact in low salinity waterfloods (LSWF): (i) how to control numerical dispersion effects for accurate and representative physical mixing in LSWF simulations in Chapter 4; (ii) the effects of the interaction between inter-well mixing and geological heterogeneity on the optimal low-salinity (LS) slug injection considering uncertainties in Chapters 5 and 6; (iii) the influence of flood pattern on such effects to aid optimal slug injection design in Chapter 6; and (iv) crossflow effects on LS displacement efficiency in the presence of mixing in Chapter 7. The low salinity effect (LSE) was modelled with the standard tracer-component approach – salinity was treated as the 'proxy' single-component tracer that controls wettability alteration towards more water-wetness. This could be modified to represent other active solute-component(s) or ion concentration(s). The main findings and results are summarized in this chapter with recommendations for future work.

8.1 Summary

Numerical dispersion was found to smear the low-salinity water front with an 'unphysical' mixed zone even at fine grid-sizes in Chapter 4. This limited the ability to adequately represent the front with conventional grid refinement. The displacement velocities of the water fronts were altered, which resulted in a misrepresentation of the amounts of *in situ* or connate and LS-injected brines in the system. With the effects similar to real mixing of the distinct brines, controlling numerical dispersion becomes even more important here than in conventional waterfloods for reliable simulation results. Effective threshold salinities evaluated from existing methods to redefine the LSE to correct these numerical dispersion effects showed limited accuracy in coarse grids. The change in the speed of the low-salinity front as a function of dispersion was not accounted for properly in these methods.

Firstly, we proposed a simple simulation-based approach to evaluate the effective thresholds to correct numerical errors in coarse-grid simulations. This approach differed from other methods in that it was based on conservation of volumes of the resident and injected brines in the reference and upscaled solutions to represent the connate water-oil bank displacement reliably in the upscaled solution. To model advective flow effects, the individual reference volumes of the distinct brines were used to cut-off the salinity-thresholds in the upscaled or coarse-grid simulation. Based on the cases presented, the procedure was validated in 1D without adjusting the relative permeabilities and demonstrated effectiveness at higher dimensions.

Secondly, a method was developed to control numerical dispersion effects in a simulation grid using effective thresholds without refining the grid further. This was based on our observation that the numerical spread of the salt or solute front in a coarse grid does change with salinity-thresholds. With this method, we demonstrated how to characterize lower representative effects of physical mixing from the inherent numerical dispersion in a coarse grid in 1D. This is useful for coarse grid simulations to either match a test with significant physical mixing or evaluate a range of dispersive LSWF predictions.

In multidimensional grids, numerical dispersion was seen to exaggerate every input longitudinal physical dispersion and varied linearly with grid-size for a fixed time-step. This implies that even when input physical dispersion dominates, there is still a contribution from the numerical component. A critical value was found to exist for input longitudinal dispersivities at every grid-size. We estimated this as 10.5 ± 2.5% of the corresponding numerical dispersion for the grid-size. Input or explicitly modelled longitudinal dispersion below this value was observed to be completely concealed (negligible) in the total dispersion represented during simulations. This indicates that simply choosing a grid-size (or numerical component) to represent additional effects of physical dispersion on mixing in LSWF is only a very crude approximation. There exist limits for input dispersion in the presence of a numerical component. This is relevant for selecting appropriate simulation grid-size when modelling physical dispersion explicitly.

Since input transverse dispersion remained active in the presence of effective salinity-thresholds, a method was considered to handle simulations with both longitudinal and transverse components of physical mixing or dispersion. Therein, physical longitudinal dispersion (less than the inherent numerical dispersion at the coarse grid) would be modelled with effective thresholds while the transverse component is explicitly defined (inputted). We demonstrated our ability to model these components accurately in multidirectional flows.

Representing physical mixing in LSWF simulations accurately is fundamental to evaluating its impact on the flood efficiency and optimal field-scale injection design reliably. Having constrained the numerical influence for desired representative physical mixing, its effects were then investigated on LS slug performance, its displacement stability, and the optimal amounts to inject. We first considered some associated technical flow uncertainties – physical longitudinal and transverse dispersivities, upper (maximum) salinity threshold, and residual oil saturation to the LSE – in 2D areal models with a line-drive flood pattern (LD) in Chapter 5. Geological uncertainty – in terms of spatial permeability distribution – was introduced later in Chapter 6 with more heterogeneous reservoir connectivity in addition to a quarter five-spot well pattern (Q5S) in 2D and 3D.

In 2D homogeneous models in Chapters 5 and 6, secondary-mode displacement (i.e. formation of a connate water bank) was observed to extend beyond an immediate LS injection regardless of the flood pattern. Meanwhile, the Q5S pattern showed further extension of the secondary-mode displacement with delayed LS injection compared to LD. Further investigation found that the reduced flow area around the injector in Q5S limits the early exposure of injected slug to physical mixing thereby sustaining its LS displacement stability further.

The flood pattern was seen to have influence on the sensitivity of LS slug performance to its injection start-time regardless of the effective displacement mode of the flood. While the slug performance remained fairly insensitive to injection start-time until the tertiary-mode displacement became established for a line-drive well pattern in Chapter 5, the performance was sensitive to injection start-time irrespective of the flood displacement mode for a Q5S well arrangement in Chapter 6. This appears important to LSWF design as line-drive pattern accommodates some delay window for slug injection with little or no impact on recovery considering the effects of mixing.

It was identified in Chapters 5 and 6 that the interaction between inter-well mixing and areal geological heterogeneity could potentially modify favourably the LS displacement stability and performance of the injected slug for both flood patterns. This was linked to transverse dispersion which, contrary to earlier reports, was found to be active when heterogeneity modifies the areal sweep. Transverse dispersion tends to improve the areal sweep efficiency depending on the spatial heterogeneity distribution.

The sensitivity of the optimal slug injection to uncertainty in the effects of physical mixing during LSWF decreases with heterogeneity. While considering the flow uncertainties could require as much as twice the nominal optimal slug size to reduce the associated performance risks, the ratio was found to reduce with heterogeneity in Chapter 5. Moreover, the extent of geological heterogeneity impact on this was seen to be significantly influenced by its spatial distribution relative to the flood displacement paths.

Next, the investigation included geological uncertainty in Chapter 6. For a cumulative water injection of 2 PV, LS slug design considering uncertainty in the physical effects would require at least 0.8 PV optimal size and 0.24 PV minimum stability-threshold size for both flood patterns studied. This could vary with the cumulative water injected and flood pattern but was found to remain generally favoured by an early injection. Injection optimization can prioritize the slug range between the stability-threshold and optimal sizes to balance the technical and financial performance of the flood. The line-drive flood pattern showed a narrower range for these slug sizes, which is of essential computational advantage when optimizing its injection.

In Chapter 6, the LS displacement stability and performance of the injected slug were observed to be very sensitive to heterogeneity while the sensitivity of its optimal design was dependent on the well pattern. Of more relevance to slug injection schemes is the optimal size which was found to be relatively insensitive to heterogeneity for the Q5S flood pattern both in 2D and 3D. Slug injection was more- and less-efficient at small and large sizes respectively for Q5S flood pattern. LS displacement in large slugs were more stable for line-drive well pattern. This indicated a slug size dependence of performance – under the effects of physical mixing in multidimensional models – that is a function of well arrangement.

Finally, in Chapter 7, the effect of crossflow was investigated on LS displacement or recovery efficiency in the presence of mixing – for different mobility ratios. The two-phase displacement along stratified media of contrasting properties was characterized with dimensionless numbers transcending the no-crossflow, viscous- and gravity-dominated crossflow regimes. For permeability contrasts $\leq 10^3$, viscous crossflow (VC) was found to be relevant in water-oil displacements. However, it was less important for EOR-chemical or LS displacement once the permeability contrast > 50. For the mobility-ratio cases considered, VC was unidirectional – from fast to slow layer – only when $M_{F,HS},\ M_{F,LS} < 1$.

VC recovery efficiency was found to be generally better than if the displacement had no crossflow for most mobility-ratio cases if sufficient slugs were injected, except when $M_{F,HS} < 1 < M_{F,LS}$. For this case, viscous-dominated crossflow was unfavourable to recovery efficiency under mixing or dispersion regardless of the displacing-phase relative velocity or mobility in both layers. Further investigation revealed that this resulted from an enhanced dilution effect on the chemical (LS) crossflow which preferentially flows through the slow layer. This is a new finding specific to LS displacements.

Unlike a typical water-oil displacement, the weak dependency of late-time recovery efficiency on VC was found to be a function of the mobility-ratio case and dispersion in LSWF. The dimensionless crossflow boundaries of Zhou et al. (1994) were observed to be consistent for an engineered waterflood or LSWF. The unfavourable effect of $M_{F,HS} < 1 < M_{F,LS}$ on crossflow recovery efficiency was of less importance to the flood design when displacement became gravity-dominated. Crossflow effects on recovery efficiency under physical mixing or dispersion were seen to be influenced by shape factor – recovery efficiency in thin layers was dominated by transverse dispersion. Following these findings, ways to improve the flood design under physical mixing were suggested for favourable viscous-dominated crossflow given $M_{F,HS} < 1 < M_{F,LS}$.

8.2 Research Directions for Future Work

In this thesis, only one rock type or pair of two-phase relative permeabilities was considered under each wetting state for all simulation models. It will be of interest to investigate the outcomes for reservoirs with multiple rock types or regions laterally and/or stratified. These rock types or regions can exhibit different residual oil and maximum water saturations or connate water-oil bank displacements to the LSE. Since they may be of distinct salinity or solute-concentration thresholds for the LSE, the methodology on the effective-thresholds concept presented in this thesis to control numerical dispersion needs further testing in such realistically complex models.

Besides heterogeneity, the presence of regionalized rock types alters the displacement velocities of the water fronts even laterally in a stratum. This is expected to influence transverse mixing and its effects on LS slug performance, its displacement stability, and the optimal amounts to inject. Further analysis is required on the sensitivity of the optimal slug injection to heterogeneity considering uncertainty in the physical effects under this case and is recommended for future research. It will be important to test the generality of the optimal slug size insensitivity to heterogeneity reported in this thesis for Q5S flood pattern in the presence of multiple or regionalized rock types.

In this thesis, crossflow effects during augmented or engineered waterflood like LSWF were limited to when the mobility ratio across identical fronts is the same in adjacent layers. However, multiple (or different) rock types stratified in layered heterogeneity can introduce unequal mobility ratios across identical shock-fronts in the adjacent layers. Examining crossflow behaviour and its effects on LS displacement or recovery efficiency in the presence of mixing under this plausible scenario is a possible future direction of this research.

Additionally, the impact of tertiary-mode displacement on the unfavorability of $M_{F,HS} < 1 < M_{F,LS}$ mobility-ratio case in the flood design is recommended for investigation in future research. An increment in the mobility ratio across the displacing-phase or chemical shock-front ($M_{F,HS}$) is anticipated in tertiary injections relative to the secondary-mode because of their different saturation profiles of the fluids. Therefore, a potential change to another mobility-ratio case with favourable viscous-dominated crossflow may evolve with delayed LS injection. Nonetheless, the overall effect on recovery or displacement efficiency relative to an immediate or early injection should be established.

In most commercial codes, the principal flow axis is fixed along a coordinate direction to model physical dispersion whose tensor is assumed diagonal. Therein, longitudinal mixing is defined with the diagonal tensor component along the predominant coordinate direction of flow while transverse dispersion is modelled with the remaining tensor component(s). This is just an approximation to

capture the effects of both components of physical mixing – transverse and longitudinal – in multidirectional flow simulations. The methodology developed in this thesis could constrain the numerical dispersion in this case to desired representative physical mixing effects during LSWF simulations. Future work can investigate this methodology further in codes (if available) where the components of mixing are defined with respect to the flow axes independent of coordinate direction.

Meanwhile, the findings from this work provide efficient tools of direct applicability for reservoir engineers to design and implement the flood. With the uncertainty associated with numerical accuracy, we can now evaluate the potential impact of field-scale physical mixing more reliably in LSWF simulations with the methodology developed here. We have shown the insensitivity of the optimal slug size to heterogeneity under a quarter five-spot flood pattern considering uncertainty in the effects of inter-well physical mixing. This is anticipated to be very important to scale-up the injection design particularly in the presence of geological uncertainty – which is inevitable in practical reservoir heterogeneity descriptions. However, the slug performance dependence on flood geometry or pattern, as observed in this study, requires careful consideration in such injection optimization scheme. A range of slug sizes – i.e. stability-threshold to optimal – proposed to target when optimizing its injection will essentially aid the flood design to balance both the technical and financial performance. The novel crossflow behaviour and regimes identified in this work will help in the flood design to mitigate any potential unfavourable effects on recovery or displacement efficiency.

References

Adegbite, J.O., Al-Shalabi, E.W., 2021. Effect of heterogeneity on engineered water injection in carbonates using five-spot sector model: A numerical study. Petroleum. https://doi.org/10.1016/j.petlm.2021.04.001.

Adegbite, J.O., Al-Shalabi, E.W., Ghosh, B., 2018. Geochemical modelling of engineered water injection effect on oil recovery from carbonate cores. J. Petrol. Sci. Eng. 170, 696-711. https://doi.org/10.1016/j.petrol.2018.06.079.

Agbalaka, C.C., Dandekar, A.Y., Patil, S.L., Khataniar, S., Hemsath, J.H., 2009. Coreflooding studies to evaluate the impact of salinity and wettability on oil recovery efficiency. Transp Porous Media, 76:77–94. https://doi.org/10.1007/s11242-008-9235-7.

Ahmed, G., Castanier, L.M., Brigham, W.E., 1988. An Experimental Study of Waterflooding From a Two-Dimensional Layered Sand Model. SPE Reservoir Engineering 3 (1): 45-54.

Aifa, T., 2014. Neural network applications to reservoirs: Physics-based models and data models. J Pet Sci Eng, 123, pp. 1-6. https://doi.org/10.1016/j.petrol.2014.10.015.

Aksulu, H., Hamsø, D., Strand, S., Puntervold, T., Austad, T., 2012. Evaluation of low-salinity enhanced oil recovery effects in sandstone: effects of the temperature and pH gradient. Energy Fuels, 26 (6) (2012), pp. 3497-3503. https://doi.org/10.1021/ef300162n.

Aladasani, A., Bai, B., Wu, Y., Salehi, S., 2014. Studying low-salinity waterflooding recovery effects in sandstone reservoirs. J Pet Sci Eng, 120, pp. 39-51. https://doi.org/10.1016/j.petrol.2014.03.008.

Aladasani, A., Bai, B., Wu, Y., 2012. Investigating low-salinity waterflooding recovery mechanisms in sandstone reservoirs. In: Proceedings of Eighteenth SPE Improved Oil Recovery Symposium, Tulsa, Oklahoma, USA, SPE 152997. https://doi.org/10.2118/152997-MS.

Al-Ibadi, H., Stephen, K.D., Mackay, E., 2019. Insights into the fractional flow of low salinity water flooding in the light of solute dispersion and effective salinity interactions. J. Pet. Sci. Eng. 174, 1236–1248. https://doi.org/10.1016/j.petrol.2018.12.001.

Al-Ibadi, H., Stephen, K., Mackay, E., 2018a. Improved Numerical Stability and Upscaling of Low Salinity Water Flooding. In SPE Asia Pacific Oil & Gas Conference and Exhibition. Society of Petroleum Engineers. SPE-192074-MS. https://doi.org/10.2118/192074-MS

Al-Ibadi, H., Stephen, K., Mackay, E., 2018b. Novel Observations of Salt Front Behaviour in Low Salinity Water Flooding. In SPE Western Regional Meeting. Society of Petroleum Engineers. SPE-190068-MS. https://doi.org/10.2118/190068-MS

Al-Ibadi, H., Stephen, K., Mackay, E., 2018c. An Updated Fractional Flow Model of Low Salinity Water Flooding with Respect to the Impact of Salt Diffusion. In SPE Trinidad and Tobago Section Energy Resources Conference. Society of Petroleum Engineers. SPE-191222-MS. https://doi.org/10.2118/191222-MS

Al-Shalabi, E.W., Sepehrnoori, K., 2016. A comprehensive review of low salinity/engineered water injections and their applications in sandstone and carbonate rocks. J. Petrol. Sci. Eng. 139, 137-161. https://doi.org/10.1016/j.petrol.2015.11.027.

Al-Shalabi, E.W., Sepehrnoori, K., Delshad, M., 2015. Simulation of wettability alteration by low-salinity water injection in waterflooded carbonate cores. Petrol. Sci. Technol. 33 (5), 604–613. https://doi.org/10.1080/10916466.2014.919005.

Alagic, E., Skauge, A., 2010. Combined low salinity brine injection and surfactant flooding in mixed-wet sandstone cores. Energy Fuels, 24 (6) (2010), pp. 3551-3559. https://doi.org/10.1021/ef1000908.

Alhamdan, M.R., Cinar, Y., Suicmez, V.S., Dindoruk, B., 2012. Experimental and numerical study of compositional two-phase displacements in layered porous media. J. Petrol. Sci. Eng. 98, 107–121. https://doi.org/10.1016/j.petrol.2012.09.009.

Alkhatib, A., King, P., 2014. An approximate dynamic programming approach to decision making in the presence of uncertainty for surfactant-polymer flooding. Comput Geosci 18, 243–263. https://doi.org/10.1007/s10596-014-9406-2.

Alkindi, A., Al-Wahaibi, Y., Bijeljic, B., Muggeridge, A., 2011. Investigation of longitudinal and transverse dispersion in stable displacements with a high viscosity and density contrast between the fluids. J. Contam. Hydrol. 120–121, 170–183. https://doi.org/10.1016/j.jconhyd.2010.06.006

Alotaibi, M.B., Nasralla, R.A., Nasr-El-Din, H.A., 2011. Wettability studies using low-salinity water in sandstone reservoirs. Soc Pet Eng. https://doi.org/10.2118/149942-PA.

AlSofi, A.M., Blunt, M.J., 2013. Control of Numerical Dispersion in Streamline-Based Simulations of Augmented Waterflooding. SPE J. 18, 1102–1111. https://doi.org/10.2118/129658-PA

AlSofi, A.M., Blunt, M.J., 2012. A segregated flow scheme to control numerical dispersion for multi-component flow simulations. Comput. Geosci. 16, 335–350. https://doi.org/10.1007/s10596-012-9278-2.

Amott, E., 1959. Observations Relating to the Wettability of Porous Rock. Petroleum Transactions, AIME 216: 156-162.

Anderson, W.G., 1986. Wettability literature survey – Part 1: Rock/oil/brine interactions and the effects of core handling on wettability. J Pet Technol 38 (10), pp. 1125-1144. https://doi.org/10.2118/13932-PA.

Appelo, C.A.J., 1994. Cation and proton exchange, pH Variations, and carbonate reactions in a freshening aquifer. Water Resour. Res. 30(10), 2793–2805.

Aronofsky, J.S., Heller, J.P., 1957. A diffusion model to explain mixing of flowing miscible fluids in porous media. Trans. Metall. Soc. AIME 210, 345–349.

Ashraf, A., Hadia, N.J., Torsaeter, O., Tweheyo, M.T. 2010. Laboratory Investigation of Low Salinity Waterflooding as Secondary Recovery Process: Effect of Wettability. Paper SPE 129012 proceedings of the SPE Oil and Gas India Conference and Exhibition, Mumbai, India.

Attar, A., Muggeridge, A., 2018. Low salinity water injection: Impact of physical diffusion, an aquifer and geological heterogeneity on slug size. J. Pet. Sci. Eng. 166, 1055–1070. https://doi.org/10.1016/j.petrol.2018.03.023.

Attar, A., Muggeridge, A.H., 2016. Evaluation of mixing in low salinity waterflooding. In: The Proceedings of the SPE EOR Conference at Oil and Gas West Asia, Muscat, Oman, 21-23 March. SPE-179803-MS. https://doi.org/10.2118/179803-MS.

Austad T, RezaeiDoust A, Puntervold T., 2010. Chemical mechanism of low salinity water flooding in sandstone reservoirs. Soc Pet Eng. https://doi.org/10.2118/129767-MS.

Aziz, R., Joekar-Niasar, V., Martínez-Ferrer, P.J., Godinez-Brizuela, O.E., Theodoropoulos, C., Mahani, H., 2019. Novel insights into pore-scale dynamics of wettability alteration during low salinity waterflooding. Sci Rep, 9(1), 9257. https://doi.org/10.1038/s41598-019-45434-2.

Babaei, M., King, P.R., 2013. An Upscaling-Static-Downscaling Scheme for Simulation of Enhanced Oil Recovery Processes. Transp. Porous Media 98, 465–484. https://doi.org/10.1007/s11242-013-0154-x

Baker, R., 1998. Reservoir Management for Waterfloods-Part II. The Journal of Canadian Petroleum Technology 37 (1): 12-17.

Bartels, W.B., Mahani, H., Berg, S., Hassanizadeh, S.M., 2019. Literature review of low salinity waterflooding from a length and time scale perspective. Fuel, 236, 338-353. https://doi.org/10.1016/j.fuel.2018.09.018.

Berg, S., Cense, A.W., Jansen, E., Bakker, K., 2010. Direct experimental evidence of wettability modification by low salinity. Petrophysics, 51 (5), pp. 314-322. https://doi.org/10.2118/144936-MS.

Bernard G.G., 1967. Effect of floodwater salinity on recovery of oil from cores containing clays. Soc Pet Eng. https://doi.org/10.2118/1725-MS.

Bertin, H., Quintard, M., Corpel, V., Whitaker, S., 1990. Two-phase flow in heterogeneous porous media III: laboratory experiments for flow parallel to a stratified system. Transp. Porous Media 5(6), 543–590. https://doi.org/10.1007/BF00203329.

Beyer, H.G., Schwefel, H.P., 2002. Evolution strategies – A comprehensive introduction. Natural Computing 1, 3–52. https://doi.org/10.1023/A:1015059928466.

Beyer, H., Sendhoff, B., 2007. Robust optimization – A comprehensive survey. Computer Methods in Applied Mechanics and Engineering 196(33-34). https://doi.org/10.1016/j.cma.2007.03.003.

Blackwell, R.J., 1962. Laboratory Studies of Microscopic Dispersion Phenomena. Soc. Pet. Eng. J. 2, 1–8. https://doi.org/10.2118/1483-G

Blunt, M.J., Lin, Q., Akai, T., Bijeljic, B., 2019. A thermodynamically consistent characterization of wettability in porous media using high-resolution imaging. Journal of Colloid and Interface Science, 552, pp.59-65. https://doi.org/10.1016/j.jcis.2019.05.026.

Blunt, M., Rubin, B., 1991. Implicit flux limiting schemes for petroleum reservoir simulation. J. Comput. Phys. 102(1), 194–210. https://doi.org/10.1016/S0021-9991(05)80015-4.

Bortolotti, V., Macini, P., Srisuriyachai, F., 2010. Wettability Index of Carbonatic Reservoirs and EOR: Laboratory Study to Optimize Alkali and Surfactant Flooding. Paper SPE 131043 proceedings of the CPS/SPE International Oil & Gas Conference and Exhibition, Beijing, China, 8-10 June.

Boussour, S., Cissokho, M., Cordier, P., Bertin, H.J., Hamon, G., 2009. Oil recovery by low-salinity brine injection: laboratory results on outcrop and reservoir cores. Soc Pet Eng. https://doi.org/10.2118/124277-MS.

Brigham, W.E., Reed, P.W., Dew, J.N., 1961. Experiments on mixing during miscible displacement in porous media. Soc. Pet. Eng. J. 1, 1–8. https://doi.org/10.2118/1430-G

Brodie, J., Jerauld, G., 2014. Impact of Salt Diffusion on Low-Salinity Enhanced Oil Recovery. In SPE Improved Oil Recovery Symposium. SPE-169097-MS. https://doi.org/10.2118/169097-MS.

Brooks, R., Corey, A., 1966. Properties of porous media affecting fluid flow. Irrigation and drainage division 92 (2), 61–88 June. https://doi.org/10.1061/JRCEA4.0000425.

Brown, C., Smith, P., 1984. The Evaluation of Uncertainty in Surfactant EOR Performance Prediction. Paper SPE 13237 presented at the 59th SPE Annual Technical Conference and Exhibition, Houston, Texas, USA, 16-19 September. https://doi.org/10.2118/13237-MS.

Buckley, J.S., Morrow, N.R., 1990. Characterization of crude oil wetting behavior by adhesion tests. Soc Pet Eng. https://doi.org/10.2118/20263-MS.

Callegaro, C., Bartosek, M., Nobili, M., Masserano, F., Pollero, M., Mousa, D., Kortam, M.M., 2015. Design and implementation of low salinity waterflood in a north African brown field. In: Paper SPE-177590-MS Proceedings of the Abu Dhabi International Petroleum Exhibition and Conference, Abu Dhabi, UAE. https://doi.org/10.2118/177590-MS.

Callegaro, C., Bartosek, M., Masserano, F., Nobili, M., Parracello, V.P., Pizzinelli, C.S., Caschili, A., 2013. Opportunity of Enhanced Oil Recovery Low Salinity Water Injection: From Experimental Work to Simulation Study up to Field Proposal. Paper 164827 proceedings of the EAGE Annual Conference & Exhibition incorporating SPE Europec, London, United Kingdom, 10-13 June.

Campbell, C.V., 1967. Lamina, laminaset, bed and bedset. Sedimentology, 8(1), 7–26. https://doi.org/10.1111/j.1365-3091.1967.tb01301.x.

Cense, A.W., Berg, S., Jansen, E., Bakker, K., 2011. Direct visualization of designer waterflooding in model experiments. SPE paper 144936 presented at the SPE enhanced oil recovery conference. https://doi.org/10.2118/144936-MS.

Chang, Y.B., Lim, M.T., Pope, G.A., Sepehrnoori, K., 1994. CO2 Flow Patterns under Multiphase Flow: Heterogeneous Field-Scale Conditions. SPE Annual technical conference and exhibition, Dallas, USA. Paper SPE 22654. https://doi.org/10.2118/22654-PA.

Chávez-Miyauch, T.E., Lu, Y., Firoozabadi, A., 2020. Low salinity water injection in Berea sandstone: Effect of wettability, interface elasticity, and acid and base functionalities. Fuel, 263, 116572. https://doi.org/10.1016/j.fuel.2019.116572.

Cheng, H., Shook, G., Taimur, M, Dwarakanath, V., Smith, B., 2012. Interwell Tracer Tests to Optimize Operating Conditions for a Surfactant Field Trial: Design, Evaluation and Implications. SPE Reservoir Evaluation & Engineering 15(2):229-242. https://doi.org/10.2118/144899-PA.

Chequer, L., Al-Shuaili, K., Genolet, L., Behr, A., Kowollik, P., Zeinijahromi, A., Bedrikovetsky, P., 2019. Optimal slug size for enhanced recovery by low-salinity waterflooding due to fines migration. J. Petrol. Sci. Eng. 177, 766-785. https://doi.org/10.1016/j.petrol.2019.02.079.

Chiles, J.P., Delfiner, P., 1999. Modeling Spatial Uncertainty. Geostatistics, Wiley Series in Probability and Statistics. New York: Wiley Interscience. 695 p.

Christie, M.A., Blunt, M.J., 2001. Tenth SPE Comparative Solution Project: A Comparison of Upscaling Techniques. SPE Reserv. Eval. Eng. 4, 308–317. https://doi.org/10.2118/72469-pa.

Christie, M., Demyanov, V., Erbas, D., 2006. Uncertainty Quantification for Porous Media Flows. J. Comput. Phys. 217, 143–158. https://doi.org/10.1016/j.jcp.2006.01.026.

Cioppa, T.M., 2002. Efficient Nearly Orthogonal and Space-Filling Experimental Designs for High-Dimensional Complex Models. PhD Dissertation. Naval Postgraduate School, Monterey CA. https://apps.dtic.mil/dtic/tr/fulltext/u2/a406957.pdf.

CMG, 2019. CMOST Manual. Computer Modelling Group Ltd. https://cmgl.ca.

Cinar, Y., Jessen, K., Berenblyum, R., Juanes, R., Orr, F.M., 2006. An experimental and numerical investigation of crossflow effects in two-phase displacements. SPE J. 11(02), 216–226. https://doi.org/ 10.2118/90568-PA.

Cissokho, M., A. Ahmadi, H. Bertin, A. Omari, G. Hamon, 2012. Some investigations on the role of microparticles on the low salinity process. Paper SCA2012-15 presented at the international symposium of the society of core analysts, Aberdeen, Scotland, UK. https://hdl.handle.net/10985/10033.

Cissokho, M., Bertin, H., Boussour, S., Cordier, P., Hamon, G., 2010. Low salinity oil recovery on clayey sandstone: experimental study. Petrophysics, 51 (5), pp. 305-313.

Coats, K.H., Whitson, C.H., Thomas, K., 2009. Modeling Conformance as Dispersion. SPE Reserv. Eval. Eng. 12(1), 33–47. https://doi.org/10.2118/90390-pa.

Coello, C.A.C., Pulido, G.T., Lechuga, M.S., 2004. Handling Multiple Objectives with Particle Swarm Optimization. IEEE Transactions on Evolutionary Computation 8(3), 256-279. https://doi.org/10.1109/TEVC.2004.826067.

Coll, C., Muggeridge, A.H., Jing, X.D., 2000. Regional Upscaling: A New Method to Upscale Waterflooding in Heterogeneous Reservoirs for A Range of Capillary and Gravity Effects. Paper SPE 59337 proceedings of the 2000 SPE/DOE Improved Oil Recovery Symposium, Tulsa, Oklahoma, USA, 3-5 April.

Couët, B., Burridge, R., Wilkinson, D., 2000. Optimization under reservoir and financial uncertainty. In: Paper presented at the European Conference on the Mathematics of Oil Recovery (ECMOR), Baveno, Italy.

Cullick, A.S., Johnson, D., Shi, G., 2006. Improved and More Rapid History Matching With a Nonlinear Proxy and Global Optimization. In: Paper SPE 101933 presented at the SPE Annual Technical Conference and Exhibition. https://doi.org/10.2118/101933-MS.

Dang, C., Nghiem, L., Fedutenko, E., Gorucu, E., Yang, C., Mirzabozorg, A., 2018. Application of artificial intelligence for mechanistic modeling and probabilistic forecasting of hybrid low salinity chemical flooding. Paper SPE 191474 presented at the SPE Annual Technical Conference and Exhibition. https://doi.org/10.2118/191474-MS.

Dang, C., Nghiem, L., Nguyen, N., Chen, Z., Yang, C., Nguyen, Q., 2017. A framework for assisted history matching and robust optimization of low salinity waterflooding under geological uncertainties. J. Pet. Sci. Eng. 152, 330–352. https://doi.org/10.1016/j.petrol.2017.03.009.

Dang, C., Nghiem, L., Chen, Z., Nguyen, Q., 2016. Mechanistic modeling of low salinity water flooding. J. Petrol. Sci. Eng. 146, 191–209. https://doi.org/10.1016/j.petrol.2016.04.024.

Dang, C., Nghiem, L., Nguyen, N., Chen, Z., Nguyen, Q., 2015. Modeling and Optimization of Low Salinity Waterflood. Paper SPE 173194 proceedings of the SPE Reservoir Simulation Symposium, Houston, Texas, USA.

Dang, C., Chen, Z., Nguyen, N., Bae, W., Phung, T., 2011. Development of Isotherm Polymer/Surfactant Adsorption Models in Chemical Flooding. Paper SPE 147872 presented at the SPE Asia Pacific Oil and Gas Conference and Exhibition, Jakarta, Indonesia. https://doi.org/10.2118/147872-MS.

Datta, S.S., Weitz, D.A., 2013. Drainage in a model stratified porous medium. Europhys. Lett. 101(1), 14002. https://doi.org/10.1209/0295-5075/101/14002.

Dawe, R.A., Wheat, M.R., Bidner, M.S., 1992. Experimental investigation of capillary pressure effects on immiscible displacement in lensed and layered porous media. Trans. Porous Media 7(1), 83–101. https://doi.org/10.1007/BF00617318.

Debbabi, Y., Jackson, M.D., Hampson, G.J., Fitch, P.J.R., Salinas, P., 2017. Viscous Crossflow in Layered Porous Media. Trans. Porous Media 117(2), 281–309. https://doi.org/10.1007/s11242-017-0834-z.

Delshad, M., Pope, G., 1989. Comparison of the Three-phase Oil Relative Permeability Models. https://doi.org/10.1007/BF00134742.

Deutsch, C.V., Journel, A.G., 1998. GSLib. Geostatistical Software Library and User's Guide, Second Edition. Oxford University Press, New York.

Deveugle, P.E.K., Jackson, M.D., Hampson, G.J., Farrell, M.E., Sprague, A.R., Stewart, J., Calvert, C.S., 2011. Characterization of stratigraphic architecture and its impact on fluid flow in a fluvial-dominated deltaic reservoir analog: upper cretaceous ferron sandstone member. Utah AAPG Bull. 95(5), 693–727. https://doi.org/10.1306/09271010025.

Ding, H., Rahman, S., 2017. Experimental and theoretical study of wettability alteration during low salinity water flooding-an state of the art review. Colloids Surf A, 520, 622–39. https://doi.org/10.1016/j.colsurfa.2017.02.006.

Donaldson, E.C., Thomas, R.D., Lorenz, P.B., 1969. Wettability Determination and Its Effect on Recovery Efficiency. Society of Petroleum Engineers Journal 9 (1): 13-20.

Drummond, C., Israelachvili, J., 2004. Fundamental studies of crude oil–surface water interactions and its relationship to reservoir wettability. J Petrol Sci Eng, 45 (1–2), pp. 61-81. https://doi.org/10.1016/j.petrol.2004.04.007.

Dykstra, H., Parsons, R.L., 1950. The Prediction of Oil Recovery by Waterflooding, Secondary Recovery of Oil in the United States pages 160-174. API, Dallas 2nd edition.

Egermann, P., Renard, G., Delamaide, E., 2001. SAGD Performance Optimization through Numerical Simulations: Methodology and Field Case Example. In: Paper SPE 69690 presented at the SPE International Thermal Operations and Heavy Oil Symposium, Venezuela. https://doi.org/10.2118/69690-MS.

Erke, S.I., Volokitin, Y.E., Edelman, I.Y., Karpan, V.M., Nasralla, R.A., Bondar, M.Y., Mikhaylenko, E.E., Evseeva, M., 2016. Low Salinity Flooding Trial at West Salym Field. In SPE Improved Oil Recovery Conference. SPE-179629-MS. https://doi.org/10.2118/179629-MS.

Ertekin, T., Abou-Kassem, J.H., King, G.R., 2001. Basic applied reservoir simulation. SPE Textbook Series, vol. 7. SPE.

Fang, K.T., Lin, D.K.J., Winker, P., Zhang, Y., 2000. Uniform Design: Theory and Application. Technometrics 42(3), pp. 237-248. https://doi.org/10.1080/00401706.2000.10486045#.YMM6J_lKiUk.

Fang, K.T., Wang, Y., 1994. Number-Theoretic Methods in Statistics, Chapman and Hall, London.

Fathi, S.J., Austad, T., Strand, S., 2010. "Smart Water" as a Wettablity Modifier in Chalk: The Effect of Salinity and Ionic Composition. Energy Fuels 24, 2514–2519. https://doi.org/10.1021/ef901304m.

Fenik, D.R., Nouri, A., Deutsch, C.V., 2009. Criteria for Ranking Realizations in the Investigation of SAGD Reservoir Performance. In: Paper PETSOC-2009-191 presented at the Canadian International Petroleum Conference, Calgary, Alberta. https://doi.org/10.2118/2009-191.

Fjelde, I., Asen, S.V., Omekeh, A. 2012. Low Salinity Water Flooding Experiments and Interpretation by Simulations. Paper SPE 154142 presented at the Eighteenth SPE Improved Oil Recovery Symposium, Tulsa, OK, USA. https://doi.org/10.2118/154142-MS

Fogden, A., Kumar, M., Morrow, N., Buckley, J., 2011. Mobilization of fine particles during flooding of sandstones and possible relations to enhanced oil recovery. Energy Fuels, 25, pp. 1605-1616. https://doi.org/10.1021/ef101572n.

Friedmann, F., Chawathe, A., Larue, D.K., 2001. Assessing Uncertainty in Channelized Reservoirs Using Experimental Designs. Paper SPE 71622 presented at the SPE Annual Technical Conference and Exhibition, New Orleans, LA. https://doi.org/10.2118/71622-MS.

Gaucher, D.H., Lindley, D.C. 1960. Waterflood Performance in a Stratified, Five-Spot Reservoir—A Scaled-Model Study. Trans., AIME 219 (01): 208–215. https://doi.org/10.2118/1311-G.

Gelhar, L.W., Welty, C., Rehfeldt, K.R., 1992. A critical review of field-scale dispersion in aquifers. Water Resources Research, 28(7), 1955–1974. https://doi.org/10.1029/92WR00607.

Goddin, C.S., Craig, F.F., Wilkes, J.O., Tek, M.R., 1966. A Numerical Study of Waterflood Performance In a Stratified System With Crossflow. Journal of Petroleum Technology 18 (6): 763-771.

Gorucu, S.E., Dang, C., Nghiem, L., Shrivastava, V., 2019. Modeling and optimization of low salinity waterflood with fines transport. SPE 195901 presented at the SPE ATCE Conference and Exhibition, Calgary, AB, Canada. https://doi.org/10.2118/195901-MS.

Grane, F.E., Gardner, G.H., 1961. Measurements of Transverse Dispersion in Granular Media," J. of Chem. and Eng. Data 6(2), 283–287. https://doi.org/10.1021/je60010a031.

Gupta, A.D., Lake, L.W., Pope, G.A., Sepehrnoori, K., King, M.J., 1991. High-resolution monotonic schemes for reservoir simulation. In Situ 15(3), 289–317. http://doi.org/10.1007/ s11242-007-9157-9.

Hadia, N.J., Hansen, T., Tweheyo, M.T., Torsaeter, O., 2012. Influence of Crude Oil Components on Recovery by High and Low Salinity Waterflooding. Energy & Fuels 26: 4328-4335.

Hadia, N., Lehne, H.H., Kumar, K.G., Selboe, K., Stensen. J.A., Torsaeter, O., 2011. Laboratory Investigation of Low Salinity Waterflooding on Reservoir Rock Samples from the Froy Field. Paper SPE 141114 proceedings of the SPE Middle East Oil and Gas Show and Conference, Manama, Bahrain, 25-28 September.

Hankins, N., Harwell, J., 1996. Case Studies for the Feasibility of Sweep Improvement in Surfactant-Assisted Waterflooding. Journal of Petroleum Science and Engineering 17(1):41-62. http://doi.org/10.1016/S0920-4105(96)00055-1

Haq, S., Reis, J.C., 1993. Predicting Capillary Crossflow in Layered Reservoirs. Paper SPE 26651 proceedings of the 68th Annual Technical Conference and Exhibition of the Society of Petroleum Engineers, Houston, Texas, 3-6 October.

Hasan, A.I., Ciaurri, D.E., Foss, B.A., Kleppe, J., 2009. Discrete Optimization of Oil Production in Thin Oil Rim Reservoir Under Geological Uncertainty. In: Paper SPE 123989-MS presented at the Asia Pacific Oil and Gas Conference & Exhibition, Jakarta. http://doi.org/10.2118/123989-MS.

Haykin, S., 1999. Neural Networks: A Comprehensive Foundation. Macmillan College Publishing Company, New York.

Henson, R., Todd, A., Corbett, P., 2002. Geologically Based Screening Criteria for Improved Oil Recovery Projects. Paper SPE 75148 proceedings of the SPE/DOE Improved Oil Recovery Symposium, Oklahoma,13-17 April.

Hiby, J.W., 1962. Longitudinal and Transverse Mixing during Single-phase Flow through Granular Beds. In Symposium on the Interaction between Fluids and Particles, London.

Hoteit, H., Firoozabadi, A., 2008. Numerical modeling of two-phase flow in heterogeneous permeable media with different capillarity pressures. Adv. Water Resour. 31, 56–73. https://doi.org/10.1016/j.advwatres.2007.06.006.

Hu, Q., Wang, J.S.Y., 2003. Aqueous-Phase Diffusion in Unsaturated Geological Media: A Review. Crit. Rev. Env. Sci. Tec. 33, 275–297. https://doi.org/10.1080/10643380390814488.

Isaaks, E.H., Srivastava, R.M., 1989. An Introduction to Applied Geostatistics. Oxford University Press, New York.

Jackson, M.D., Muggeridge, A.H., Yoshida, S., Johnson, H.D., 2003. Upscaling permeability measurements within complex heterolithic tidal sandstones. Math. Geol. 35, 499–520. https://doi.org/10.1023/A:1026236401104.

Jackson, M.D., Vinogradov, J., Hamon, G., Chamerois, M., 2016. Evidence, mechanisms and improved understanding of controlled salinity waterflooding part 1: Sandstones. Fuel 185, pp. 772-793. http://doi.org/10.1016/j.fuel.2016.07.075.

Jadhunandan, P.P., Morrow, N.R., 1995. Effect of wettability on waterflood recovery for crude-oil/brine/rock systems. Soc Pet Eng. https://doi.org/10.2118/22597-PA.

Jensen, J.L., Currie, I.D., 1990. A New Method for Estimating the Dykstra-Parsons Coefficient To Characterize Reservoir Heterogeneity. SPE Reservoir Engineering, 5 (3): 369-374.

Jensen, J.L., Lake, L.W., 1988. The Influence of Sample Size and Permeability Distribution on Heterogeneity Measures. SPE Reservoir Engineering 3 (2): 629-637.

Jerauld, G.R., Lin, C.Y., Webb, K.J., Seccombe, J.C., 2008. Modeling Low-Salinity Waterflooding. SPE Reserv. Eval. Eng. 11(6), 1000–1012. https://doi.org/10.2118/102239-MS.

Jessen, K., Wang, Y., Ermakov, P., Zhu, J., Orr Jr, F.M., 2001. Fast, approximate solutions for 1D multicomponent gas-injection problems. SPE J. 6(4), 442–451. https://doi.org/10.2118/74700-PA.

Jones, A., Doyle, J., Jacobsen, T., Kjonsvik, D., 1995.Which sub-seismic heterogeneities influence waterflood performance? A case study of a low net-to-gross fluvial reservoir. Geological Society, London, Special Publications 84: 5-18.

Jones, A.D.W., Verly, G.W., Williams, J.K., 1994. What reservoir characterization is required for predicting waterflood performance in a high net-to-gross fluvial environment? North Sea Oil and Gas Reservoirs-III, pp. 223–232. https://doi.org/10.1007/978-94-011-0896-6_18.

Kabir, C.S., Chawathe, A., Jenkins, S.D., Olayomi, A.J., Aigbe, C., Faparusi, D.B., 2002. Developing New Fields Using Probabilistic Reservoir Forecasting. Paper SPE 77564 presented at the SPE Annual Technical Conference and Exhibition, San Antonio, TX. https://doi.org/10.2118/77564-MS.

Kalla, S., White, C.D., 2005. Efficient Design of Reservoir Simulation Studies for Development and Optimization. Paper SPE 95456 presented at the SPE Annual Technical Conference and Exhibition, Dallas, TX. https://doi.org/10.2118/95456-MS.

Katende, A., Sagala, F., 2019. A critical review of low salinity waterflooding: Mechanism, laboratory and field application. J. Mol. Liq. 278, 627-649. https://doi.org/10.1016/j.molliq.2019.01.037.

Kazemi Nia Korrani, A., Jerauld, G.R., Sepehrnoori, K., 2016. Mechanistic Modeling of Low-Salinity Waterflooding Through Coupling a Geochemical Package with a Compositional Reservoir Simulator. SPE Reserv. Eval. Eng. 19, 142–162. https://doi.org/10.2118/169115-PA.

Kelkar, M., Perez, G., Chopra, A., 2002. Applied Geostatistics for Reservoir Characterization. Society of Petroleum Engineers Inc., Richardson, Texas.

Kennedy, J., Eberhart, R.C., 1995. Swarm Intelligence. Morgan Kaufmann Publishers.

Kereluk, M.J., Crawford, P.B., 1968. Comparison between observed and calculated sweeps in oil displacement from stratified reservoirs. Paper 851 (CONF-680483-) presented at API Prod. Div. Mid-Cont. Dist. Spring Mtg, Texas. https://www.osti.gov/biblio/5922994

King, M.J., Mansfield, M., 1999. Flow simulation of geologic models. SPE Reserv. Eval. Eng. 2(4), 351–367. https://doi.org/10.2523/38877-ms.

Kjonsvik, D., Doyle, J., Jacobsen, T., Jones, A., 1994. The Effects of Sedimentary Heterogeneities on Production from A Shallow Marine Reservoir- What Really Matters? Paper SPE 28445 proceedings of the European Petroleum Conference, London, 25-27 October.

Koltermann, C.E., Gorelick, S.M., 1996. Heterogeneity in sedimentary deposits: a review of structure-imitating, process-imitating, and descriptive approaches. Water Resour. Res. 32(9), 2617–2658. https://doi.org/10.1029/96WR00025.

Korrani, A.K.N., Jerauld, G.R., Sepehrnoori, K. 2014. Coupled Geochemical-Based Modeling of Low Salinity Waterflooding. Paper SPE 169115 proceedings of the SPE Improved Oil Recovery Symposium, Tulsa, Oklahoma, USA, 12-16 April.

Korrani, A.K.N., Sepehrnoori, K., Delshad, M., 2013. A Novel Mechanistic Approach for Modeling Low Salinity Water Injection. Paper SPE 166523 presented at the SPE ATCE, New Orleans, Louisiana, USA. https://doi.org/10.2118/166523-MS.

Kossack, C., Bilhartz, H., 1976. The Sensitivity of Micellar Flooding to Reservoir Heterogeneities. Paper SPE 5808 presented at the SPE Improved Oil Recovery Symposium, Tulsa, Oklahoma, USA. 22-24 March. http://doi.org/10.2118/5808-MS.

Koval, E.J. 1963. A Method for Predicting the Performance of Unstable Miscible Displacement in Heterogeneous Media. Society of Petroleum Engineers Journal 3 (2): 145-154.

Kuznetsov, D., Cotterill, S., Giddins, M.A., Blunt, M.J., 2015. Low-Salinity Waterflood Simulation: Mechanistic and Phenomenological Models. Paper SPE 174615 proceedings of the SPE Enhanced Oil Recovery Conference, Kuala Lumpur, Malaysia, 11-13 August.

Ladipo, L., Blunt, M.J., King, P.R., 2022. Crossflow effects on low salinity displacement in stratified heterogeneity. J. Pet. Sci. Eng. 208 (C), 109565. https://doi.org/10.1016/j.petrol.2021.109565.

Ladipo, L., Blunt, M.J., King, P.R., 2020a. A salinity cut-off method to control numerical dispersion in low-salinity waterflooding simulation. J. Pet. Sci. Eng. 184, 106586. https://doi.org/10.1016/j.petrol.2019.106586.

Ladipo, L., Blunt, M.J., King, P.R., 2020b. Optimizing Low Salinity Waterflooding with Controlled Numerical Influence of Physical Mixing Considering Uncertainty. In: ECMOR XVII - 17th European Conference on the Mathematics of Oil Recovery. pp. 1–23. https://doi.org/10.3997/2214-4609.202035035.

Ladipo, O., Ogbe, D.O., 2015. Improved Data-driven Models for Forecasting Production Performance with Uncertainty Analysis. In: Paper SPE-178412-MS Proceedings of the SPE Nigeria Annual International Conference and Exhibition. https://doi.org/10.2118/178412-MS.

Lager, A., Webb, K.J., Black, C.J.J., Singleton, M., Sorbie, K.S., 2008a. Low salinity oil recovery – an experimental investigation. Petrophysics, 49 (1), pp. 28-35.

Lager, A., Webb, K.J., Collins, I.R., Richmond, D.M., 2008b. LoSal™ enhanced oil recovery: evidence of enhanced oil recovery at the reservoir scale. In: Paper SPE 113976 presented at the SPE/DOE improved oil recovery symposium, Tulsa; 2008. http://doi.org/10.2118/113976-MS.

Lager A., Webb K.J., Black C.J.J., 2007. Impact of brine chemistry on oil recovery. Paper A24 presented at the 14th European symposium on improved oil recovery. https://doi.org/10.3997/2214-4609-pdb.24.A24.

Lager, A., Webb, K. J., Black, C. J. J., Singleton, M., Sorbie, K. S. 2006. Low Salinity Oil Recovery: An Experimental Investigation. Paper SCA2006-36 proceedings of the International Symposium of the Society of Core Analysts, Trondheim, Norway.

Lake, L.W., 1989. Enhanced Oil Recovery. Prentice-Hall, London, 175–181. ISBN 0-13-281601-66.

Lake, L.W., Hirasaki, G.J., 1981. Taylor's Dispersion in Stratified Porous Media. SPE J. 21(04), 459–468. https://doi.org/10.2118/8436-PA.

Lake, L.W., Jensen, J.L., 1989. A Review of Heterogeneity Measures Used in Reservoir Characterization. Paper SPE 20156. General for the Society of Petroleum Engineers.

Lake, L.W., Johns, R., Rossen, W.R., Pope, G.A., 2014. Fundamentals of enhanced oil recovery. ISBN: 978-1-61399-328-6.

Lantuéjoul, C., 2002. Geostatistical Simulation. Springer, Berlin. DOI:10.1007/978-3-662-04808-5.

Lantz, R.B., 1971. Quantitative Evaluation of Numerical Diffusion (Truncation Error). Soc. Pet. Eng. J. 11, 315–320. https://doi.org/10.2118/2811-PA.

Law, S., Sutcliffe, P., Fellows, S., 2014. Secondary Application of Low Salinity Waterflooding to Forties Sandstone Reservoirs. Paper SPE 170725 proceedings of the SPE Annual Technical Conference and Exhibition, Amsterdam, 27-29 October.

Lebedeva, E.V., Fogden, A., 2010. Adhesion of oil to kaolinite in water. Environ Sci Technol, 44, pp. 9470-9475. https://doi.org/10.1021/es102041b.

Li, Y., 2011. Oil recovery by low salinity water injection into a reservoir: a new study of tertiary oil recovery mechanism. Transp Porous Media, 90 (2), pp. 333-362. https://doi.org/10.1007/s11242-011-9788-8.

Ligthelm D.J., Gronsveld, J., Hofman, J.P., Brussee, N., Marcelis F., van der Linde, H.A., 2009. Novel waterflooding strategy by manipulation of injection brine composition. In: Paper SPE 119835 presented at the EUROPEC/EAGE annual conference and exhibition, Amsterdam. https://doi.org/10.2118/119835-MS.

Liu, F., Wang, M., 2020. Review of low salinity waterflooding mechanisms: Wettability alteration and its impact on oil recovery. Fuel, 267, 117112. https://doi.org/10.1016/j.fuel.2020.117112.

Liu, J., Pope, G.A., Sepehrnoori, K., 1995. A high-resolution, fully implicit method for enhanced oil recovery simulation. In: SPE Reservoir Simulation Symposium. https://doi.org/10.2118/ 29098-MS.

Lowry, P., Ferrell, H., Dauben, D., 1986. A Review and Statistical Analysis of Micellar-Polymer Field Test Data. National Petroleum Technology Office, US DOE.

Mahadevan, J., Lake, L.W., Johns, R.T., 2003. Estimation of true dispersivity in field-scale permeable media. SPE Journal, 8(3), 272–279. https://doi.org/10.2118/86303-PA.

Mahani, H., Sorop, T.G., Ligthelm, D., Brooks, A.D., Vledder, P., Mozahem, F., Ali, Y., 2011. Analysis of field responses to low-salinity waterflooding in secondary and tertiary mode in Syria. In: Paper SPE 142960 Proceedings of the SPE EUROPEC/EAGE Annual Conference and Exhibition, Vienna, Austria. SPE-142960-MS. https://doi.org/10.2118/142960-MS.

Mahmoudpour, M., Pourafshary, P., 2021. Investigation of the effect of engineered water/nanofluid hybrid injection on enhanced oil recovery mechanisms in carbonate reservoirs. J. Petrol. Sci. Eng. 196, 107662. https://doi.org/10.1016/j.petrol.2020.107662.

Mattax, C.C., Dalton, R.L. (eds.), 1990. Reservoir simulation. SPE Monograph Series, vol. 13. SPE.

Mallison, B.T., Gerritsen, M.G., Jessen, K., Orr Jr, F.M., 2005. High order upwind schemes for two-phase, multicomponent flow. SPE J. 10(3), 297–311. https://doi.org/10.2118/79691-PA.

McGuire, P.L., J.R. Chatham, F.K. Paskvan, D.M. Sommer, Carini, F.H., 2005. Low salinity oil recovery: an exciting new EOR opportunity for Alaska's North Slope Soc Pet Eng. https://doi.org/10.2118/93903-MS.

McKay, M.D., Beckman, R.J., Conover, W.J., 1979. A Comparison of Three Methods for Selecting Values of Input Variables in the Analysis of Output from a Computer Code. Technometrics 21(2), pp. 55-61. https://doi.org/10.1080/00401706.2000.10485979#.YMM2s_lKiUk.

McLennan, J.A., Deutsch, C.V., 2005. Ranking Geostatistical Realizations by Measures of Connectivity. In: Paper SPE 98168-MS presented at the SPE International Thermal Operations and Heavy Oil Symposium, Calgary, Alberta. https://doi.org/10.2118/98168-MS .

McMillan, M., Rahnema, H., Romiluy, J., Kitty, F., 2016. Effect of exposure time and crude oil composition on low-salinity water flooding. Fuel 185, 263–272. https://doi.org/10.1016/j.fuel.2016.07.090.

Morrow N, Buckley J., 2011. Improved oil recovery by low-salinity waterflooding. Soc Pet Eng. https://doi.org/10.2118/129421-JPT.

Muggeridge, A.H., Hongtong, P., 2014. An Upscaling Methodology for EOR. In ECMOR XIV-14th European Conference on the Mathematics of Oil Recovery. https://doi.org/10.3997/2214-4609.20141862.

Muskat, M. 1949. Effect of Permeability Stratification in Cycling Operations. Transactions of AIME 179 (1): 313-328.

Nasralla, R.A., Bataweel, M.A., Nasr-El-Din, H.A., 2013. Investigation of Wettability Alteration and Oil-Recovery Improvement by Low-Salinity Water in Sandstone Rock. Journal of Canadian Petroleum Technology 52 (2): 144-154.

Nasralla, R.A., Nasr-El-Din, H.A., 2014. Double-layer expansion: is it a primary mechanism of improved oil recovery by low-salinity waterflooding? Soc Pet Eng. https://doi.org/10.2118/154334-PA.

Nelder, J.A., Mead, R., 1965. A simplex method for function minimization", Computer Journal 7(4), pp 308-313. https://doi.org/10.1093/comjnl/7.4.308.

Nelson, P.H., 1994. Permeability-porosity relationships in sedimentary rocks. Log Anal. 35(03), 38–62.

Nguyen, N., Dang, C., Gorucu, S.E., Nghiem, L., Chen, Z., 2020. The role of fines transport in low salinity waterflooding and hybrid recovery processes. Fuel, 263, 116542. https://doi.org/10.1016/j.fuel.2019.116542

Omekeh, A.V., Friis, H.A., Fjelde, I., Evje, S., 2012. Modeling of Ion-Exchange and Solubility in Low Salinity Water Flooding. In SPE Improved Oil Recovery Symposium. SPE 154144. https://doi.org/10.2118/154144-MS.

Orr, F.M. Jr. 2004. High Resolution Prediction of Gas Injection Process Performance for Heterogeneous Reservoirs. Final Report for DOE Project, DE-FC26-00BC15319, Stanford U., Stanford, California. https://doi.org/10.2172/829919.

Osman, M.E., Tiab, D., 1981. Waterflooding Performance and Pressure Analysis of Heterogeneous Reservoirs. Paper SPE 9656 proceedings of the Middle East Oil Technical Conference of the Society of Petroleum Engineers, Manama, Bahrain, 9-12 March.

Peaceman, D.W., 1977. Fundamentals of numerical reservoir simulation. Development in Petroleum Science, vol. 6. Elsevier.

Peake, W.T., Abadah, M., Skander, L., 2005. Uncertainty Assessment Using Experimental Design: Minagish Oolite Reservoir. Paper SPE 91820 presented at the SPE Reservoir Simulation Symposium, The Woodlands, TX. https://doi.org/10.2118/91820-MS.

Perkins, T.K., Johnston, O.C., 1963. A Review of Diffusion and Dispersion in Porous Media. SPEJ, 3(1), 70–84; Trans., AIME, 228. SPE- 480-PA. https://doi.org/10.2118/480-PA.

Peterson, J., Riva, D., Edmunds, N., Solanki, S., 2010. The Application of Solvent-Additive SAGD Processes in Reservoirs With Associated Basal Water. In: Paper SPE 137833 presented at the Canadian Unconventional Resources & International Petroleum Conference, Alberta. https://doi.org/10.2118/137833-MS.

Pope, G.A., 1980. The Application of Fractional Flow Theory to Enhanced Oil Recovery. Society of Petroleum Engineers Journal 20 (3): 191-205.

Pu H, Xie X, Yin P, Morrow NR. 2010. Low salinity waterflooding and mineral dissolution. In: Paper SPE 134042 presented at the SPE annual technical conference and exhibition, Florence, Italy. https://doi.org/10.2118/134042-MS.

Puntervold, T., Strand, S., Austad, T., 2015. Modified seawater as a smart EOR fluid in chalk. J. Petrol. Sci. Eng. 133, 440–443. https://doi.org/10.1016/j.petrol.2015.06.034.

Rashid, B., Muggeridge, A.H., Bal, A., Williams, G., 2012. Quantifying the Impact of Permeability Heterogeneity on Secondary-Recovery Performance. SPE Journal 17 (2): 455-468.

RezaeiDoust, A., Puntervold, T., Strand, S., Austad, T., 2009. Smart water as wettability modifier in carbonate and sandstone: A discussion of similarities/differences in the chemical mechanisms. Energy Fuels, 23 (9), 4479–4485. https://doi.org/10.1021/ef900185q.

RezaeiDoust, A., Puntervold, T., Austad, T., 2010. A discussion of the low-salinity EOR potential for a North Sea sandstone field. Soc Pet Eng. https://doi.org/10.2118/134459-MS.

RezaeiDoust, A., Puntervold, T., Austad, T., 2011. Chemical verification of the EOR mechanism by using low saline/smart water in sandstone. Energy Fuels, 25, 2151-2162. https://doi.org/10.1021/ef200215y.

Riaz, A., Tchelepi, H.A., 2006. Influence of relative permeability on the stability characteristics of immiscible flow in porous media. Transp. Porous Media 64(3), 315–338. https://doi.org/10.1007/s11242-005-4312-7.

Richardson, J.G., Perkins, F.M. Jr., 1957. A Laboratory Investigation of the Effect of the Rate on Recovery of Oil by Waterflooding. Trans., AIME 210 (01): 114–121. https://doi.org/10.2118/693-G.

Robbana, E., Buikema, T., Mair, C., Williams, D., Mercer, D., Webb, K., Hewson, A., Reddick, C., 2012. Low Salinity Enhanced Oil Recovery- Laboratory to Day One Field Implementation- LoSal EOR into the Clair Ridge Project. Paper SPE 161750 proceedings of the Abu Dhabi International Petroleum Exhibition & Conference, Abu Dhabi, 11-14 November.

Robertson EP. 2010. Oil recovery increases by low-salinity flooding: minnelusa and green river formations. In: Paper SPE 132154 presented at the SPE annual technical conference and exhibition, Florence, Italy. https://doi.org/10.2118/132154-MS.

Saad, N., Pope, G.A., Sepehrnoori, K., 1990. Application of higher- order methods in compositional simulation. SPE Reserv. Eng. 5(4), 623–630. https://doi.org/10.2118/18585-PA.

Sall, J., 1990. Leverage Plots for General Linear Hypotheses. The American Statistician 44(4), 308–315. https://doi.org/10.1080/00031305.1990.10475750.

Salter, S.J., Mohanty, K.K., 1982. Multiphase Flow in Porous Media: I. Macroscopic Observations and Modeling. In SPE 57th Annual Technical Conference and Exhibition. SPE-11017-MS. https://doi.org/10.2118/11017-MS.

Sandengen, K., Arntzen, O.J., 2013. Osmosis During Low Salinity Water Flooding. Paper A19 proceedings of the IOR 2013-17th European Symposium on Improved Oil Recovery, St. Petersburg, Russia, 16-18 April.

Satterthwaite, F.E., 1959. Random Balance Experimentation. Technometrics 1(2), pp. 111-137. https://doi.org/10.1080/00401706.1959.10489853.

Schlumberger, 2015. ECLIPSE Technical Description. https://slb.com.

Schlumberger, 2020. PETREL Technical Manual. https://slb.com.

Schmalz, J.P., Rahme, H.D., 1950. The Variation of Waterflood Performance with Variation in Permeability Profile. Prod.Monthly, 15 (9): 9-12.

Seccombe, J., Lager, A., Jerauld, G., Jhaveri, B., Buikema, T., Bassler, S., Denis, J., Webb, K., Cockin, A., Fueg, E., Paskvan, F., 2010. Demonstration of Low-Salinity EOR at Interwell Scale, Edicott Field, Alaska. Paper SPE 129692 proceedings of the 2010 SPE Improved Oil Recovery Symposium, Tulsa, Oklahoma, USA, 24-28 April.

Seccombe, J.C., Lager, A., Webb, K., Jerauld, G., Fueg, E., 2008. Improving Waterflood Recovery: LoSal^{TM} EOR Field Evaluation. In: Paper SPE-113480-MS Proceedings of the SPE Improved Oil Recovery Symposium, Tulsa. https://doi.org/10.2118/113480-MS.

Shaddel, S., Tabatabae-Nejad, S.A., 2015. Alkali/surfactant improved low-salinity waterflooding. Transp Porous Med 106 (3), 621–642. https://doi.org/10.1007/s11242-014-0417-1.

Sheng J., 2010. Modern Chemical Enhanced Oil Recovery: Theory and Practice. Gulf Professional Publishing. ISBN 978-1-85617-745-0.

Shojaei, M.J., Ghazanfari, M.H., Masihi, M., 2015. Relative permeability and capillary pressure curves for low salinity water flooding in sandstone rocks. J. Nat. Gas Sci. Eng. 25, 30–38. https://doi.org/10.1016/j.jngse.2015.04.023.

Shook, M., Li, D., Lake, L.W., 1992. Scaling immiscible flow through permeable media by inspectional analysis. In Situ 16 (4): 311.

Shook, G.M., Mitchell, K.M., 2009. A Robust Measure of Heterogeneity for Ranking Earth Models: The F-PHI Curve and Dynamic Lorenz Coefficient. Paper SPE 124625 proceedings of the 2009 SPE Annual Technical Conference and Exhibition, New Orleans, Louisiana, USA, 4-7 October.

Skrettingland, K., Holt, T., Tweheyo, M.T., Skjevark, I. 2011. Snorre Low-Salinity-Water Injection-Coreflooding Experiments and Single-Well Field Pilot. SPE Reservoir Evaluation & Engineering 14 (2): 182-192.

Solairaj, S., Britton, C., Kim, D., Weerasooriya, U., Pope, G., 2012. Measurement and Analysis of Surfactant Retention. Paper SPE 154247 presented at the Eighteenth SPE Improved Oil Recovery Symposium, Tulsa, Oklahoma, USA. https://doi.org/10.2118/154247-MS.

Solano, R., Johns, R.T., Lake, L.W., 2001. Impact of reservoir mix- ing on recovery in enriched-gas drives above the minimum miscibility enrichment. SPE Reserv. Evalu. Eng. 4(5), 358– 365. https://doi.org/10.2118/73829-PA.

Sorbie, K.S., Mackay, E.J., 2000. Mixing of injected, connate and aquifer brines in waterflooding and its relevance to oilfield scaling. Journal of Petroleum Science and Engineering, 27(1–2), pp.85–106. https://doi.org/10.1016/S0920-4105(00)00050-4.

Sorbie, K.S., Wat, R.M.S., Rowe, T.C. 1987. Oil Displacement in Heterogeneous Cores: Analysis of Recovery Mechanisms. Paper SPE 16706 proceedings of the 62nd Annual Technical Conference and Exhibition of the Society of Petroleum Engineers, Dallas, Texas, 27-30 September.

Spagnuolo, M., Callegaro, C., Bartosek, M., Masserano, F., Nobili, M., Sabatino, R., Blunt, M.J., 2016. Low Salinity Waterflooding: From Single Well Chemical Tracer Test Interpretation to Sector Model Forecast Scenarios. In: Paper SPE-179626-MS Proceedings of the SPE Improved Oil Recovery Conference, Tulsa. https://doi.org/10.2118/179626-MS.

Spagnuolo, M., Callegaro, C., Guadagnini, A., Sabatino, R., 2015. Low Salinity Waterflooding for Enhanced Oil Recovery – Stochastic Model Calibration and Uncertainty Quantification. In: Proceedings of 18th European Symposium on Improved Oil Recovery, Dresden, Germany. https://doi.org/10.3997/2214-4609.201412146.

Storn, R., Price, K., 1995. Differential Evolution - A Simple Efficient Adaptive Scheme for Global Optimization over Continuous Spaces. International Computer Science Institute, Berkeley, CA.

Suijkerbuijk, B.M.J.M., Hofman, J.P., Ligthelm, D.J., Romanuka, J., Brussee, N., Van Der Linde, H.A., Marcelis, F., 2012. Fundamental investigations into wettability and low salinity flooding by parameter isolation. In SPE Improved Oil Recovery Symposium. Society of Petroleum Engineers. SPE 154204. https://doi.org/10.2118/154204-MS.

Suman, Y.K., Shirif, E., Ibrahim, H., Ala-Ktiwi, A. 2014. Evaluation of Low Saline "Smart Water" Enhanced Oil Recovery in Light Oil Reservoirs. World Journal of Engineering and Technology 2: 13- 22.

Tang, B., 1993. Orthogonal Array-Based Latin Hypercubes. Journal of the American Statistical Association: Theory and Methods, 88(424), pp.1392–1397. DOI: 10.1080/01621459.1993.10476423.

Tang, G.Q., Morrow, N.R., 1999. Influence of Brine Composition and Fines Migration on Crude Oil/Brine/Rock Interactions and Oil Recovery. J. Pet. Sci. Eng. 24, 99–111. https://doi.org/10.1016/S0920-4105(99)00034-0.

Taylor, G. 1953. Dispersion of soluble matter in solvent flowing slowly through a tube. Proceedings of The Royal Society 219 (1137): 186-203.

Taylor, G. 1954. Conditions under which dispersion of a solute in a stream of solvent can be used to measure molecular diffusion. Proceedings of The Royal Society 225 (1163): 473-477.

Tchelepi, H.A. 1994. Viscous fingering, gravity segregation and permeability heterogeneity in two-dimensional and three-dimensional flows. PhD dissertation, Stanford U., Stanford, California.

Thiele, M. R., Batycky, R. P., Pollitzer, S., Clemens, T., 2010. Polymer-flood modeling using streamlines. SPE Reserv. Eval. Eng. 13, 313–322. https://doi.org/10.2118/115545-PA.

Thomas, G.W., 1982. Principles of hydrocarbon reservoir simulation, 2 edn. Prentice Hall, New Jersey.

Thompson, A.H., Katz, A.J., Krohn, C.E., 1987. The microgeometry and transport properties of sedimentary rock. Adv. Phys. 36(5), 625–694. https://doi.org/10.1080/00018738700101062.

Thyne, G., Gamage, P., 2011. Evaluation of the Effect of Low Salinity Waterflooding for 26 Fields in Wyoming. Paper SPE 147410 proceedings of the SPE Annual Technical Conference and Exhibition, Colorado, 30 October- 2 November.

Tian, H., Wang, M., 2017. Electrokinetic mechanism of wettability alternation at oil-water-rock interface. Surf Sci Rep, 72(6), 369–391. https://doi.org/10.1016/j.surfrep.2018.01.001.

Tran, T.T., 1994. Improving variogram reproduction on dense simulation grids. Comput Geosci 20(7–8):1161–1168. https://doi.org/10.1016/0098-3004(94)90069-8.

Tripathi, I., Mohanty, K.K., 2008. Instability due to wettability alteration in displacements through porous media. Chem. Eng. Sci. 63 (21), 5366–5374. https://doi.org/10.1016/j.ces.2008.07.022.

van Essen, G., Zandvliet, M., Van den Hof, P., Bosgra, O., Jansen, J., 2009. Robust Waterflooding Optimization of Multiple Geological Scenarios. SPE J. 14(01), 202–210. https://doi.org/10.2118/102913-PA.

Vledder, P., Fonseca, J. C., Wells, T., Gonzalez, I., Ligthelm, D., 2010. Low Salinity Water Flooding: Proof of Wettability Alteration on A Field Wide Scale. Paper SPE 129564 proceedings of the 2010 SPE Improved Oil Recovery Symposium, Tulsa, Oklahoma, USA, 24-28 April.

Wang, F.H.L., 1988. Effect of Wettability Alteration on Water/Oil Relative Permeability, Dispersion, and Flowable Saturation in Porous Media. SPE Reservoir Engineering, 3(02). SPE-15019-PA. https://doi.org/10.2118/15019-PA.

Wang, W., Yue, X.A., Zhao, R.B., Yang, H., 2012. Experimental and theoretical studies on effects of heterogeneity on channeling in waterflooding. Adv. Mater. Res., 518–523, pp. 4084-4087. https://doi.org/10.4028/www.scientific.net/AMR.518-523.4084.

Webb, K.J., Black, C.J.J., Al-Ajeel, H., 2004. Low salinity oil recovery – log-inject-log. Soc Pet Eng. https://doi.org/10.2118/89379-MS.

Webb, K.J., Black, C.J.J., Edmonds, I.J., 2005. Low Salinity Oil Recovery – The Role of Reservoir Condition Corefloods. In 13th EAGE European Symposium on Improved Oil Recovery, pp. 25–27. https://doi.org/10.3997/2214-4609-pdb.12.C18.

Wright, R.J., Wheat, M.R., Dawe, R.A., 1987. Slug Size and Mobility Requirements for Chemically Enhanced Oil Recovery Within Heterogeneous Reservoirs. SPE Reservoir Engineering 2 (1): 92-102.

Wylie, P., Mohanty, K.K., 1997. Effect of Water Saturation on Oil Recovery by Near-Miscible Gas Injection. SPERE 12 (4): 264–268. SPE-36718-PA. https://doi.org/10.2118/36718-PA.

Yortsos, Y.C., 1995. A theoretical analysis of vertical flow equilibrium. Transp. Porous Media 18(2), 107–129. https://doi.org/10.1007/BF01064674.

Yang, C., Nghiem, L.X, Card, C., Bremeier, M., 2007. Reservoir Model Uncertainty Quantification Through Computer-Assisted History Matching. Paper SPE 109825 presented at the SPE Annual Technical Conference and Exhibition, Anaheim, CA. https://doi.org/10.2118/109825-MS.

Yang, C., Card, C., Nghiem, L., 2009. Economic Optimization and Uncertainty Assessment of Commercial SAGD Operations. Journal of Canadian Petroleum Technology, 48(09). PETSOC-09-09-33. https://doi.org/10.2118/09-09-33.

Yang, C., Card, C., Nghiem, L., Fedutenko, E., 2011. Robust Optimization of SAGD Operations under Geological Uncertainties. In: Paper SPE-141676-MS Proceedings of the SPE Reservoir Simulation Symposium, Texas. https://doi.org/10.2118/141676-MS.

Ye, K.Q., 1998. Orthogonal Column Latin Hypercubes and Their Application in Computer Experiments. Journal of the American Statistical Association: Theory and Methods, 93(444), pp.1430–1439. DOI: 10.1080/01621459.1998.10473803.

Yeten, B., Durlofsky, L.J., Aziz, K., 2003. Optimization of Nonconventional Well Type, Location and Trajectory. SPE J. 8(03), 200-210. https://doi.org/10.2118/86880-PA.

Yortsos, Y.C., 1995. A theoretical analysis of vertical flow equilibrium. Transp. Porous Media 18(2), 107–129. https://doi.org/10.1007/BF01064674.

Youden, W.J., Kempthorne, O., Tukey, J.W., Box, G.E.P., Hunter, J.S., 1959. Discussion of the Papers of Messrs. Satterthwaite and Budne. Technometrics 1(2), pp. 157-193. https://doi.org/10.1080/00401706.1959.10489855.

Zapata, V.J., Lake, L.W., 1981. A theoretical analysis of viscous crossflow. Paper SPE 10111 presented at SPE Annual Technical Conference and Exhibition. Society of Petroleum Engineers, San Antonio, TX. https://doi.org/10.2523/10111-MS.

Zeinijahromi, A., Ahmetgareev, V., Ibatullin, R., Bedrikovetsky, P., 2015. Sensitivity study of low salinity water injection in Zichebashskoe Oilfield. Chem. Eng. 6 (1), 10–21. https://doi.org/10.5897/JPGE 2014.0212.

Zhang, P., Tweheyo, M.T., Austad, T., 2006. Wettability alteration and improved oil recovery in chalk: The effect of calcium in the presence of sulfate. Energy and Fuels 20, 2056–2062. https://doi.org/10.1021/ef0600816.

Zhang, Y., Xie, X., Morrow, N.R., 2007. Waterflood performance by injection of brine with different salinity for reservoir cores. In: Paper SPE 109849 presented at the SPE annual technical conference and exhibition, Anaheim, California, USA. https://doi.org/10.2118/109849-MS.

Zhang, Y., Morrow, N.R., 2006. Comparison of secondary and tertiary recovery with change in injection brine composition for crude oil/sandstone combinations. In: Proceedings of the SPE/DOE Symposium on Improved Oil Recovery, Tulsa, Oklahoma, U.S.A, SPE 99757. https://doi.org/10.2118/99757-MS.

Zhou, D., Fayers, F.J., Orr, F.M., 1994: Scaling of multiphase flow in simple heterogeneous porous media. SPE Reserv. Eng. 12(03), 173–178. https://doi.org/10.2118/27833-PA.

Zhou, Y., Muggeridge, A.H., Berg, C.F., King, P., 2019. Effect of Layering on Incremental Oil Recovery from Tertiary Polymer Flooding. SPE Res Eval & Eng, 22(03), 941–951. https://doi.org/ 10.2118/194492-PA.

Zubarev, D.I., 2009. Pros and Cons of Applying Proxy-Models as a Substitute for Full Reservoir Simulations. In: Paper SPE 124815 presented at the SPE Annual Technical Conference and Exhibition. https://doi.org/10.2118/124815-MS.

Appendices

Appendix A – Evaluation of Longitudinal Dispersivity

The analytical solution to the 1D advection-dispersion equation for the concentration (c) profile of a miscible displacement in a homogeneous porous medium (Aronofsky and Heller, 1957) is given as:

$$c = \frac{1}{2} erfc\left(\frac{x - vt}{2\sqrt{\alpha_L vt}}\right) + \frac{e^{\frac{x}{\alpha_L}}}{2} erfc\left(\frac{x + vt}{2\sqrt{\alpha_L vt}}\right) \qquad (A.1)$$

where x is the position in the system along the longitudinal direction of flow and equals *L* at the end of the model, t is the displacement or injection time, v is the advection velocity of the displacement or concentration front, and α_L is the longitudinal dispersivity defined, under negligible diffusion, as

$$\alpha_L = \frac{1}{P_e} L \qquad (A.2)$$

P_e is the dimensionless Peclet number, and the normalized longitudinal dispersivity, D_L and normalized grid-size, Δx_D are defined in this work as

$$D_L = \frac{1}{P_e} = \frac{\alpha_L}{L}\ , \qquad \Delta x_D = \frac{x_L}{L} = \frac{1}{N} \qquad (A.3)$$

where x_L is the grid-size in the longitudinal direction of flow (along x), and N is the number of grid-blocks.

The normalized numerical longitudinal dispersivity, $D_{L,num}$ is evaluated using the formula of Sorbie and Mackay (2000):

$$D_{L,num} = \frac{1}{P_e} = \frac{\alpha_{L,num}}{L} = \left(\frac{\Delta x_D}{2} + v\frac{\Delta t}{2L}\right) \qquad (A.4)$$

where Δt and v are the time step length and salt front velocity respectively.

The dispersivity of the effluent concentration profile is fitted using the approximate solution to equation (**A.1**) developed by Brigham et al. (1961):

$$P_e = \left(\frac{2.380}{U_{80} - U_{20}}\right)^2 = \left(\frac{3.625}{U_{90} - U_{10}}\right)^2 = \left(\frac{4.65}{U_{95} - U_5}\right)^2 \qquad (A.5)$$

where U is a volume modifying function at different percentiles given as

$$U = \frac{(Q_D - 1)}{\sqrt{Q_D}} \qquad (A.6)$$

and Q_D is the dimensionless pore volumes injected at the percentile point of the reference U.

Al-Ibadi et al. (2018a) modified the advection velocity, v in equation (**A.1**) for the salt front in a LSWF as

$$v = v_{LS} + \left(\left(1 - C_d^{mid_eff}\right)^3 \frac{(v_{HS} - v_{LS})}{\sqrt{P_e}} \right) \quad (A.7)$$

where v_{HS} and v_{LS} are the analytical velocities of the leading high-salinity and trailing low-salinity water fronts respectively, and $C_d^{mid-eff}$ is the dimensionless mid salinity threshold in the simulation grid defined as

$$C_d^{mid_eff} = \frac{C_s^{mid_eff} - C_s^{inj}}{C_s^{formation} - C_s^{inj}} \quad (A.8)$$

where $C_s^{mid_eff}$, C_s^{inj} and $C_s^{formation}$ are the mid salinity threshold, injected brine salinity and formation brine salinity respectively in the simulation grid. The mid salinity threshold is defined as

$$C_s^{mid_eff} = \frac{C_s^{LS} + C_s^{HS}}{2} \quad (A.9)$$

where C_s^{LS} and C_s^{HS} are the minimum and maximum salinity thresholds in the grid. For any evaluated $C_s^{mid_eff}$ to correct numerical dispersion effects in a grid, the arbitrarily selected C_s^{LS} and C_s^{HS} must satisfy equation (**A.9**).

The velocity of each effluent salinity or concentration (C_s) is defined in terms of the injection time, t till its breakthrough at the end of the model, L as

$$v_s = \frac{L}{t} = \frac{q_t}{\phi Q_D} \quad (A.10)$$

where $\frac{q_t}{\phi}$ is the total interstitial velocity and Q_D is the dimensionless pore volumes injected till the breakthrough of v_s at L. In dimensionless terms,

$$v_{s_D} = \frac{1}{Q_D} \quad (A.11)$$

Appendix B – Evaluation of Transverse Dispersivity in a Model

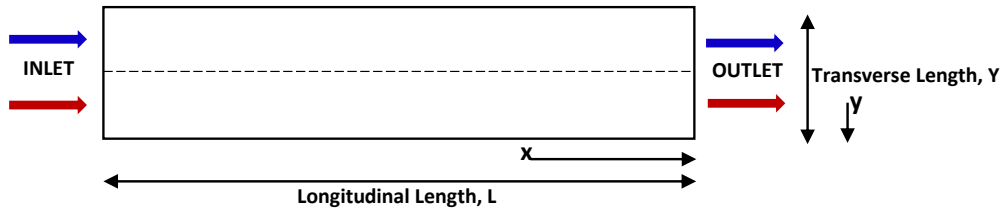


Fig. B.1: A schematic of the 2D-model used for the evaluation of transverse dispersion.

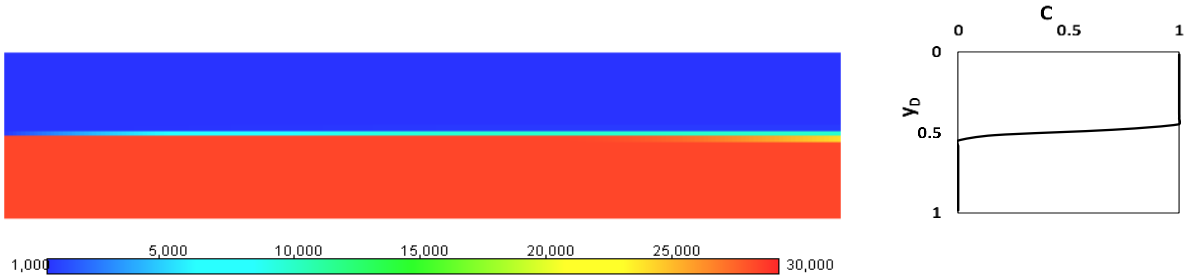


Fig. B.2: An example of a concentration map showing the effect of transverse dispersion (mixing across the mid-line). Also shown is the concentration profile along the transverse direction at the right-end face.

The model is shown in **Fig. B.1**. Low-salinity brine (red) and in situ high-salinity brine (blue) are continuously injected across the first and second halves of the inlet face of the model respectively. Both brines are injected at equal rates until a steady-state distribution of the two injected brines is reached as shown in **Fig. B.2**. This state is reliably achieved at approximately 100% water-cut. The production and injection rates are equal throughout the simulations. The permeability in the transverse direction to flow is controlled throughout the simulation to prevent flow along this direction. Transverse dispersion therefore mixes the brines across the midline of the model (**Fig. B.1**) and the width of the mixing zone increases towards the outlet end (**Fig. B.2**). This arrangement is similar to those of various reported transverse dispersion experiments, such as Blackwell (1962) and Alkindi et al. (2011).

Taking the distances along the transverse (Y) and longitudinal (L) directions as y and x respectively, we define dimensionless distances y_D and x_D along the directions respectively as

$$y_D = \frac{y}{Y}, \qquad x_D = \frac{x}{L} \tag{B.1}$$

The normalized grid-size in the longitudinal direction has been defined in equation (**A.3**). The normalized grid-size in the transverse direction, Δy_D is given as:

$$\Delta y_D = \frac{y_Y}{Y} \tag{B.2}$$

where y_Y is the grid-size in the transverse (Y) direction.

The concentration profile $(c - y_D)$ taken transversely (along the Y-direction) at any longitudinal point, x (away from the inlet face) shows a smooth transition from the concentration of the low-salinity brine to that of the in situ brine rather than a step change. This profile is fitted for the transverse dispersivity using the analytical solution of Hiby (1962):

$$c = \frac{1}{2} erf\left(\frac{y + b}{2\sqrt{\alpha_T x}}\right) - \frac{1}{2} erf\left(\frac{y - b}{2\sqrt{\alpha_T x}}\right) \tag{B.3}$$

where α_T is the transverse dispersivity (with the unit of length), and b is the y_D-location of the midline of the model.

The normalized transverse dispersivity, D_T is defined as:

$$D_T = \frac{\alpha_T}{Y} \tag{B.4}$$

Equation (B.3) is written in terms of dimensionless parameters as

$$c = \frac{1}{2} erf\left(\frac{y_D + b}{2\sqrt{D_T x_D}} R\right) - \frac{1}{2} erf\left(\frac{y_D - b}{2\sqrt{D_T x_D}} R\right) \tag{B.5}$$

R is a constant for the system, and is defined as:

$$R = \sqrt{\frac{Y}{L}} \tag{B.6}$$

The transverse dispersivity is evaluated in this work at $b = y_D = 0.5$ and $x_D = 1$.

Appendix C – Relative permeabilities resulting from the Corey exponents and end-point relative permeabilities set for the different mobility-ratio cases

Relative permeabilities used to define the mobilities under high- and low-salinity conditions for the four mobility-ratio cases considered which are likely of real systems are presented in **Fig. C.1**. Besides, the viscosities of the fluids are varied to generate representative fractional flow behaviour (e.g., **Fig. 4.1**b) of each mobility-ratio case especially when $M_{F,HS} > 1$.

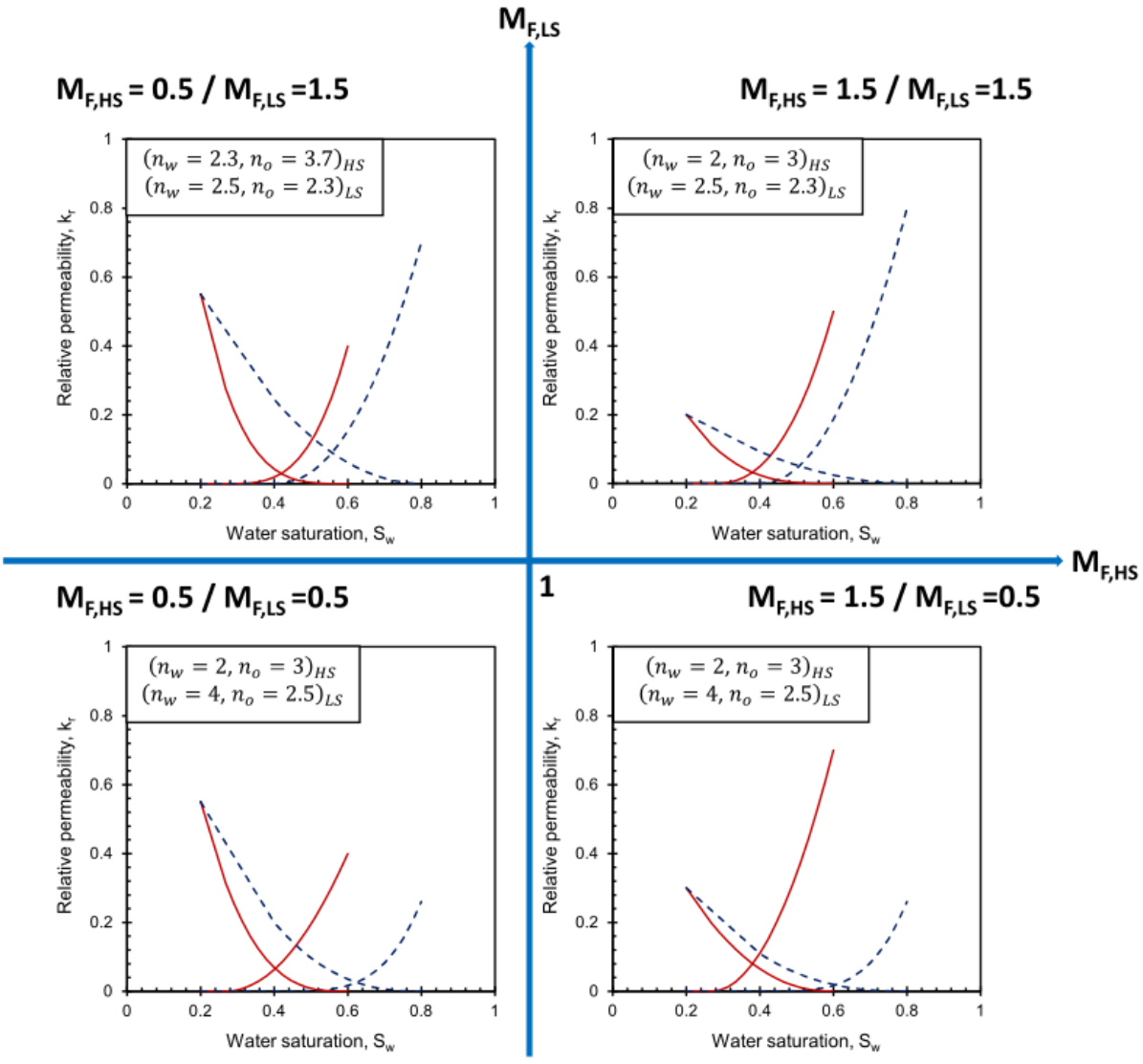


Fig. C.1: Relative permeabilities for the various shock-front mobility-ratio cases under different wettability conditions: high-salinity (HS) in the red solid lines, low-salinity (LS) in the blue dashed lines. Inset: Corey exponents for water ($\boldsymbol{n_w}$) and oil ($\boldsymbol{n_o}$).

Appendix D – Viscous Crossflow Recovery Efficiency as Function of Shock-front Mobility Ratios in the Presence of Physical Dispersion

Viscous crossflow recovery efficiency relative to no-crossflow displacement at different shock-front mobility ratios combination under dispersion (similar to evaluated crossflow performance in **Fig. 7.9** but for other levels of physical mixing, *Pe*) are shown in **Figs. D1-D3.**

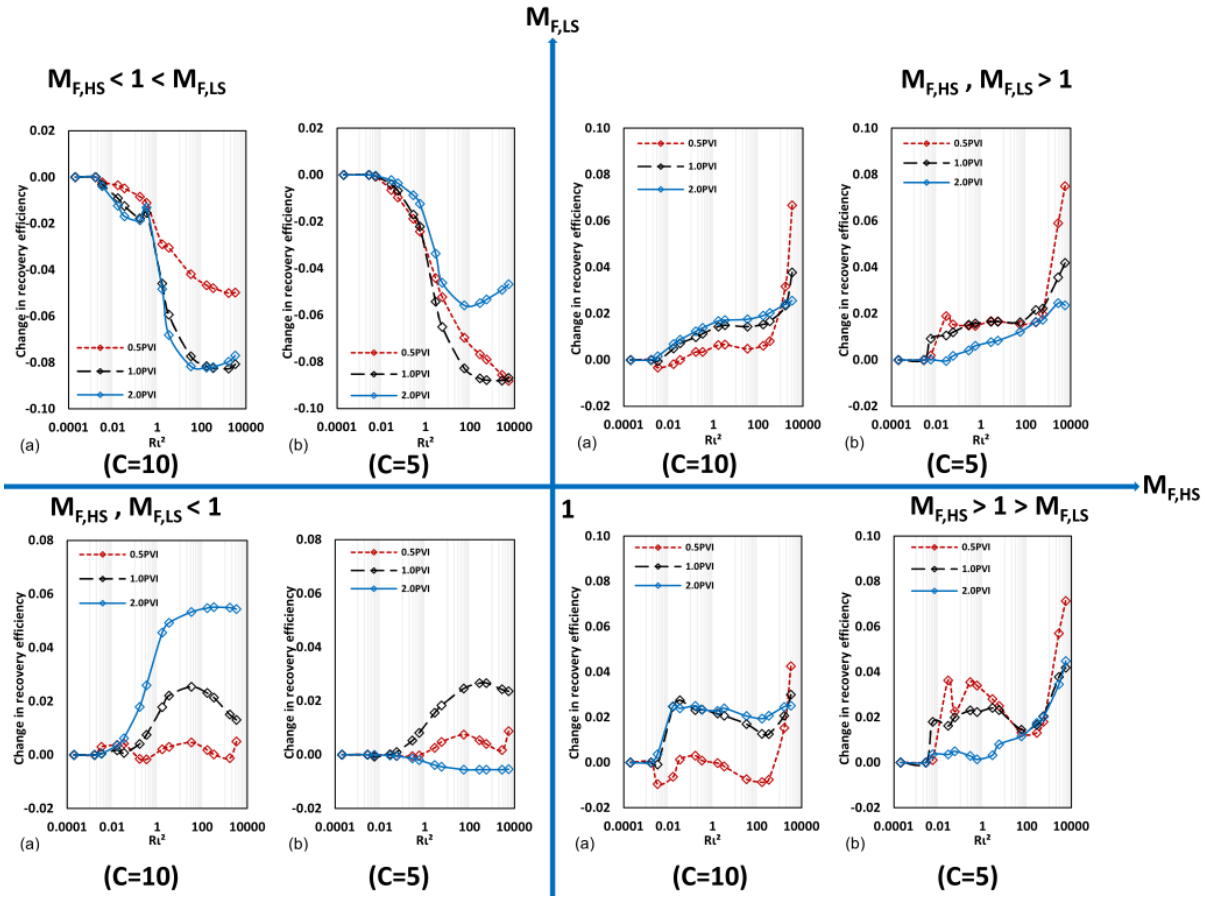


Fig. D1: Change in recovery efficiency due to crossflow (ΔURF) as a function of crossflow amount (R_i^2) for various shock-front mobility-ratio cases in a secondary LSWF under dispersion (*Pe* of 1.0% of the model-length L). Results are shown for $C = 5$ and $C = 10$ at different performance times (or injected LS-slug sizes: *red* $0.5\ PVI$, *black* $1.0\ PVI$, *blue* $2.0\ PVI$).

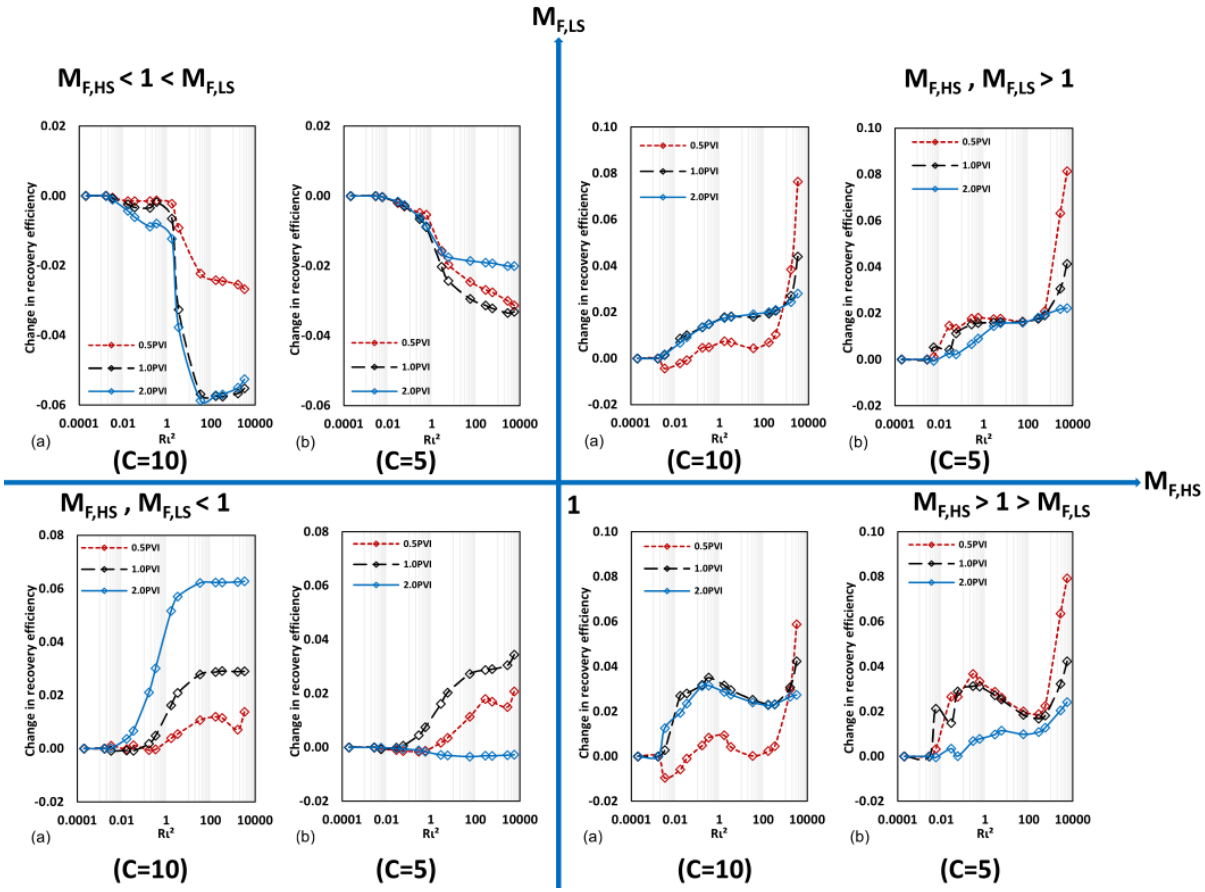


Fig. D2: Change in recovery efficiency due to crossflow (ΔURF) as a function of crossflow amount (R_l^2) for various shock-front mobility-ratio cases in a secondary LSWF under dispersion (*Pe* of 3.5% of the model-length L). Results are shown for $C = 5$ and $C = 10$ at different performance times (or injected LS-slug sizes: *red* 0.5 PVI, *black* 1.0 PVI, *blue* 2.0 PVI).

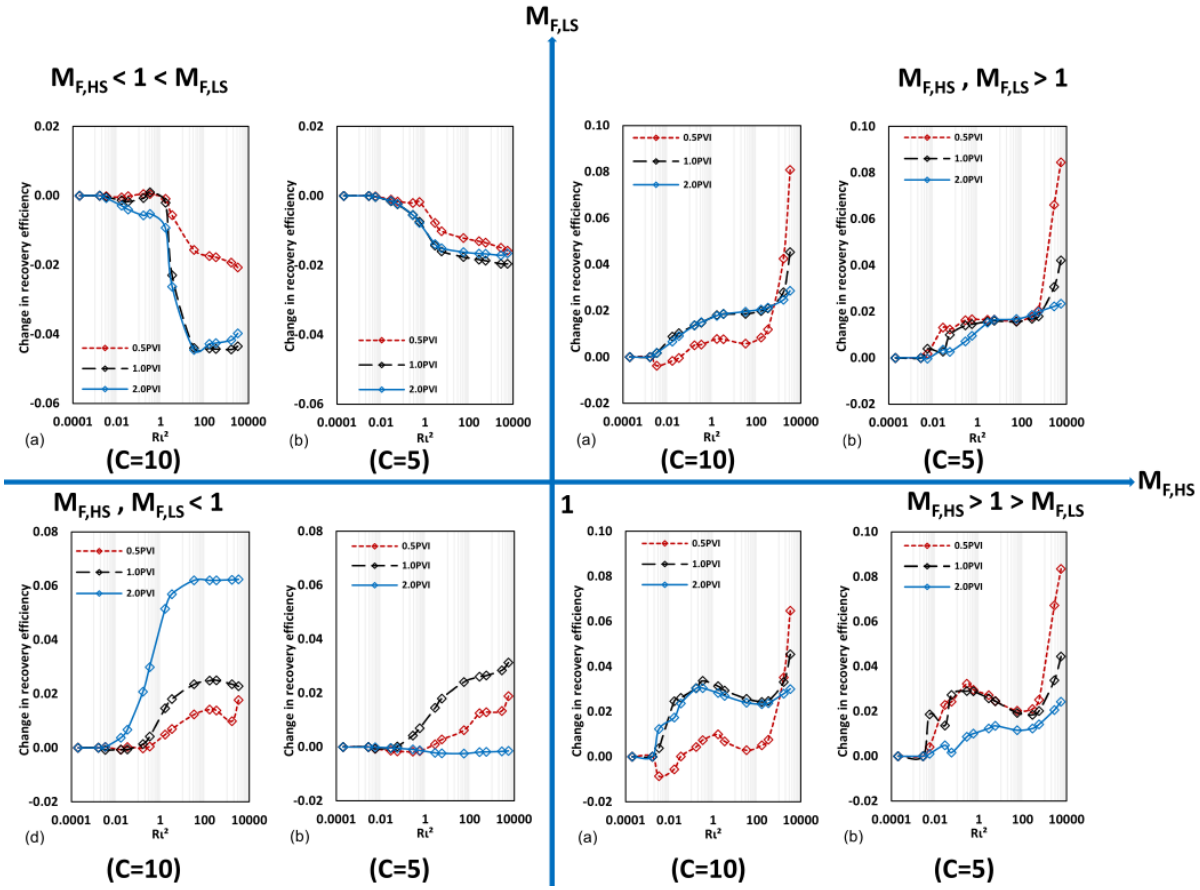


Fig. D3: Change in recovery efficiency due to crossflow (ΔURF) as a function of crossflow amount (R_l^2) for various shock-front mobility-ratio cases in a secondary LSWF under dispersion (*Pe* of 5.0% of the model-length L). Results are shown for $C = 5$ and $C = 10$ at different performance times (or injected LS-slug sizes: *red* $0.5\ PVI$, *black* $1.0\ PVI$, *blue* $2.0\ PVI$).

Appendix E – Influence of Gravity-Induced Crossflow on Recovery Efficiency Under Physical Mixing

The impact of gravity on the effect of crossflow on recovery efficiency relative to no-crossflow displacement for the $M_{F,HS} < 1 < M_{F,LS}$ mobility-ratio case (similar to evaluated change in recovery performance due to crossflow in **Fig. 7.12** but for other levels of physical dispersion, *Pe*) is shown in **Figs. E1-E3**.

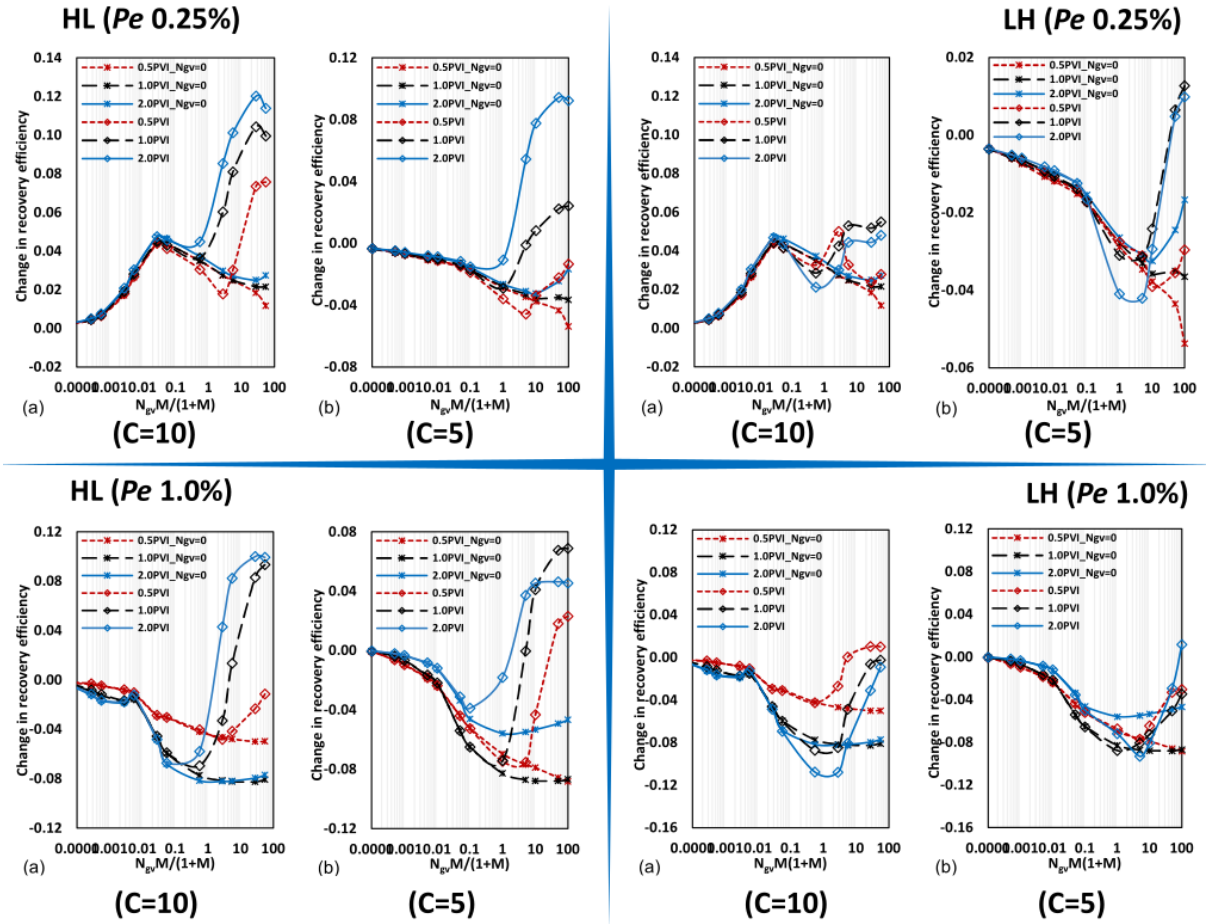


Fig. E1: Change in recovery efficiency due to gravity-assisted crossflow (ΔURF) as a function of crossflow amount ($N_{gv}M_F(1+M_F)$) in comparison to that without gravity (i.e. viscous-dominated, $N_{gv}=0$) in a secondary LSWF under a convective flow regime (*Pe* of 0.25% of the model-length) and dispersion (*Pe* of 1.0% of the model-length). Results are shown for two layer-orderings (HL – fast-layer ordered above; LH – slow-layer ordered above), each at $C=5$ and $C=10$, for different performance times (or injected LS-slug sizes: *red* $0.5\ PVI$, *black* $1.0\ PVI$, *blue* $2.0\ PVI$).

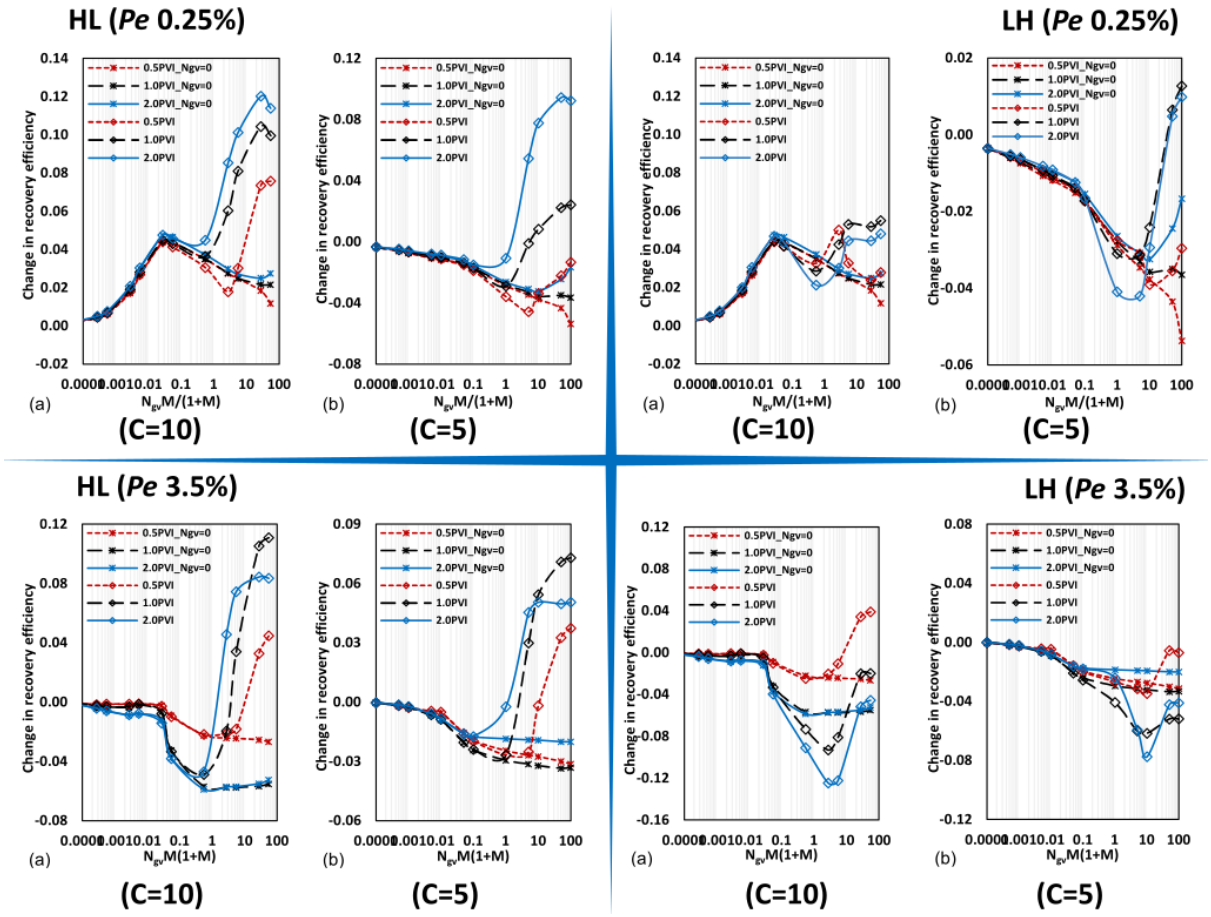


Fig. E2: Change in recovery efficiency due to gravity-assisted crossflow (ΔURF) as a function of crossflow amount ($N_{gv}M_F(1+M_F)$) in comparison to that without gravity (i.e. viscous-dominated, $N_{gv}=0$) in a secondary LSWF for a convective flow regime (*Pe* of 0.25% of the model-length) and dispersion (*Pe* of 3.5% of the model-length). Results are shown for two layer-orderings (HL – fast-layer ordered above; LH – slow-layer ordered above), each at $C=5$ and $C=10$, for different performance times (or injected LS-slug sizes: *red* $0.5\ PVI$, *black* $1.0\ PVI$, *blue* $2.0\ PVI$).

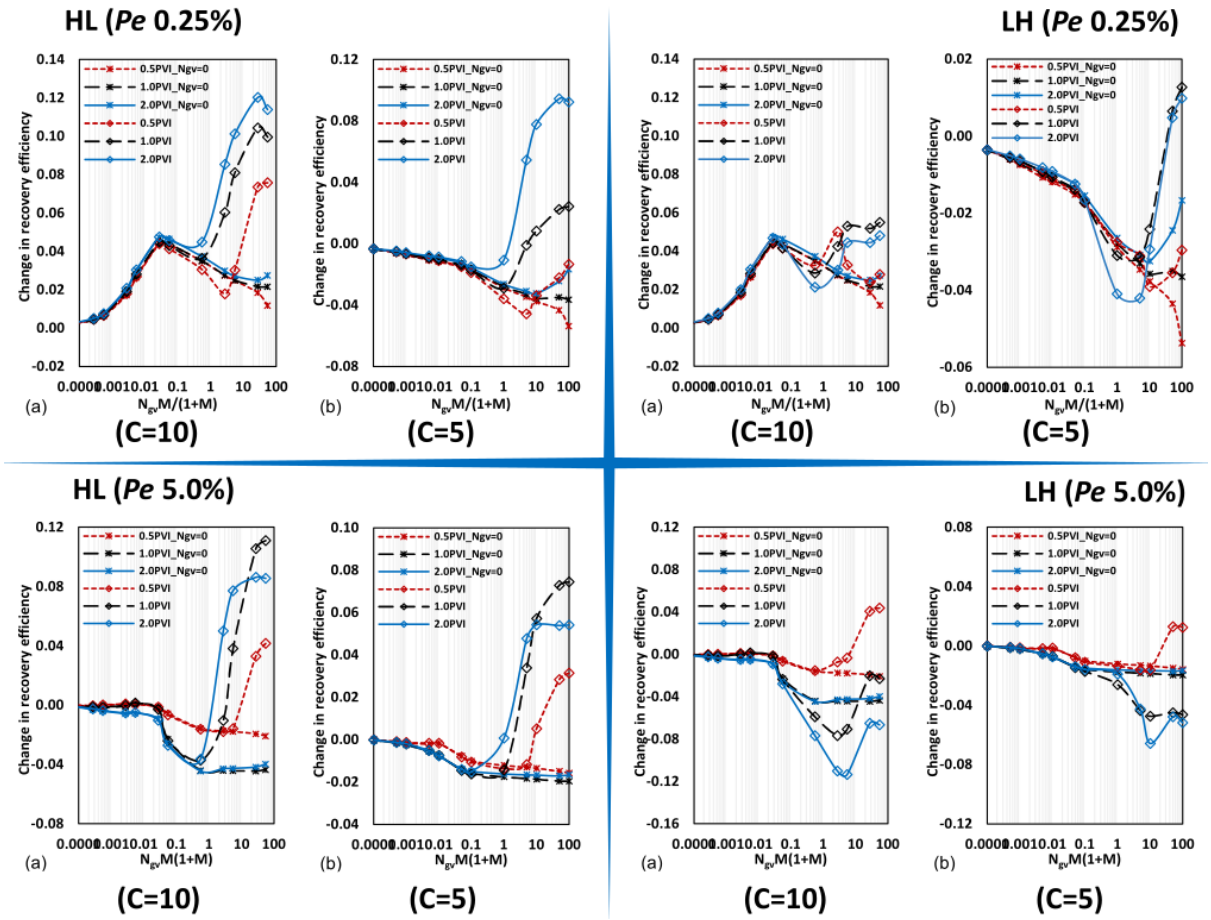


Fig. E3: Change in recovery efficiency due to gravity-assisted crossflow (ΔURF) as a function of crossflow amount ($N_{gv}M_F(1+M_F)$) in comparison to that without gravity (i.e. viscous-dominated, $N_{gv}=0$) in a secondary LSWF under a convective flow regime (*Pe* of 0.25% of the model-length) and dispersion (*Pe* of 5.0% of the model-length). Results are shown for two layer-orderings (HL – fast-layer ordered above; LH – slow-layer ordered above), each at $C=5$ and $C=10$, for different performance times (or injected LS-slug sizes: *red* $0.5\ PVI$, *black* $1.0\ PVI$, *blue* $2.0\ PVI$).